From pattern recognition to pro-inflammatory cell death - Functional characterization of the proteins NLRP7 and GSDMD

Anja Kopp

ORCID ID:
0000-0001-5484-7109
from Berlin, Germany

Submitted in total fulfilment of the requirements of the joint degree of
Doctor of Philosophy (PhD)
of
The Medical Faculty
The Rheinische Friedrich-Wilhelms-Universität Bonn
and
The Department of Microbiology and Immunology
The University of Melbourne

Bonn/Melbourne, 2023

Performed and approved by The Medical Faculty of The Rheinische Friedrich-Wilhelms-Universität Bonn and The University of Melbourne

1. Supervisor: Prof. Matthias Geyer
2. Supervisor: Prof. Seth L. Masters

Month and year of the original thesis submission: April 2023
Date of oral examination: 08th November 2023

Institute of Structural Biology, Bonn,
Director: Prof. Matthias Geyer

Table of Contents

Abbreviations

β-ME	β-mercaptoethanol
µg	microgram
µl	microliter
µm	micrometer
µM	micromolar
°	degree
°C	degree Celsius
xg	times gravity

A

Å	Ångstrom
A	Alanine
AAA+ ATPases	ATPases associated with various cellular activities
ADP	adenosine diphosphate
AIM2	absent in melanoma 2
ALR	AIM2-like receptor
AMP	adenosine monophosphate
Amp	ampicillin
AP-1	Activator protein 1
APAF-1	Apoptotic protease activating factor
APS	ammonium persulfate
ASC	apoptosis-associated speck-like protein containing a CARD
ATP	adenosine triphosphate

B

Bp	base pairs
BFP	blue fluorescent protein
BIR	Baculo-virus inhibitor of apoptosis repeat
BMDMs	murine bone marrow-derived macrophages

bp	base pairs
BSA	bovine serum albumin

C

C	Cysteine
CAPS	cryopyrin-associated periodic syndrome
CARD	caspase activation and recruitment domain
CDR	complementarity determining region
CIITA	Class II major histocompability complex transactivator
CLR	C-type lectin receptor
CMV	cytomegalovirus
CRISPR	clustered regularly interspaced short palindromic repeats
Cryo-EM	cryogenic electron microscopy
CTD	C-terminal domain
CV	column volume

D

D	Aspartate
Da	Dalton
DAMP	damage-associated molecular pattern
DC	Dendritic cell
Del	deletion
DESY	Deutsches Elektronen Synchroton
DLS	dynamic light scattering
DMEM	Dulbecco’s Modified Eagle Medium
DMSO	dimethyl sulfoxide
DNA	desoxyribonucleic acid
dNTP	deoxyribonucleotide triphosphate
Dox	doxycycline
DPBS	Dulbecco’s Phosphate Buffered Saline
dsRNa	double-stranded ribonucleic acid
DSF	Differential Scanning Fluorimetry

DTT	Dithiothreitol

E

E	Glutamate
E. *coli*	*Escherichia coli*
EDTA	Ethylenediaminetetraacetic acid
EGFP	enhanced GFP
ELISA	enzyme-linked immunosorbent assay
ESCRT	endosomal sorting complexes required for transport
ER	endoplasmic reticulum
EV	Empty vector

F

F	Phenylalanine
FACS	fluorescence-activated cell sorting
FCS	fetal calf serum
FDA	Food and Drug Administration
FISNA	fish-specific NACHT-associated domain
FMF	familial Mediterranean fever
FSC	forward scatter
FSL-1	Fibroblast-stimulating lipopeptide-1

G

G	Glycine
GFP	green fluorescent protein
GSDMD	gasdermin D
GSH	glutathione
GST	glutathione S-transferase
GTP	guanosine triphosphatase

H

H	Histidine

h	human
HA	human influenza hemagglutinin
HD	helical domain
HEK	human embryonic kidney
HEPES	4-(2-hydroxyethyl)-1-piperazineethanesulfonic acid
His	Histidine
HRP	horseradish peroxidase

I

I	Isoleucine
IBD	inflammatory bowel disease
IC_{50}	half maximal inhibitory concentration
IFN	type I interferons
IKK-β	IκB kinase
IL	interleukin
IL-R	IL receptor
IPTG	isopropyl β-D-1-thiogalactopyranoside
IRF	Interferon-regulatory factor

K

K	Lysine
kan	kanamycin
kb	kilobase
KD	dissociation constant
kDa	kilodaltons
KO	knockout

L

L	Leucine
LB	Luria Bertani
LDH	lactate dehydrogenase
LGP2	Laboratory of Genetics and Physiology 2

LPS	lipopolysaccharide
LRR	leucine-rich repeat domain
LUV	large unilamellar vesicles

M

M	Methionine
MALS	Multi Angle Light Scattering
MAVS	Mitochondrial antiviral signalling
MBP	maltose-binding protein
MDA5	Melanoma Differentiation Associated gene 5
min	minute
ml	millilitre
MW	Molecular weight
MyD88	Myeloid Differentiation primary response gene 88

N

N	Asparagine
NACHT	NAIP, CIITA, HET-E, and TP1
NaCl	Sodium chloride
NAIP	Neuronal apoptosis inhibitory protein
NBD	Nucleotide binding domain
NEK7	NIMA-related kinase 7
NF-κB	Nuclear Factor kappa-light-chain-enhancer of activated B cells
ng	Nanogram
NLR	nucleotide-binding oligomerization domain (NOD)-like receptors
NLRA	Nod-like receptor containing an acidic transactivation domain
NLRB	Nod-like receptor containing an BIR domain
NLRC	Nod-like receptor containing an CARD
NLRP	NOD-like receptor containing a PYD
nm	nanometer
nM	nanomolar
NOD	Nucleotide-binding oligomerization domain

NTD	N-terminal domain

O

OD_{600}	Optical density ar 600 nm

P

P	Proline
Pam2CSK4	Pam(2)-Cys-Ser-Lys(4)
Pam3CSK4	Pam(3)-Cys-Ser-Lys(4)
PAMP	pathogen-associated molecular pattern
PBMC	peripheral blood mononuclear cell
PBS	phosphate buffered saline
PBS-T	phosphate buffered saline + Tween 20
PCR	polymerase chain reaction
PDB	Protein Data Bank
PEG	Polyethylene glycol
PMSF	phenylmethylsulfonyl fluoride
POPC	1-palmitoyl-2-oleoyl-glycero-3-phosphocholine
POPE	1-palmitoyl-2-oleoyl-sn-glycero-3-phosphoethanolamine
PRR	Pattern recognition receptor
PTM	Posttranslational modification
PVDF	Polyvinylidenfluoride
PYD	Pyrin domain

Q

Q	Glutamine

R

R	Arginine
RIG-I	Retinoic acid Inducible Gene I
RLR	RIG-I like receptor
RNA	ribonucleic acid
RPM	revolutions per minute
RT	room temperature
RU	Response units

S

s	seconds
S	Serine
SD	Standard deviation
SDS	sodium dodecyl sulfate
SDS-PAGE	sodium dodecylsulfate polyacrylamide gel electrophoresis
SEC	Size-exclusion chromatography
SEM	Standard error of the mean
SPR	Surface Plasmon Resonance

T

T	Threonine
TAE	Tris base, acetic acid and EDTA
TB	Terrific broth
TCEP	tris(2-carboxyethyl)phosphine
TES	Tris base, EDTA and sucrose
TEMED	tetramethylethylenediamine
TEV	Tobacco Etch Virus
TIR	Toll/interleukin-1 receptor
TLR	Toll-like receptor
TMB	3 3' 5 5'-tetramethylbenzidine
TEMED	Tetramethylethylenediamine
TNF	tumor necrosis factor
TRIS	tris(hydroxymethyl)aminomethane

V

V	Valine
v/v	Volume per volume
VHH	VH domain derived from camelid heavy chain antibodies

W

W	Tryptophane
WHD	Winged helix domain
WT	Wild type
w/v	Weight per volume

Y

Y	Tyrosine

List of tables

List of figures

Abstract

Inflammasomes are cytosolic multi-protein complexes that form in response to infection or other harmful stimuli to induce innate immune responses. The core components of inflammasomes are pattern recognition receptors (PRRs) that sense conserved pathogen- or damage-associated molecular patterns. Upon recognition of their activation signal, these PRRs are able to self-oligomerize and bind to the adaptor protein apoptosis associated speck-like protein containing a CARD (ASC), which in turn recruits pro-caspase-1. Caspase-1 processes the pro-inflammatory cytokines IL-1β and IL-18 into their mature forms and cleaves the protein gasdermin D (GSDMD), causing the N-terminal domain of GSDMD to oligomerize and form large pores in the plasma membrane. GSDMD pore formation leads to cytokine release, and ultimately cell death, known as pyroptosis.

Among the PRRs involved in inflammasome formation, members of the NOD-like receptor protein family, including NLRP1, NLRP3 and NLRP6, are best desribed. However, the role of the NLRP family member NLRP7 in inflammasome activation remains largely unknown. Here, HEK cell-based inflammasome reconstitution assays were used to investigate its role as an inflammasome-assembling PRR. In contrast to other well-established inflammasome forming PRRs such as NLRP3, NLRC4 and pyrin, neither overexpression nor stimulation of NLRP7 induced ASC speck formation in HEK cells. Co-expression of NLRP7 together with NLRP3 reduced NLRP3-mediated ASC speck formation, whereas, co-expression of NLRP7 together with NLRC4 and pyrin increased the ASC speck formation induced by these PRRs. To provide a new tool for studying NLRP7, NLRP7-targeting nanobodies were generated. Eight high affinity binders were identified that recognize two distinct epitopes on the NLRP7 pyrin domain. The nanobodies can be expressed intracellularly as intrabodies and can be used as primary detection agents in western blots.

GSDMD is the key mediator of pyroptosis which occurs downstream of all inflammasome pathways. Pyroptosis is observed in many diseases with excessive inflammation, making GSDMD an attractive drug target. In this study, six GSDMD binding nanobodies were characterized in terms of their binding

affinity, stability, and effect on GSDMD pore formation. Three of the nanobodies inhibited GSDMD pore formation in a liposome leakage assay, although caspase cleavage was not perturbed. The crystal structure of human GSDMD in complex with two nanobodies, one inhibitory and one non-inhibitory, was determined at 1.9 Å resolution, providing detailed insights into the GSDMD-nanobody interactions and epitope binding. The pore formation is sterically blocked by one of the nanobodies that binds to the oligomerization interface of the N-terminal domain in the multi-subunit assembly. These biochemical and structural findings provide new tools for studying inflammasome biology and build a framework for the design of novel GSDMD targeting drugs.

Preface

The work presented in this thesis was conducted in the laboratories of Prof. Matthias Geyer (Institute of Structural Biology, The Rheinische Friedrich-Wilhelms-Universität Bonn, Germany) and Prof. Seth L. Masters (Walter and Eliza Hall Institute of Medical Research (WEHI), University of Melbourne, Australia). I was supported by DFG funded International Graduate School GRK 2168. My contribution to experiments presented in each chapter of this thesis is listed below:

Chapter 3: 90 %

Shouya Feng, Masters lab, WEHI, contributed to Figure 11. She repeated the co-transfection experiments of NLRP3 and NLRC4 plus NLRP7$_{1009}$ to achieve n = 2. (Figure 11a, b, right panels). Shouya carried out both experiments presented in Figure 11c, right panel (co-transfection of pyrin and NLRP7$_{1009}$). The experiment was designed by me.

Chapter 4: 90 %

The process of generating NLRP7 targeting nanobodies was started by Heide Behrmann, Institute of Structural Biology, University of Bonn. She expressed and purified the proteins used for immunization. The immunization of llamas, cloning of a nanobody library and selection of initial binders by phage display were carried out by the Core Facility Nanobodies, Medical Faculty, University of Bonn. The SPR measurements depicted in Figure 15 and Figure 16 were carried out by Karl Gatterdam, Institute of Structural Biology, University of Bonn. I purified the analysed proteins and assisted in conducting the experiment.

Chapter 5: 90 %

Parts of Chapter 5 are based on the manuscript “Pyroptosis inhibiting nanobodies block Gasdermin D pore formation” which has been submitted for review and is available as preprint on BioRxiv (https://doi.org/10.1101/2023.04.20.537705). I am the first author of this publication and wrote the first version of the manuscript. I expressed and purified the proteins, carried out biochemical experiments and

crystallized the GSDMD complex. I determined the structure with the help of Gregor Hagelüken, Institute of Structural Biology, University of Bonn. I conceptualized the study together with Matthias Geyer, Institute of Structural Biology, University of Bonn, and Florian I. Schmidt, Institute of Innate Immunity, University of Bonn.

Isabell Jamitzky, University of Bonn, supported the liposome leakage assay. Data represented in Figure 22 were generated by me.

Jonas Möcking performed the SPR measurements shown in Figure 21 and Figure 22, Institute of Structural Biology, University of Bonn. I provided the purified proteins and assisted in conducting the experiment.

Gregor Hagelüken, Institute of Structural Biology, University of Bonn, helped me to determine the structure of the GSDMD nanobody complex.

Florian I. Schmidt, Institute of Innate Immunity, University of Bonn provided the plasmids for the GSDMD targeting nanobodies, which he identified with together with Lisa D. J. Schiffelers.

Acknowledgments

This thesis would not have been possible without the help and support of many people to whom I would like to express my gratitude.

First and foremost, I would like to thank my primary supervisors Matthias Geyer and Seth Masters. I would like to thank you for giving me the opportunity to join your labs, and your invaluable guidance throughout my entire PhD and the process of writing this thesis. I really learned a lot from both of you! I would like to thank both of you for your availability and responsiveness whenever I needed assistance.

To Matthias, thank you for your great advice on structural biology, your passion for this field of research has really motivated me to pursue my own project! Thank you for providing such a well-equipped lab and creating a working environment where the whole team gets along well and supports each other.

To Seth, thank you for all your scientific advice, encouragement and constructive feedback that motivated me during my time in Melbourne and even beyond! Thank you for the warm welcome in your lab, integrating me into the team and inviting me to the really nice lab retreat.

To my thesis advisory committee members in Melbourne, Melissa Call, James Vince and Melanie Dietrich, thank you so much for finding the time to give me advice on my thesis although I was on another continent for most of the time. I really appreciate your insightful suggestions that helped me to strengthen my arguments.

To my committee members, Eicke Latz and the external reviewers nominated by the University of Melbourne, thank for examining my thesis!

To Gregor Hagelüken, thank you for teaching me so much about protein X-ray crystallography, starting from the theory to lab practice to structure determination. You really are a great teacher! Thank you for your patience and always being approachable when I had questions!

To Florian Schmidt, thank you for letting me join the GSDMD-nanobody project and for the great collaboration! Thank you for your scientific input and for always being open for meetings and project discussions!

To Lisa Schiffelers, thank you for being my project partner and friend! Thank you for working with me and discussing some science, but also for sharing some coffee breaks with me!

To all past and present members of the Institute of Structural Biology in Bonn and the Masters lab in Melbourne, you are all awesome colleagues and it was a great pleasure to work together with you! In Bonn, I would like to especially thank Inga Hochheiser, Martin Peter, Maximilian Schmitz, Ines Kaltheuner, Sophie Binder, Jonas Möcking, Niels Schneberger, Jale Sariyar, Elif Tokmak, Robert Düster and Michael Marleaux for being always friendly and supportive and cheering me up, be it in the lab or after work! In Melbourne I would like to especially thank Annemarie Steiner, June Sun, Klara Kong, Cassandra Harapas, Pawat Laohamonthonkul, Brooke McDonald, Katja Hrovat-Schaale, Elizabeth Mulazzani, Thomas Reygaerts, Sophia Davidson, Sophie Collard, Shouya Feng and Yaoyuan Zhang for being great colleagues and making my time in Melbourne unforgettable!

To Annemarie Steiner and Jonas Möcking, thank you for being my IRTG2168 buddies and mentors! It was really helpful to have both of you around and getting advice from you on my project, the program, both labs, thesis writing and so much more!

To the IRTG2168 program, especially Christian Kurts, Sammy Bedoui, Lucie Delforge, Marie Greyer, Sandra Rathmann and Annabelle Blum, thank you for making this PhD program possible! Thank you for all your help and organisational support and the opportunity to participate in this program!

To my friends and family, thank you for always being there for me! Your love and support was important for all the steps I have taken in my career and private life so far!

List of publications

Hochheiser, I. V., Behrmann, H., Hagelueken, G., Rodriguez-Alcazar, J. F., **Kopp, A.**, Latz, E., Behrmann, E., Geyer, M. Directionality of PYD filament growth determined by the transition of NLRP3 nucleation seeds to ASC elongation. (2022) *Science Advances* **8**, https://doi.org/10.1126/sciadv.abn7583

Kopp, A., Hagelueken, G., Jamitzky, I., Moecking, J., Schiffelers, L. D. J., Schmidt, F. I., Geyer, M. Pyroptosis inhibiting nanobodies block Gasdermin D pore formation. (2023) *submitted.*
Available as preprint on BioRxiv: https://doi.org/10.1101/2023.04.20.537705

Schiffelers, L. D. J., Normann, S., Binder, S. C., Hagelauer, E., **Kopp**, **A.**, Alon, A., Geyer, M., Ploegh, H. L., Schmidt, F. I. Antagonistic nanobodies reveal mechanism of GSDMD pore formation and unexpected therapeutic potential. (2023) *submitted*.
Available as preprint on BioRxiv: doi: https://doi.org/10.1101/2023.04.20.537718

1. Introduction

1.1. Innate Immunity

The mammalian immune system is a complex network of organs, cells and molecules that work together to protect the body from infection and toxic substances. It can be divided into two interacting subsystems: the innate and the adaptive immune systems. The innate immune system is the first line of defence against sterile inflammation and invading pathogens including bacteria, viruses and fungi. It provides a rapid immune response that can lead to direct clearance of the invading organism, or initiate responses from the adaptive immune system. The innate immune system consists of physical and chemical barriers as well as molecular and cellular components. Physical barriers such as the skin, and chemical barriers including antimicrobial enzymes in the mucosa, prevent pathogens from entering the body (Murphy, Kenneth, 2017). Another chemical barrier is the complement system, a large group of plasma- and membrane-associated proteins, with antimicrobial functions (Gadjeva, 2014). The cellular component of the innate immune system includes three different types of phagocytes - macrophages, dendritic cells and granulocytes, as well as natural killer (NK) cells (Marshall *et al.*, 2018). Granulocytes can be further subdivided into neutrophils, eosinophils, basophils and mast cells, of which the neutrophils are the most abundant and important cell type (Lin and Loré, 2017). Together, the innate immune cells are involved in the killing of pathogens, secretion of inflammatory mediators, and presentation of antigens to cells of the adaptive immune system (Voehringer, 2012; Ravin and Loy, 2016; Collin and Bigley, 2018; Agier *et al.*, 2018; Silvestre-Roig *et al.*, 2019).

Innate immune cells recognize pathogens via genetically encoded pattern recognition receptors (PRRs). PRRs detect conserved microbial structures called pathogen associated molecular patterns (PAMPs) and/or endogenous molecules that are released from damaged or dying cells called damage associated molecular patters (DAMPs). Recognition of the pathogen triggers internal mechanisms that result in the production of antimicrobial substances or signalling

molecules, including cytokines, chemokines and type I interferons, which coordinate the inflammatory response (Takeuchi and Akira, 2010).

In contrast to the innate immune response, the adaptive immune response takes longer to develop, but is more specific and capable of developing a memory. The adaptive immune system relies on B and T lymphocytes, which are equipped with receptors to recognize pathogen-specific antigens. Moreover, the B cells of the adaptive immune system secrete circulating antibodies. Although adaptive immune responses are very effective in fighting pathogens, they rely on the involvement of the innate immune system for their activation and regulation (Clark and Kupper, 2005).

1.2. Pattern recognition receptors

Pattern recognition receptors (PRRs) are innate immune sensors that are responsible for the detection of harmful microorganisms and cell damage. They recognize conserved pathogen- or damage- associated molecular patterns (PAMPs/DAMPs) leading to the initiation of antimicrobial processes (Amarante-Mendes *et al.*, 2018). PRRs can be membrane-bound, such as Toll-like receptors (TLRs) and C-type lectin receptors (CLRs), cytoplasmic, such as RIG-I-like receptors (RLRs), NOD-like receptors (NLRs) and absent in melanoma-2 (AIM2)-like receptors (ALRs), or extracellular, such as pentraxins, collectins and ficolins (Rathinam *et al.*, 2010; P. Zhang *et al.*, 2015; Murphy, Kenneth, 2017). PRRs typically consist of ligand recognition-, intermediate-, and effector domains. Sensing of the ligand often leads to the recruitment of adaptor molecules that share the same effector domain as the PRR. This initiates downstream signalling events leading to the production of inflammatory mediators and antimicrobial substances (Li and Wu, 2021). Today, information on approximately 470 unique PRRs and their ligands can be found in the PRRDB 2.0 database (Kaur *et al.*, 2019). Four major PRR families shall be described here: the families of TLRs, CLRs, RLRs and NLRs.

1.2.1. Toll-like receptors (TLRs)

The human TLR family comprises 10 membrane-bound receptors that can recognize both extracellular and intracellular pathogens. They consist of an N-terminal ligand sensing leucine rich repeat (LRR) domain, a transmembrane region and a cytoplasmic Toll/IL-1R homology (TIR) domain (Akira *et al.*, 2006). The different TLRs are located at distinct cellular sites and recognize different PAMPs and therefore different types of microbes. TLR1, TLR2, TLR4, TLR5, TLR6 and TLR10 are located at the plasma membrane, whereas TLR3, TLR7, TLR8 and TLR9 are found at the endolysosomal membranes. The plasma membrane-bound TLRs detect a wide range of PAMPs including bacterial cell wall components and components of viruses and fungi. TLR2 forms heterodimers together with either TLR1 or TLR6. The TLR2/TLR6 complex recognizes microbial diacylated lipopeptides whereas the TLR2/TLR1 complex detects triacylated lipopetides (Takeuchi and Akira, 2010). TLR4 recognizes lipopolysaccharide (LPS), a component of the cell wall of Gram-negative bacteria, and TLR5 specifically detects bacterial flagellin. TLR10 is capable of homodimerization as well as heterodimerization with TLR1 or TLR2. The TLR10 homodimer is the only known TLR that can elicit anti-inflammatory functions (Fore *et al.*, 2020). Several TLR10 ligands have been proposed, including LPS, di- and triacylated lipopeptides and dsRNA, however the full range of TLR10 agonists needs further exploration(Su *et al.*, 2021). and The TLRs at the endolysosmal membranes sense nucleic acids taken up by endocytosis, for example TLR3 senses viral dsRNA and TLR7 viral ssRNA. In addition to viral ssRNA, TLR8 also detects bacterial RNA, whereas TLR9 recognizes bacterial and viral DNA (Kawasaki and Kawai, 2014). Activation TLRs initiates a signalling cascade involving a number of adaptor molecules leading to the activation of the transcription factors nuclear factor kappa B (NF-κB), activator protein 1 (AP-1), and interferon regulatory factor 3 and 7 (IRF3, IRF7). This leads to the production of pro-inflammatory cytokines and chemokines, antimicrobial substances and type I interferons (IFN), a class of cytokines that promotes antiviral responses (Moynagh, 2005; Kawai and Akira, 2007).

1.2.2. C-type lectin receptors (CLRs)

Transmembrane C-type lectin receptors (CLRs) are a group of proteins that bind to a variety of PAMPs derived from pathogens such as bacteria, viruses, fungi, and parasites. They are a superfamily of proteins with distinct ligand binding specificities and signalling pathways, that share an extracellular carbohydrate recognition domain (CRD) as a common feature (Kingeter and Lin, 2012; Brown *et al.*, 2018). Many CLRs bind carbohydrates, that are often found on the surface of pathogens, including mannose, fucose, and β-glucan, but others are also specific for lipids or inorganic molecules (Monteiro and Lepenies, 2017; Brown *et al.*, 2018). Carbohydrate binding usually occurs in a calcium-dependent manner (Drouin *et al.*, 2020). CLRs are expressed by a variety of immune cells, including dendritic cells, macrophages, and mast cells (Ebner *et al.*, 2004; Guasconi *et al.*, 2011; Agier *et al.*, 2018; Sosa Cuevas *et al.*, 2022). A well characterized example for CLRs is Dectin-1, a sensor of fungal β-glucans. Next to the extracellular CRD, Dectin-1 is composed of an intracellular tail displaying an immunoreceptor tyrosine-based activation motif (ITAM)-like motif (Brown, 2006). Upon ligand binding, dectin-1 becomes tyrosine phosphorylated by Syk kinase, which initiates signalling cascades resulting in the production of a number of cytokines and chemokines, including tumour-necrosis factor (TNF), CXC-chemokine ligand 2 (CXCL2), and the interleukins IL-2, IL-10 and IL-12 (Rogers *et al.*, 2005; Brown, 2006).

1.2.3. RIG-I-like receptors (RLRs)

Retinoic acid-inducible gene I (RIG-I)-like receptors (RLRs) are a group of cytoplasmic RNA sensors that are critical for the detection of viral nucleic acids. The RLR family consists of three members: RIG-I, melanoma differentiation-associated 5 (MDA5), and laboratory of genetics and physiology 2 (LGP2), which each possess a DExD/H-box RNA helicase-like domain that allows them to bind viral RNA (Rehwinkel and Gack, 2020). RIG-I and MDA5 recognize various features typical for viral RNA such as uncapped ssRNA and dsRNA with a 5'-triphosphate (Kell and Gale, 2015). However, MDA5 and RIG-I are non-redundant and have different ligand specificities and recognize different types of

viruses (Kato *et al.*, 2006; Loo *et al.*, 2008; Mitchell and Colwell, 2018). LGP2 lacks the CARD domain present in RIG-I and MDA5 which is essential for the initiation of downstream antiviral signalling (Bruns and Horvath, 2015). Nevertheless, LGP2 is important for antiviral responses and is thought to interact cooperatively with MDA5 and regulate RIG-I signaling (Bruns and Horvath, 2015; Sanchez David *et al.*, 2019). Binding of viral RNA to RIG-I and MDA5 induces conformational changes in their protein structure, leading to the exposure of their caspase recruitment domains (CARDs) which allows binding of the signalling adaptor mitochondrial antiviral signalling protein (MAVS) at the mitochondrial membrane (Seth *et al.*, 2005; Kawai *et al.*, 2005). This activates signalling pathways that culminate in the activation of IRF3/7 and NF-κB, leading to the production of antiviral molecules and type I interferons (IFN) (Paz *et al.*, 2011; Wang *et al.*, 2012; McNab *et al.*, 2015).

1.2.4. NOD-like receptors (NLRs)

Another class of cytosolic PRRs are the nucleotide-binding oligomerization domain (NOD)-like receptors (NLRs), which comprise 22 members in humans (Figure 1). The NLR family can be divided into the subfamilies of NLRA, NLRB, NLRC, NLRP and NLRX proteins according to their N-terminal effector domains. These N-terminal domains are acidic transactivation, baculovirus inhibitor of apoptosis repeat (BIR)-like, CARD, PYRIN (PYD) or X/MTS domain, respectively (Meunier and Broz, 2017; Chen *et al.*, 2021) (Figure 1B). NLRs belong to the signal transduction ATPases with numerous domains (STAND) clade within the superfamily of AAA+ ATPases and are for this reason thought to function as molecular switches which exist in an ADP-bound inactive and an ATP-bound active state. It is believed that the activation of NLRs allows the exchange of ADP with ATP (Proell *et al.*, 2008).

Common to all NLR proteins is their central NACHT domain followed by a leucine rich repeat (LRR) domain (Figure 1A)., with the exception of NLRP10, which lacks the LRR domain. The NACHT domain is capable of ATP-binding and hydrolysis, and plays an important role in the activation and self-oligomerization of NLR proteins (L. Zhang *et al.*, 2015; Xiao *et al.*, 2023). The LRR domains are

important in maintaining the proteins in an inactive state in the absence of an activating stimulus (Moghaddas *et al.*, 2018; Andreeva *et al.*, 2021; Hochheiser, Pilsl, *et al.*, 2022). While the physiological function of some NLRs is well characterized, the role of other NLRs remains still elusive. Overall, NLRs have been described to exert diverse functions in immunity such as regulation of antigen presentation, inflammation and cell death, but also in embryonic development (Meunier and Broz, 2017).

The NLRA family consists of a single member: the major histocompatibility complex (MHC) class II transactivator (CIITA), which acts as a transcription factor to regulate of MHC-II expression. This is important for antigen presentation in order to activate T cells (León Machado and Steimle, 2021). Like the NLRA family, also the NLRB family has only one member: the NLR family Apoptosis Inhibitory Protein (NAIP) which exerts anti-apoptotic functions by inhibiting the necessary caspases-3, -7 and -9, and is an important component of the NLRC4 inflammasome (Velloso *et al.*, 2019). Further, the NLRC family consists of five members, NLRC1-5. NLRC1 and NLRC2 are also known as NOD1 and NOD2 and sense specific bacterial peptidoglycans, components of the cell wall of Gram-positive bacteria (Inohara *et al.*, 2001; Girardin *et al.*, 2003). Ligand sensing leads to self-oligomerization of NOD1 and NOD2 via their NACHT domains, followed by interaction with the adaptor protein receptor-interacting serine-threonine kinase 2 (RIPK2). This stimulates signalling pathways leading to the activation of NF-κB, AP-1 and IRF7 and thereby the production of pro-inflammatory mediators (Trindade and Chen, 2020). Less well characterized is NLRC3, or NOD3, which has been reported to have a regulatory function in pathways important for cell proliferation, autophagy and apoptosis (Karki *et al.*, 2016; Zou *et al.*, 2020). NLRC4 cooperatively forms inflammasomes together with NAIP, which is described in more detail in chapter 1.3.2. The NLRC4 inflammasome forms in response to bacterial stimuli such as type III or type IV secretion systems or flagellin (Wen *et al.*, 2021). NLRC5 is also known as CITA. In contrast to CIITA which is important for the transcriptional regulation of MHC class II genes, NLRC5 is a key regulator of MHC class I expression and thus antigen presentation to T cells (Kobayashi and van den Elsen, 2012). Next, the NLRP family comprises 14

members, some of which have been reported to be involved in innate immune processes through the formation of inflammasomes, whereas others are involved in reproduction (Tian *et al.*, 2009; MacDonald *et al.*, 2013). The best studied NLRP inflammasome, the NLRP3 inflammasome, is summarized in chapter 0, but other NLRPs such as NLRP1, NLRP2, NLRP6, NLRP7, NLRP9, NLRP11 and NLRP12 have also been implicated in inflammasome formation (Khare *et al.*, 2012; Vladimer *et al.*, 2012; Minkiewicz *et al.*, 2013; Zhu *et al.*, 2017; D *et al.*, 2021; Gangopadhyay *et al.*, 2022). In addition, NLRP2, NLRP7, NLRP9 and NLRP5, and NLRP14 have been shown to be involved in reproduction and embryonic development (Abe *et al.*, 2017; Amoushahi *et al.*, 2019; Mullins and Chen, 2021; Sang *et al.*, 2021). The physiological functions of NLRP4, NLRP8, NLRP10, NLRP13 and NLRP14 are less well characterized. However, NLRP4 is thought to be involved in negative regulation of type I interferon signalling (Cui *et al.*, 2012). Finally, the only member of the NLRX family, NLRX1, is located in the mitochondria and functions as a negative regulator of inflammation by interfering with RLR pathways (Liu *et al.*, 2022).

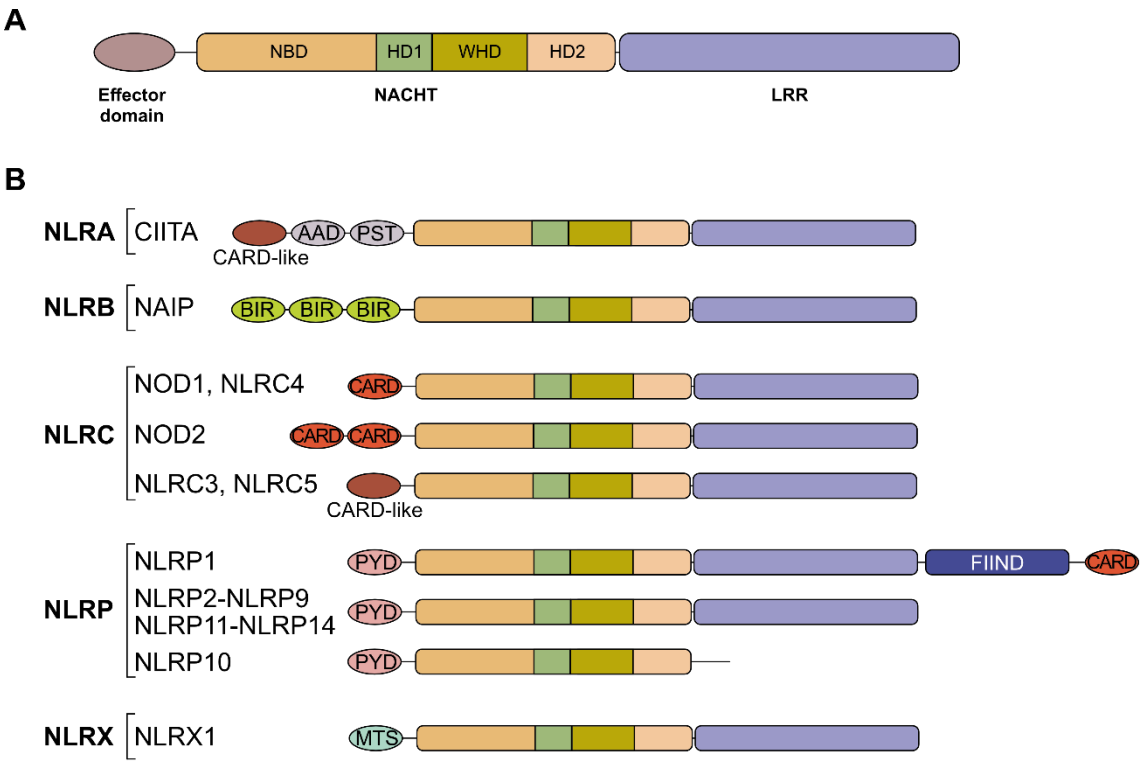

Figure 1:The NLR protein family. A) Members of the NLR protein family contain an N-terminal effector domain, a central NACHT domain and a C-terminal LRR domain. The NACHT domain can be further subdivided into the nucleotide binding domain (NBD), helical domain 1 (HD1), winged helix domain (WHD) and helical domain 2 (HD2) subdomains **B)** Domain architecture of the NLR protein family members. CARD: caspase activation and recruitment domain, AAD: acidic domain, PST: proline, serine and threonine rich domain, BIR: baculovirus inhibitor of apoptosis repeat like domain, PYD: pyrin domain, FIIND: Function to find domain, MTS: mitochondria targeting sequence domain. Figure adapted from Chou et al. 2023 Mar 27.

1.3. Inflammasomes

Upon recognition of their activation signals, some cytosolic PRRs form multi-protein complexes, called inflammasomes. Inflammasome assembly leads to the activation of pro-inflammatory caspases, triggering further immune responses (Martinon *et al.*, 2002). Several PRRs from different protein families have been described to initiate inflammasome formation. In many cases, inflammasome activation requires a priming step involving the transcriptional upregulation of inflammasome components and effector molecules, including sensor proteins and pro-IL-1β. This is often achieved by the activation of NF-κB through TLR

signalling (Patel *et al.*, 2017). Inflammasomes can be divided into canonical and non-canonical inflammasomes. In canonical inflammasomes, activation of the sensor protein by recognition of PAMPs or DAMPs results in conformational changes in the PRR that allow oligomerization and interaction with an adapter protein, which is in many cases the apoptosis-associated speck-like protein containing a CARD (ASC). Through its CARD domain, ASC can recruit caspase-1 via CARD-CARD domain interactions, completing the inflammasome assembly and leading to the proximity-induced activation of caspase-1 (Broz and Dixit, 2016; Xiao *et al.*, 2023). Activated caspase-1 cleaves the precursors of the pro-inflammatory cytokines IL-1β and IL-18, and the pore-forming protein Gasdermin D (GSDMD) into their active forms (Kostura *et al.*, 1989; Akita *et al.*, 1997; Kayagaki *et al.*, 2015; Shi *et al.*, 2015; He *et al.*, 2015). The N-terminal domain of GSDMD forms large pores in the plasma membrane through which the mature cytokines IL-1β and IL-18 are released and ultimately, GSDMD pore formation leads to a pro-inflammatory form of cell death termed pyroptosis (Figure 2) (Shi *et al.*, 2015; He *et al.*, 2015; Liu *et al.*, 2016). The best studied canonical inflammasomes are the NLRP1, NLRP3, NLRC4, AIM2 and pyrin inflammasomes (Broz and Dixit, 2016). The details of the assembly of the NLRP3, NLRC4 and pyrin inflammasomes are summarized below.

In contrast to the canonical inflammasome pathway, in the non-canonical pathway, caspase-4 or caspase-5 (or caspase-11 in mice) are activated by direct recognition of cytosolic LPS, a bacterial cell wall component (Kayagaki *et al.*, 2011; Shi *et al.*, 2014; Schmid-Burgk *et al.*, 2015; Viganò *et al.*, 2015). Sensing of LPS leads to self-oligomerization and activation of these caspases that are then able to cleave GSDMD but not pro-IL-1β and pro-IL-18 (Kayagaki *et al.*, 2011; Shi *et al.*, 2014; Shi *et al.*, 2015). However, GSDMD pore formation induces imbalances in the cellular ion homeostasis that can lead to activation of NLRP3 which in turn leads to the activation of the canonical inflammasome pathway (Kayagaki *et al.*, 2011; Shi *et al.*, 2014; Schmid-Burgk *et al.*, 2015; Kayagaki *et al.*, 2015).

Dysregulation of inflammasome pathways can cause numerous auto-inflammatory diseases. For example, gain of function mutations in NLRP3 lead

to a group of diseases summarized as cryopyrin-associated periodic syndrome (CAPS), including familial cold autoinflammatory syndrome (FCAS), Muckle-Wells syndrome (MWS), and neonatal onset multi-system inflammatory disease (NOMID)/chronic infantile neurologic cutaneous articular syndrome (CINCA), characterized by systemic chronic inflammation, rashes, fevers and limb pain (Kile and Rusk, 1940; Muckle, 1979; Booshehri and Hoffman, 2019; Welzel and Kuemmerle-Deschner, 2021). Mutations in the *MEFV* gene encoding pyrin cause the autoinflammatory disease Familial Mediterranean Fever (FMF) with recurrent episodes of systemic inflammation and pain in the abdomen, chest or joints (The International FMF Consortium 1997; The French FMF Consortium et al. 1997). Moreover, mutations in NLRP1 and NLRC4 have been found to cause NLRP1-associated autoinflammation with arthritis and dyskeratosis (NAIAD) and NLRC4-associated autoinflammatory disease, respectively (Grandemange *et al.*, 2017; Romberg *et al.*, 2017; Steiner *et al.*, 2022).

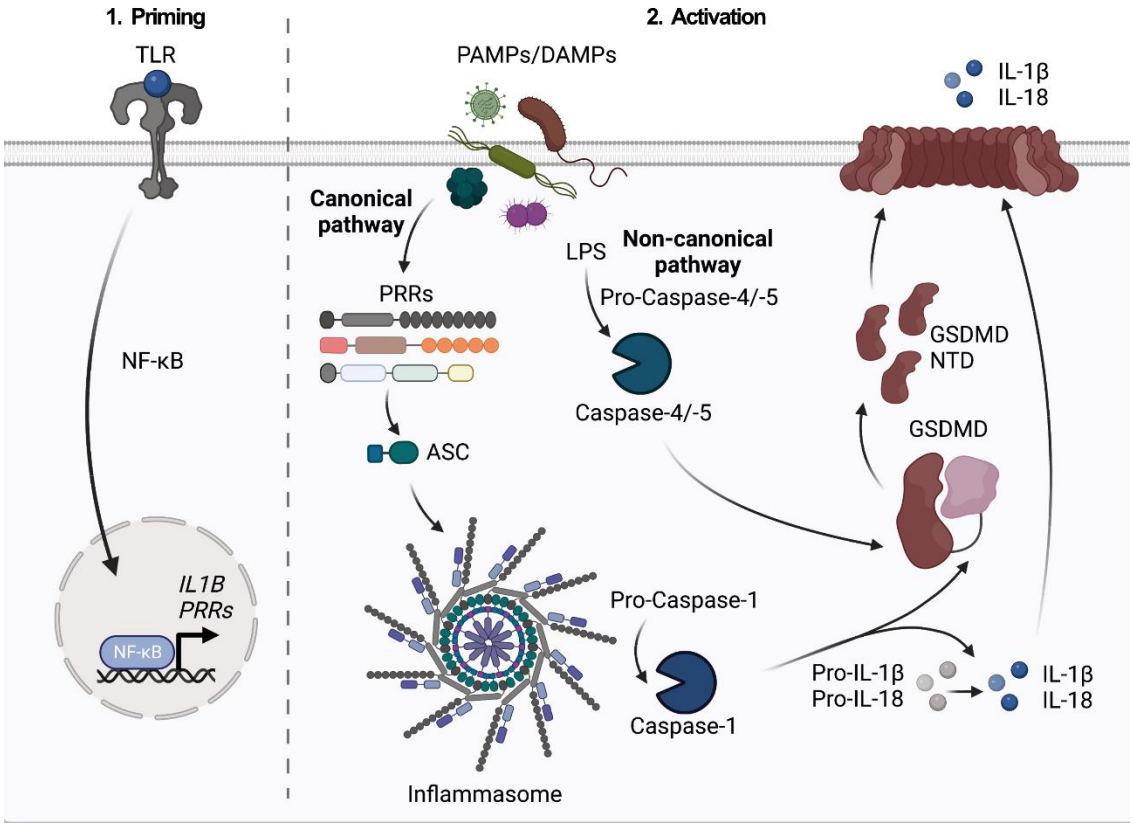

Figure 2: The inflammasome signaling pathways. Inflammasome activation often requires a priming step involving the transcriptional upregulation of inflammasome components and effector molecules, including sensor proteins and pro-IL-1β. This is often achieved by the activation of NF-κB through TLR signalling. In the canonical inflammasome pathway, pathogen- or damage-associated molecular patterns (PAMPs/DAMPs) are recognized by specific cytosolic pattern recognitions receptors (PRRs) including NLRP1, NLRP3, NLRP6, NAIP/NLRC4, AIM2 and pyrin. This leads to oligomerization of the PRRs and the recruitment of adaptor proteins (typically ASC) and caspase-1 to a multi-protein complex termed inflammasome. In the non-canonical inflammasome pathway, caspase-4 and caspase-5 sense cytosolic bacterial LPS which leads to their oligomerization and activation. The activated pro-inflammatory caspases-1/-4/-5 cleave and activate GSDMD so that the NTD of GSDMD can oligomerize and form pores at the plasma membrane. Caspase-1 moreover processes the pro-inflammatory cytokines IL-1β and IL-18 into their mature forms, which are then released through GSDMD pores. GSDMD pore formation eventually leads to pyroptotic cell death. Figure created with Biorender.

1.3.1. The NLRP3 inflammasome

The NLRP3 inflammasome was first described in the early 2000s and is now the most extensively studied inflammasome (Manji *et al.*, 2002; Agostini *et al.*, 2004). Unlike other PRRs, NLRP3 does not bind directly to pathogen derived ligands, but functions as a sensor of perturbations in the cellular homeostasis and is therefore able to respond to a wide range of pathogens and conditions (Liston and Masters, 2017).

Activation of the NLRP3 inflammasome is thought to involve a two-step mechanism. In a first priming step, the expression of NLRP3, and also the NLRP3 inflammasome substrates IL-1β and IL-18, is increased. This is achieved by TLR and/or cytokine signalling induced activation of NF-κB (Bauernfeind *et al.*, 2009; McKee and Coll, 2020). In the second step, an activating stimulus initiates the inflammasome assembly. Many stimuli have been shown to activate NLRP3, including imbalances in the cellular ion homeostasis caused by the efflux of potassium, chloride or calcium, and molecules associated with damage to cell organelles such as mitochondria, lysosomes, the endoplasmic reticulum and the Golgi apparatus (Akbal *et al.*, 2022). Post-translational modifications (PTMs) are also necessary for NLRP3 activation. PTMs that are described to regulate NLRP3 activity include phosphorylation, sumoylation and ubiquitination (Seok *et al.*, 2021). In addition, the NIMA related kinase 7 (NEK7) has been identified as a binding partner of NLRP3 and binding of NEK7 to NLRP3 downstream of potassium efflux is required to induce inflammasome formation (Schmid-Burgk *et al.*, 2016; He *et al.*, 2016). Recent studies revealed that inactive NLRP3 exists as a membrane-bound decameric complex, in which the LRRs of the NLRP3 molecules form a cage that shields their PYDs, which are essential for the interaction with ASC (Andreeva *et al.*, 2021; Hochheiser, Pilsl, *et al.*, 2022). The cryo-EM structure of the active NLRP3 inflammasome disc comprising NLRP3, NEK7 and ASC has recently been determined by Xiao and colleagues (Xiao *et al.*, 2023). This structure showed that, upon activation, the fish-specific NACHT-associated (FISNA) domain of NLRP3 undergoes conformational changes and mediates critical NLRP3-NLRP3 interactions, whereas neither NEK7 nor the NLRP3 LRRs participate in the oligomerization. Therefore, Xiao and colleagues

propose a new mechanism of NLRP3 inflammasome activation that goes in concert with previous studies, that showed NLRP3 binding to the trans-Golgi network (TGN) and association with the microtubule-organizing center (MTOC) (Chen and Chen, 2018; Magupalli *et al.*, 2020). This mechanism includes the formation of inactive NLRP3 cages at the TGN, conformational changes in NLRP3, and dispersion of the TGN upon addition of an activating stimulus and trafficking of dispersed TGN vesicles to the MTOC, followed by opening of the NLRP3 cage through the NEK7, and formation of the active NLRP3 disc, ready for ASC recruitment. However, further investigations are required to fully clarify the mechanism of NLRP3 activation and inflammasome assembly.

1.3.2. The NLRC4 inflammasome

The NLRC4 inflammasome plays a critical role in defence against bacterial pathogens (Wen *et al.*, 2021). In 2006, two independent groups showed for the first time that cytoplasmic bacterial flagellin leads to the activation of caspase-1 in an NLRC4-dependent manner (Franchi *et al.*, 2006; Miao *et al.*, 2006). Later, it was found that NAIP proteins are required for the activation of the NLRC4 inflammasome in mice, and that these proteins mediate ligand sensing, whereas NLRC4 serves as a signalling adaptor (Zamboni *et al.*, 2006; Lightfield *et al.*, 2008; Kofoed and Vance, 2011). The mouse genome encodes seven different NAIP proteins that recognize different bacterial ligands thereby driving NLRC4 inflammasome specificity (Endrizzi *et al.*, 2000; Kofoed and Vance, 2011). In contrast, humans express only one NAIP protein (hNAIP), which recognizes several bacterial pathogens by their T3SS needle proteins (Yang *et al.*, 2013). Upon recognizing ligands, NAIPs co-oligomerize with NLRC4 and NLRC4 recruits caspase-1 via its CARD domain (Vance, 2015). Hence, although it is often referred to the NLRC4 inflammasome, NAIPs function as PRRs, whereas NLRC4 functions as adaptor protein to recruit caspase-1. The structures of inactive mouse NLRC4 and the activated NAIP2/NLRC4 and NAIP5/NLRC4 complexes have been determined by X-ray crystallography and cryo-EM, respectively (Hu *et al.*, 2013; L. Zhang *et al.*, 2015; Paidimuddala *et al.*, 2023). NLRC4 exists as a monomer in the inactive state, a conformation that is stabilized

by ADP-mediated interactions of the NBD and WHD domains and the LRR blocking one site of the NBD (Hu *et al.*, 2013). Interaction of inactive NLRC4 monomers with activated, ligand bound NAIPs leads to a conformational change in NLRC4 which exposes a basic catalytic cluster on the activated NLRC4 molecule. This basic cluster can then bind to the acidic acceptor cluster on another inactive NLRC4 molecule, leading to its activation. In this manner a process is started that leads to the formation of an inflammasome disc containing 10-12 NLRC4 molecules but only one NAIP (L. Zhang *et al.*, 2015; Paidimuddala *et al.*, 2023).

1.3.3. The Pyrin inflammasome

The pyrin inflammasome is activated in response to bacterial infections (Schnappauf *et al.*, 2019). Pyrin belongs to the TRIM protein family and is encoded by the *MEFV* gene. Pyrin is activated in response to bacterial inactivating modifications of the GTPase RhoA (Xu *et al.*, 2014). RhoA is involved in the regulation of actin polymerization and is therefore important for cell morphology (Nguyen *et al.*, 2018). Some bacterial strains secrete toxins targeting and inactivating RhoA, leading to cytoskeleton rearrangements that allow their entry into the host cell (Popoff, 2014). Inactivation of RhoA is thought to induce downstream signalling pathways that supress phosphorylation of pyrin by inhibitory kinases (Gao *et al.*, 2016; Magnotti *et al.*, 2019). Pyrin comprises an N-terminal PYD which allows interaction with ASC upon activation, resulting in the assembly of a pyrin inflammasome and the processing of caspase-1 (Yu *et al.*, 2006). Recently, the small GTP-binding protein CDC42, which is involved in the regulation of the actin cytoskeleton, has been identified as a prerequisite for pyrin inflammasome assembly, however the mechanism behind this remains unclear (Spel *et al.*, 2022).

1.4. Cell death pathways

Cell death is required for many processes in the body, such as embryonic development, the maintenance of tissue homeostasis, and immunity. There are several pathways leading to cell death, each displaying distinct molecular

mechanisms, morphological characteristics, and physiological outcomes (Bertheloot *et al.*, 2021). Cell death pathways are often referred to as programmed cell death, meaning that the cell death is regulated and initiated by intracellular signalling (Alberts *et al.*, 2002). Programmed cell death stands in contrast to necrosis, an uncontrolled form of cell death that occurs in the context of severe cell injury and leads to tissue damage and inflammation (Khalid and Azimpouran, 2022). The three best understood pathways of programmed cell death are apoptosis, necroptosis, and pyroptosis (Bertheloot *et al.*, 2021). Necroptosis and pyroptosis are also described as regulated forms of necrotic cell death, since they occur in response to cell damage or infections and lead to an inflammatory response (Pasparakis and Vandenabeele, 2015). Other regulated cell death pathways include parthanatos, ferroptosis and extracellular trap (ET)-osis (David *et al.*, 2009; Guimarães-Costa *et al.*, 2012; Li *et al.*, 2020). Increasing evidence manifests crosstalk between the different cell death pathways and suggest an integrated concept of inflammatory cell death (Christgen *et al.*, 2020; Gullett *et al.*, 2022).

1.4.1. Apoptosis

Apoptosis is a highly controlled form of cell death responsible for normal cell turnover in healthy tissues and important for eukaryotic development and aging (Tower, 2015; Singh *et al.*, 2019). It is characterized by cell shrinkage, including the cytoplasm and the nucleus, and the fragmentation of the cell into membrane-bound apoptotic bodies. These apoptotic bodies are rapidly phagocytosed by neighbouring endothelial cells or phagocytes such as macrophages and dendritic cells (Kerr *et al.*, 1972; Hart *et al.*, 2008). Apoptosis is a “silent” form of cell death that does not trigger inflammatory responses (Fogarty and Bergmann, 2015). Apoptotic cell death is an energy-dependent process, that can be triggered by intrinsic or extrinsic stimuli. Extrinsic apoptosis involves extracellular ligands that bind to specific death receptors on the plasma membrane, such as FasL/FasR and TNF-α /TNFR1 (Elmore, 2007). Ligand sensing induces the recruitment of cytoplasmic adaptors and these adaptors in turn recruit caspase-8, leading to caspase-8 activation (Hsu *et al.*, 1995; Huang *et al.*, 1999; Beaudouin *et al.*,

2013). Caspase-8 then cleaves the precursors of caspase-3 and caspase-7 into their active forms (Tummers and Green, 2017). These executioner caspases cleave various target proteins, including endonucleases and proteins involved in cytoskeleton formation, thus initiating the apoptotic process (Kothakota *et al.*, 1997; Sakahira *et al.*, 1998). Intrinsic apoptosis can be triggered by various stimuli, including nutrient or growth factor deprivation, that culminate in mitochondrial outer membrane permeabilization and the release of apoptogenic molecules, such as second mitochondria-derived activator of caspases (SMAC), the serine protease OMI and cytochrome *c* (Singh *et al.*, 2019). Cytochrome *c* binds to apoptotic protease-activating factor 1 (Apaf-1) leading to the formation of an apoptosome and the activation of caspase-9, which can then activate caspase-3 and -7 (Zou *et al.*, 1999). SMAC and OMI interact with X-linked inhibitor of apoptosis protein (XIAP), an inhibitor of caspase-3, -7 and -9, abolishing the inhibition of these caspases (Du *et al.*, 2000; van Loo *et al.*, 2002).

1.4.2. Necroptosis

Necroptosis can occur in the context of inflammation, infection, cell stress or tissue injury. It can be induced by several signalling pathways, including TNF, IFN and Toll-like receptor signalling, of which the TNF/TNFR1 is the best characterized pathway (Degterev *et al.*, 2005; Pasparakis and Vandenabeele, 2015; Frank and Vince, 2019). Necroptosis is often observed when apoptotic signalling is impaired, which can for example happen during microbial infection (Naderer and Fulcher, 2018; Frank and Vince, 2019). All necroptotic signalling pathways result in the activation of the receptor interacting protein kinase 1 (RIPK1), which recruits RIPK3 to a complex called ripoptosome, resulting in the activation of RIPK3 by auto-phosphorylation (He *et al.*, 2009; Thapa *et al.*, 2013; Najjar *et al.*, 2016). Off note, RIPK1 and RIPK3 also have other physiological functions apart from inducing necroptosis, and their mode of action is determined by their biochemical environment (Bertrand and Vandenabeele, 2011). The ripoptosome recruits the mixed lineage kinase domain-like protein (MLKL), leading the assembly of a complex termed necrosome, which results in the activation of MLKL by phosphorylation through RIPK3 (Sun *et al.*, 2012).

Activated MLKL oligomerizes and is trafficked to the plasma membrane, where it accumulates and disrupts the cellular integrity, leading to cell death (Wang *et al.*, 2014; Samson *et al.*, 2020).

1.4.3. Pyroptosis

Pyroptosis is a highly inflammatory form of programmed cell death that is triggered by inflammasome formation and the activation of the pro-inflammatory caspases -1, -4 and -5 (or caspase-11 in mice) (Kayagaki *et al.*, 2015; He *et al.*, 2015). Since inflammasomes respond to various stimuli, pyroptosis is initiated under a plethora of circumstances, including microbial infection, sterile injury, and cytotoxic stress. Morphological changes characterizing pyroptosis include cell swelling, membrane blebbing and the formation of pyroptotic bodies, followed by explosion-like membrane rupture and flattening of the cell (Chen *et al.*, 2016). These events are driven by the formation of large pores in the plasma membrane by the protein GSDMD. GSDMD becomes activated downstream of inflammasome formation by cleavage through pro-inflammatory caspases, which allows the N-terminal domain of GSDMD to oligomerize and insert into the plasma membrane (Kayagaki *et al.*, 2015; He *et al.*, 2015; Liu *et al.*, 2016; Sborgi *et al.*, 2016). The mature pro-inflammatory cytokines IL-1β and IL-18 are selectively released through GSDMD pores and initiate further immune responses (Xia *et al.*, 2021). Plasma membrane rupture following GSDMD pore formation is mediated by oligomerization of the membrane protein Ninjurin-1 (NINJ1) (Kayagaki *et al.*, 2021). Plasma membrane rupture leads to the release of larger cytosolic components, such as high-mobility group box 1 (HMGB1) and lactate dehydrogenase (LDH), which function as DAMPs (Kayagaki *et al.*, 2021).

Since pyroptosis is the final common step of all inflammasome pathways it plays a central role in innate immunity and has been implicated in numerous diseases with aberrant inflammasome activation such as familial Mediterranean fever (FMF), atherosclerosis, inflammatory bowel disease (IBD), gout, Alzheimer's disease and sepsis (Rashidi *et al.*, 2019; Friker *et al.*, 2020; Opoku *et al.*, 2021; Gao *et al.*, 2021; Shen *et al.*, 2021; Liu *et al.*, 2021). In these diseases, pyroptosis contributes to the excessive or chronic inflammatory

responses that aggravate tissue damage and disease progression (Wu *et al.*, 2022). Therefore, inhibiting pyroptosis is an attractive strategy to treat inflammatory diseases.

1.5. The role of the Gasdermin protein family in pyroptosis

The best studied Gasdermin family member is GSDMD, which mediates pyroptosis by assembling large pores in the plasma membrane. GSDMD pores allow the release of pro-inflammatory cytokines that trigger further immune responses and induce imbalances in cell homeostasis, ultimately resulting in cell death. The expression of GSDMD in tissues that are likely entry points for pathogens, such as the skin, gastrointestinal tract and respiratory system underlines its importance in host defence (Feng et al. 2018; The Human Protein Atlas - Tissue expression of GSDMD). Besides GSDMD, the human Gasdermin protein family comprises five more members (Gasdermin A-E and GSDMF/PJVK/DFNB59) that exert diverse physiological functions (Broz *et al.*, 2020; Zou *et al.*, 2021). Apart from GSDMF, all Gasdermin family members adopt a similar structure in the auto-inhibited state with an N- and a C-terminal domain (NTD and CTD) connected by a flexible linker (Ding *et al.*, 2016; Liu *et al.*, 2019; Yin *et al.*, 2023). Overexpression of the NTDs of GSDMA-E induced pyroptosis in HEK293T cells, but the roles of Gasdermin besides GSDMD in pyroptosis are not well characterized yet (Ding *et al.*, 2016).

Recently, GSDMA was shown to trigger pyroptosis in skin cells infected with Streptococcus pyogenes. Unlike GSDMD, GSDMA is not activated by host caspases, but is cleaved by the streptococcal cysteine protease SpeB, thereby acting as a sensor of streptococcus infection, as well as an effector in the defence against this pathogen (Deng *et al.*, 2022). GSDMB is involved in the immune response against bacterial infections and has been shown to directly lyse gram-negative bacteria by forming pores in their cell membranes, and to induce pyroptosis by pore formation in the plasma membrane (Z. Zhou *et al.*, 2020; Hansen *et al.*, 2021). Like GSDMA, GSDMB is also not activated by pro-inflammatory caspases. Instead, it is cleaved by the serine protease granzyme A, which is produced by T lymphocytes and natural killer cells (Z. Zhou *et al.*,

2020; Hansen *et al.*, 2021). The role of GSDMC in lytic cell death is not well understood. Recently, it was found that overexpression of mouse GSDMC2 triggers pyroptosis and that GSDMC expression is upregulated and associated with lytic cell death in mouse intestine upon worm infection (Xi *et al.*, 2021). GSDME targets not only the plasma membrane, where it mediates cytokine release, but has also been shown to permeabilize the mitochondrial membrane promoting the mitochondrial apoptotic pathway (Rogers *et al.*, 2019; Zhou and Abbott, 2021). In contrast to GSDMD which is activated by pro-inflammatory caspases, GSDME is cleaved by the apoptotic caspase-3 (Wang *et al.*, 2017). GSDMF (also known as PJVK and DFNB59) is the only Gasdermin member in which overexpression of the NTD does not induce lytic cell death (Angosto-Bazarra, Alarcón-Vila, *et al.*, 2022). Mutations in GSDMF are associated with hearing loss by a yet unknown mechanism (Collin *et al.*, 2007; Domínguez-Ruiz *et al.*, 2022).

1.5.1. Activation and regulation of GSDMD pore formation

GSDMD is activated through cleavage by the inflammatory caspases-1, -4 and -5 in human, and caspase-1 and -11 in mice. These caspases are activated in the canonical and non-canonical inflammasome pathways and cleave GSDMD at a conserved sequence motif ($FLTD_{275}$|GV in humans, $LLSD_{276}$|GI in mice), which resides in the flexible linker region between the N- and C-terminal domains of GSDMD (Figure 3) (Shi *et al.*, 2015). For successful cleavage, theses caspases engage an exosite in the GSDMD CTD (Wang *et al.*, 2020; Liu *et al.*, 2020). During extrinsic apoptosis, also caspase-8 can directly cleave GSDMD leading to lytic inflammatory cell death (Sarhan *et al.*, 2018; Chen *et al.*, 2019). Caspase-8 mediated GSDMD cleavage can also occur when TAK1 or IKK signalling is inhibited, which is the case in Yersinia infection, where the Yersinia effector molecule YopJ inhibits TAK1 and IKK function (Orning *et al.*, 2018). GSDMD can be inactivated during apoptosis by apoptotic caspases-3 and -7, which cleave GSDMD at D_{87}, thereby cleaving and inactivating the NTD, which inhibits pyroptosis (Taabazuing *et al.*, 2017).

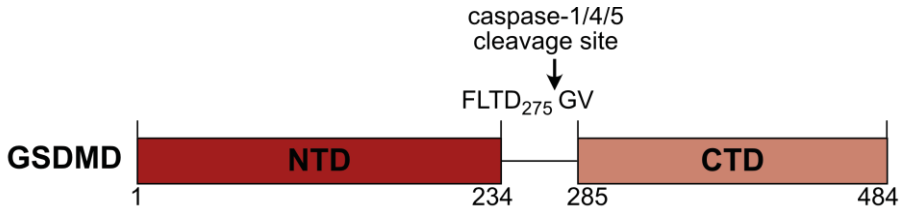

Figure 3: GSDMD domain architecture. GSDMD consists of an N- and a C-terminal domain (NTD and CTD, respectively), which are connected by a long, flexible linker. Inflammatory caspases can cleave GSDMD at a specific cleavage site which is located in the linker region.

Cleavage of GSDMD allows the GSDMD NTD to undergo conformational changes that enable the oligomerization of the GSDMD NTD, lipid binding, membrane insertion and pore formation. GSDMD binds to negatively charged lipids such as phosphatidyl serine (PS) and phosphatidylinositol phosphates (PIPs) which are found at the plasma membrane, and cardiolipin (CL) which is found at the mitochondrial membrane (Xia *et al.*, 2019). In line with this, GSDMD pore formation has also been observed at the mitochondrial membrane, where it induces the release of mitochondrial ROS and mitochondrial DNA (Platnich *et al.*, 2018; Huang *et al.*, 2020; Weindel *et al.*, 2022).

GSDMD pores mediate the release of small molecules such as the pro-inflammatory cytokines IL-1β and IL-18. Larger DAMPs released during pyroptosis, including high-mobility group box 1 (HMGB1) and LDH, are not released through GSDMD pores. Instead these molecules are released following plasma membrane rupture, the final step of pyroptosis (Chan *et al.*, 2013; Volchuk *et al.*, 2020). Although GSDMD pores allow water influx into the cell which causes cell swelling and imbalances in the cellular ion homeostasis (Fink and Cookson, 2006), osmosis is not sufficient to cause plasma membrane rupture. Instead, in a yet undefined mechanism, the plasma membrane protein NINJ1 mediates plasma membrane rupture downstream of pyroptotic, necrotic and apoptotic stimuli through self-oligomerization (Kayagaki *et al.*, 2021).

GSDMD pore formation and pyroptosis are regulated on multiple levels, including GSDMD cleavage and oligomerization, pore assembly and pore stability. Although GSDMD pore formation induces imbalances in the cellular ion homeostasis, the assembly of GSDMD pores at the plasma membrane does not

necessarily lead to cell death. Living cells that secrete IL-1 without undergoing cell death are referred to as hyperactivated cells (Zanoni *et al.*, 2016). A hyperactivated state has been observed in dendritic cells, macrophages, monocytes and neutrophils, and the IL-1 secretion from these cells was GSDMD dependent (Zanoni *et al.*, 2016; Evavold *et al.*, 2018; Heilig *et al.*, 2018). This implies that cells can regulate whether GSDMD pore formation leads to the secretion of IL-1 only or induces pyroptosis. Minor damage to the plasma membrane can be repaired by processes involving the endosomal sorting complex required for transport (ESCRT) machinery (Jimenez *et al.*, 2014). GSDMD pore formation leads to Ca^{2+} influx into the cell which serves as a signal to induce ESCRT-mediated membrane repair, resulting in reduced pyroptotic cell death (Rühl *et al.*, 2018). Moreover, GSDMD pores open and close dynamically, providing another mechanism to regulate pyroptosis. GSDMD pore dynamics are reported to be regulated through changes in the local phosphoinositide environment, which are induced by Ca^{2+} influx through GSDMD pores (Santa Cruz Garcia *et al.*, 2022). The Ragulator-Rag complex has been reported to be a necessary factor for GSDMD oligomerization and pore formation, although being dispensable for GSDMD cleavage or the plasma membrane localization of the GSDMD NTD (Evavold *et al.*, 2021). Rather, the Ragulator-Rag complex in involved in the production of reactive oxygen species (ROS), which are required for the oligomerization of the GSDMD NTD (Evavold *et al.*, 2021). ROS directly target mouse GSDMD by oxidative modification of C192 (C191 in human) which enhances GSDMD oligomerization and pyroptosis (Devant *et al.*, 2023). How oxidation of C192/C191 influences GSDMD oligomerization is not clear yet. Next to ROS, also oxidized mitochondrial DNA has been found to directly interact with the GSDMD NTD promoting its oligomerization (Miao *et al.*, 2023). GSDMD activity is also regulated by the metabolic state of the cell. Upon activation, macrophages undergo a metabolic switch from oxidative phosphorylation to glycolysis which requires remodelling of their tricarboxylic acid (TCA) cycle (Kelly and O'Neill, 2015). TCA cycle intermediates are involved in regulating cellular immune responses. The TCA cycle intermediate fumarate accumulates in activated macrophages and exerts an anti-inflammatory function by modifying

GSDMD at C192/C191 in a process called succination, which blocks GSDMD processing by inflammatory caspases and inhibits pyroptosis(Humphries *et al.*, 2020).

1.6. The pro-inflammatory cytokines IL-1β and IL-18

IL-1β and IL-18 both belong to the interleukin-1 family and are pro-inflammatory cytokines that are released following inflammasome activation and GSDMD pore formation (Kaneko *et al.*, 2019). IL-1β is expressed as inactive precursor protein (pro-IL-1β) and its expression is upregulated following activation of the transcription factor NF-κB (Kostura *et al.*, 1989; Cogswell *et al.*, 1994; Liu *et al.*, 2017). Cells expressing IL-1β include monocytes, macrophages and dendritic cells (Fields *et al.*, 2019). Prior to secretion, pro-IL-1β needs to be processed into its active form by caspase-1 (Kostura *et al.*, 1989; Xia *et al.*, 2021). IL-1β can also be processed by caspase-8, a caspase-1 independent pathway, following TLR3/4 or Dectin-1 activation (Chan and Schroder, 2019). IL-1β binds to the IL-1R1 receptor which is expressed on a wide range of target cells, such as innate and adaptive immune cells including dendritic cells, macrophages, neutrophils, T- and B cells, but also endothelial and epithelial cells (Sims and Smith, 2010; Song *et al.*, 2018). Binding of IL-1β to IL-1R1 induces heterodimerization with the IL-1R3 receptor. The IL-1R1/IL-1R3 receptor recruits MyD88 via its TIR domain, which starts a signalling cascade leading to the activation of NF-κB (Loiarro *et al.*, 2010). IL-1β induced gene expression triggers a variety of cellular responses that promote inflammation. These processes include the production of nitric oxides (NO) and the inflammatory mediators prostaglandin E2 and platelet activating factor, as well as molecules facilitating the infiltration of circulating immune cells (Dinarello, 2009). IL-1β is also involved in the activation and regulation of adaptive immune responses by amplifying T cell responses and influencing T cell differentiation (Van Den Eeckhout *et al.*, 2021).

IL-18 is produced by immune cells, primarily macrophages and dendritic cells, but also endothelial cells, such as keratinocytes (Sims and Smith, 2010). In contrast to IL-1β, IL-18 is constitutively expressed, but also IL-18 requires processing by caspase-1 for maturation (Gu *et al.*, 1997; LOREY *et al.*, 2004). IL-

18 binds to the IL-18 receptor α (IL-18Rα) which then hetero-dimerizes with IL-18Rβ, leading to the recruitment of MyD88 and the induction of signalling pathways resulting in the activation of NF-κB (Dinarello *et al.*, 2013). IL-18 influences a wide range of target cells, including innate and adaptive immune cells, endothelial cells, and epithelial cells (Rex *et al.*, 2020). IL-18 induced gene expression leads to the production of other cytokines, such as IFN-γ and TNF-α, chemokines and Fas ligand (Dinarello *et al.*, 1998). IL-18 signalling is regulated by the IL-18 binding protein (IL-18BP), which binds to IL-18 and thereby blocks binding to the IL-18 receptor (Novick *et al.*, 1999).

1.7. The NOD-like receptor NLRP7

NLRP7 belongs to the NLRP family of NOD-like receptors. Although the function of NLRP7 is not well understood to date, it has been reported to function as an inflammasome forming PRR in human macrophages (Khare *et al.*, 2012). Of note, NLRP7 is only found in primates. The closest relative to the *NLRP7* gene is *NLRP2* and it is assumed that *NLRP7* arouse from a duplication of the *NLRP2/NLRP7* ancestor gene (Tian *et al.*, 2009; Duéñez-Guzmán and Haig, 2014).

NLRP7 transcripts were detected in a wide range of human tissues including lung, liver, spleen, thymus, testis, small intestine and colon, and NLRP7 expression was found in peripheral blood mononuclear cells (PBMCs), placenta, endometrium, all oocyte stages and pre-implantation embryos (Kinoshita *et al.*, 2005; Huang *et al.*, 2017; Onoufriadis *et al.*, 2018; Abi Nahed *et al.*, 2019; Amoushahi *et al.*, 2019; Tsai *et al.*, 2019). The physiological functions NLRP7 exhibits in these tissues, including processes in innate immunity and reproduction, are diverse and not yet fully understood.

1.7.1. Domain architecture

NLRP7 presents the typical NLRP protein architecture and comprises an N-terminal PYD, a central NACHT and a C-terminal LRR domain. The full length structure of NLRP7 is not available yet, but the structure of the NLRP7-PYD was determined by nuclear magnetic resonance (NMR) spectroscopy. As common for

PYDs, the NLRP7-PYD adopts a 6-α-helical bundle death domain fold (Pinheiro *et al.*, 2010). The function of PYDs is mainly to mediate protein-protein interactions, and in the process of inflammasome assembly, the PYDs of activated NLRPs interact with the PYD of the adaptor molecule ASC (Chu *et al.*, 2015).

The NACHT domain is named after its presence in a group of proteins including NAIP, CIITA, HET-E (incompatibility locus protein from Podospora anserina), and TP1 (telomerase-associated protein 1) (Damiano *et al.*, 2004). It is characterized by a highly conserved nucleotide-binding fold, comprising the Walker A [GxxxxGK(S/T)] and Walker B motifs [hhhhD(D/E)] required for nucleotide binding and hydrolysis (Miller and Enemark, 2016). In the NLRP protein family the Walker A and Walker B motifs are degenerated to GxxGxGKT and hhhhDGxDE, respectively (Brinkschulte *et al.*, 2022). Binding of ATP is thought to go hand in hand with conformational changes that activate NLRs and allow the oligomerization required for inflammasome assembly (Sandall *et al.*, 2020; Brinkschulte *et al.*, 2022). ATP binding and hydrolysis has been observed for the NLRP7 NACHT domain (Radian *et al.*, 2015).The NACHT domain can be further subdivided into the FISNA, nucleotide binding domain (NBD), helical domain 1 (HD1), winged helix domain (WHD) and helical domain 2 (HD2) subdomains (Hochheiser, Pilsl, *et al.*, 2022).

LRR domains are composed of a series of leucine rich repeat units, each of which consists of approximately 20-30 amino acids, which assemble in a short β-strand followed by an α-helix (Ng and Xavier, 2011). The number of leucine rich repeats can vary between 2 and 45, according to the protein (Enkhbayar *et al.*, 2004). LRR domains are involved in a wide range of biological processes, including protein-protein interactions, ligand binding, and signal transduction (Ng and Xavier, 2011).

1.7.2. NLRP7 isoforms

Protein isoforms are different proteins produced from the same gene through alternative splicing. As they differ in their amino acid sequence, protein isoforms can also differ in their biological function (Gunning and Hardeman, 2018). A number of NLRP7 isoforms are listed on the common webservers, including

UniProt, Ensembl and NCBI. The UniProt server lists three NLRP7 protein isoforms derived from alternative splicing and twelve computationally mapped potential isoforms (UniProt: Q8WX94). The three most annotated protein isoforms are summarized in Table 1. In this study, the isoforms are referred to as $NLRP7_{980}$, $NLRP7_{1009}$ and $NLRP7_{1037}$ according to the number of amino acids they are composed of.

The three protein isoforms differ in the length and composition of their LRR domains. The $NLRP7_{1009}$ isoform misses 28 residues present in the other two isoforms, starting from R644 and ending with F671, which form an acidic loop in the transition LRR in the $NLRP7_{980}$ and $NLRP7_{1009}$ isoforms. The $NLRP7_{980}$ isoform lacks residues $L938_{(NLRP71037)}/L910_{(NLRP71009)}$ – $R994_{(NLRP71037)}/R966_{(NLRP71009)}$ (two LRR repeats), present in the other two isoforms (Figure 4A). Based on the alphafold models of the three isoforms, these differences in the amino acid composition result in a shortened transition LRR for $NLRP7_{1009}$ in comparison to $NLRP7_{980}$ and $NLRP7_{1037}$ and a shortened canonical LRR for $NLRP7_{980}$ in comparison to $NLRP7_{1009}$ and $NLRP7_{1037}$, while the overall structure and domain architecture are very similar for all three isoforms (Figure 4B,C,D). Whether these isoforms exhibit different functions or vary in their activity remains largely unknown until today. In this study, two different isoforms were analysed: The UniProt canonical $NLRP7_{980}$ isoform was used for recombinant protein expression and generation of NLRP7 targeting nanobodies, as well as in HEK293T based inflammasome activation assays. The $NLRP7_{1009}$ isoform was used in HEK cell based assays to study variants specific for this isoform that have been associated with disease.

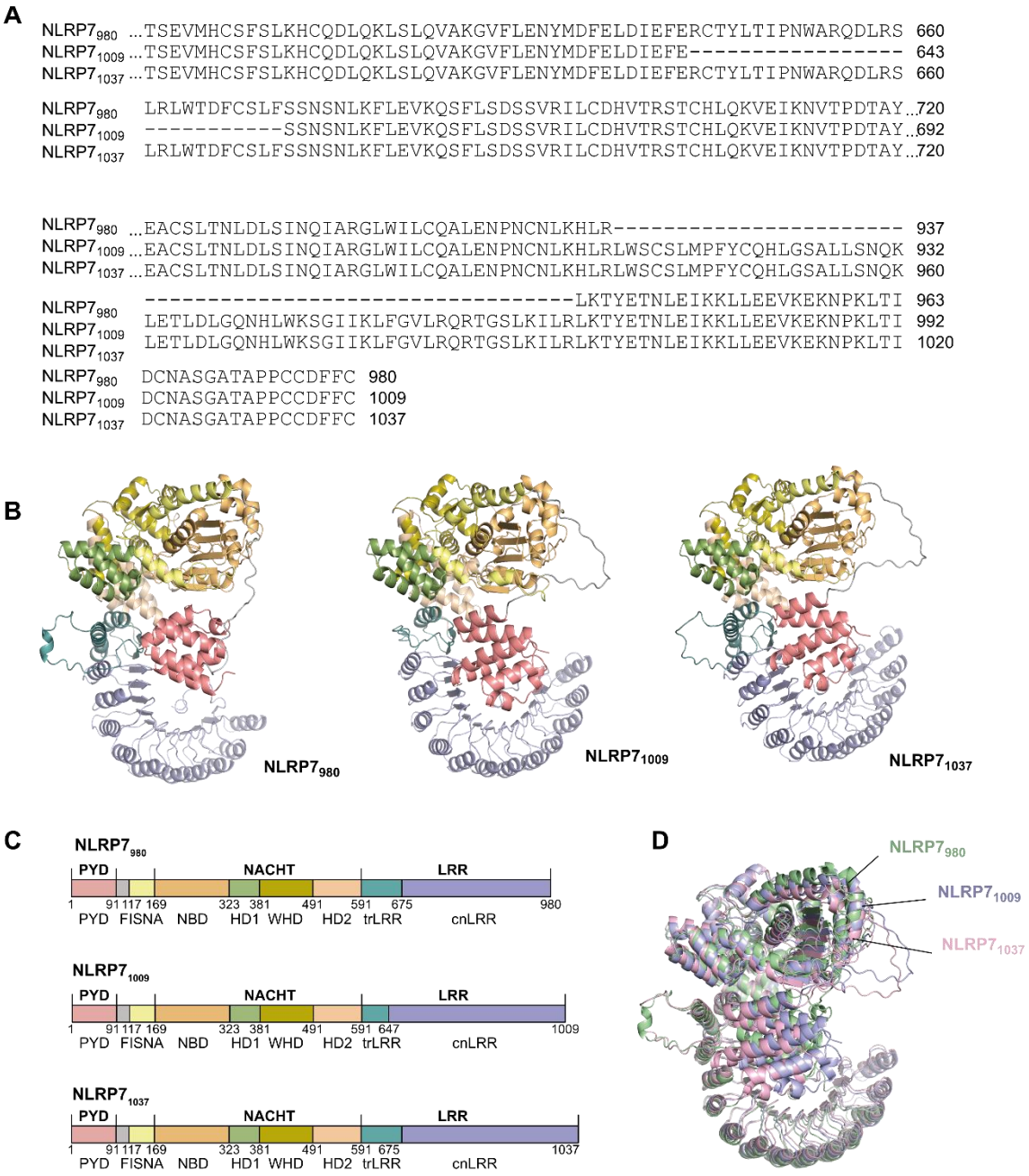

Figure 4: Most commonly annotated NLRP7 isoforms. A) Amino acid sequence alignment of the three most annotated NLRP7 isoforms which comprise 980, 1009 and 1037 amino acids, respectively. **B)** Alphafold models of the NLRP7 isoforms. **C)** Domain architecture of the NLRP7 isoforms. **D)** Superimposotion of the three NLRP7 isoforms.

Table 1: Most commonly annotated NLRP7 isoforms.

Name (Thesis)	Uniprot ID	Ensembl ID	NCBI ID	Amino acids	Evidence	Reference	Relevance
$NLRP7_{980}$	Q8WX94	ENST00000590030.5 ENST00000340844.6	NP_996611.2	980	Transcriptional level	Wang et al. 2002, Hayward et al. 2009), Wang et al. 2009	Uniprot canonical
$NLRP7_{1009}$	Q8WX94-2	ENST00000328092.9	NP_631915.2	1009	Transcriptional level	Hayward et al. 2009, Onoufriadis et al. 2018	
$NLRP7_{1037}$	Q8WX94-3	ENST00000592784.5 ENST00000588756.5	NP_001120727.1 NP_001392460.1	1037	Transcriptional level	Slim et al. 2022, Sazhenova et al. 2021, Aguinaga et al. 2021	Ensembl canonical, NCBI canonical

1.7.3. The role of NLRP7 in innate immunity

NLRP7 belongs to the NLR protein family which comprises well characterized inflammasome forming PRRs, including NLRC4, NLRP1, NLRP3 and NLRP6. In contrast, the role of NLRP7 in innate immunity is not well understood and to some extent controversial. Here, the literature describing NLRP7 as an inflammasome component is summarized, a detailed discussion about the broader role of NLRP7 in innate immunity can be found in chapter 3.3. An NLRP7 containing inflammasome was reported for the first time by Khare et al. in 2012, identifying microbial lipopeptides as NLRP7 activators in human macrophages (Khare *et al.*, 2012). These di- and tri-acylated bacterial lipopeptides (acLP) are well characterized TLR2/6 and TLR2/1 activators, respectively, and later, an NLRP7 inflammasome was also described in THP-1 macrophages stimulated with the TLR4 ligand LPS (Jin *et al.*, 2007; Kang *et al.*, 2009; Bednash, *et al.*, 2017), implicating an interplay of TLR and NLRP7 signalling pathways. However, Khare et al., found that NLRP7 activation occurs independently of TLR2 activation and requires cytosolic acLP. Moreover, NLRP7 abundance in human macrophages is reported to be regulated by ubiquitination and lysosomal degradation of NLRP7, and it is thought that deubiquitination of NLRP7 by the deubiquitinase STAMBP in response to TLR activators enhances NLRP7 abundance resulting in NLRP7 inflammasome formation (Bednash, *et al.*, 2017). Variants in NLRP7 have been associated with the inflammatory diseases ulcerative colitis and inflammatory bowel syndrome (Onoufriadis *et al.*, 2018).

1.7.4. The role of NLRP7 in reproduction

NLRP7 is essential for early embryonic development, although its mechanism of action remains largely unknown. In human embryonic development, fertilization results in the formation of a one-cell zygote that undergoes cleavage divisions and develops into a blastocyst around 5-6 days after fertilization. The blastocyst contains an inner cell mass and an outer trophoectoderm and begins to implant into the maternal uterine epithelium around day 7 after fertilization (Popovic *et al.*, 2021). The trophoectoderm gives rise to the trophoblast cells in the placenta and is required for embedding the blastocyst in the uterine stroma (Rossant and Tam,

2022). NLRP7 is expressed in the uterus, endometrium, oocytes and preimplantation embryos and has been reported to play a role in trophoblast differentiation and proliferation (Murdoch *et al.*, 2006; Akoury *et al.*, 2015; Abi Nahed *et al.*, 2019). In addition, NLRP7 is expressed in decidual macrophages and was reported to promote differentiation into M2 macrophages (Tsai *et al.*, 2019). The importance of NLRP7 in reproduction is further illustrated by the number of NLRP7 sequence variants associated with reproductive disorders. The Infevers registry lists 117 NLRP7 sequence variants associated with hydatidiform mole, miscarriage and stillbirth (Infevers: an online database for autoinflammatory mutations. Copyright. Available at https://infevers.umai-montpellier.fr/, accessed 23.04.2023). These variants affect all protein domains of NLRP7 and include deletions, insertions, deletion-insertions (delins), substitutions and duplications.

Hydatidiform mole (HM) is a type of gestational trophoblastic disease characterized by cystic degeneration of the placental vili, excessive trophoblastic proliferation and abnormal embryonic development (Slim and Wallace, 2013; Kalogiannidis *et al.*, 2018; Soper, 2021). Hydatidiform moles are often diagnosed after a miscarriage, or by ultrasound in early pregnancy. In most cases molar pregnancies need to be terminated and the molar tissue evacuated, with only a 1:22,000-100,000 chance of developing a normal fetus in coexistence with the molar placenta (Soper, 2021). Germline mutations in NLRP7 are found in 40-80 % of patients presenting recurrent molar pregnancies (Soper, 2021). Some of the HM-causing mutations identified in females were also found in males, but in males they did not have a negative effect on reproduction (Qian *et al.*, 2007). Further studies identified *NLRP7* as a maternal effect gene, which is a gene that encodes factors that are expressed in oocytes and are required for early embryonic development. Therefore, variants in NLRP7 affect the embryo, whereas the maternal carrier of the NLRP7 variant is healthy (Akoury *et al.*, 2015; Soellner *et al.*, 2017; Mitchell, 2021). Hydatidiform moles from patients with mutations in NLRP7 are characterized by defects in genomic imprinting, an epigenetic process important for embryonic development, that leads to the silencing of genes by DNA methylation, depending on their maternal or paternal

origin. A loss of maternal DNA methylation markers is observed in HM, suggesting a role of NLRP7 in imprinting (Kou *et al.*, 2008; Sanchez-Delgado *et al.*, 2015; Eggermann *et al.*, 2022). It remains largely unknown what role NLRP7 plays as an immune sensor in healthy reproduction or HM. However, PBMCs isolated from HM patients displayed a decrease in IL-1β secretion in response to LPS stimulation (Messaed *et al.*, 2011).

1.8. Nanobodies as tool in biochemistry and structural biology

Studying the biochemistry and structural biology of proteins such as the above described in innate immune proteins NLRP7 and GSDMD sometimes requires specific tools that allow for example their inhibition, or analysis by X-ray crystallography or cryo-EM. Recently, nanobodies have been established as such a tool. The discovery that led to the development of nanobodies was made in 1993, when it was observed that camels naturally produce heavy-chain only antibodies (HCAbs) lacking the light chains present in conventional antibodies, and that these HCAbs have an extensive antigen-binding repertoire (Hamers-Casterman *et al.*, 1993). Nowadays, using biotechnological approaches, the variable antigen-binding domain (VHH) of HCAbs raised against a protein of interest in camelids, typically llamas and alpacas, can be amplified and used as a single-domain antibody (van der Linden *et al.*, 2000; Muyldermans, 2013). These VHHs, or nanobodies, are very stable, soluble and small in size (15 kDa). HCAbs are also found in in cartilaginous fishes and in this case termed Ig-NAR. The single-domain antibodies derived from Ig-NARs are known as V-NAR fragments (Matz and Dooley, 2019). Nanobodies can bind conformational epitopes with high affinities, can access cryptic clefts and are able to penetrate tissues, which is often not possible for conventional antibodies, making nanobodies ideal tools for biotechnological and biomedical applications (Wang *et al.*, 2016; Uchański *et al.*, 2020). The structure of nanobodies was analyzed by X-ray crystallography and reveals an IgV fold consisting of nine β-strands. Two cysteines located on the second and seventh β-strand form a conserved disulfide bond. An optional disulfide bond can be present between the complementary-determining regions CDR1 and 3 or the CDR2 and 3. Nevertheless, disulfide-

bond formation is not required for the formation of the antigen-binding properties in many cases. The antigen-binding site, or paratope, is formed by the three highly variable CDRs 1, 2 and 3, at one site of the protein which are connected by four conserved framework regions (FR1-4) (Ingram *et al.*, 2018a).

Nanobodies find a variety of applications in different fields, including structural biology, biotechnology, diagnostics, and therapeutics. In structural biology, nanobodies can be used as crystallization chaperones for challenging proteins and protein complexes. There are different mechanisms by which nanobodies can facilitate crystallization. First of all, nanobodies tend to self-assemble and provide crystallization-compatible structures in complex with their target protein. Moreover, nanobody-binding can increase the amount of structured polypeptides by sandwiching the target protein and capturing it in a defined conformation in the crystal lattice built by the nanobody frameworks (Traenkle *et al.*, 2016).

Since nanobodies bind conformational epitopes, they can selectively stabilize transient conformational states of their target protein, which allows the crystallization of different activation states of the target protein. This phenomenon was used to determine the crystal structures of different conformational states of GPCRs and ion channels (Uchański *et al.*, 2020). Due to their small size, the applications for nanobodies in single-particle cryo-EM are restricted. To circumvent this problem, megabodies can be generated which incorporate the nanobody into a protein scaffold and can be used to increase the resolution in cryo-EM experiments by increasing the particle size and overcoming problems due to preferential orientation (Uchański *et al.*, 2019). Nanobodies can also be used for cell-biological applications. Many nanobodies fold properly and retain their antigen-binding properties when expressed in the reducing milieu of the cytosol. Therefore, they can be used for the construction of fusion proteins combining the antigen-specificities of the nanobody with the properties of the fusion partner. Fusion partners can for example be fluorescent proteins or ubiquitin ligases enabling the spatiotemporal analysis and selective degradation of the target protein, respectively(Ingram *et al.*, 2018b). Using a fluorescently tagged nanobody circumvents changes in cell behavior that might arise due to overexpression of a fluorescently-tagged target protein (Beghein and Gettemans,

2017a). Nanobodies can also be used to translocate or trap the target protein to a certain compartment by fusing the nanobody to a protein or a domain that naturally occurs in this compartment (Aguilar *et al.*, 2019). Moreover, nanobodies can be used to study protein-protein interactions, as in the fluorescent-three-hybrid (F3H) screen, a commonly used alternative to yeast-two-hybrid screens (Herce *et al.*, 2013).

1.9. Thesis aims

Although the role of some NLRP proteins in inflammasome formation and innate immunity is well understood, the function and mechanism of activation of the NLRP family member NLRP7 is less well characterized. NLRP7 has been reported to be involved in inflammasome activation (Khare *et al.*, 2012; Bednash, *et al.*, 2017), but how NLRP7 is activated remains largely unknown. Furthermore, structural information on NLRP7 is sparse. Therefore, this thesis aims to investigate the role of NLRP7 as a PRR and to generate NLRP7-targeting nanobodies as a tool for the biochemical and structural analysis of NLRP7.

Inflammasome activation results in pyroptotic cell death mediated by the protein GSDMD through pore formation in the plasma membrane. As pyroptosis is observed in many diseases with excessive inflammation, GSDMD is an attractive drug target. However, there are currently no drugs available that specifically target GSDMD. Here, it was aimed to biochemically characterize GSDMD-targeting nanobodies and analyse their effect on GSDMD pore formation.

The aims of this thesis are:

1. To improve the understanding of the role of NLRP7 as a PRR and its role in inflammasome formation.
2. Generation of NLRP7-targeting nanobodies for biochemical and structural studies of NLRP7.
3. Biochemical, biophysical and structural biological characterisation of GSDMD-targeting nanobodies.

To achieve this, a combination of cell biological and protein biochemical techniques were used, including HEK cell based-inflammasome reconstitution assays, protein-protein interaction analysis, as well X-ray crystallography.

2. Materials and Methods

2.1. Materials

The chemicals and consumables used in this thesis were bought from the following suppliers: Carl Roth (Karlsruhe, Germany), Sigma-Aldrich (St Louis, USA), AppliChem (Darmstadt, Germany), Thermo Fisher Scientific (Waltham, USA), Merck Millipore (Burlington, USA), VWR (Radnor, USA), Jena Bioscience (Jena, Germany), Avanti Polar Lipids (Alabaster, USA), Sapphire Bioscience (Redfern, Australia), New England Biolabs (Ipswich, USA), Cayman Chemical (Ellsworth USA), NanoTemper Technologies (München, Germany), IBID (Gräfelfing, Germany) and Linde plc (Dublin, Ireland). Standard chemicals and consumables and their suppliers are listed in Table 2.

Table 2: Chemicals and consumables.

Chemical/Consumable	**Supplier**
Acetic acid	Carl Roth
Acrylamide (Rotiphorese Gel 30)	AppliChem
Agar-Agar	Carl Roth
Agarose	Carl Roth
Ammoniumperoxodisulfate (APS)	Carl Roth
Amicon® Ultra	Sigma-Aldrich, Merck Millipore
Ampicillin	Carl Roth
Blasticidin S	Sapphire Bioscience
β-ME	AppliChem
Bromophenol blue (Bonn)	Carl Roth
Bromophenol blue (Melbourne)	Alfa Aesar
BSA	Carl Roth
Calcein	Sigma-Aldrich
Cardiolipin	Avanti Polar Lipids,
cOmplete™ protease inhibitor	Roche Biochemicals
Coomassie Brilliant Blue R-250	Carl Roth
Chambered coverslips (8-well) with glass bottom	IBIDI
Chloroform	Carl Roth
CutSmart® Buffer	New England Biolabs
DMSO	Sigma Aldrich
DPBS (for tissue culture)	Gibco

Chemical/Consumable	Supplier
DTT	Carl Roth
dNTPs	New England Biolabs
DOPC	Avanti Polar Lipids, Inc.
EDTA (Bonn)	Carl Roth
EDTA (Melbourne)	Thermo Fisher Scientific
Ethanol	Carl Roth
FCS	Sigma life science
FSL-1	Abcam
GelRed™	Biotium
Gentamycin	Carl Roth
Glucose	Carl Roth
Glycerol	AppliChem GmbH
Glycine	Carl Roth
Glutathione Resin	VWR
HEPES	Carl Roth
Hygromycin B	Thermo Fisher Scientific Inc.
Hydrochloric acid	Carl Roth
IPTG	Carl Roth
Imidazole	Carl Roth
Kanamycin	Carl Roth
Lactose	Carl Roth
Lipofectamine®2000	Thermo Fisher Scientitic
LipoFectMax™	ABP Biosciences
Immobilon-P ® Transfer Membrane (PVDF)	Merck Millipore, Sigma-Aldrich
Immobilon® Forte Western HRP Substrate	Merck Millipore
IPTG	Carl Roth
Isopropanol	Carl Roth
Magnesium chloride	Carl Roth
Methanol	Chem-Supply
Ni-NTA beads	Thermo Fisher Scientific
NuPAGE™ 4-12 % Bis-Tris Gel (Melbourne)	Thermo Fisher Scientific
Pam2CSK4	Cayman chemical
Pam3CSK4	Cayman chemical
PD-10 column	Cytiva
PEG400	Carl Roth
Penicillin/Streptomycin	Sigma-Aldrich

Chemical/Consumable	Supplier
PMSF	Carl Roth
Polybrene	Sigma-Aldrich
Poly D lysine	Gibco
POPC	Avanti Polar Lipids, Inc
POPE	Avanti Polar Lipids, Inc
Ponceau S	Carl Roth
Prometheus standard capillaries	NanoTemper Technologies
SDS	Carl Roth
Skim milk powder	Sigma-Aldrich
Sodium acetate	Carl Roth
Sodium chloride	Carl Roth
Sodium citrate	Carl Roth
Sodium dodecyl sulfate	Carl Roth
Sodium hydroxide	Carl Roth
Spectinomycin	Sigma-Aldrich
(D+)-Saccharose	Carl Roth
TEMED	AppliChem GmbH
Tetracycline	Carl Roth
TMB substrate	Thermo Fisher Scientific
TransIT-LT1 transfection reagent (MIR6100)	MirusBio
TRIS	Carl Roth
Triton X-100	Carl Roth
Trypan Blue Dye	Bio-RAD
Trypsin-EDTA	Sigma Aldrich
Tween® 20 (Bonn)	Carl Roth
Yeast extract	Carl Roth
Tween® 20 (Melbourne)	Sigma
X-Gal	Carl Roth
Zeocin	Thermo Fisher Scientific

Table 3: Kits.

Kit	Supplier
Pierce™BCA Protein Assay Reagent A and B	Thermo Fisher Scientific Scientific (Waltham, USA)
Wizard® Plus SV Minipreps DNA purification System	Promega (Madison, USA)
ExtractMe Mini Kit	BLIRT (Gdansk, Poland)
PureLink™ HiPure Plasmid Maxiprep	Thermo Fisher Scientific Inc.
QIAquick PCR purification	Qiagen (Venlo, Netherlands)
Extractme DNA Clean-Up & Gel-Out Kit	BLIRT (Gdansk, Poland)
DuoSet® Human IL-1β ELISA kit	R&D Systems (Minneapolis, USA)

Table 4: Crystallization screens.

Screen	Supplier
Ligand-Friendly Screen	Molecular Dimensions
LMB Crystallization Screen™	Molecular Dimensions
MemGold™	Molecular Dimensions
Morpheus®	Molecular Dimensions
JBScreen JCSG++	Jena Bioscience GmbH
PACT premier™	Molecular Dimensions
ProPlex	Molecular Dimensions
Additive Screen HR2-428	Hampton Research (Aliso Viejo, USA)

Table 5: Tissue culture media.

Medium	Supplier
DMEM	Gibco
FluoroBrite™ DMEM	Gibco
LB	Carl Roth / WEHI Media Kitchen
Opti-MEM®	Gibco
RPMI 1640	Home made
TB	Home made

Table 6: Bacterial strains and insect cell lines.

***E. coli* strain or cell line**	**Type**	**Supplier**
E. coli ArcticExpress (DE3)	Chemically competent	Agilent (Santa Clara, USA)
E. coli β10	Chemically competent	New England Biolabs (Ipswich, USA)
E. coli DH5α	Chemically competent	Thermo Fisher Scientific (Waltham, USA
E. coli DH10 MultiBac^{Turbo}	Electrocompetent	Geneva Biotech (Pregny-Chambésy, Switzerland
E. coli BL21 (DE3) Rosetta	Chemically competent	Thermo Fisher Scientific (Waltham, USA)
E. coli WK6	Chemically competent	ATCC (Manassas, USA)
Sf9 insect cells		Thermo Fisher Scientific (Waltham, USA)

Table 7: Mammalian cell lines.

Cell line	**Source**
HEK293T	CellBank Australia (code 12022001)
HEK293T ASC-BFP	Institute of Innate Immunity,Medical faculty, University of Bonn
Flp-In^{TM} 293 T-REx^{TM}	Thermo Fisher Scientific, Cat. No. R78007
Flp-In^{TM} 293 T-REx^{TM} ASC-EGFP	Annemarie Steiner, Masters Lab, WEHI
THP-1	ATCC TIB-202

Table 8: Buffer and solutions.

Buffer	**Composition**
Coomassie stain	40 % ethanol (v/v), 10 % acetic acid (v/v), 0.1 % Coomassie R250 (w/v)
Coomassie destain	10 % ethanol (v/v), 5 % acetic acid (v/v)
FACS buffer	2 % FCS in PBS
4x Laemmli buffer	240 mM Tris-HCl (pH 6.8), 40 % glycerol (v/v), 8 % SDS (w/v), 0.04 % bromophenol-blue, 5 % β-mercaptoethanol, pH 6.8
PBS	20 mM Na2HPO4, 4.6 mM NaH2PO4, 150 mM NaCl, pH 7.5
1xRIPA buffer	20 mM Tris-HCl (pH 7.3), 150 mM NaCl, 5 mM EDTA, 1 % Triton X-100, 0.5 % sodium deoxycholate, 0.1 % SDS, 10 % glycerol
SDS-PAGE resolving gel buffer	1.5 M Tris-HCl, 0.4 % (w/v) SDS, pH 8.8
SDS-PAGE stacking gel buffer	0.5 M Tris-HCl, 0.4 % (w/v) SDS, pH 6.8
SDS-PAGE running buffer (10x)	0.25 M Tris, 1.94 M glycin, 1 % SDS (w/v), pH 8.3
1xTAE buffer	40 mM Tris, 20 mM acetic acid, 1 mM EDTA
10xTBS	0.5 M Tris, 1.5 M NaCl, pH 8.0
10x wet transfer buffer	200 mM Tris, 1.5 M glycine, pH 8.3
1x wet transfer buffer	20 mM Tris, 0.15 M glycine, 20% methanol, pH 8.3
Purification Caspase-4	
Lysis buffer	50 mM Tris, 150 mM NaCl, 5 mM imidazole, 2 mM β-ME, pH 8.0
Wash buffer	50 mM Tris, 150 mM NaCl, 20 mM imidazole, 2 mM β-ME, pH 8.0
Elution buffer	50 mM Tris, 150 mM NaCl, 300 mM imidazole, 2 mM β-ME, pH 8.0
Purification GSDMD	
Lysis and wash buffer	25 mM Tris (pH 8.0), 300 mM NaCl, 10 % glycerol, 10 mM imidazole, 5 mM DTT
Elution buffer	25 mM Tris (pH 8.0), 300 mM NaCl, 300 mM imidazole, 5 mM DTT
Cutting buffer	25 mM Tris (pH 8.0), 200 mM NaCl, 5 % glycerol, 5 mM DTT
SEC buffer	20 mM HEPES (pH 8.0), 200 mM NaCl, 5 mM DTT

Buffer	Composition
Purification Nanobodies	
TES buffer	20 mM Tris (pH 8.0), 0.65 mM EDTA, 500 mM sucrose
Wash buffer	50 mM Tris (pH 7.5), 150 mM NaCl, 10 mM imidazole
Elution buffer	50 mM Tris (pH 7.5), 150 mM NaCl, 500 mM imidazole
SEC buffer	20 mM HEPES (pH 7.5), 150 mM NaCl
Purification mMBP-/MBP-tev-NLRP7	
Lysis buffer	50 mM Tris (pH 8.0), 300 mM NaCl, 10 % glycerol, 0.25 % CHAPS, 50 mM Glu/Arg, 2 mM DTT
Wash buffer	50 mM Tris (pH 8.0), 300 mM NaCl, 0-7.5 % glycerol, 50 mM Glu/Arg, 2 mM DTT
Elution buffer	50 mM Tris (pH 8.0), 300 mM NaCl, 50 mM Glu/Arg, 25 mM maltose, 2 mM DTT
SEC buffer	20 mM HEPES (pH 7.4), 200 mM NaCl, 50 mM Glu/Arg, 0.5 mM TCEP
Purification of NLRP7-PYD	
Lysis buffer	50 mM HEPES (pH 7.0), 500 mM NaCl, 10 % glycerol, 2 mM DTT
Wash buffer	50 mM HEPES (pH 7.0), 500 mM NaCl, 2 mM DTT
Elution buffer	50 mM HEPES (pH 7.0), 500 mM NaCl, 10 mM GSH, 2 mM DTT
SEC buffer	20 mM HEPES (pH 7.0), 200 mM NaCl, 1 mM TCEP
Column regeneration	
GSTrap	6 M Gnd-HCl
HisTrap/Ni-NTA beads	6 M Gnd-Hcl, 200 mM acetic acid
MBPTrap/Amylose beads	0.5 M NaOH

Table 9: Markers and loading dyes.

Reagent	Supplier
100 bp DNA ladder	Carl Roth (Karlsruhe, Germany)
GeneRuler 1 kb DNA ladder	Thermo Fisher Scientific (Waltham, USA)
Gel Loading Dye Purple (6x)	New England Biolabs (Ipswich, USA)
PageRuler plus prestained protein ladder	Thermo Fisher Scientific (Waltham, USA)
Presciscion Plus Protein™ Standard Kaleidoskop	Bio-Rad (Hercules, USA)

Table 10: Plasmids.

Name	Protein Expression	Tag	Expression species	Source
pEXPR-His-SUMO-GSDMD	GSDMD	His-SUMO	*E. coli*	Schmidt lab
pEXPR-His-SUMO-GSDMD-Del1	$GSDMD_{\Delta 184\text{-}194\Delta 247\text{-}272}$	His-SUMO	*E. coli*	
pEXPR-His-SUMO-GSDMD-Del2	$GSDMD_{\Delta 181\text{-}197\Delta 247\text{-}272}$	His-SUMO	*E. coli*	
pEXPR-His-SUMO-GSDMD-Del3	$GSDMD_{\Delta 247\text{-}272}$	His-SUMO	*E. coli*	
pEXPR-His-SUMO-GSDMD-PP	GSDMD (with prescission cleavage site)	His-SUMO	*E. coli*	Schmidt Lab
pHEN6-$VHH_{GSDMD\text{-}1}$-LPTEG-His	VHH-1	LPTEG-His	*E. coli*	Schmidt Lab
pHEN6-$VHH_{GSDMD\text{-}2}$-LPTEG-His	VHH-2	LPTEG-His	*E. coli*	Schmidt Lab
pHEN6-$VHH_{GSDMD\text{-}3}$-LPTEG-His	VHH-3	LPTEG-His	*E. coli*	Schmidt Lab

Name	**Protein Expression**	**Tag**	**Expression species**	**Source***
pHEN6-$VHH_{GSDMD-4}$-HA-His	VHH-4	HA-His	*E. coli*	Schmidt Lab
pHEN6-$VHH_{GSDMD-5}$-HA-His	VHH-5	HA-His	*E. coli*	Schmidt Lab
pHEN6-$VHH_{GSDMD-6}$-HA-His	VHH-6	HA-His	*E. coli*	Schmidt Lab
pHEN6-33-A02-HA-His	VHH-33-A02	HA-His	*E. coli*	
pHEN6-33-A04-HA-His	VHH-33-A03	HA-His	*E. coli*	
pHEN6-33-B02-HA-His	VHH-33-B02	HA-His	*E. coli*	
pHEN6-33-D02-HA-His	VHH-33-D02	HA-His	*E. coli*	
pHEN6-33-F09-HA-His	VHH-33-D02	HA-His	*E. coli*	
pHEN6-33-H10-HA-His	VHH-33-H10	HA-His	*E. coli*	
pHEN6-33-H11-HA-His	VHH-33-H11	HA-His	*E. coli*	
pHEN6-34-A11-HA-His	VHH-34-A11	HA-His	*E. coli*	
pHEN6-34-D05-HA-His	VHH-34-D05	HA-His	*E. coli*	
pHEN6-34-D09-HA-His	VHH-34-D09	HA-His	*E. coli*	
pHEN6-34-E02-HA-His	VHH-34-E02	HA-His	*E. coli*	
pHEN6-34-F11-HA-His	VHH-34-F11	HA-His	*E. coli*	
pHEN6-35-A12-HA-His	VHH-35-A12	HA-His	*E. coli*	
pHEN6-35-B01-HA-His	VHH-35-B01	HA-His	*E. coli*	
pHEN6-35-D07-HA-His	VHH-35-D07	HA-His	*E. coli*	

Name	Protein Expression	Tag	Expression species	Source
pHEN6-35-F09-HA-His	VHH-35-F09	HA-His	*E. coli*	
pHEN6-38-A10-HA-His	VHH-38-A10	HA-His	*E. coli*	
pHEN6-38-B03-HA-His	VHH-38-B03	HA-His	*E. coli*	
pHEN6-38-F01-HA-His	VHH-38-F01	HA-His	*E. coli*	
pHEN6-38-G05-HA-His	VHH-38-G05	HA-His	*E. coli*	
pHEN6-38-G06-HA-His	VHH-38-G06	HA-His	*E. coli*	
pET28a-GST-tev-NLRP7-PYD	NLRP7-PYD$_{2\text{-}96}$	GST	*E. coli*	Geyer Lab
pET28a-His-PreScission	HisPreScission	His	*E. coli*	Geyer Lab
pACEBac1-MBP-tev-NLRP7	NLRP7$_{2\text{-}980}$	MBP	*Sf9*	Geyer Lab
pACEBac1-mMBP-NLRP7	NLRP7$_{2\text{-}980}$	mMBP	*Sf9*	Geyer Lab
pACEBac1-His-SUMO-Caspase-4	Caspase-4$_{1\text{-}377}$	His-SUMO	*Sf9*	
pCAGGS-VHH-HA	VHH-HA	HA	Mammalian	Schmidt Lab
pDEST-GFP-N1		GFP	Mammalian	Addgene
pDEST-mCherry-N1		mCherry	Mammalian	Addgene
pENTR-NLRP7$_{1009}$				
pENTR-NLRP7-S361L				
pENTR-NLRP7-D657V				
pENTR-NLRP7-R693P				
pENTR-NLRP7-R693W				
pEXPR-NLRP7-SH	NLRP7	Streptavidin-HA	Mammalian	Schmidt lab

Name	Protein Expression	Tag	Expression species	Source
pEXPR-NLRP7-Renilla	NLRP7-Renilla		Mammalian	Schmidt lab
pDEST-NLRP7-GFP	NLRP7	GFP	Mammalian	
pDEST-NLRP7-mCherry	NLRP7	mCherry	Mammalian	
pDEST-NLRP7-iso201-GFP	NLRP7 isoform 201	GFP	Mammalian	
pDEST-NLRP7-iso201-mCherry	NLRP7 isoform 201	mCherry	Mammalian	
pDEST-NLRP7-S361L-GFP	NLRP7-S361L	GFP	Mammalian	
pDEST-NLRP7-S361L-mCherry	NLRP7-S361L	mCherry	Mammalian	
pDEST-NLRP7-D657V-GFP	NLRP7-D657V	GFP	Mammalian	
pDEST-NLRP7-D657V-mCherry	NLRP7-D657V	mCherry	Mammalian	
pDEST-NLRP7-R693P-GFP	NLRP7-R693P	GFP	Mammalian	
pDEST-NLRP7-R693P-mCherry	NLRP7-R693P	mCherry	Mammalian	
pDEST-NLRP7-R693W-GFP	NLRP7-R693W	GFP	Mammalian	
pDEST-NLRP7-R693W-mCherry	NLRP7-R693W	mCherry	Mammalian	

*if not self-made

Table 11: Primers. All primers and gene fragments were purchased from Metabion International AG (Germany) or Integrated DNA Technologies (Singapore).

Primer	**Forward/ Reverse**	**Sequence 5'→3'**
hNLRP7 K85M	F	GAACCTGACCGAGCTGTGCATGATGGCTAA GGCTGAGATGATGG
	R	GAACCTGACCGAGCTGTGCATGATGGCTAA GGCTGAGATGATGG
hNLRP7 S361L	F	TGCTCTGTTCCAACTGGGTTTAGCTCCCGCT GTGTGCTGGATCG
	R	CGATCCAGCACACAGCGGGAGCTAAACCCA GTTGGAACAGAGCAG
hNLRP7 K511R	F	GTCCGGCGAGGAACGCCTGAGGAACCCCG ACCTGATCCAAGTGGG
	R	CCCACTTGGATCAGGTCGGGGTTCCTCAGG CGTTCCTCGCCGGAC
hNLRP7 D657V	F	CCCCAACTGGGCTAGGCAGGTCCTGCGTTC CCTGAGGCTGTGG
	R	CCACAGCCTCAGGGAACGCAGGACCTGCCT AGCCCAGTTGGGG
hNLRP7 R693P	F	TCCTGTCCGACTCCTCCGTGCCCATCCTGTG CGATCACGTGACCC
	R	GGGTCACGTGATCGCACAGGATGGGCACGG AGGAGTCGGACAGGA
hNLRP7 R693W	F	TCCTGTCCGACTCCTCCGTGTGGATCCTGTG CGATCACGTGACCC
	R	GGGTCACGTGATCGCACAGGATCCACACGG AGGAGTCGGACAGGA
hNLRP7 S702N	F	GTGCGATCACGTGACCCGTAATACCTGCCA CTTGCAGAAGGTCGAG
	R	CTCGACCTTCTGCAAGTGGCAGGTATTACG GGTCACGTGATCGCA
hNLRP7 R801H	F	TGTTGTCGTTGGAAAACTGTCacCTTACAGAA GCCAGTTGCAAGG
	R	CCTTGCAACTGGCTTCTGTAAGgtGACAGTTT TCCAACGACAACA
hNLRP7 seq1	F	TTTGTACAAAAAAGCAGGCTTAGCCATGACC TCCCCCCAGCT

Primer	Forward/ Reverse	Sequence 5'→3'
hNLRP7 seq2	F	ATCTACGTGCGTGTCGAGG
hNLRP7 seq3	R	CTGCTGTGACTTCTTCTGCAACCCAGCTTTC
EcoRI-hGSDMD	F	TACGACGGTATTAGAATTCAAGCTGAT
hGSDMD HindIII	R	ATACTTAAGCTTGTCTCTAGTGGGGCTCCTGGCT
hGSDMD Δ184-194	F	CGGGAGGGCTCGGGCCGGGAGGGCCAGGGCCATCTGAGCCAGAAG
	R	CAGATGGCCCTGGCCCTCCCGGCCCGAGCCCTCCCGCTTGTGGGT
hGSDMD Δ181-197	F	ACCCACAAGCGGGAGGGCGGCCATCTGAGCCAGAAGAAGACGGTC
	R	CTTCTGGCTCAGATGGCCGCCCTCCCGCTTGTGGGTGCGCGTGAC
hGSDMD Δ247-272	F	CAGCCACCCGCGACAGGCCTGACAGATGGGGTCCCTGCGGAGGGG
	R	AGGGACCCCATCTGTCAGGCCTGTCGCGGGTGGCTGGAAGGTCCT

Table 12: Enzymes. If not stated otherwise, restriction enzymes were purchased from New England Biolabs.

Enzyme	Supplier
DpnI	Promega (Madison, USA)
Gateway™ LR Clonase™ II Enzyme mix	Thermo Fisher Scientific (Waltham, USA)
Pfu DNA Polymerase	Promega (Madison, USA)
T4 DNA Ligase (Bonn)	New England Biolabs (Ipswich, USA)
T4 DNA ligase (Melbourne)	Promega (Madison, USA)
Q5® High-Fidelity DNA Polymerase	New England Biolabs (Ipswich, USA)

Table 13: Antibodies

Antibody	Origin species	Supplier	Catalogue Nr.	Dilution
anti-HA-HRP	Mouse	Biolegend (San Diego, USA)	16B12	1:5000
anti-NLRP7	Rabbit	Novusbio (Centennial, USA)	NBP2-94507	1:3000
Anti-myc-tag	Mouse	Cell Signaling Technology (Danvers, USA)	#2276	1:1000
anti-rabbit-HRP	Goat	Cell signaling (Danver, USA)	7074S	1:10000
anti-mouse-HRP	Sheep	Sigma-Aldrich (St. Louis, USA)	NA931	1:10000
anti-Actin-HRP clone C4	Chicken	Santa Cruz Biotechnology	Sc-47778	1:1000

Table 14: Chromatography columns.

Column	Supplier
HisTrap FF	GE Healthcare (Chicago, USA)
GSTrap FF	GE Healthcare (Chicago, USA)
MBPTrap HP	GE Healthcare (Chicago, USA)
Superdex 75 Increase 10/300 GL	GE Healthcare (Chicago, USA)
HiLoad 16/600 Superdex 75 pg	GE Healthcare (Chicago, USA)
Superdex 200 Increase 10/300 GL	GE Healthcare (Chicago, USA)
HiLoad 16/600 Superdex 200 pg	GE Healthcare (Chicago, USA)
Superose 6 Increase 10/300 GL	GE Healthcare (Chicago, USA)

Table 15: Devices and equipment.

Device	Supplier
Agarose gel chamber, DNA-SUB-Cell	Bio-Rad (Hercules, USA)
Centrifuge (5427R, 5804R, 5810, 5425, 5424R)	Eppendorf (Hamburg, Germany)
Centrifugre Avanti Jxn-26, Optima XPN-100	Beckman Coulter (Brea, USA)
CO_2 incubator MCO-20AIC	Sanyo (Ōsaka, Japan)
Cryo-loops (crystallisation)	MiTiGen (Ithaca, USA

Device	**Supplier**
ChemiDoc™imaging system	Bio-Rad (Hercules, USA)
DLS instrument Dynapro NanoStar 672	Wyatt Technologies (Santa Barbara, USA)
Flow cytometer LSR Fortessa X-20	BD Bioscience (Franklin Lakes, USA)
FPLC-System Äkta prime plus	GE Healthcare (Chicago, USA)
FPLC-System Äkta Pure	GE Healthcare (Chicago, USA)
Gel casting and PAGE system Mini-Protean Tetra Cell	Bio-Rad (Hercules, USA)
MALS detector miniDawn 3141-MD3	Wyatt Technologies (Santa Barbara, USA
Microscope Leica SP8	Leica (Wetzlar, Germany)
Mini-Extruder	Avanti Polar Lipids (Alabaster, USA)
nanoDSF instrument Prometheus NT.48	NanoTemper Technologies (München, Germany
Incubator Heratherm	Thermo Fisher Scientific (Waltham, USA)
Incubator Innova 40	New Brunswick Scientific (Jersey, USA)
PCR cycler Mastercycler nexus SX1, X	Eppendorf (Hamburg, Germany)
PCR cycler T100 Thermal Cycler	Bio-Rad (Hercules, USA)
pH meter Lab855	SI Analytics (Mainz, Germany)
Pipetting robot Crystal Gryphon LCP	Art Robins Instruments (Sunnyvale, USA)
Plate reader Spectramax i3	Molecular devices (San José, USA)
Protein crystallization imager RI-1000	Formulatrix (Bedford, USA)
Rotor (JLA 8.1000, JA 25.50)	Beckman Coulter (Brea, USA)
Scale PCB-6000-1	Kern & Sohn (Balingen-Frommern, Germany)
Spectrophometer nanodrop 2000c	Thermo Fisher Scientific (Waltham, USA)
SPR system Biacore 8K	GE Healthcare (Chicago, USA)
Shaking incubator (Minitron, Multitron, Multitron Pro)	Infors HT (Bottmingen, Switzerland)
Ultrasonic homogenizer Sonopuls HD3100	Bandelin (Berlin, Germany)
Thermomixer comfort	Eppendorf (Hamburg, Germany
Vortex Genie 2	Scientific Industries (Bohemia, USA)
Waterbath ED-5	Julabo (Seebach, Germany)
Western Blot System	Bio-Rad (Hercules, USA)

Table 16: Softwares and websites.

Software/Website	Developer/Distributer/URL
Affinity Designer 1.10.4	Serif (West Bridgford, England)
AlphaFold Protein Structure Database	https://alphafold.ebi.ac.uk/, 25.04.2023
BioRender	https://www.biorender.com/
Biacore Insight Evaluation 3.0.12.15655	Cytiva (Marlborough, USA)
Clustal Omega	https://www.ebi.ac.uk/Tools/msa/clustalo/, 11.04.2023
Coot 0.8.9.2	(Emsley and Cowtan, 2004)
Ensembl	https://www.ensembl.org/index.html, 25.04.2023
FlowJo 10.6.1	BD Bioscience (Franklin Lakes, USA)
GraphPad Prism 7	Dotmatics (Boston, USA)
Ensembl	https://www.ensembl.org/index.html, 11.04.2023
Image J 1.53u	(Schneider *et al.*, 2012)
Jalview 2.11.2.0	(Waterhouse *et al.*, 2009)
NCBI - Protein	https://www.ncbi.nlm.nih.gov/protein/, 11.04.2023
Phenix 1.17.1	(Adams *et al.*, 2010)
PR.ThermControl 2.1.5	NanoTemper Technologies (München, Germany)
PubMed	https://pubmed.ncbi.nlm.nih.gov/, 11.04.2023
PyMOL 2.0	Schrödinger (New York City, USA)
SnapGene 6.2	Dotmatics (Boston, USA)
RCSB PDB	https://www.rcsb.org/, 25.04.2023
The Human Protein Atlas	https://www.proteinatlas.org/, 11.04.2023
UniProt	https://www.uniprot.org/, 11.04.2023
XDS Version January 31, 2020	Kabsch, 1993
Zotero 6.0.23	Digital Scholar (Vienna, USA)

2.2. Methods – Molecular Biology

2.2.1. Polymerase chain reaction

Polymerase chain reaction (PCR) was applied to amplify double stranded DNA fragments for subsequent cloning and for the site-directed mutagenesis of plasmids.

2.2.1.1. DNA amplification for subcloning

PCR-based amplification of DNA fragments was used for cloning of GSDMD truncation constructs and cloning of plasmids expressing fluorescently-tagged NLRP7 isoforms. Standard PCR conditions and programs are listed in Table 17 and Table 18.

Table 17: PCR conditions for the amplification of DNA fragments.

Reagent	Volume
5x Q5 reaction buffer	10 µl
Primer fw (10 µM)	4 µl
Primer rev (10 µM)	4 µl
dNTPs (10 mM)	4 µl
DNA template	100 ng
DMSO	2.5 µl
H_2O	Ad 50 µl
Q5 DNA polymerase	0.5 µl

Table 18: PCR program for the amplification of DNA fragments.

Reaction step	Temperature	Time	Nr. Of cycles
Initial denaturation	98°C	1 min	
Denaturation	98°C	10 s	40x
Annealing	72°C	30 s	
Extension	72°C	30 s/kb	
Final extension	72°C	2 min	
Storage	10°C	hold	

2.2.1.2. Site-directed mutagenesis

Site-directed mutagenesis was used to introduce mutations into pENTR vectors encoding the $NLRP7_{980}$ and $NLRP7_{1009}$ isoforms. The following mutations were introduced into the $NLRP7_{980}$ isoform: K85M, S361L, D657V, K511R, S702N, R693P, R693W; and the mutations K85M, S361L and R801H were introduced into the $NLRP7_{1009}$ isoform. Products obtained from mutagenesis PCRs were further subjected to DpnI restriction digestion as described in chapter 2.2.2 to remove methylated, unmutated DNA templates.

Table 19: PCR conditions for the site-directed mutagenesis of plasmids.

Reagent	Volume
10x Pfu buffer	5 µl
dNTPs (10 mM)	1 µl
Forward primer (100 µM)	0.25 µl
Reverse primer (100 µM)	0.25 µl
Template DNA (75 ng/µl)	2 µl
Pfu polymerase	0.5 µl
H_2O	41 µl

Table 20: PCR program for the site-directed mutagenesis of plasmids.

Reaction step	Temperature	Time	Nr. of cycles
Initial denaturation	95°C	3 min	1
Denaturation	95°C	15 s	30
Annealing/extension	72°C	2 min/kb	
Final extension	72°C	2 min	1
Storage	16°C	hold	1

2.2.2. DNA restriction digest

DNA restriction digests were performed to prepare DNA fragments and plasmids for ligation into a new plasmid and to digest of unmutated DNA templates from mutagenesis PCRs. The reagents listed in Table 21 were combined in a 1.5 ml reaction tube, mixed gently and incubated at 37 °C for at least 1 h. DNA amounts and incubation times varied depending on the further application. An exemplary reaction setup is displayed in Table 21 which was upscaled if needed.

Table 21: Reagents used for DNA restriction digests.

Reagent	Amount
10x CutSmart® Buffer	1 µl
DNA	100 ng – 2 µg
Enzyme(s)	1 µl/µg DNA
H_2O	Ad 10 µl

2.2.3. Agarose gel electrophoresis

Agarose gels for the analysis of PCR products and DNA fragments obtained from restriction digests were prepared at a concentration of 1 % agarose (w/v) in 1x TAE buffer and stained with peqGreen (1:20,000, Bonn) or GelRed™ (1:20,000, Melbourne). Prior to loading, DNA samples were mixed with 6x DNA loading dye in a 1:6 ratio. Depending on the expected size of the DNA sample analysed, a 100 bp or 1 kb DNA standard was loaded to determine the size of the bands observed in the gel. Gels were run at 120 V for 20-30 min in 1 x TAE buffer and visualized using a Biorad Gel Doc imager.

2.2.4. Ligation of DNA fragments

DNA fragments obtained from restriction digests were ligated using T4 DNA ligase. The ligation reaction was set up as described in Table 22 and incubated at RT for 4 h or overnight at 16 °C. The ligation reaction was transformed into 50 µl of chemically competent β10 *E. coli* cells as described in Chapter 2.2.8.

Table 22: Standard conditions for the ligation of DNA fragments.

Reagent	Amount
10x T4 DNA ligase buffer	2 µl
Insert DNA	3:1 molar ratio of vector DNA
Vector DNA	50 ng
T4 DNA ligase	1 µl
ddH_2O	Ad 20 µl

2.2.5. Gateway® cloning

Gateway® cloning is a cloning strategy that allows the transfer of DNA fragments from a donor vector to a destination vector without the use of restriction enzymes. In the entry vector, the DNA fragment is flanked by *attL* sequences which recombine with *attR* sequences in the destination vector. This reaction is catalyzed by the LR enzyme mix (Gateway® Technology - Invitrogen user guide). Gateway® cloning was used to generate mammalian expression vectors for the expression of fluorescently labelled NLRP7 constructs. pENTR vectors were amplified in One Shot™ E.*coli* cells harbouring the ccdb resistance gene.

To set up the ligation reaction, the reagents were mixed as described in Table 23. The ligation reaction was incubated overnight at RT. The following day, 0.5 µl of Proteinase K were added and the reaction was incubated at 37°C for 10 min to inactivate the LR enzyme mix. 4 µl of the LR reaction mix were transformed into 50 µl chemically competent β10 *E. coli* cells as described in chapter 2.2.8 and plated on kanamycin containing agar plates.

Table 23: Conditions used for the LR reaction in gateway cloning.

Reagent	**Amount**
pENTR vector (75 ng/µl)	1 µl
pDEST vector (75 ng/µl)	1 µl
TE buffer	1 µl
LR clonase	1 µl

2.2.6. Sanger sequencing

Sanger sequencing was used to validate plasmids obtained from molecular cloning. Sequencing was performed by external services (Microsynth Seqlab GmbH, Göttingen, Germany and AGRF Ltd, Melbourne, Australia). Samples were prepared according to the requirements of the service provider.

2.2.7. Preparation of chemically competent bacteria

Bacteria were plated on an LB agar plate without antibiotics and grown overnight in an incubator at 37 °C. The next day, a single colony was used to inoculate a 50 ml LB starter culture without antibiotics. The culture was grown overnight at 37 °C and shaken at 180 rpm in an incubator. The starter culture was used the next day to inoculate a 600 ml LB culture. The culture was grown until the OD_{600} reached 0.5-0.8. Bacteria were harvested by centrifugation at 5000 rpm (F10S-6x500y rotor) for 10 minutes at 4 °C and resuspended in 300 ml of a cold 0.1 M $MgCl_2$ solution. The suspension was pelleted by centrifugation as described above. The pellet was resuspended in 60 ml of a cold 0.1 M $CaCl_2$ solution, transferred to Eppendorf tubes (1 ml each) and incubated on ice for one hour. The aliquots were then centrifuged in a table top centrifuge at 13000 rpm for 1 min at 4 °C and the pellets were resuspended in 500 µl of a cold solution consisting of 0.1 M $CaCl_2$ and 15 % glycerol. The samples were sterile transferred to 100 µl aliquots and immediately snap frozen on dry ice. Aliquots were stored at -80 °C until usage.

2.2.8. Transformation of chemically competent bacteria

For transformation of chemically competent *E. coli* cells, 50 µl aliquots of bacteria were thawed on ice, carefully mixed with 100-800 ng purified vector DNA, 2.5-10 µl ligation reaction or 2.5 µl of DpnI digested PCR product and incubated for 20 min on ice. Cells were heat shocked at 42 °C for 45 s and incubated for a further 2 min on ice. LB-medium was added to a volume of 600 µl and the cell suspension was incubated for 1 h at 37 °C with shaking at 250 rpm to allow expression of the antibiotic resistance marker. Cells were plated on LB-agar plates containing the appropriate antibiotic (100 µg/ml) and incubated overnight at 37 °C.

2.2.9. Plasmid amplification and purification

For DNA mini-preparations, 5 ml of LB-medium containing the appropriate antibiotic were inoculated with a single colony of transformed bacteria picked from an agar plate. Cultures were incubated overnight at 37 °C with vigorous shaking

at 250 rpm. Cells were harvested by centrifugation at 3000 x g for 3 min. Plasmids were extracted using the ExtractMe Plasmid Mini Kit (Bonn) or the Wizard® Plus SV Minipreps DNA Purification System kit (Melbourne) according to the manufacturer's instructions. DNA obtained from mini preparations was used for sanger sequencing and transformation of *E. coli*.

For maxi preparations, 200-300 ml of LB medium containing the appropriate antibiotic were inoculated with transformed bacteria and incubated overnight at 37 °C with vigorous shaking at 250 rpm. Cells were harvested by centrifugation at 3000 x g for 15 min. Plasmids were extracted with using the PureLink™ HiPure Plasmid Maxiprep kit following the manufacturer's instructions. DNA obtained from maxi preparations was used for transfection of eukaryotic cells.

2.2.10. Generation and purification of recombinant bacmid-DNA

Recombinant baculoviruses were used as vectors to express proteins of interest in infected insect cells. The first step in virus production was the generation and purification of plasmids encoding the baculovirus genome (bacmids). The gene of interest was cloned into the pACEBac1 vector under the control of a baculoviral polyhedrin promoter. In this vector, the expression cassette is flanked by sequences required for T7n transposition (Tn7L and Tn7R). The vector was transformed into E.*coli* DH10 MultiBac^{Turbo} cells carrying the bacmid shuttle vector and a helper plasmid encoding the Tn7 transposase, which mediates the transfer of the pACEBac1 vector into the bacmid vector via the Tn7L and Tn7R transposition sites. Successful transposition disrupts the LacZα coding sequence on the bacmid, allowing blue/white screening of bacterial colonies after transformation (Bieniossek *et al.*, 2012). Transformed bacteria were recovered for 3-4 h at 37°C with vigorous shaking before plating on agar plates containing ampicillin (100 µg/ml), gentamycin (10 µg/ml), kanamycin (50 µg/ml), tetracycline (10 µg/ml), X-Gal (100 µg/ml) and IPTG (40 µg/ml). After 24-48 h, white colonies were used to inoculate 5 ml of LB medium containing the above antibiotics at the same concentrations. Bacterial cultures were harvested by centrifugation 3,000 x g for 3 min. Pellets were lysed using the resuspension, lysis and neutralization

buffers of the ExtractMe Plasmid Mini Kit according to the manufacturer's instructions. Cleared supernatants were transferred to a fresh tube and the bacmid DNA was precipitated by adding 800 µl of ice-cold isopropanol. Samples were centrifuged at 15,000 x g for 30 min at 4°C and the resulting DNA pellets were washed twice with 800 µl of ice-cold 70 % ethanol. Between washes, bacmid DNA was pelleted by centrifugation at 15,000 x g for 10 min and 4°C. Bacmid-DNA pellets were air-dried at RT and resuspended in 20 µl ddH_2O and stored at -20°C or in 100 µl *Sf9* cell medium and used directly for transfection.

2.3. Methods – Cell biology

2.3.1. *Sf9* insect cell culture

Sf9 insect cells were used for the expression of recombinant full length NLRP7 and caspase-4.

2.3.1.1. Cultivation of *Sf9* insect cells

Sf9 insect cells were cultured in suspension in serum- and antibiotic-free Sf-900™ SFM II medium. Cultures were incubated in Erlenmeyer flasks at 27°C and shaken at 80 rpm. Cell densities were maintained between 0.3 and 3.0x10^6 cells/ml for continuous cell culture. Cell density, viability and size were checked using an automatic cell counter. Viabilities between from 95 to 99 % and cell sizes between 10 and 12 µm indicated healthy cells.

2.3.1.2. Transfection of *Sf9* insect cells

Sf9 insect cells were transfected with bacmid-DNA to produce infectious baculovirus as a delivery vector for recombinant protein expression in *Sf9* insect cells. *Sf9* insect cells were seeded into a 6-well dish at a density of 0.35x10^6 cells/ml (2 ml/well) and incubated for 1-2 h at 27°C without shaking to allow attachment. For one transfection reaction, the bacmid DNA from one bacmid prep was resuspended in 100 µl of medium, and in another tube 5 µl of MIR6100

TransIT®-Insect Transfection Reagent were mixed with 100 µl medium. Both samples were incubated for 5 min at RT, combined and incubated for a further 20 min at RT. The transfection mix was added dropwise to the cells. The cells were incubated for 3-5 h at 27 °C, then the medium was changed and the cells were incubated for a further 72 h at 27 °C. After 72 h, the initial virus stock V_0 was harvested by removing the supernatant and filtering it through a 0.22 µm filter.

2.3.1.3. Baculovirus amplification

Baculovirus was amplified to generate high-titer virus stocks for the infection of expression cultures. For this purpose, the entire V_0 virus stock (2 ml) was used to infect a 30-50 ml culture of *Sf9* cells grown to a density of $0.6x10^6$ cells/ml. Cells were cultured in suspension at 27°C and shaken at 80 rpm. After three days, V_1 viruses were harvested by centrifugation at 500 x g for 10 min and the supernatants were filtered through a 0.22 µm filter. Next, an *Sf9* culture grown to a density of $1.0x10^6$ cells/ml was infected with 2 % (v/v) of the the V_1 virus stock and cultured for three days as described above to obtain the V_2 virus. V_2 virus was harvested in the same manner as the V_1 virus and used to infect expression cultures or stored at 4°C until usage. During the virus amplification process, cell viability and size were monitored. A decrease in viability and an increase in cell size (13-15 µm) indicated successful viral infection.

2.3.2. Mammalian cell culture

The cell lines used in this study were obtained from the sources listed in Table 7. HEK293T cells were used for transfection experiments. HEK293T ASC-BFP reporter cells were engineered by lentiviral transduction to constitutively express the protein ASC with a C-terminal BFP-tag.

The Flp-In™ T-Rex 293 cell line is an engineered cell line that contains an Flp Recombination Target (FRT) site in its genome that allows the integration of a gene of interest at a specific genomic locus via Flp recombinase mediated DNA recombination (Thermofisher - Flp-In System). The Flp-In™ T-Rex 293 ASC-

EGFP cell line was engineered by lentiviral transduction to constitutively express ASC-EGFP. These cells were used to integrate the gene encoding NLRP7 into their genome as described in Chapter 2.3.3.

2.3.2.1. Cultivation of mammalian cells

HEK293T cell lines were cultured in DMEM medium supplemented with 10 % FCS, 100 U/ml penicillin and 100 µg/ml streptomycin at 37 °C and 10 % CO_2 in a humidified incubator. For Flp-In™ T-Rex 293 cells, the medium (DMEM) was supplemented with 10 % FCS, 4 µg/ml blasticidin and 50 µg/ml zeocin. After integration of the gene of interest, the cells were cultured in DMEM supplemented with 10 % FCS, 4 µg/ml blasticidin and 50 µg/ml hygromycin. For serial passaging, cell monolayers were washed with PBS and detached by addition of 0.05 % trypsin and incubation for 2-5 min at 37 °C. Trypsinization was stopped by the addition of growth medium and the cells were seeded into a new flask at the desired confluence.

2.3.2.2. Conservation of mammalian cells

To prepare cells for long-term storage, adherent cells were trypsinized and resuspended in medium. Resuspended cells or suspension cells were centrifuged at 300 x g for 5 min and cell pellets were resuspended in FCS supplemented with 10 % DMSO to a density of $3x10^6$ cells/ml. The cell suspension was transferred to cryo-tubes (1 ml/tube), placed in a cryo-freezing container and frozen at -80 °C. The next day, the cells were transferred to liquid nitrogen tanks for long-term storage.

To reactivate cells stored in liquid nitrogen, aliquots were rapidly thawed in a water bath at 37 °C, immediately transferred to a falcon tube containing 9 ml pre-warmed medium and carefully mixed. The cells were centrifuged at 300 x g for 5 min, resuspended in fresh medium and transferred to a culture flask.

2.3.2.3. Transfection of mammalian cells

One day prior to transfection, cells were seeded into a cell culture dish to reach a confluence of 70-80 % at the time of transfection. For transient transfections, the lipid-based transfection reagent Lipofectamine™2000 was used as. 1 µl of Lipofectamine™2000 was used to transfect up to 800 ng of plasmid DNA or acylated lipopeptides. Unless otherwise stated, the following protocol was used. For a single transfection, 1 µl of Lipofectamine™2000 was mixed with 24 µl of Opti-MEM™ in one tube and the desired amount of DNA or stimulant was mixed with Opti-MEM™ in another tube to a final volume of 24 µl. Both solutions were incubated for 5 min at RT, then combined and incubated for a further 25 min at RT. The transfection mixture was added dropwise to the cells.

2.3.3. Generation of a reporter cell line with inducible NLRP7 expression using the Flp-In system

Flp-In™ T-Rex 293 ASC-EGFP cells were used to generate a reporter cell line with doxycycline-inducible NLRP7 expression. Flp-In™ T-Rex 293 cells were cultured in the presence of 4 µg/ml blasticidin and 50 µg/ml zeocin. Prior to transfection, cells were seeded in a 6-well dish to reach a confluence of 70-80 % at the time of transfection. For one transfection, 5.5 µl Lipofectamine™2000 were mixed with 150 µl Opti-MEM™ in one tube, and 0.2 µg of the vector pEXPR-TO-FRT-NLRP7-SH and 1.8 µg of the vector pOG44 expressing the Flp recombinase were mixed with 150 µl Opti-MEM™ in another tube. Both solutions were incubated at RT for 5 min, combined and incubated for a further 20 min. Meanwhile, the cells were covered with 2 ml of fresh DMEM supplemented with 10 % FCS. The transfection mix was added in a drop-wise manner to the cells. The cells were incubated for 4-6 h in an incubator before the medium was replaced with fresh medium without antibiotics. The next day, the cells were transferred to a 10-cm dish and 3 h later, blasticidin was added to a final concentration of 4 µg/ml. Insertion of the transgene at the FRT site destroys the zeocin resistance gene and adds hygromycin B resistance instead. Therefore, the next day, the medium was replaced with DMEM supplemented with 10 %

FCS containing 4 µg/ml blasticidin and 50 µg/ml hygromycin B to select cells with successful integration of the transgene. Cells were monitored until all cells in the non-transfected control well had died, then single colonies were pooled and expanded for further applications.

2.3.4. Time of flight inflammasome evaluation (ASC speck assay)

To investigate inflammasome activation, flow cytometry analysis using time-of-flight inflammasome evaluation (TOFIE) was applied (Sester *et al.*, 2015). Two different ASC-expressing cell lines were used in this study: HEK293T ASC-BFP cells and Flp-In 293 T-REx ASC-EGFP cells. Experiments were performed in technical duplicates and repeated two to three times. One day prior to transfection or target gene induction, cells were seeded in 24-well plates ($0.75x10^5$ cells/well) to reach 70-85 % confluence on the day of the experiment. Transient transfection of HEK293T ASC-BFP cells was performed using the transfection reagent Lipofectamine 2000 and OptiMEM as described in chapter 2.3.2.3. In co-transfection experiments, empty vector was used to maintain the DNA amount in all samples equal. In Flp-In 293 T-REx ASC-EGFP cell lines, NLRP7 expression was induced by overnight doxycycline treatment (1 µg/ml). The transfected cells, or cells in which NLRP7 expression was induced with doxycycline, were incubated overnight. The following day, the cells were either harvested for FACS analysis or transfected for a second time with Pam2CSK4, Pam3CSK4 or FSL-1. To harvest the cells, the culture medium was removed, cells were washed with PBS and detached from the plates using trypsin. Fresh medium was added to stop the trypsinization, then the cells were transferred to a 96-well U-bottom plate and centrifuged at 400 xg for 5 min. The medium was discarded and the cells were resuspended in FACS buffer (PBS supplemented with 2 % FCS) and kept on ice until analysis. Flow cytometry analysis was performed using the LSR Fortessa to quantify ASC speck formation. Analysis was performed using FlowJo 10.7.1 software with the gating strategy shown in Figure 5.

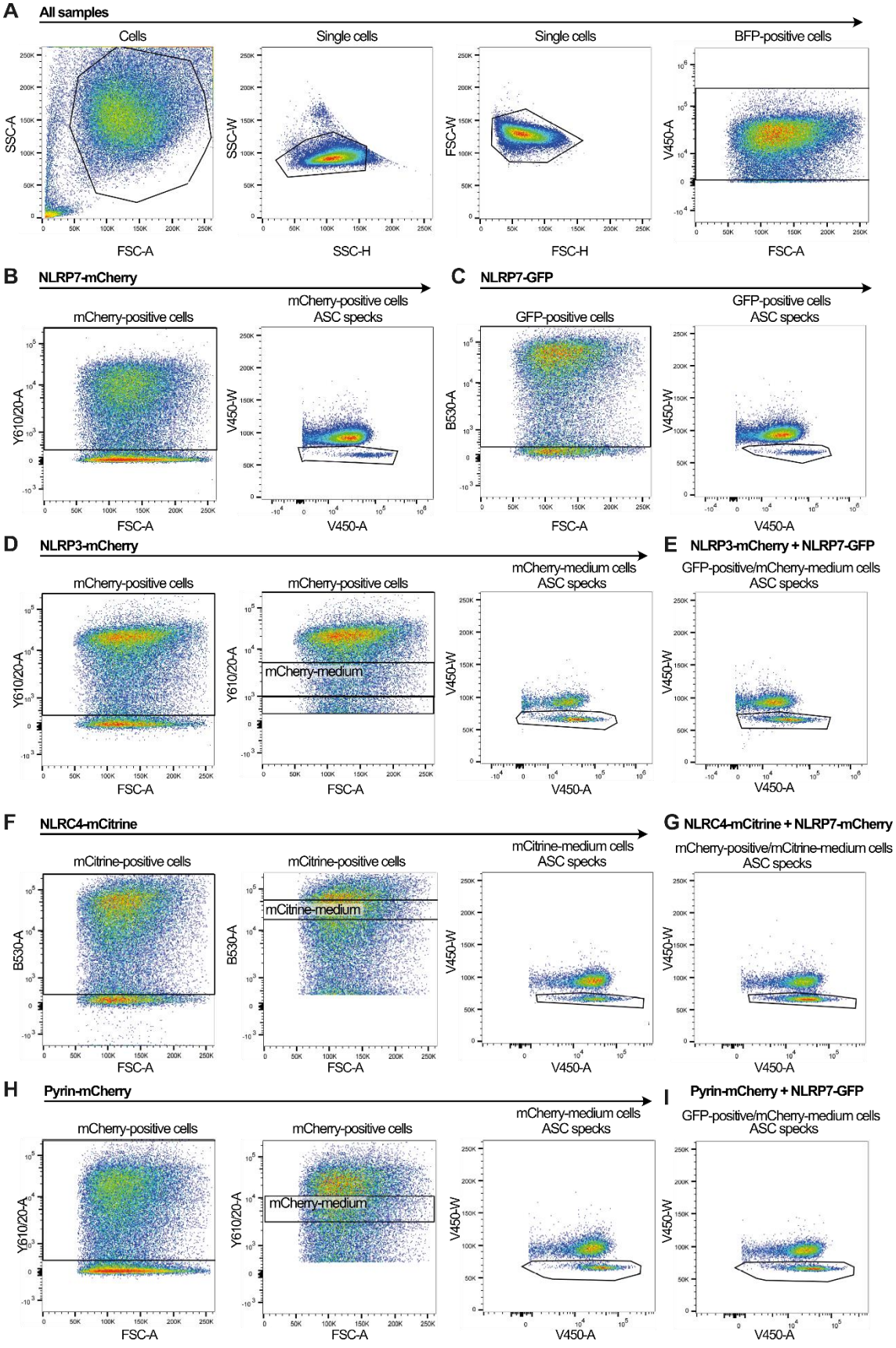
A
All samples
Cells
Single cells
Single cells
BFP-positive cells
SSC-A
FSC-A
SSC-W
SSC-H
FSC-W
FSC-H
V450-A
FSC-A
B
NLRP7-mCherry
mCherry-positive cells
mCherry-positive cells
ASC specks
Y610/20-A
FSC-A
V450-W
V450-A
C
NLRP7-GFP
GFP-positive cells
GFP-positive cells
ASC specks
B530-A
FSC-A
V450-W
V450-A
D
NLRP3-mCherry
mCherry-positive cells
mCherry-positive cells
mCherry-medium cells
ASC specks
Y610/20-A
mCherry-medium
FSC-A
FSC-A
V450-W
V450-A
E
NLRP3-mCherry + NLRP7-GFP
GFP-positive/mCherry-medium cells
ASC specks
V450-W
V450-A
F
NLRC4-mCitrine
mCitrine-positive cells
mCitrine-positive cells
mCitrine-medium cells
ASC specks
B530-A
mCitrine-medium
FSC-A
FSC-A
V450-W
V450-A
G
NLRC4-mCitrine + NLRP7-mCherry
mCherry-positive/mCitrine-medium cells
ASC specks
V450-W
V450-A
H
Pyrin-mCherry
mCherry-positive cells
mCherry-positive cells
mCherry-medium cells
ASC specks
Y610/20-A
mCherry-medium
FSC-A
FSC-A
V450-W
V450-A
I
Pyrin-mCherry + NLRP7-GFP
GFP-positive/mCherry-medium cells
ASC specks
V450-W
V450-A

Figure 5: Gating strategy for time of flight inflammasome evaluation of ASC speck formation. A) All samples were gated for single cells with ASC-BFP expression. **B, C)** Cells transfected with NLRP-mCherry or NLRP7-GFP constructs were gated for mCherry- or GFP-positive cells, respectively. The percentage of ASC specks refers to mCherry- or GFP-positive cells, respectively. **D)** Cells transfected with NLRP3-mCherry were gated for a population with medium expression in which approx. 40% of cells presented ASC specks. **E)** Cells transfected with NLRP7-GFP and NLRP3-mCherry were gated for GFP-positive cells with medium NLRP3-mCherry expression. **F)** Cells transfected with NLRC4-mCitrine were gated for a population with medium expression in which approx. 20% of cells presented ASC specks. **G)** Cells transfected with NLRP7-mCherry and NLRC4-mCitrine were gated for mCherry-positive cells with medium NLRC4-mCitrine expression. **H)** Cells transfected with pyrin-mCherry were gated for a population with medium expression in which approx. 40% of cells presented ASC specks. **I)** Cells transfected with NLRP7-GFP were and pyrin-mCherry gated for GFP-positive cells with medium pyrin-mCherry expression.

2.3.5. LUMIER

HEK293T cells were seeded in a 24-well plate at a density of $2.5x10^5$ cells/well and incubated overnight at 37°C, 5 % CO_2. Cells were transfected with 250 ng pCAGGS expression plasmids for the HA-tagged nanobodies and 250 ng pEXPR-NLRP7-renilla using the Lipofectamine 2000 transfection reagent and incubated overnight. Lumitrac 600 white high-binding 96-well plates were coated with mouse αHA antibody (clone 16B12) at a concentration of 0.5 µg/well and incubated overnight. Plates were blocked with a buffer containing 1 % BSA, 5 % sucrose and 0.5 % Tween-20 in PBS for 2 h at RT. Cells were washed with PBS and lysed with lysis buffer containing 50 mM HEPES-KOH (pH 7.9), 150 mM NaCl, 2 mM EDTA, 0.5 % Triton X-100, 5 % glycerol and complete protease inhibitor by incubation on ice for 10 min. 90 µl of the lysate were added to the Lumitrac plates and incubated at 4°C for 3 h. The luciferase substrate mixture was prepared according to the manufacturer's instructions and kept in the dark for 25 min. Lumitrac plates were washed and 50 µl of luciferase substrate mixture were added per well. After incubation for 2 min, luminescence was measured at 480 nm using a plate reader.

2.3.6. Enzyme-linked Immunosorbent Assay (ELISA)

THP-1 cells were seeded in a 96-well plate at a density of $0.5x10^5$ per well. The cells were treated with either Pam2CSK4 (2 µg/ml), Pam3CSK4 (2 µg/ml) or FSL-1 (2 µg/ml) or left untreated and incubated overnight. Supernatants were collected by centrifuging the plate for 5 min at 400xg and transferring the supernatant to a fresh 96-well plate. TNF-α levels in the samples were analysed using the DuoSet® Human TNF-α ELISA kits according to the manufacturer's instructions.

2.3.7. Fluorescence microscopy

Glass bottom chamber coverslips (8-well) with glass bottom were coated with 300 µl/well poly D-lysine at a concentration of 50 ug/ml in PBS for 1 h at RT. The coverslips were then washed four times with 300 µl of distilled sterile water. The coverslips were dried in a laminar flow hood for 3 h at RT. Then, $1.5x10^4$ HEK293T ASC-BFP cells were seeded per well in 300 µl of medium. Cells were cultured for 48 h prior to transfection. Transfection was performed as described in section 2.3.2.3 using 100 and 500 ng of vector DNA of either pyrin-mCherry, $NLRP7_{980}$-GFP or $NLRP7_{1009}$-GFP. The following day, the medium was replaced with 150 µl FluoBright DMEM. Z-stack images were acquired with a Leica SP8 microscope using immersion oil with a refractive index of 1.518 and an Olympus PlanApo 60x/1.42 NA oil immersion objective. Microscopic images were analysed using the software Fiji version 2.1.0 and are presented as maximum intensity projections.

2.4. Methods – Protein biochemistry

2.4.1. Protein expression in *E. coli*

The NLRP7-PYD, all nanobodies, GSDMD constructs and proteases were expressed in *E. coli*. Different *E. coli* strains, expression times and temperatures were used to meet the requirements of the different proteins. For all proteins, a preculture was grown overnight at 37 °C with shaking at 180 rpm. 25 ml of the

preculture were used to inoculate 1 l of the expression culture the following day. All expression cultures were cultivated in an incubator shaking at 180 rpm.

2.4.1.1. GSDMD constructs

Human full length $GSDMD_{1-484}$ and truncated GSDMD constructs ($GSDMD_{\Delta 247-272}$, $GSDMD_{\Delta 184-194/\Delta 247-272}$ and $GSDMD_{\Delta 181-197/\Delta 247-272}$) were expressed with N-terminal His_6-SUMO-tags using the pEXPR vector.

The expression constructs were transformed in *E. coli* Rosetta (DE3) cells, and the cells were grown in 2x-LB-medium containing 0.5 % glucose and 50 µg/ml kanamycin at 37°C until the OD_{600} reached 0.8. Expression was induced overnight at 20 °C with 0.2 mM IPTG and 0.6 % (w/v) lactose.

2.4.1.2. Nanobodies

The pHEN6 vectors for bacterial, periplasmic expression of GSDMD-targeting nanobodies were transformed into *E. coli* WK6 cells. $VHH_{GSDMD-1}$, $_{GSDMD-2}$, and $_{GSDMD-3}$ were expressed with C-terminal LPTEG-His-tags, and $VHH_{GSDMD-4}$, $_{GSDMD-5}$, and $_{GSDMD-6}$ were expressed with C-terminal HA-His-tags. All NLRP7 targeting nanobodies were expressed with C-terminal HA-His-tags. Cells were grown at 37°C in TB medium containing 100 µg/ml ampicillin until the OD_{600} reached 0.6. Expression was induced overnight with 1 mM IPTG at 20°C.

2.4.1.3. ULP1

The SUMO protease ULP1 was expressed as His-fusion protein in *E. coli* BL21 (DE3) cells. Cells were grown at 37°C in LB medium containing 100 µg/ml ampicillin and chloramphenicol until the OD_{600} reached 0.8. Expression was induced overnight with 0.75 mM IPTG at 30°C.

2.4.1.4. Prescission (3C) protease

The pET-28a vector encoding His-3C protease was transformed into *E. coli* Rosetta BL21 (DE3) cells. Cells were grown at 37 °C in TB auto-induction

medium (TB medium supplemented with 17 mM KH_2PO_4, 72 mM K_2HPO_4, 0.4 % lactose, 0.05 % glucose, 2 mM $MgSO_4$) containing 50 µg/ml until the OD_{600} reached 0.6. Then, cultures were transferred to 20°C for protein expression overnight.

2.4.1.5. NLRP7-PYD

The bacterial expression vector for the human GST-tagged NLRP7-PYD_{2-96} was transformed into *E. coli* Artic Express (DE3) cells and cells were grown at 37 °C in 2x-LB-medium containing 0.5 % glucose and kanamycin (50 µg/ml) until the OD_{600} reached 0.8. Expression was induced with 0.2 mM IPTG and 0.6 % (w/v) glucose. The NLRP7-PYD was expressed at 14°C overnight.

2.4.2. Protein expression in *Sf9* insect cells

For protein expression, *Sf9* cultures (250 ml - 1 l) were grown to a density of $1.5x10^6$ cells/ml and infected with V_2 virus. For the expression of NLRP7 constructs, 3 % of V_2 virus (v/v) were used and proteins were expressed for 72 h. For the expression of caspase-4, 1 % V_2 virus was used and the protein was expressed for 48 h.

2.4.3. Protein purification

To purify the proteins expressed recombinantly in *E. coli* or baculovirus-infected *Sf9* insect cells, the cells were harvested and lysed, and proteins were isolated from the cell lysates using affinity chromatography. For some proteins, a second purification step was performed by size-exclusion chromatography (SEC). The principles of affinity chromatography and SEC are explained below followed by descriptions of the purification procedures for the individual proteins used in this study.

2.4.3.1. Affinity chromatography

Affinity chromatography was used to isolate recombinant proteins from crude cell lysates. The proteins of interest were expressed as fusion proteins with different affinity-tags such as the poly-histidine- (His_6), maltose-binding-protein- (MBP) or glutathione-S-transferase- (GST) tag. Affinity chromatography is based on the specific interaction of the affinity-tag with its ligand (Ni2+-NTA, amylose or glutathione, respectively) which is immobilized on the agarose resin of the affinity column. In a first step, the affinity-tagged protein is allowed to bind to the affinity resin. This is followed by a washing step to remove unbound proteins. Finally, specifically bound proteins are eluted using an elution buffer containing high concentrations of chemicals or proteins that outcompete the binding of the affinity-tagged protein to the affinity-resin (imidazole, maltose or glutathione, respectively).

2.4.3.2. Size-exclusion chromatography (SEC)

Size exclusion chromatography (SEC) is a method to separate proteins according to their hydrodynamic radius. SEC columns consist of a resin with porous beads that allow proteins to diffuse according to their size. While proteins with a smaller hydrodynamic radius are able to enter the pores of the resin and are therefore retained longer, proteins with a larger hydrodynamic radius are unable to penetrate the pores and are therefore eluted first. SEC columns are available in a range of dimensions to allow the purification of different sample sizes and different resins, allowing the separation of a wide range of hydrodynamic radii.

2.4.3.3. GSDMD constructs

His_6-SUMO-tagged GSDMD constructs were expressed in *E. coli* Rosetta (DE3) cells. Cells were harvested by centrifugation at 5000 x g for 20 min at 4 °C. The pellet was resuspended in a lysis buffer containing 25 mM Tris (pH 8.0), 200 mM NaCl, 10 % glycerol, 10 mM imidazole, and 5 mM DTT. A spatula tip of DNase and lysozyme, as well as 1 mM PMSF were freshly added to the suspension and cells were lysed by sonication (40 % amplitude, 10s on/ 5 s off, 4 min). Cell lysates

were cleared by centrifugation at 36000xg for 45 min and passed through a 0.45 µm filter. The His-SUMO fusion proteins were enriched on Ni-NTA beads. For this, 3-5 ml of Ni-NTA slurry were loaded onto a gravity flow column and equilibrated with lysis buffer. The equilibrated beads were added to the cell lysates and incubated for 1 h at 4 °C on a rotator. The mixture was again loaded onto the gravity flow column, and after the supernatant had flown through, the beads were washed with 60 ml of lysis buffer. Bound proteins were eluted using a buffer containing 25 mM Tris (pH 8.0), 200 mM NaCl, 300 mM imidazole, and 5 mM DTT. Protein-containing fractions were pooled and concentrated using an Amicon® concentrator with a 50 kDa cut-off. A buffer exchange to cleavage buffer (25 mM Tris (pH 8.0), 200 mM NaCl, 5 % glycerol, 5 mM DTT) was performed using a PD10 column according to the manufacturer instructions. Samples were incubated with the SUMO protease ULP1 (homemade, ratio ULP1/GSDMD 1:20) at 4°C overnight, followed by a second Ni-NTA chromatography to remove uncleaved protein, ULP1 protease, and the His-SUMO-tag. To do so, the Ni-NTA beads were equilibrated with cutting buffer and incubated with the GSDMD/ULP1 mixture for 1 h at 4°C on a rotator. The bead suspension was loaded onto a gravity flow column and the flow through containing the tag-free GSDMD variants was collected. Samples were concentrated using a 30 K cut-off Amicon® concentrator. Subsequently, the samples were subjected to size-exclusion chromatography using an S200 column and a buffer containing 20 mM HEPES (pH 8.0), 200 mM NaCl and 5 mM DTT.

2.4.3.4. ULP1

The SUMO protease ULP1 was expressed as His-fusion protein in *E. coli* BL21 (DE3) cells. Cells were harvested by centrifugation at 5000 x g for 20 min at 4 °C. The pellet was resuspended in a lysis buffer containing 50 mM Tris (pH 8.0), 350 mM NaCl, 20 mM sucrose, 10 mM imidazole, and 1 mM β-ME. A spatula tip of DNase and lysozyme, as well as 1 mM PMSF were freshly added to the suspension and cells were lysed by sonication (40 % amplitude, 10s on/ 5 s off, 4 min). Cell lysates were cleared by centrifugation at 36000xg and 4°C for 45 min

and passed through a 0.45 µm filter. The His-fusion protein were enriched on Ni-NTA beads. For this, 3-5 ml of Ni-NTA slurry were loaded on a gravity flow column and equilibrated with lysis buffer. The equilibrated beads were added to the cell lysates and incubated for 1 h at 4 °C on a rotator. The mixture was again loaded on the gravity flow column, and after the supernatant had flown through, the beads were washed with 60 ml of wash buffer consisting of 50 mM Tris (pH 8.0), 300 mM NaCl, 20 mM imidazole, and 1 mM β-ME. Bound proteins were eluted using a buffer containing 50 mM Tris (pH 8.0), 300 mM NaCl, 300 mM imidazole, and 1 mM β-ME. Fractions containing protein were pooled and concentrated using an Amicon® concentrator with a 10 kDa cut-off. A buffer exchange to storage buffer (50 mM Tris (pH 8.0), 0.2 % NP40, 500 mM NaCl, 50 % glycerol and 1 mM TCEP) was performed using a PD-10 column according to the manufacturer's instructions.

2.4.3.5. Prescission (3C) protease

The 3C protease was expressed with an N-terminal His-tag in *E. coli* Rosetta BL21 (DE3) cells. Cells were harvested by centrifugation at 5000 x g for 20 min at 4 °C. and lysed by sonication (40 % amplitude, 10 s on/5 s off, 3 min) in a buffer containing 50 mM HEPES (pH 7.5), 500 mM NaCl, 25 mM imidazole, 5 % glycerol and 5 mM β-ME supplemented with a spatula tip of DNase and 1mM PMSF. Lysates were cleared by centrifugation at 36000xg rpm for 30 min and filtered through a 0.45 µm filter. 3-5 ml Ni-NTA beads were equilibrated with lysis buffer. The equilibrated beads were added to the cleared cell lysates and incubated for 1 h at 4 °C and then washed with 100 ml lysis buffer. Bound protein was eluted in a buffer containing 50 mM HEPES (pH 7.5), 500 mM NaCl, 250 mM imidazole, and 5 mM β-ME. Protein-containing elution fractions were pooled, and concentrated in an Amicon® concentrator with a 10 kDa cut-off and subjected to gel filtration using an S75 16/600 column in a buffer containing 20 mM HEPES (pH 7.5), 150 mM NaCl, 5 % glycerol, and 1 mM TCEP.

2.4.3.6. Nanobodies

Cells were harvested by centrifugation at 5000 x g for 20 min at 4 °C and periplasmic extracts were generated using osmotic shock. For this purpose, cell pellets were resuspended in 15 ml TES buffer (20 mM Tris (pH 8.0), 0.65 mM EDTA, 0.5 M sucrose) and incubated for 1 h at 4°C on a rotator. Subsequently, 35 ml of 0.25x TES were added to the suspension and samples were incubated for at least 1 h at 4°C. Lysates were cleared by centrifugation at 15000 xg for 45 min and the His-tagged nanobodies were enriched using Ni-NTA beads. 3-5 ml Ni-NTA beads were loaded on a gravity flow column and equilibrated with 0.25 TES buffer. The equilibrated beads were added to the cleared cell lysates and incubated for 1 h at 4 °C.

Beads were washed using a buffer containing 50 mM Tris (pH 7.5), 150 mM NaCl, and 10 mM imidazole and proteins were eluted in the same buffer supplemented with 0.5 M imidazole. Protein containing elution fractions were pooled and subjected to gel filtration in a buffer containing 20 mM HEPES (pH 7.5), and 150 mM NaCl using an S75 16/600 column.

2.4.3.7. Caspase-4

Caspase-4 was expressed with an N-terminal His_6-SUMO tag in baculovirus infected *Sf9* insect cells. Cells were harvested by centrifugation for 10 min at 1000 xg and lysed by sonication (40 % amplitude, 10 s on/5 s off, 2 min) in a buffer containing 50 mM Tris (pH 8.0), 150 mM NaCl, 5 mM imidazole, and 2 mM β-ME supplemented with a spatula tip of DNase and 1mM PMSF. Cell lysates were cleared by centrifugation at 36000 xg for 45 min and filtered through a 0.45 µm filter. His-SUMO-caspase-4 was purified using Ni-NTA affinity chromatography. 3 ml of Ni-NTA resin were equilibrated with lysis buffer and incubated with the cell lysate for 1 h at 4°C on a rotator. Then, the suspension was loaded onto a gravity flow column and beads were washed with 60 ml of wash buffer (50 mM Tris (pH 8.0), 150 mM NaCl, 20 mM imidazole, and 2 mM β-ME) prior to elution with elution buffer (50 mM Tris (pH 8.0), 150 mM NaCl, 300 mM imidazole, 2 mM β-ME). Elution fractions containing the His-SUMO-fusion protein were pooled and

concentrated in a 30 K Amicon® concentrator to a concentration of 10 mg/ml. The sample was incubated at 4 °C overnight to enhance the auto-activation of the protease. Caspase-4 activity was evaluated by incubating the protein in a 0.5:1 ration with recombinant GSDMD for 1 h at 37°C and analysing GSDMD cleavage via SDS-PAGE.

2.4.3.8. Full length NLRP7

MBP-tev-NLRP7$_{2-980}$ and mMBP-NLRP7$_{2-980}$ were expressed in baculovirus infected *Sf9* insect cells. Cells were harvested by centrifugation and lysed by sonication (40 % amplitude, 5 s on/ 5 s off, 1 min) in lysis buffer (50 mM Tris (pH 8.0), 300 mM NaCl, 10 % glycerol, 0.35 % CHAPS, 50 mM Glu/Arg and 2 mM DTT) supplemented with a spatula tip of DNase and 1 mM PMSF. Cell lysates were cleared by centrifugation at 36000 xg at 4°C for 45 min and filtered through a 0.45 µm filter. 3-5 ml of amylose resin were equilibrated with lysis buffer and incubated with the cell lysates for 1h at 4°C. Beads were washed using 60 ml wash buffer to gradiently reduce the glycerol content. In a first step, beads were washed with 20 ml of a buffer containing 50 mM Tris, pH 8.0, 300 mM NaCl, 50 mM Arg/Glu, 2 mM DTT and 7.5 % glycerol, in the next washing step the glycerol content was reduced to 5 %, then to 2.5 % and in the final washing step to 0 %. The proteins were eluted using a buffer consisting of 50 mM Tris (pH 8.0), 300 mM NaCl, 50 mM Arg/Glu, 25 mM Maltose, and 2 mM DTT. Fractions containing protein were pooled and concentrated using an Amicon® concentrator with 100 kDa cut-off and subjected to size-exclusion using a Superose 6 10/300 GL (increase) column and a buffer consisting of 20 mM HEPES pH 7.4, 200 mM NaCl and 0.5 mM TCEP.

2.4.3.9. NLRP7-PYD

The NLRP7-PYD$_{2-96}$ was expressed with a TEV-cleavable N-terminal GST-tag in *E. coli* Arctic express (DE3) cells. Cells were harvested by centrifugation and lysed by sonication (60 % amplitude, 10 s on/ 10 s off, 3 min) in lysis buffer (50 mM HEPES (pH 7.0), 500 mM NaCl, 10 % glycerol, and 2 mM DTT)

supplemented with a spatula tip of DNase and lysozyme and 1 mM PMSF. Cell lysates were cleared by centrifugation at 36000 xg at 4°C for 45 min and filtered through a 0.45 µm filter. 3-5 ml of glutathione resin were equilibrated with lysis buffer and incubated with the cell lysates for 1h at 4°C. Beads were washed using 60 ml wash buffer containing 50 mM HEPES, pH 7.0, 300 mM NaCl, and 2 mM DTT. The protein was eluted using a buffer consisting of 50 mM HEPES (pH 7.0), 300 mM NaCl, 10 mM GSH, and 2 mM DTT. Fractions containing protein were pooled and concentrated using an Amicon® with 10 kDa cut-off and the GST-tag was cleaved off by incubation with TEV-protease at 4°C overnight. The following day, the sample was again applied to the glutathione beads equilibrated with wash buffer to remove the cleaved GST-tag. The affinity purified protein was concentrated using an Amicon® with 10 kDa cut-off and subjected to size-exclusion using a S75 16/600 column and a buffer consisting of 20 mM HEPES (pH 7.0), 200 mM NaCl, 1 mM TCEP.

2.4.4. SDS-PAGE and Coomassie blue staining

SDS-PAGE was used to separate proteins according to their molecular weight and to analyse protein samples in regard of their homogeneity. Protein samples were denatured by addition of Laemmli buffer (Table 8) and heating at 95°C for 5 min. Samples were loaded on home-made 12 % or 15 % SDS-PAGE gels that were prepared as described in Table 24. Gel electrophoresis was performed in SDS running buffer (Table 8) at 250V for 45 min. To determine the molecular weight of the analysed proteins, 2 µl of Precision Plus protein standard were loaded. Proteins were visualized using Coomassie blue by covering the gel in staining solution (Table 8) and heating up gel and staining solution in the microwave (800 W, 2 min) followed by incubation for 5-10 min at RT. Gels were destained using Coomassie destain solution (Table 8) following the same heating and incubation procedure as for staining until protein bands were visible.

Table 24: SDS gel recipe.

	Stacking gel	**Separation gel**	
Reagent	5 %	12 %	15 %

ddH_2O	1.8 ml	3.4 ml	2.3 ml
Rotiphorese Gel 30	0.5 ml	4.2 ml	5.3 ml
Stacking gel buffer (Table 8)	0.4 ml	-	-
Separation gel buffer(Table 8)	-	2.9 ml	2.9 ml
10 % APS	26.5 µl	118.8 µl	118.8 µl
TEMED	2.7 µl	3.5 µl	3.5 µl

2.4.5. SEC-MALS

Size-exclusion chromatography (SEC) combined with multi-angle light scattering (MALS) was used to determine the size and molecular weight of individual proteins and multi-protein complexes. For SEC-MALS analysis of the GSDMD-$VHH_{GSDMD-2}$-$VHH_{GSDMD-6}$, $GSDMD_{\Delta 184-194/\Delta 247-272}$ was mixed with $VHH_{GSDMD-2}$, $VHH_{GSDMD-6}$ or both nanobodies at equimolar concentrations (188.8 µM) and injected into a Superose 6 10/300 GL column equilibrated with GSDMD-SEC buffer. The chromatography system was attached to a three-angle light scattering detector (miniDAWN, Wyatt) and a refractive index detector (Optilab T-rEX, Wyatt). Data were collected every 0.5 s at a flow rate of 0.5 ml/min and analysed using the ASTRA V software (Wyatt).

2.4.6. Thermal shift assay (nanoDSF)

Nano differential scanning fluorimetry (nanoDSF) was used to determine the thermal stability of single proteins and protein complexes. Samples containing varying concentrations of protein (5 µM-50 µM) were loaded into glass capillaries and applied to the Prometheus NT.48 nanoDSF instrument. Samples were heated from 20 to 90°C at a rate of 1.5°C/min and protein unfolding was monitored by detecting shifts in the fluorescence at 330 and 350 nm. Data were analysed using the Nanotemper PR.ThermControl software.

2.4.7. Surface plasmon resonance (SPR)

Surface plasmon resonance (SPR) was used to analyse protein-protein interactions, determine binding affinities and perform epitope binning experiments. SPR is a label-free technique in which one binding partner, the

ligand, is immobilized on the surface of the sensor ship, while the other interacting molecule, the analyte, is in free solution in the liquid phase that is constantly flown over the surface of the sensor chip surface (Piliarik *et al.*, 2009).

All experiments were performed using a Biacore 8K instrument. The flow system was cleaned using the “Desorb” maintenance function (Desorb Kit, GE Healthcare). The system was flushed with running buffer (SEC buffer of the respective protein) and all steps were performed at 25°C chip temperature.

For GST-NLRP7-PYD or GST capture, a CM5 sensor chip was covalently modified with a goat anti-GST polyclonal antibody (GST capture Kit, GE Healthcare). For mMBP-NLRP7 or MBP coupling, a high affinity polyclonal anti-MBP antibody was used. The surface of flow cells 1 and 2 was activated for 60 s with 50 mM NaOH (30 µL/min), followed by activation of both flow cells for 7 min with a 1:1 mixture of 0.1 M NHS (N-hydroxysuccinimide) and 0.1 M EDC (3-(N,N-dimethylamino) propyl-N-ethylcarbodiimide) (10 µL/min). Prior to amine-coupling, the flow system was washed with 1 M ethanolamine pH 8.0. The anti-GST pAb (30 µg/mL in 10 mM sodium acetate pH 5.0, 2 µL/min) or anti-MBP pAb (14 µg/mL in 10 mM sodium acetate pH 5.0, 2 µL/min) were immobilized at a density of 4000-6000 RU on flow cell 1 and 2. The surfaces were blocked by injection of 1 M ethanolamine pH 8.0 (10 µL/min) for 7 min. To block of high affinity sites, recombinant GST or MBP was injected for three consecutive cycles of 180 s each (30 µL/min, 200 mM) followed by 120 s regeneration with 10 mM glycine pH 2.0 (30 µL/min). GST-NLRP7-PYD or mMBP-NLRP7 were immobilized on flow cell 2 for 360 s (3 µL/min, 200 nM), followed by 300 s stabilization time (30 µL/min).

For kinetic binding measurements, the analyte was injected in “single cycle kinetics” over both flow cells at concentrations of 125 pM - 16 nM (30 µL/min). Increasing analyte concentrations were injected sequentially (association: 120 s, dissociation: 55 s, final dissociation: 600 s).

Epitope binding measurements with nanobodies were performed using the A-B-A injection function (30 µL/min, analyte contact time: 60 s, pre-analyte contact time: 60 s, post-analyte contact time: 60 s, flanking solution: 256 nM VHH 1, analyte solution: 256 nM VHH 1 / 256 nM VHH 2). After each cycle, the surfaces were regenerated with two 45 s injections of 10 mM glycine pH 2.0 (20 µL/min).

Data were collected at a rate of 10 Hz. Data were double referenced by blank cycle and reference flow cell subtraction. Processed data were fitted with a 1:1 interaction model using Biacore Insight Evaluation Software (version 2.0. 15.12933).

For experiments with GSDMD and GSDMD-targeting nanobodies, the system was flushed with running buffer (20 mM HEPES (pH 8.0), 200 mM NaCl, 5 mM DTT, 0.05 % Tween20) and all steps were performed at 25°C chip temperature. Chemically biotinylated GSDMD at a concentration of 100 nM was immobilized for 180 s on the flow cell 2 of a Series S Sensor Chip CAP using a biotin capture kit at a flow rate of 30 µl/min. The system was washed with running buffer for 600 s at a flow rate of 30 µl/min. Binding affinities were determined using multi-cycle kinetics. To account for different binding affinities, the nanobodies were injected at different concentrations ($VHH_{GSDMD-1, -2, -3, -5}$: 0.5–32 nM, $VHH_{GSDMD-4}$, and $VHH_{GSDMD-6}$: 64–4096 nM) at a flow rate of 30 µl/min. The association step was carried out for 120 s and the dissociation step for 300 s.

For epitope binning experiments, the nanobodies were pairwise tested for competitive binding. The first analyte was injected at a concentration of 128 nM at a flow rate of 10 µl/min for 120 s. This step was followed by a dissociation step for 60 s. Then, a mixture of the first and the second analyte (both 128 nM) was injected at a flowrate of 10 µl/min for 120 s, followed by a dissociation step of 30 s. After each cycle, surfaces were regenerated for 120 s using the regeneration solution of the capture kit with a flow rate of 10 µl/min. Data were referenced by a blank cycle (no analyte injected) and subtraction of the reference flow cell (flow cell 1). Data were analysed using the Biacore Insight Evaluation Software. Dissociation constants were determined from fits using a 1:1 binding model.

2.4.8. X-ray crystallography

X-ray crystallography is a widely used method for determining the three-dimensional structure of macromolecules, including proteins and nucleic acids, with near-atomic resolution (Dessau and Modis, 2011). The technique uses X-rays to analyse the electron density of molecules in a crystal lattice, which can be

used to determine the positions of the atoms in the molecule (Smyth and Martin, 2000).

The first step in protein X-ray crystallography is to produce a highly homogeneous protein sample from which crystals with good X-ray diffraction properties can be grown. Protein crystals are three-dimensional arrays in which multiple individual protein molecules are periodically arranged in a crystal lattice. Crystals are needed for diffraction experiments to amplify the diffraction signal, as single molecules diffract only weakly (Gawas *et al.*, 2019, p.5). To produce protein crystals, the protein sample must be brought to supersaturation. This is often achieved by mixing the protein sample with a suitable buffer solution, followed by vapour diffusion to slowly increase the concentration of all components in the protein solution, allowing the proteins to slowly form a crystal lattice. Identifying the conditions that allow a particular sample to crystallize, including the buffer composition and pH, protein concentrations and temperatures, is empirical and requires trial and error procedures (McPherson and Gavira, 2014). To facilitate the identification of initial crystallization conditions, commercial screens with different buffer solutions are available that vary in their precipitant, buffer, salt and pH composition. The quality of the crystal is critical to the success of the experiment, as well-diffracting crystals are required for structure determination.

In the next step, the crystal is exposed to a beam of X-rays with a wavelength of about 1 Å (Gawas *et al.*, 2019, p.5). The X-rays interact with the electrons in the crystal lattice and are diffracted. The diffracted X-rays interfere with each other and constructive interference produces a diffraction pattern of spots on a detector. Computational methods are then used to interpret the diffraction data. The positions and intensities of the diffraction spots can be used to calculate the electron density of the molecule in the crystal lattice. To determine the electron density, information about the amplitude and the phase of the scattered X-rays is required. However, while the amplitude can be calculated from the spot intensity, the diffraction pattern does not contain any information about the phase of the diffracted X-rays. The phases can be determined experimentally or inferred from the atomic coordinates of a structurally similar protein, a method known as

molecular replacement (Taylor, 2010). The electron density can be used to build a model of the molecule in the crystal The resulting structural model is further modified in iterative cycles of model building and refinement, in which the model is adjusted to fit the experimental data more accurately (Adiyaman and McGuffin, 2019).

2.4.8.1. Crystallization of the NLRP7-PYD in complex with nanobodies

To obtain homogeneous protein samples, the NLRP7-PYD was mixed with the nanobodies 38-A10, 38-B03 or both nanobodies in a 1:3 ratio and incubated on ice for 10 min. Unbound nanobody was then removed by SEC using a HiLoad 16/600 Superdex 200 pg column. Fractions containing both proteins were pooled and concentrated to 20 mg/ml. Crystallization screens were performed using the commercial screens LMB (Molecular Dimensions), JCSG+ (Jena Biosciences), PACT (Molecular Dimensions), Ligand friendly (Molecular Dimensions), Proplex (Molecular Dimensions) and Morpheus (Molecular Dimensions) and a drop volume of 0.1 µl protein in a 96-well format using the sitting drop vapour diffusion method at 20°C. When initial crystals were obtained, the salt concentrations and pH were varied in second screen in order to obtain better diffracting crystals. Optimization screens were performed in a 24-well plate format using hanging drops of 1 µl protein volume. For the NLRP7-PYD-38-A10 complex, optimization screens were performed for the conditions A6 of the LMB screen (1.4 M Ammonium di-hydrogen phosphate, 0.1 M Tris pH 7.5) and B1 of the JSCG+ screen (0.8 ammonium sulphate, 0.1 M tri-sodium citrate pH 4.0) by varying the pH in 0.2 steps from 7.0 - 8.0 (LMB A6) and 3.4 - 4.4 (JCSG+ B1). Ammonium phosphate and ammonium sulphate concentrations were varied from 1-2 M and 0.5-1.5 M, respectively. An additive screen was also performed using a condition of 0.5 M ammonium sulphate, 0.1 M tri-sodium citrate pH 3.4 and the HR2-428 additive screen (Hampton Research). Crystals obtained from the additive screen were further used for seeding by streaking and micro seeding in a condition of 0.1 M tri-sodium citrate pH 3.4, 0.5 M ammonium sulphate, and 0.1 % dichloromethane.

For the NLRP7-PYD-38-B03 complex, optimization screens were performed for the condition C2 of the JCSG+ screen (1.0 M lithium chloride, 0.1 M sodium citrate pH 4.0, and 20 % w/v PEG 6000). The lithium chloride concentration was varied from 0.4-1.4 M and a pH range between 3.4-4.0 was used. An additive screen was carried out using the HR2-428 additive screen (Hampton Research) and a reservoir solution consisting of 0.6 M lithium chloride, 0.1 M sodium citrate pH 3.4, and 20 % w/v PEG 6000.

Crystals were frozen in the reservoir solutions plus glycerol at a final concentration of 35 % in liquid nitrogen. X-ray diffraction data were collected at the BESSY II Light Source in Berlin, Germany.

2.4.8.2. Crystallization of GSDMD in complex with nanobodies

To obtain homogeneous protein samples, the nanobodies were added to GSDMD in 1.5 fold excess and unbound nanobody was removed by gel filtration on an S200 Increase 10/300 GL column. Crystallization conditions were screened for wild-type GSDMD and truncated GSDMD constructs ($GSDMD_{\Delta 247\text{-}272}$, $GSDMD_{\Delta 184\text{-}194/\Delta 247\text{-}272}$, $GSDMD_{\Delta 181\text{-}197/\Delta 247\text{-}272}$ in complex with nanobodies $VHH_{GSDMD\text{-}1\ -\ -6}$ and the combination of $GSDMD_{VHH\text{-}2}$ plus $GSDMD_{VHH\text{-}6}$ was performed using the commercial kits from Molecular Dimensions (Maumee, OH, USA) and Jena Bioscience (Jena, Germany) listed in Table 4 with the sitting drop vapour diffusion method. Initial crystals of the sample containing $GSDMD_{\Delta 184\text{-}194/\Delta 247\text{-}272}$ in complex with $GSDMD_{VHH\text{-}2}$ and $GSDMD_{VHH\text{-}6}$ were obtained at a protein concentration of 20 mg/ml using a reservoir solution containing 0.07 M NaCl, 22 % (v/v) PEG 400 and 0.05 M Na_3Cit pH 4.5 at 20°C (Memgold screen, F12). Optimization of crystallization conditions by varying the salt and PEG concentrations and the pH in a 96-well format using the sitting drop vapour diffusion method resulted in well diffracting crystals grown at 20 mg/ml in a reservoir solution consisting of 0.04 M NaCl, 25.8 % (v/v) PEG 400 and 0.05 M Na_3Cit pH 4.4 at 20°C.

Crystals were frozen in the reservoir solutions plus PEG 400 at a final concentration of 35 % in liquid nitrogen. X-ray diffraction data were collected at

beamline P13 of the PETRA III synchrotron at the “Deutsches Elektronen-Synchrotron” (DESY) in Hamburg, Germany, at a wavelength of λ = 0.976255 Å.

2.4.8.3. Data processing and structure determination of the GSDMD-$VHH_{GSDMD-2}$-$VHH_{GSDMD-6}$ complex

Diffraction data were processed using the program *XDS* (Kabsch, 2010). Phases were determined by molecular replacement using the program *Phaser* (McCoy *et al.*, 2007). For GSDMD, the previous crystal structure of human GSDMD (PDB: 6N9O) (Liu *et al.*, 2019) was used as a search model. To account for possible movements between the N- and C-terminal domains of GSDMD, the structure was split into the GSDMD-NTD or -CTD, resulting in two separate search models. In addition, the structure of the BC2 nanobody (PDB: 5IVO) (Braun *et al.*, 2016) was used as a search model for VHH-2 and VHH-6. Manual model building and refinement was performed using Coot (Emsley and Cowtan, 2004) and Phenix (Adams *et al.*, 2010), respectively. The crystal structures were validated using the MolProbity server (Chen *et al.*, 2010). Structure figures were prepared using PyMOL (The PyMOL Molecular Graphics System, Version 2.0 Schrödinger, LLC).

2.4.9. Preparation of cell lysates for SDS-PAGE and Western Blot

Cell lysates were prepared to analyse protein expression in different cell lines. Cells were harvested by trypsinisation (adherent cells) or centrifugation (suspension cells). Cells were washed with PBS and resuspended in RIPA buffer supplemented with cOomplete™ Protease Inhibitor Cocktail and 1 mM PMSF and incubated for 30 min on ice. Cell debris was pelleted by centrifugation of the lysates for 15 min at 14000 xg and 4°C. The supernatant was transferred to a fresh tube and the protein content was determined by BCA assay as described in 2.4.10. Cell lysates were stored at -20°C or mixed with 4x Laemmli buffer, boiled at 95°C for 5 min and subjected to SDS-PAGE followed by western blot.

2.4.10. BCA assay

The protein content of cell lysates for western blot was determined by BCA assay using the Pierce™BCA Protein Assay kit. 5 µl of cell lysate were mixed with 95 µl of BCA reagent solution in a 96-well plate and incubated at 37°C for 30 min. Absorbance at 526 nm was measured using a plate reader.

2.4.11. SDS-PAGE and Western Blot

SDS-PAGE combined with Western blot was used to specifically detect proteins expressed in different cell lines. Samples prepared from cell lysates were loaded on pre-cast 4-12 % gradient SDS-PAGE gels and run in MES buffer at 120 V for 90 min using the Prescion Plus Protein™ Kaleidoscope ladder as protein standard. Proteins were transferred to a PVDF membrane using the wet transfer method. PVDF membranes were activated by soaking in methanol and filter papers were soaked in western blot buffer (Table 8). Blots were assembled in the following order: sponge, 3x filter paper, gel, membrane, 3xfilter paper, sponge and loaded into the Biorad Western Blot system. Blots were run at 100 mA for 100 min at 4°C. The membranes were then blocked with 5 % skim milk in PBS for 1 h at RT. The membranes were then washed three times with TBST and incubated with primary antibody diluted in 5 % BSA/TBST overnight at 4°C. The next day, the membranes were washed three times in TBST before incubation with the HRP-coupled secondary antibody diluted in TBST for 1 h at RT. The antibodies used in this study are listed in Table 13. For detection of protein bands, Immobilon Forte Western horseradish peroxidase (HRP) Substrate was added to membranes and imaging was performed using the BioRad ChemiDoc Touch Imaging System.

2.4.12. Preparation of LUVs

LUVs were prepared for analysis of GSDMD pore formation in a liposome leakage assay. Lipids for the perparation of LUVs were obtained from Avanti Polar Lipids and dissolved in chloroform to a final concentration of 25 mg/ml. Liposomes were prepared by mixing 80 µl phosphatidylcholine (POPC), 128 µl

phosphatidylethanolamine (POPE) and 64 µl cardiolipin in a glass tube. The chloroform was evaporated under a steady stream of nitrogen and the lipids were rehydrated in 400 µl of an 80 mM calcein solution in H2O (pH 7.0). The liposome suspension was vortexed vigorously and subjected to five freeze- and thaw cycles, followed by extrusion through a 100 nm pore diameter polycarbonate membrane 31-times using an Avanti mini-extruder (Avanti Polar Lipids, Inc., Alabaster, AL). The extruded liposomes were passed through a PD-10 column equilibrated with 20 mM HEPES (pH 7.4), 150 mM NaCl and 1 mM EDTA to remove excess calcein. For this purpose, 100 µl of liposomes were applied to the column and 200 µl elution fractions were collected. The homogeneity and quality of the liposomes obtained were checked by DLS and packaging was assessed by measuring the fluorescence at 525 nm after lysis with 1 % Triton-X 100, respectively. Fractions containing liposomes of good quality were pooled and diluted 1:10 in buffer.

2.4.13. Liposome leakage assay

For the liposome leakage assay, 120 µl of a liposome solution, 0.5 µM GSDMD, 0.2 µM His-SUMO-caspase-4, and 0.5 µM VHH were mixed in a final volume of 200 µl in a dark-well glass bottom plate and incubated at 37°C for 180 minutes. In a second experiment, 120 µl of a liposome solution, 0.5 µM GSDMD-3C, 0.2 µM 3C-protease (homemade), and 0.5 µM VHH were mixed in a final volume of 200 µl in a dark-well glass bottom plate and incubated at 37°C for 45 minutes. The fluorescence emitted at 525 nm after excitation at 485 nm was measured every minute using a plate reader.

The degree of inhibition at high nanobody concentrations was determined for all nanobodies added to GSDMD at a concentration of 10 µM (20:1 ratio). The sample containing GSDMD and caspase-4 but no nanobody was used to determine the maximal fluorescence (100 %). For the determination of IC_{50} values, the nanobodies were applied at concentrations ranging from 0-10 µM, using the similar setup as before with caspase-4 as cleaving protease and fluorescence measurements after 180 minutes of incubation.

2.5. Generation of nanobodies

Nanobodies were generated for the structural and biochemical investigation of the protein NLRP7. The nanobody generation was carried out in collaboration with the Core Facility Nanobodies at the Medical Faculty of the University of Bonn. The critical first steps in the process, including the immunization of llamas, generation of a nanobody plasmid library and identification of potential binders by phage display were carried out by members of the core facility (Jan Tödtmann and Paul-Albert König). These steps are briefly described here. More detailed protocols for the generation of nanobodies have been published elsewhere. (Pardon *et al.*, 2014; Schmidt *et al.*, 2016).

2.5.1. Immunization of Llamas with NLRP7 variants

Two different NLRP7 constructs were used to raise heavy chain only antibodies against NLRP7. Tag-free NLRP7-PYD_{2-96} was used to immunize the llama *Paco* and mMBP-tagged full length NLRP7 was used to immunize the llama *Zwerg*. The animals were immunized subcutaneously 6 times over 12 weeks with 100 µg of protein in a HEPES-based buffer mixed 1:1 with GERBU-FAMA adjuvants.

2.5.2. VHH library generation

After the immunization of llamas was complete, 100 ml of blood was collected from the animals and PBMCs were isolated by centrifugation on a Ficoll gradient. Cells were lysed, total RNA was extracted and reverse transcribed into cDNA using three different primers. The coding sequences for all VHHs were amplified by PCR using VHH-specific primers (AIVHH-F1+AIVHH-shR1 or AIVHH-F1+AIVHH-Ih-R1). PCRs performed with the same primers on the three different cDNA samples were pooled and cloned into pD GFP phagemid-vectors using AscI and NotI HF restriction enzymes. The purified vectors were transformed into *E. coli* Tg1 cells by electroporation until the entire ligation reaction was used up. Transformed cells were serially diluted and plated on 10 cm 2YT Amp plates with 2 % glucose. The diversity of the library was determined according to the number

of colonies obtained per plate. Bacteria were harvested and glycerol stocks were prepared, frozen and stored at -80°C until further use.

2.5.3. VHH phage display panning

NLRP7 binding nanobodies were identified by phage display. A culture of *E. coli* TG1 cells containing the phagemid library was grown and infected with VCSM13 helper phage resulting in the production of phages displaying the encoded VHH on their outside as pIII fusion protein. Phages were harvested and concentrated by precipitation. Nanobodies directed against MBP or GST were removed by incubating the phages in a tissue culture flask coated with MBP or GST. The NLRP7 constructs were immobilized on magnetic beads, and NLRP7-binding nanobodies were enriched by incubating the negatively selected phages with the protein bound beads. The phages were eluted by low pH elution (0.2 M glycine, pH 2.2 and used to infect tet resistant *E.coli* ER2738 cells. Bacteria were plated on 15 cm 2YT/2 % glucose dishes containing Amp and Tet. The next day, bacteria were harvested and used for a second round of panning. Bacteria obtained from the second round of phage display were serially diluted and plated on 10 cm 2YT/2 % glucose/Amp/Tet plates. The next day, single colonies were picked and transferred to a 96- well plate (Master plate) containing SOC+Amp+Tet. Bacteria were grown over night and used for “bug sup” ELISA.

2.5.4. “Bug sup” ELISA

Single bacterial colonies obtained from the second round of phage display that were grown overnight in a 96- well plate were used to inoculate another 96-well plate containing SOC+Amp+Tet. Cultures were grown for 4 h before VHH expression was induced by addition of IPTG overnight. Nanobodies that leaked into the supernatant were then tested for NLRP7 binding the next day. The supernatant was harvested by centrifugation and transferred to ELISA plates coated with the NLRP7 constructs or the control proteins MBP or GST. Nanobody binding was detected using an HRP-coupled anti-E-tag-antibody and TMB substrate. For each binder identified in the bug sup ELISA, a miniprep culture was inoculated with bacteria from the master plate.

2.5.5. Small scale expression and purification of VHHs

The protocol for the small scale expression of nanobodies was obtained from the Core facility Nanobodies and the experiment was performed by me. Small scale expression of nanobodies was performed to validate binding of the hits obtained by bug sup ELISA in another round of ELISA.

The coding sequences of the nanobodies obtained from the bug sup ELISA were cloned into pHEN6 vectors for periplasmic expression. 1 µl of pHEN6 vector was transformed into 100 µl of chemically competent *E. coli* WK6 cells. Transformed bacteria were used to inoculate a 5 ml culture of LB medium containing 100 µg/ml ampicillin. The culture was grown overnight and used to inoculate a 50 ml culture of 2YT medium containing 100 µg/ml ampicillin. Cultures were grown at 37°C until the OD_{600} reached 0.6. VHH expression was induced by the addition of 50 µl 1 M IPTG and cultures were grown incubated overnight at 30°C. Cells were harvested by centrifugation at 8000 rpm for 10 min at 4°C. Pellets were resuspended in 0.75 ml TES buffer (200 mM Tris pH 8.0, 0.65 mM EDTA, 0.5 M sucrose), transferred to a 1.5 ml tube and incubated for at least 1 h at 4°C. on a rotator. For osmotic lysis, samples were transferred to 15 ml tubes, 3.5 ml 0.25x TES was added and samples were incubated overnight at 4°C. Periplasmic extracts were harvested by centrifugation at 8000 rpm and 4°C for 10 min.

Nanobodies were harvested by Ni-NTA purification. Ni-NTA spin columns were equilibrated with 0.5 ml 0.25x TES and spun at 700xg for 2 min to remove the buffer. The beads were resuspended in the periplasmic extracts and incubated at 4°C for 30 min on a rotator. The periplasmic extracts were transferred to the spin columns and the suspension was run through a vacuum manifold. The beads were washed three times by adding 0.5 ml of wash buffer (50 mM Tris pH 7.5, 150 mM NaCl, 10 mM imidazole) and centrifuged at 700xg for 2 min. Bound nanobodies were eluted in three elution steps using 200 µl of elution buffer (50 mM Tris pH 7.5, 150 mM NaCl, 500 mM imidazole). Fractions containing protein were pooled and desalted using PD MiniTrap G-25 columns. The columns were equilibrated with desalting buffer (Tris buffer pH 7.5. 150 mM NaCl, 10 %

glycerol), the protein sample was loaded and, after the liquid had entered the column, eluted with 1 ml desalting buffer. The process of purification was followed by SDS-PAGE and protein concentrations were determined by measuring the absorption at 280 nm.

2.5.6. Nanobody ELISA

The protocol for the nanobody ELISA was obtained from the Core facility Nanobodies and the experiment was performed by me. ELISA plates were coated with a solution of the target and control proteins (1 ng/well in PBS) overnight at 4°C. The plates were blocked with 10 % FCS in PBS for 2 h at RT, followed by five washes with PBS-T. The HA-tagged nanobodies were diluted in 10-fold serial dilutions ranging from 100 nM to 1 pM in PBS containing 10 % FCS. 100 µl of the nanobody dilutions were added per well and incubated at RT for 1 h. The plates were washed and incubated with a mouse αHA-HRP antibody (1:5000) for 1 h at RT. The plates were washed again with PBS-T and incubated with 100 µl TMB substrate per well. The reaction was stopped with 100 µl 1M HCl per well and the absorbance at 450 nm was measured using a plate reader.

3. Examining a role for NLRP7 in inflammasome formation

3.1. Introduction

The physiological role of NLRP7 is not well understood today. While defects in NLRP7 are mostly associated with reproductive disorders, the function of NLRP7 in innate immunity remains largely elusive. The first study to describe NLRP7 as an inflammasome-forming PRR was published in 2012 by Khare and colleagues (Khare *et al.*, 2012). This study reported that NLRP7, together with ASC and caspase-1, assembles an inflammasome in human macrophages stimulated with bacterial di- and tri-acylated lipopeptides (acLP), such as Pam2CSK4, Pam3CSK4 and FSL-1. Di- and triacylated lipopeptides are well characterized TLR2/6 and TLR2/1 agonists, respectively, and activation of TLR2 signalling leads to transcriptional upregulation of pro-IL-1β, TNF-α and type 1 interferons (Jin *et al.*, 2007; Kang *et al.*, 2009). Khare et al. found, that silencing NLRP7 in macrophages did not affect the transcription of IL-1β in response to acLP, leading them to conclude that NLRP7 is not involved in the TLR2 signalling pathway. The authors also performed inflammasome reconstitution experiments in HEK293 cells. Since HEK293 cells do not naturally express inflammasome components, including the sensor proteins, ASC and caspase-1, these must be introduced into the cells by transient transfection or lentiviral transduction (Compan and López-Castejón, 2016). Using transient transfection, Khare et al. observed colocalization of NLRP7, ASC and pro-caspase-1 in a punctate structure called ASC speck. ASC speck formation is a widely used indicator of inflammasome activation, and usually overexpression of the inflammasome forming PRR together with ASC in HEK cells is sufficient to induce ASC-specking (Stutz *et al.*, 2013; Machtens *et al.*, 2022). Khare et al. also found that HEK293 cells with reconstituted NLRP7 inflammasomes and additional pro-IL-1β transfection were able to secrete IL-1β. This IL-1β secretion was even enhanced when heat-killed bacteria or acLP were in addition transfected, suggesting that NLRP7 directly senses cytoplasmic acLP. However, no direct binding of acLP to NLRP7 was observed. In 2017, Bednash and colleagues found that NLRP7 also forms inflammasomes in THP-1 macrophages in response to the TLR4 ligand LPS, as

observed by ASC speck formation using confocal microscopy (Bednash et al. 2017). In a cycloheximide chase assay, they observed a stabilization of NLRP7 in cells treated with TLR agonists and found in subsequent experiments that NLRP7 is constitutively ubiquitinated and degraded in the endolysosome. Deubiquitination by the deubiquitinase STAMBP increased NLRP7 stability, but the link between TLR stimulation and STAMBP activation remained unclear.

Both of these studies (Khare et al. 2012; Bednash et al. 2017) suggest a role for NLRP7 as an inflammasome-forming PRR in human macrophages, but it remains unclear, which pathway leads to NLRP7 activation, which interacting proteins or PTMs are required for NLRP7 activation, and whether NLRP7 binds directly to PAMPs or DAMPs. To address these questions, HEK-cell based inflammasome reconstitution systems similar to that described by Khare et al. were generated, and NLRP7 activation was quantitatively studied in a flow cytometry-based time of flight inflammasome evaluation (TOFIE) assay. This assay detects changes in the distribution of fluorescently labelled ASC within the cell. The formation of an ASC-speck results in a decreased width and an increased height of the detected fluorescent signal (Sester *et al.*, 2015). This approach allows the quantification of ASC specks in a large number of cells.

3.2. Results

3.2.1. NLRP7 does not induce ASC-speck formation in Flp-In 293 T-Rex ASC-EGFP reporter cells

Based on the literature describing the activation of a reconstituted NLRP7 inflammasome in HEK293 cells, we decided to generate a stable HEK293 reporter cell line with inducible NLRP7 expression for inflammasome activation experiments. For this purpose, Flp-In 293 T-Rex cells with constitutive ASC-EGFP expression and a low background of ASC specking were chosen. This cell line has been engineered to contain a single Flp Recombination Target (FRT) site at a transcriptionally active genomic locus. The gene of interest can be introduced at this site using an expression vector in which the gene of interest is flanked by FRT sites, and the enzyme Flp recombinase. Once integrated into the genome, this system allows the isogenic and stable expression of the gene of interest (Flp-In System-Thermofisher). Here, the gene for the UniProt canonical isoform of NLRP7 ($NLRP7_{980}$) under a doxycycline-inducible CMV promotor was chosen for integration at the FRT site. The gene for constitutive ASC-EGFP expression had previously been introduced into the cells by lentiviral transduction by Annemarie Steiner (Masters lab). This process was successful as the addition of doxycycline to the culture medium led to NLRP7 expression as observed by western blot (Figure 6A). The anti-NLRP7 antibody was validated in a control experiment. As positive control, a plasmid expressing NLRP7980-myc and an anti-myc-tag antibody were used (SI Figure 3). The high molecular weight bands observed in the doxycycline treated sample are likely attributed to NLRP7 aggregates resistant to denaturation, although this requires further investigation (Figure 5A). As a readout for NLRP7 inflammasome activation, ASC-EGFP specking was evaluated using flow cytometry. Surprisingly, induction of NLRP7 expression without further treatment (UT), did not induce ASC-specking, which was in contrast to the previous report that NLRP7 induced ASC-speck formation HEK cells (Khare *et al.*, 2012) (Figure 6B). Additional stimulation of the cells by transfection of the reported NLRP7 activators Pam2CSK4, Pam3CSK4 and FSL-1 also failed to induce NLRP7-mediated ASC-specking, regardless of whether

500 or 1000 ng of acLPs were transfected per well (Figure 6B). That the used stimulants were functional was tested in a control experiment using THP-1 cells endogenously expressing TLR2, since it was previously shown that di- and tri-acylated lipopeptides are TLR2 agonists (Jin *et al.*, 2007; Kang *et al.*, 2009). All stimulants effectively activated TLR2 signalling as observed by TNF-α release from treated cells (SI Figure 4). As positive control in the ASC-speck experiment, pyrin-mCherry was transfected, which resulted in 20-30 % of transfected cells in ASC-speck formation, demonstrating that the reporter system was functional (Figure 6B).

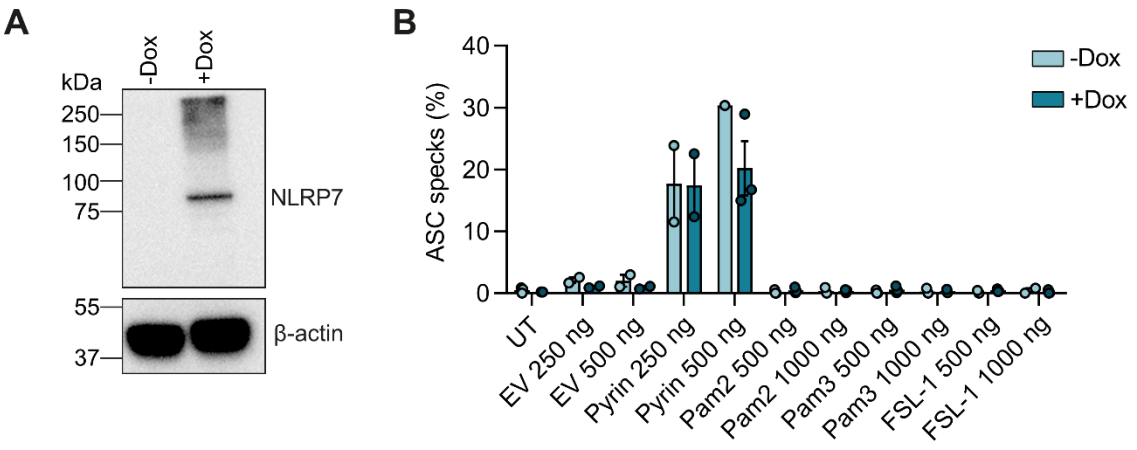

Figure 6: Overexpression and stimulation of NLRP7 in Flp-In 293 T-REx cells does not trigger ASC-speck formation. A) Western blot of NLRP7 expression levels in Flp-In 293 T-REx ASC-EGFP cells with doxycycline (Dox) inducible NLRP7-Strep2x-HA expression 18 h after Dox treatment. Primary antibody: anti-NLRP7 (NBP2-94507, Novusbio). **B)** Flow cytometry analysis of ASC-speck formation in cells without (-Dox) and with Dox (+Dox) induced expression of NLRP7. Pam2CSK4 (Pam2), Pam3CSK4 (Pam3) and FSL-1 were transfected for 24 h using lipofectamine. Positive control: pyrin-mCherry. As empty vector control (EV) pcDNA3.1 was used. n = 3 (pyrin 250 ng: n = 2, pyrin 500 ng -Dox: n = 1), means are displayed with SEM.

3.2.2. Overexpression of two NLRP7 isoforms in HEK293T ASC-BFP reporter cells does not induce ASC-speck formation

Surprisingly, neither overexpression nor stimulation of NLRP7$_{980}$ in Flp-In 293 T-Rex cells was sufficient to induce NLRP7-mediated ASC-specking. To confirm these results, another HEK cell-based reporter system was introduced. In this

system, HEK293T cells had been lentivirally engineered to constitutively express ASC-BFP with low levels of background ASC-specking, and NLRP7 was introduced into the cells by transient transfection. In this system, two different NLRP7 isoforms, $NLRP7_{980}$ and $NLRP7_{1009}$, with C-terminal fluorescent mCherry-tags were tested for their ability to induce ASC specks, to test whether there are differences in activity among different NLRP7 isoforms. Both isoforms are found under the most commonly annotated NLRP7 isoforms, the third dominant isoform, $NLRP7_{1037}$, was not tested in the course of this thesis. Transient transfection of increasing amounts of vector DNA (50-800 ng/24-well) resulted in increasing protein expression for both NLRP7 isoforms as observed by western blot using an NLRP7-specific antibody (Figure 7A,D). Also in this western blot, high molecular weight bands were observed, which may be caused by NLRP7 aggregates resistant to denaturation. Transfection efficiencies were further analysed by flow cytometry. With 50 ng/well of vector DNA transfected, mCherry fluorescence was already observed in 50 % of cells. The amount of transfected cells could be increased to 60-80 % by using 200-500 ng of DNA for the transfection (Figure 7B,E). Although the transfection efficiencies were high for both isoforms and the proteins were well expressed, neither isoform induced the formation of ASC-specks regardless of the amount of transfected DNA. In contrast, transfection of 100 ng of pyrin-mCherry expressing vector resulted in ASC-specking in 50-60 % of the cells analysed (Figure 7C,F).

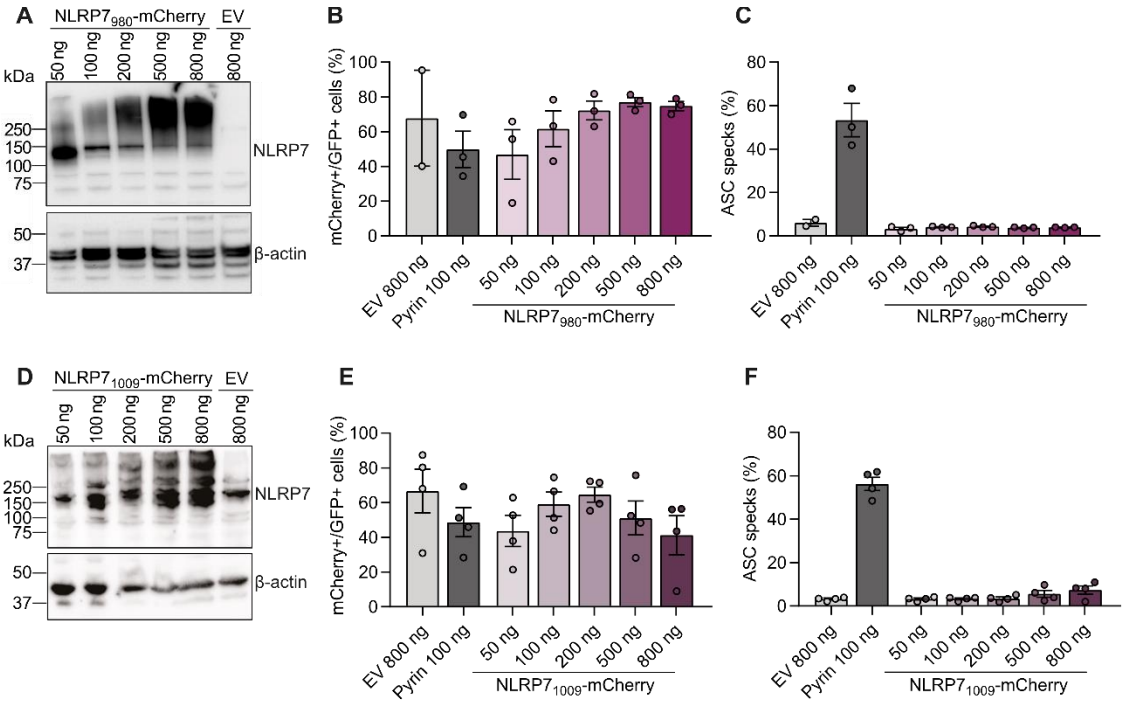

Figure 7: Overexpression of NLRP7 in HEK293T-ASC-BFP reporter cells does not trigger ASC-speck formation. A) Western blot showing NLRP7$_{980}$-expression levels in HEK293T ASC-BFP reporter cells 24 h after transfection with indicated amounts of pDEST-NLRP7$_{980}$-mCherry or empty vector (pDEST-mCherry). Primary antibody: anti-NLRP7 (NBP2-94507, Novusbio). **B)** HEK293T ASC-BFP reporter transfected as in A) and using pEGFP as empty vector were analysed for transfection efficiency using flow cytometry by gating for the respective fluorescence. n = 3, means are displayed with SEM. **C)** Flow cytometry analysis of ASC-speck formation in HEK293T-ASC-BFP reporter cells transfected as in a, and using pEGFP as empty vector. n = 3, means are displayed with SEM. **D)** Western blot showing NLRP7$_{1009}$-expression levels in HEK293T ASC-BFP reporter cells 24 h after transfection with indicated amounts of pDEST-NLRP7$_{1009}$-mCherry or empty vector (pDEST-mCherry). Primary antibody: anti-NLRP7 (NBP2-94507, Novusbio). **E)** HEK293T ASC-BFP reporter transfected as in d, and using pEGFP as empty vector were analysed for. transfection efficiency using flow cytometry by gating for the respective fluorescence. n = 4, means are displayed with SEM. **F)** Flow cytometry analysis of ASC speck formation in HEK293T ASC-BFP reporter cells transfected as in d, and using pEGFP as empty vector. n = 4, means are displayed with SEM.

3.2.3. NLRP7 does not colocalize with ASC-specks in HEK293T ASC-BFP reporter cells

In contrast to previous findings (Khare *et al.*, 2012), NLRP7 overexpression in HEK cells did not induce ASC-speck formation as observed by flow cytometry. In previous studies, immunofluorescence was used to analyse NLRP7-mediated

ASC-specking in HEK293 and THP-1 cells (Khare et al. 2012; Bednash, et al. 2017). Therefore, it was decided to examine HEK-293T ASC-BFP cells transfected with different NLRP7 constructs by fluorescence microscopy.

For this, the HEK293T ASC-BFP cells were transfected with either 100 or 500 ng of $NLRP7_{980}$-EGFP or $NLRP7_{1009}$-EGFP vector DNA. As positive control, the same amounts of pyrin-mCherry vector were transfected (Figure 8). It was observed that cells transfected with pyrin-mCherry exhibited a greater frequency of ASC-BFP specks than the cells transfected with either NLRP7 isoform, which presented only background levels of ASC-specks (UT ctrl). Furthermore, ASC-specks in pyrin-mCherry transfected cells were mostly found in cells expressing pyrin-mCherry, whereas the ASC-specks in the NLRP7 samples were mostly found in non-transfected cells. While pyrin-mCherry was found to form aggregated structures in close proximity to the ASC-specks, especially when 500 ng of DNA were transfected, both NLRP7-EGFP isoforms were distributed throughout the cytoplasm. This confirms our observations made in the flow cytometry based ASC speck assay described above and shows that overexpression of these two NLRP7 isoforms is not sufficient to induce ASC-speck formation.

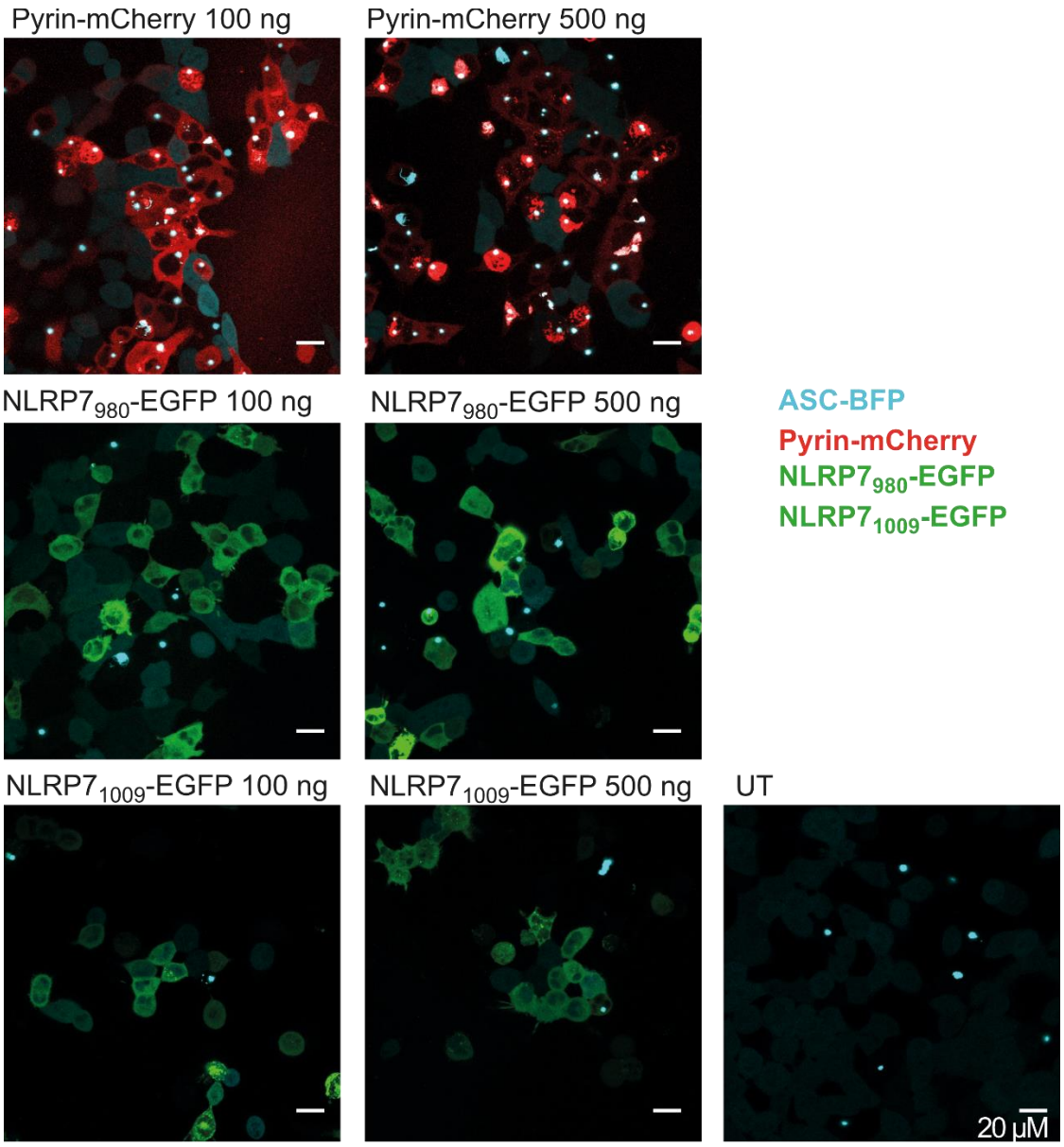

Figure 8: Fluorescence microscopy of HEK293T-ASC-BFP reporter cells transfected with NLRP7. Cells were left untransfected (UT) or were transfected with indicated amounts of pyrin-mCherry, NLRP7$_{980}$-EGFP or NLRP7$_{1009}$-EGFP. Z-stack images were acquired using a Lecia SP8 microscope. The scale bar represents 20 µm. N=1.

3.2.4. Treatment of overexpressed NLRP7 in HEK293T-ASC-BFP reporter cells does not trigger ASC-speck formation

Overexpression of NLRP7 in HEK293T ASC-BFP reporter cells was not sufficient to induce NLRP7-mediated ASC specking. It has previously been reported that transfection of acLP could increase NLRP7 inflammasome activity in HEK293 cells (Khare *et al.*, 2012). Therefore, first, cells transfected with varying amounts of NLRP7 vector DNA were transfected with a stable amount of the acLPs Pam2CSK4, Pam3CSK4 and FSL-1, and second, cells transfected with a stable amount of vector DNA were transfected with varying amounts of acLPs. For both isoforms, no significant increase in ASC-specking was observed when 50-800 ng of vector DNA were transfected followed by a second transfection of 500 ng of acLP (Figure 9A,C). Also when 500 ng of vector were transfected followed by a second transfection of 250, 500 or 1000 ng of acLP, no increase in ASC specks was observed (Figure 9B,D).

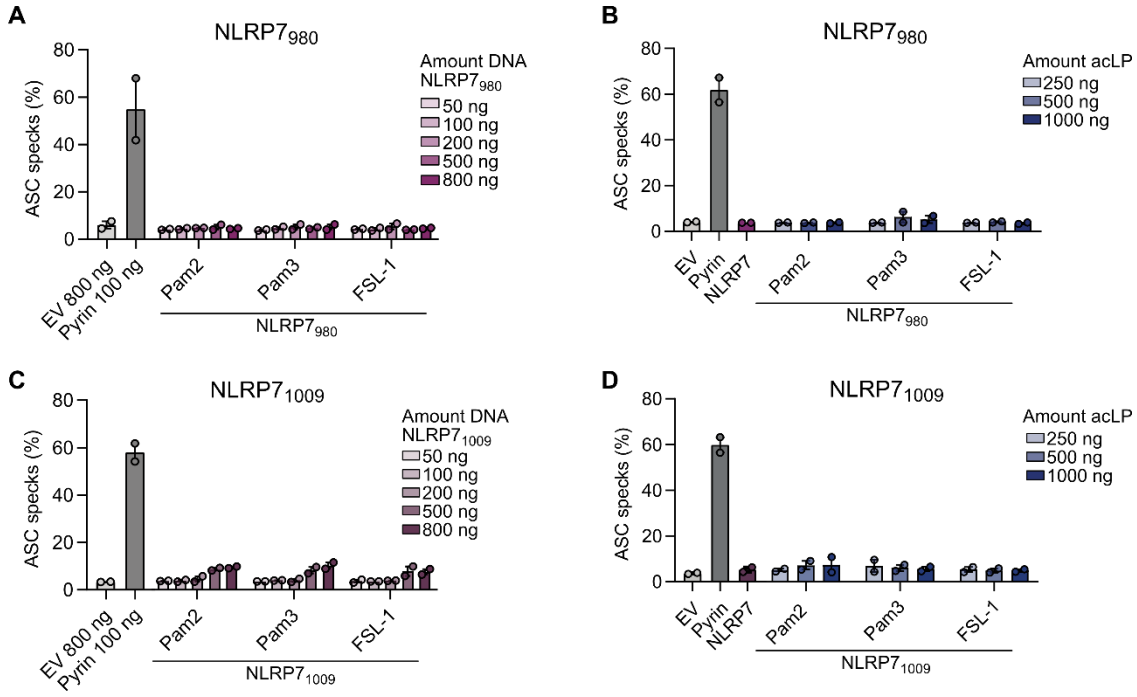

Figure 9: Treatment of overexpressed NLRP7 in HEK293T ASC-BFP reporter cells does not trigger ASC-speck formation. **A)** HEK293T ASC-BFP reporter cells were transfected for 18-24 h with the indicated amounts of empty vector (pEGFP), pyrin-mCherry or NLRP7$_{980}$-mCherry. Cells were transfected a second time with the acylated lipopeptides (acLP) Pam2CSK4, Pam3CSK4 or

FSL-1 (500 ng/well). Formation of ASC-specks was analysed using flow cytometry. n = 2, means are displayed with SEM. **B)** HEK293T ASC-BFP reporter cells were transfected for 18-24 h with 500 ng of empty vector (pEGFP), 100 ng pyrin-mCherry or 500 ng NLRP7$_{980}$-mCherry. Cells were transfected a second time with the indicated amounts of the acylated lipopeptides (acLP) Pam2CSK4, Pam3CSK4 or FSL-1. Formation of ASC-specks was analysed using flow cytometry. n = 2, means are displayed with SEM. **C)** As in A), using NLRP7$_{1009}$-mCherry. n = 2, means are displayed with SEM. **D)** As in B), using NLRP7$_{1009}$-mCherry. n = 2, means are displayed with SEM. n=2, means are displayed with SEM.

3.2.5. Overexpression of NLRP7 variants associated with disease in HEK293T-ASC-BFP reporter cells does not trigger ASC-speck formation

So far, no NLRP7-mediated ASC-speck formation was observed in HEK cells, regardless of the reporter system and NLRP7 isoforms used, and whether additional stimulation by acLP was applied. Next, the influence of disease-associated NLRP7 variants was analysed (Table 25). The selected variants affect all domains of NLRP7 and have been associated with inflammatory bowel disease (IBD) and ulcerative colitis (UC), as well as hydatidiform mole (HM) (Figure 10A). The variants S361L and R801H have been identified by whole-exome sequencing of families affected by IBD and are associated with a significantly increased risk of ulcerative colitis (Onoufriadis *et al.*, 2018). Notably, the R801H variant is specific to the NLRP7$_{1009}$ isoform, as R801 is not found in the other NLRP7 isoforms.Variants K85M, K511R and S702N were obtained from the IBD web server (https://dmz-ibd.broadinstitute.org/gene/ENSG00000167634, 16.09.2022). The K511R variant is present at an increased frequency in HM patients (Messaed *et al.*, 2011). Variants D657V, R693P and R693W are also associated with HM (Murdoch *et al.*, 2006; Qian *et al.*, 2007; Wang *et al.*, 2009) and have also been analysed by Khare et al. (Khare *et al.*, 2012). All variants were expressed with a C-terminal mCherry-fusion tag and protein expression was analysed using western blot. The R693P and R693W variants showed significantly lower expression levels than the other variants and were therefore excluded from further analysis (Figure 10B). Overexpression of the NLRP7 variants, did not induce ASC-speck formation (Figure 10C). ASC-speck formation was also not induced by additional stimulation with acLP (Figure 10D).

Table 25: NLRP7 variants associated with disease analysed in this thesis.

Variant	Associated disease	Reference
K85M	IBD	IBD web server
S361L	UC	(Onoufriadis *et al.*, 2018)
K511R	IBD, HM	IBD web server, (Messaed *et al.*, 2011)
D657V	HM	(Qian *et al.*, 2007)
R693P	HM	(Murdoch *et al.*, 2006; Wang *et al.*, 2009)
R693W	HM	(Murdoch *et al.*, 2006; Wang *et al.*, 2009)
S702N	IBD	IBD web server
R801H	UC	(Onoufriadis *et al.*, 2018)

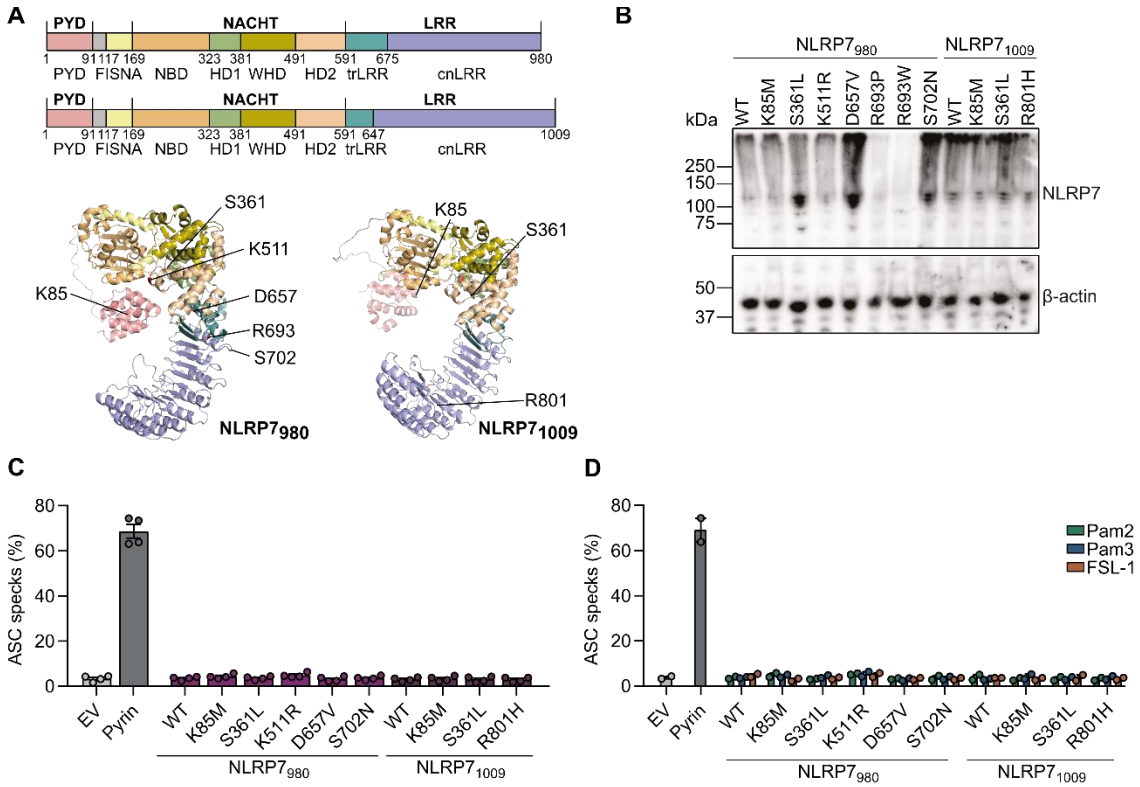

Figure 10: Overexpression of NLRP7 variants associated with disease in HEK293T ASC-BFP reporter cells does not trigger ASC speck formation. A) Schematic presentation of the domain architecture and alphafold models of NLRP7$_{980}$ and NLRP7$_{1009}$. Residues associated with disease are highlighted. **B)** Western blot showing expression levels of wild type and mutant NLRP7$_{980}$-mCherry and NLRP7$_{1009}$-mCherry in HEK293T ASC-BFP reporter cells 24 h after transfection. Primary antibody:anti-NLRP7 (NBP2-94507, Novusbio). **C)** Flow cytometry analysis of ASC-speck formation in HEK293T ASC-BFP cells 18-24 h after transfection with 500 ng empty vector (pEGFP), 100 ng pyrin-mCherry or 500 ng of WT or mutant NLRP7-mCherry. n = 4, means are displayed with SEM. **D)** Flow cytometry analysis of ASC speck formation in HEK293T ASC-BFP cells transfected as in c, and additional transfection with Pam2CSK4 (Pam2), Pam3CSK4 (Pam3) or FSL-1 for 18-24 h. n = 2, means are displayed with SEM.

3.2.6. Effect of NLRP7 expression on ASC-speck formation triggered by other PRRs

Since NLRP7 did not induce ASC speck formation in HEK cells, either spontaneously or with reported NLRP7 triggers, the question arouse whether NLRP7 influences the ASC speck formation induced by overexpression of other inflammasome forming PRRs. Here, the effect of NLRP7 on NLRP3, NLRC4 and

pyrin induced ASC-speck formation was examined. In order to keep the amount of transfected DNA stable for all samples, empty vector was used to add DNA where needed. In samples transfected with NLRP3, NLRC4 or pyrin, cells with medium expression of the respective PRR were analysed. Transfection of 50 ng NLRP3-mCherry vector DNA yielded in approximately 40 % of the cells with medium NLRP3-mCherry expression ASC-specks (Figure 11A). Additional transfection of a lower or equal amount (25 or 50 ng) of $NLRP7_{980}$-EGFP or $NLRP7_{1009}$-EGFP vector DNA did not significantly affect NLRP3-mediated ASC-speck formation. However, when a fourfold excess of NLRP7 vector DNA was transfected, the number of ASC-specking cells was reduced to 26 % for both $NLRP7_{980}$-EGFP and $NLRP7_{1009}$-EGFP (Figure 11A).

Interestingly, the opposite effect was observed for the co-transfection of NLRC4 and NLRP7 (Figure 11B). Transfection of NLRC4-mCitrine alone resulted in 20 % of the cells with medium NLRC4-mCitrine expression in ASC-speck formation. Additional co-transfection of 25 ng of $NLRP7_{980}$-mCherry or $NLRP7_{1009}$-mCherry vector DNA increased the number of ASC-speck presenting cells to 45 % and 53 %, respectively. The effect was even more pronounced when 200 ng of vector DNA of either isoform was transfected. For $NLRP7_{980}$, the ASC-specking was increased to 68 % and for $NLRP7_{1009}$ to 66 % of cells analysed (Figure 11B).

Co-transfection of pyrin and NLRP7 also resulted in an increase in pyrin-induced ASC-speck formation (Figure 11C). Transfection of pyrin-mCherry alone resulted in 40 % of the analysed cells in ASC-speck formation. Additional co-transfection of 25 ng of $NLRP7_{980}$-EGFP or $NLRP7_{1009}$-EGFP vector DNA resulted increased the number of ASC-specks to 53 % and 55 %, respectively. Transfection of an excess of NLRP7 vectors of either isoform did not further increase the percentage of ASC specking cells significantly.

Taken together, both NLRP7 isoforms behaved similarly in the co-transfection experiments, having a decreasing effect on NLRP3-mediated ASC-speck formation and an increasing effect on NLRC4- and pyrin- mediated ASC-speck formation. Whether this is a result of direct interaction of NLRP7 with the PRRs or ASC remains to be investigated.

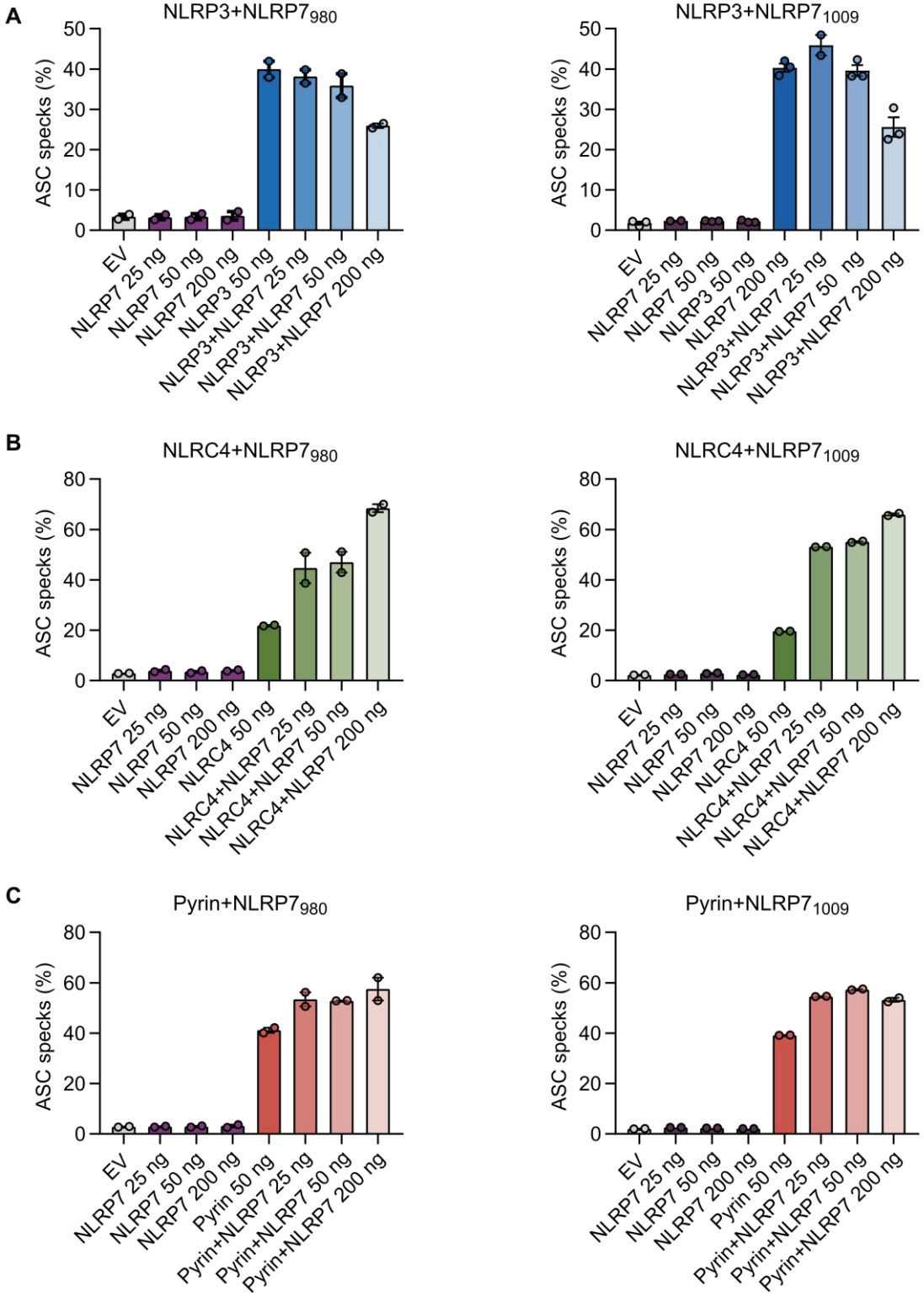
A
NLRP3+NLRP7980
NLRP3+NLRP71009
ASC specks (%)
0
10
20
30
40
50
EV
NLRP7 25 ng
NLRP7 50 ng
NLRP7 200 ng
NLRP3 50 ng
NLRP3+NLRP7 25 ng
NLRP3+NLRP7 50 ng
NLRP3+NLRP7 200 ng
B
NLRC4+NLRP7980
NLRC4+NLRP71009
0
20
40
60
80
NLRC4 50 ng
NLRC4+NLRP7 25 ng
NLRC4+NLRP7 50 ng
NLRC4+NLRP7 200 ng
C
Pyrin+NLRP7980
Pyrin+NLRP71009
Pyrin 50 ng
Pyrin+NLRP7 25 ng
Pyrin+NLRP7 50 ng
Pyrin+NLRP7 200 ng

Figure 11: Effect of NLRP7 expression on ASC speck formation induced by other PRRs. **A)** Flow cytometry analysis of ASC speck formation in HEK293T ASC-BFP cells 18-24 h after transfection with the indicated amounts of empty vector, NLRP7-EGFP and NLRP3-mCherry. A total of 250 ng DNA was transfected per 24-well, where needed, empty vector was used to keep the amount of DNA stable. Samples containing NLRP3 were gated for medium mCherry expression. n = 2 (n = 3 for $NLRP7_{1009}$), means are displayed with SEM. **B)** As in a. Transfected vectors: empty vector, NLRP7-mCherry and NLRC4-mCitrine. Samples containing NLRC4 were gated for medium mCitrine expression, means are displayed with SEM. **C)** As in a. Transfected vectors: empty vector, NLRP7-EGFP and pyrin-mCherry. Samples containing pyrin were gated for medium mCherry expression, n = 2, means are displayed with SEM.

3.3. Discussion

In this chapter, the role of NLRP7 as a PRR was investigated using HEK-cell based reporter systems. Two different inflammasome reconstitution systems were tested in order to mimic NLRP7 inflammasome activation as previously described by Khare et al. (Khare *et al.*, 2012). First, a stable cell line with dox-inducible NLRP7 expression was generated using the Flp-In™ T-REx™293 cell line, which also constitutively expressed ASC-EGFP. Secondly, HEK293T cells with constitutive expression of ASC-BFP and transient transfection of NLRP7 were used. Although NLRP7 was well expressed in both systems, its overexpression did not induce ASC-speck formation, nor could ASC-speck formation be induced by additional stimulation with acLP. This is in contrast to the findings of Khare et al., however some methodological differences exist. First of all, Khare et al. used the $NLRP7_{1037}$ isoform, whereas here the $NLRP7_{980}$ and $NLRP7_{1009}$ isoforms were used. The three isoforms vary in the length and composition of their LRR domain. The $NLRP7_{1037}$ isoform comprises the $NLRP7_{980}$ and $NLRP7_{1009}$ isoforms and displays residues R645-R671 which are absent in $NLRP7_{1009}$ (acidic loop in transition LRR) and residues $L938_{(NLRP71037)}$/$L910_{(NLRP71009)}$ – $R994_{(NLRP71037)}$/$R966_{(NLRP71009)}$ which are absent in the $NLRP7_{980}$ isoform (two LRR repeats). The $NLRP7_{980}$ and $NLRP_{1009}$ isoforms did not show any differences in their ability to induce ASC-speck formation, but whether the $NLRP7_{1037}$ isoform would behave differently in the setups used here requires experimental validation. Moreover, Khare et al. used

immunofluorescence to visualize the colocalization of NLRP7 with ASC specks. Here, this colocalization was not observed when fluorescently-tagged NLRP7 was transfected into HEK293T ASC-BFP cells and analysed using fluorescence microscopy. In addition, we used flow cytometry to quantify the amount of ASC specks in cells transfected with NLRP7, whereas Khare et al. did not quantify ASC specking.

The ability of NLRP7 to interact with ASC in HEK-cell based reconstitution experiments has also been investigated by other groups. After it was first discovered by the Bertin lab in 2002 that NLRP3 and NLRP12 can interact with ASC, leading to the activation of caspase-1, the same group initiated a screen to test interaction of other NLRPs with ASC (Manji *et al.*, 2002). In this screen, no interaction of NLRP7 and ASC was detected using immunofluorescence microscopy of transfected HEK293T cells (Manji *et al.*, 2002; Wang *et al.*, 2002; Grenier *et al.*, 2002). In 2005, Kinoshita and colleagues reported that co-transfection of HEK293 cells with NLRP7, ASC, pro-caspase-1 and pro-IL1β did not result in IL-1β secretion (Kinoshita *et al.*, 2005). In contrast, IL-1β secretion was observed for a reconstituted inflammasome using NLRP3ΔLRR as sensor protein (Kinoshita *et al.*, 2005). This IL-1β secretion was decreased by co-transfection of increasing amounts of NLRP7 (Kinoshita *et al.*, 2005), which is similar to the results obtained here, showing a decrease of NLRP3 mediated ASC-speck formation by co-transfection of NLRP7.

Taking into account the literature and the results obtained here, an NLRP7 inflammasome does not seem not to be easily reproducible in HEK cells. However, independent groups have described NLRP7 inflammasomes in macrophages and macrophage-like cell lines. Aside from Khare et al., who described the NLRP7 inflammasome in human macrophages and THP-1 cells, also Bednash et al., observed an NLRP7 inflammasome in THP-1 macrophages in response to TLR2 and TLR4 agonists using confocal microscopy (Khare *et al.*, 2012; Bednash *et al.*, 2017). A third study describes NLRP7 inflammasome activation in THP-1 macrophages in response to *mycobacterium bovis (M. bovis*) infection (Zhou *et al.*, 2016). Using siRNAs to knockdown NLRP7, this study showed a reduction of activated caspase-1 and IL-1β secretion upon *M. bovis*

infection in comparison to control cells. However, ASC speck formation was not quantified in that study. In a fourth paper, NLRP7 inflammasome activation was studied in embryonal membranes, specifically human amnion and choriodecidua sheets, as well as human amnion epithelial cells (AECs) (Lavergne *et al.*, 2020). It was found that two mycoplasma strains, *Mycoplasma salivarium* and *Mycoplasma fermentans* are found in human embryonic membranes, which is interesting since the synthetic acLP FSL-1 is derived from *Mycoplasma salivarium* (Shibata *et al.*, 2000). In AECs, NLRP7 as well as ASC and caspase-1 are endogenously expressed, and NLRP7 expression was upregulated in response to FSL-1, however ASC speck formation following FSL-1 stimulation was again not quantified (Lavergne *et al.*, 2020). Hence, cells endogenously expressing NLRP7 such as THP-1 cells, AECs or other cell lines should be used to further examine the involvement of NLRP7 in inflammasome activation, or whether its role is as a regulator of NLRP3, NLRC4 or even other inflammasome forming PRRs.

It is well established that activation of the NLRP3 inflammasome requires a priming step through TNFR or TLR signaling leading to the upregulation of NLRP3 expression (Bauernfeind *et al.*, 2009; McGeough *et al.*, 2017). Whether NLRP7 expression is upregulated in response to TLR agonists is still under debate. Using RT-PCR, Kinoshita et al. observed an increase in NLRP7 mRNA levels in THP-1 cells and PBMCs in response to stimulation with LPS for 6-14 h (Kinoshita *et al.*, 2005). In agreement with this, also Zhou et al. observed elevated NLRP7 mRNA levels in THP-1 cells 14 h post infection with *M. bovis* (Zhou *et al.*, 2016). Also Lavergne et al. observed an increase in NLRP7 mRNA and protein levels in AECs following FSL-1 stimulation (Lavergne *et al.*, 2020). In contrast, Khare et al., report no increase of NLRP7 expression levels after treatment of THP-1 cells with heat killed bacteria, and also Bednash et al. did not observe changes in NLRP7 mRNA levels after treatment of THP-1 cells with LPS or Pam3CSK4 (Khare *et al.*, 2012; Bednash, *et al.*, 2017).

The role of NLRP7 as an inflammasome forming PRR in reproductive disorders is still unclear. However, isolated PBMCs from HM patients have been analyzed for IL-1β and TNF-α secretion in response to LPS. In these patients,

protein truncating (E99X, G118X, L825X) and missense mutations (C89Y, K379N, G380R, C399Y, D657V, R693W, A719V, N913S) as well as rare non-synonymous variants (NSVs) (A481T, G487E, K511R) in NLRP7 were found (Messaed *et al.*, 2011). The PBMCs from patients with NLRP7 mutations and variants secreted significantly less IL-1β and TNF-α in response to LPS stimulation than the controls, suggesting a role of NLRP7 in IL-1β processing downstream of TLR signalling.

Another study using HM patient derived PBMCs was conducted in 2020 (P. Zhang *et al.*, 2020). In this study, the IL-1β and TNF-α secretion from the PBMCs of 12 new patients in response to LPS were investigated. Also these patients presented truncating mutations (R432X, L825X) and missense mutations (L379N, D1021V, C84Y, A719T, R693Q, R659L, D722G, R721W, W920Ter, C704Y) which also led to a reduction in IL-1β and TNFα secretion from isolated PBMCs in response to LPS. It is not known, whether the HM associated mutations in NLRP7 cause a loss or gain of NLRP7 function and as long as the function of NLRP7 is not characterized, it will not be possible to characterize the mutations accordingly. Nevertheless, many of the HM causing mutations are protein truncation or frame shift mutations so it is highly likely that these mutations cause a loss of NLRP7 function. Therefore, it can be hypothesized that the reduction in IL-1β secretion from PBMCs of HM patients results from a defective NLRP7 inflammasome, which should be further analysed in future studies.

Here, the activity of a set of disease associated NLRP7 variants was tested in HEK cell based reporter assays. However, neither wild type nor mutant NLRP7 caused ASC speck formation in this system. Therefore, ASC speck formation in HEK cells is not a suitable method to test the activity of these NLRP7 variants. The D657V and R693W mutants that caused a reduction in IL-1β secretion from HM patient PBMCs were also analysed by Khare et al., as well as in this thesis. While the R693W mutant was not well expressed in HEK293T cells in this thesis, the D657V mutant was not more active than wild type NLRP7 and did not induce ASC-speck formation. Opposing results were obtained by Khare et al., who observed increased IL-1β secretion in HEK293T reconstituted with NLRP7 D657V or R693W in comparison to wild type NLRP7, which is also in contrast to

the results obtained from HM patient PBMCs (Messaed *et al.*, 2011; S *et al.*, 2012). To make a meaningful statement about the consequences of NLRP7 variants, a reporter system in which the NLRP7 inflammasome can be reliably activated has to be established. This system could also be based on another readout for NLRP7 activation independent of interaction with ASC.

Since no interaction of NLRP7 and ASC was observed in this study, it was investigated, whether NLRP7 has an effect on other PRRs. Co-expression of NLRP7 with NLRP3, NLRC4, or pyrin affected their ability to induce ASC-speck formation in HEK cells, which could be a result of direct interaction of NLRP7 and the PRRs or NLRP7 and ASC. Such interactions have been shown for other PRRs. For example, NLRP3 and NLRC4 were reported to be recruited to the same ASC-speck in macrophages in response to *Salmonella* infection (Man *et al.*, 2014). Recently, also NLRP11 was described to interact with NLRP3 in human macrophages and to be a component of the NLRP3 inflammasome (Gangopadhyay *et al.*, 2022).

Taken together, the role of NLRP7 in innate immunity is still controversial. Different groups have obtained varying results regarding the interaction of NLRP7 and ASC in HEK cells, and in the last decade, only three studies have reported NLRP7 activation in THP-1 macrophages. This leaves a lot of room for further research. To build on the results obtained in this thesis, the following experiments can be performed. First of all, the ability of the $NLRP7_{1037}$ isoform to induce ASC speck formation in HEK cells should be tested to exclude isoform specific differences in the interaction of NLRP7 and ASC. Next, it should be tested, whether NLRP7 can interact with ASC without inducing ASC speck formation. This could be done using pull-down assays or co-immunoprecipitation (co-IP). In addition, it should be tested whether NLRP7 can directly interact with other PRRs, as co-transfection of NLRP7 with NLRP3, NLRC4 or pyrin had an effect on the percentage of ASC specks induced by these PRRs.

That NLRP7 may not induce ASC speck formation HEK cells, does not exclude the possibility that NLRP7 interacts with ASC in cells with endogenous expression of both proteins. Using cells with endogenous NLRP7 expression, it should first be investigated whether NLRP7 expression is upregulated in response to TNF or

TLR ligands including LPS, Pam2CSK4, Pam3CSK4 or FSL-1, using qPCR and western blot. Then, it should be examined, whether NLRP7 does indeed form an inflammasome in response to the reported activators LPS, Pam2CSK4, Pam3CSK4 or FSL-1 (Khare *et al.*, 2012; Bednash, *et al.* 2017) for which ASC speck formation can be used as readout applying immunofluorescence and flow cytometry analysis. Until today, all studies investigating the NLRP7 inflammasome have used siRNAs to knock down NLRP7 in control cells. Cells with a complete NLRP7 knockout could provide a more robust answer to whether NLRP7 is involved in inflammasome activation. Once knockout cell as controls are available, it would also be interesting to reconstitute monocytic cell lines with disease associated NLRP7 mutations to study their effect on IL-1β secretion. In addition, proteomics studies could be carried out, to test whether wild type and mutant NLRP7 interact differently with other proteins. If NLRP7 can be activated, proteomics could also be used to identify proteins that contribute to NLRP7 activation. Moreover, a possible interaction of NLRP7 with other PRRs should also be tested in cells with endogenous expression of these receptor. For this wild type and NLRP7 knockout cells could be stimulated with the known NLRP3, NLRC4 or pyrin activators and IL-1β secretion could be used as a readout for inflammasome activation. In summary, future studies will be required to shed light on the function and activation mechanism of NLRP7.

4. Generation and characterization of NLRP7 targeting nanobodies

4.1. Introduction

NLRP7 is a poorly understood protein and not only do many aspects of its physiological functions in normal pregnancy and innate immunity remain elusive – also its biochemical properties are understudied. To date, only the structure of the NLRP7-PYD has been determined, the structures of the NACHT and LRR domains as well as the full length protein still require experimental determination (Pinheiro *et al.*, 2010). The NLRP7-PYD can be expressed in *E. coli* and purified as a soluble monomer, but so far, successful purification and biochemical characterization of other NLRP7 domains has not been reported (de Sa Pinheiro *et al.*, 2009; Pinheiro *et al.*, 2010). Here, NLRP7 specific nanobodies were generated with the aim of providing a tool that may facilitate the purification of other NLRP7 domains, or the full length protein, and/or act as crystallization chaperone for NLRP7 structure determination. Nanobodies have already been used to enhance the solubility of inclusion body-prone proteins during protein expression and as crystallization chaperones for membrane proteins, demonstrating their value in protein biochemistry (Löw *et al.*, 2013; Duhoo *et al.*, 2017; Yao *et al.*, 2022). In addition, nanobodies can bind their target proteins with high specificities and affinities and NLRP7 targeting nanobodies could be used for affinity purification of tag-free NLRP7, immobilization of NLRP7 on SPR sensor chips, or pull-downs of NLRP7 with interacting proteins. Apart from applications in biochemistry or structural biology, nanobodies also find applications in cell biology and diagnostics. NLRP7 is expressed in a variety of tissues and cell types, including blood cells, reproductive organs and tissues, lung, liver, spleen, thymus and intestine (Kinoshita *et al.*, 2005; Huang *et al.*, 2017; Onoufriadis *et al.*, 2018; Abi Nahed *et al.*, 2019; Amoushahi *et al.*, 2019; Tsai *et al.*, 2019), but whether its function is tissue specific remains unclear. Moreover, NLRP7 has been implicated in auto-inflammatory diseases and cancer, although it is not well understood, how NLRP7 contributes to these diseases (Onoufriadis *et al.*, 2018; Reynaud *et al.*, 2021). NLRP7 nanobodies

could be used to detect NLRP7 in healthy and pathological tissues which might give insights on the regulation of NLRP7 expression under different conditions. Some nanobodies can also be expressed as intrabodies in the cytoplasm of cells. This allows for example the visualization of their target protein in live cells when the nanobody is expressed in fusion with a fluorescent tag (Rothbauer *et al.*, 2006). Fusion of the intrabody to ubiquitin E3 ligases moreover allows the targeted degradation of the protein of interest (Ibrahim *et al.*, 2020; Jenster *et al.*, 2023). Nanobodies have also been found to selectively activate or inhibit their target proteins or to trap their target proteins in their activated or inhibited states, which could provide a strategy to study NLRP7 activation (Koenig *et al.*, 2021; Haubrich *et al.*, 2021; Zhang *et al.*, 2022; Hou *et al.*, 2022). The properties and possible applications of NLRP7-specific nanobodies make them a valuable tool for biochemical and structural biological experiments.

4.2. Results

4.2.1. Generation of NLRP7 targeting Nanobodies

To generate NLRP7 specific nanobodies, two different NLRP7 constructs were recombinantly expressed and purified. Full-length $NLRP7_{980}$ was expressed with an N-terminal mMBP-fusion tag in *Sf9* insect cells and the NLRP7-PYD_{2-96} was expressed with a cleavable N-terminal GST-tag in E. *coli*. The proteins were purified by Ni-NTA and GST affinity chromatography, respectively, followed by fractionation through size exclusion chromatography (SEC). For the PYD construct, the GST-tag was cleaved off with TEV protease prior to SEC. Exemplary SEC-elution chromatograms and SDS-PAGE gels for both proteins are shown in Figure 12. Full length mMBP-$NLRP7_{980}$ eluted in two major peaks from the SEC column, the first peak comprising void protein, the second peak supposedly monomeric NLRP7 (Figure 12A). Hence, protein eluting in Peak 2 was used for immunization and further biochemical experiments. As described in the literature, the NLRP7-PYD could be purified as homogenous monomeric protein that did not show any oligomerization or aggregating behaviour (Figure 12B).

The nanobody generation was performed in collaboration with the Core Facility Nanobodies at the Medical Faculty of the University of Bonn and is described in detail in the methods section. In brief, two llamas were immunized six times with either mMBP-tagged full length NLRP7 (mMBP-$NLRP7_{2-980}$) or the NLRP7-PYD over a course of 12 weeks. To generate a nanobody library, mRNA was extracted from lymphocytes isolated from the llama's blood, transcribed into cDNA using primers specific for the VHH region of the HCAbs, and cloned into phagemid vectors to generate a phage display library. In two rounds of phage display and subsequent BugSup ELISA, 20 potentially NLRP7 binding nanobodies (Table 26) were identified, of which four binders were derived from the immunization with the NLRP7-PYD_{2-96} and 16 from the immunization with full length mMBP-$NLRP7_{2-980}$. The potential NLRP7 binders identified by the Core Facility Nanobodies were further analysed for their binding specificity in the course of this thesis.

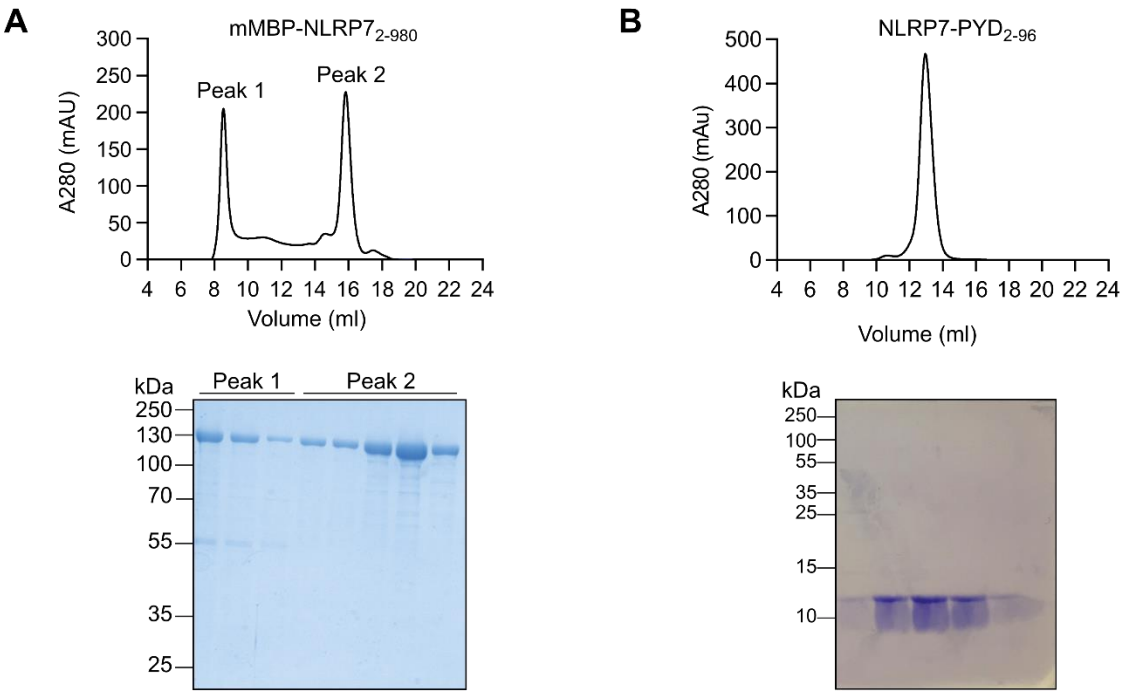

Figure 12: NLRP7 variants used for immunization of two llamas to raise NLRP7 specific heavy chain-only antibodies. A) SEC elution chromatogram of mMBP-NLRP7$_{980}$ using a Superose 6 Increase 10/300 GL column. The protein eluted in two major peaks (Peak 1 and Peak2) which were analysed for homogeneity by SDS-PAGE. **B)** SEC elution chromatogram of the NLRP7-PYD$_{2-96}$ using a S75 10/300 column. Before SEC, the GST-tag was cleaved off using TEV protease and removed by reverse GST affinity chromatography.

Table 26: Potentially NLRP7 binding nanobodies identified by the Core Facility Nanobodies (UKB) using phage display and BugSup ELISA.

Nanobody	Immunization	Animal
33-A02	mMBP-NLRP7$_{2-980}$	Zwerg
33-A04	mMBP-NLRP7$_{2-980}$	Zwerg
33-B02	mMBP-NLRP7$_{2-980}$	Zwerg
33-D02	mMBP-NLRP7$_{2-980}$	Zwerg
33-F09	mMBP-NLRP7$_{2-980}$	Zwerg
33-H10	mMBP-NLRP7$_{2-980}$	Zwerg
33-H11	mMBP-NLRP7$_{2-980}$	Zwerg
34-A11	mMBP-NLRP7$_{2-980}$	Zwerg
34-D05	mMBP-NLRP7$_{2-980}$	Zwerg
34-D09	mMBP-NLRP7$_{2-980}$	Zwerg
34-E02	mMBP-NLRP7$_{2-980}$	Zwerg
34-F11	mMBP-NLRP7$_{2-980}$	Zwerg
35-A12	mMBP-NLRP7$_{2-980}$	Zwerg
35-B01	mMBP-NLRP7$_{2-980}$	Zwerg
35-D07	mMBP-NLRP7$_{2-980}$	Zwerg
35-F09	mMBP-NLRP7$_{2-980}$	Zwerg
38-A10	NLRP7-PYD$_{2-96}$	Paco
38-B03	NLRP7-PYD$_{2-96}$	Paco
38-G05	NLRP7-PYD$_{2-96}$	Paco
38-G06	NLRP7-PYD$_{2-96}$	Paco

4.2.2. Identification of NLRP7-PYD binding nanobodies by ELISA and SPR

Based on the results obtained from phage display and BugSup ELISA, 20 potential NLRP7 binders were selected for further analyses. The nanobody sequences were cloned into bacterial expression vectors for the expression with a C-terminal HA-His-tag in the periplasm of *E. coli* WK6 cells and purified via their His-tag. The binding of the purified nanobodies to their target proteins was tested using ELISA plates coated with mMBP-NLRP7$_{2-980}$, GST-tev-NLRP7-PYD$_{2-96}$ or the respective control proteins alone (mMBP, GST). Nanobody-binding was detected using an HRP-coupled antibody directed against the HA-tag fused to the nanobody. Out of the binders obtained from both immunizations, seven

nanobodies (33-A04, 33-B02, 33-D02, 33-F09, 38-A10, 38-B03 and 38-G05) showed strong binding to full-length mMBP-NLRP7$_{2-980}$ and no or only weak binding to mMBP (Figure 13A). Yet, these nanobodies were also found to bind the NLRP7-PYD$_{2-96}$ alone in a second ELISA (Figure 13B). In addition, two nanobodies that bound weakly to full length NLRP7 showed strong binding to the NLRP7-PYD$_{2-96}$ (33-A02, 33-H11), resulting in a total of nine NLRP7-PYD binding nanobodies (Figure 13B). Five potential binders did not interact with NLRP7 in the ELISA and were excluded from further experiments. To unambiguously validate that the nanobodies bind to NLRP7 and not the fusion tag used for expression and purification of the proteins, binding of the nanobodies to mMBP and GST was analysed by surface plasmon resonance (SPR). mMBP and GST were coupled to the SPR sensor chips using specific antibodies. The interaction of the nanobodies with the control proteins was tested at a single concentration of 256 nM. Eight nanobodies that showed strong NLRP7 binding in the ELISA did not interact mMBP or GST, confirming their specific binding to NLRP7. However, nanobody 33-F09 as well as four nanobodies with ambiguous binding in the ELISA bound to mMBP in the SPR experiment and were excluded from further experiments (Figure 13C).

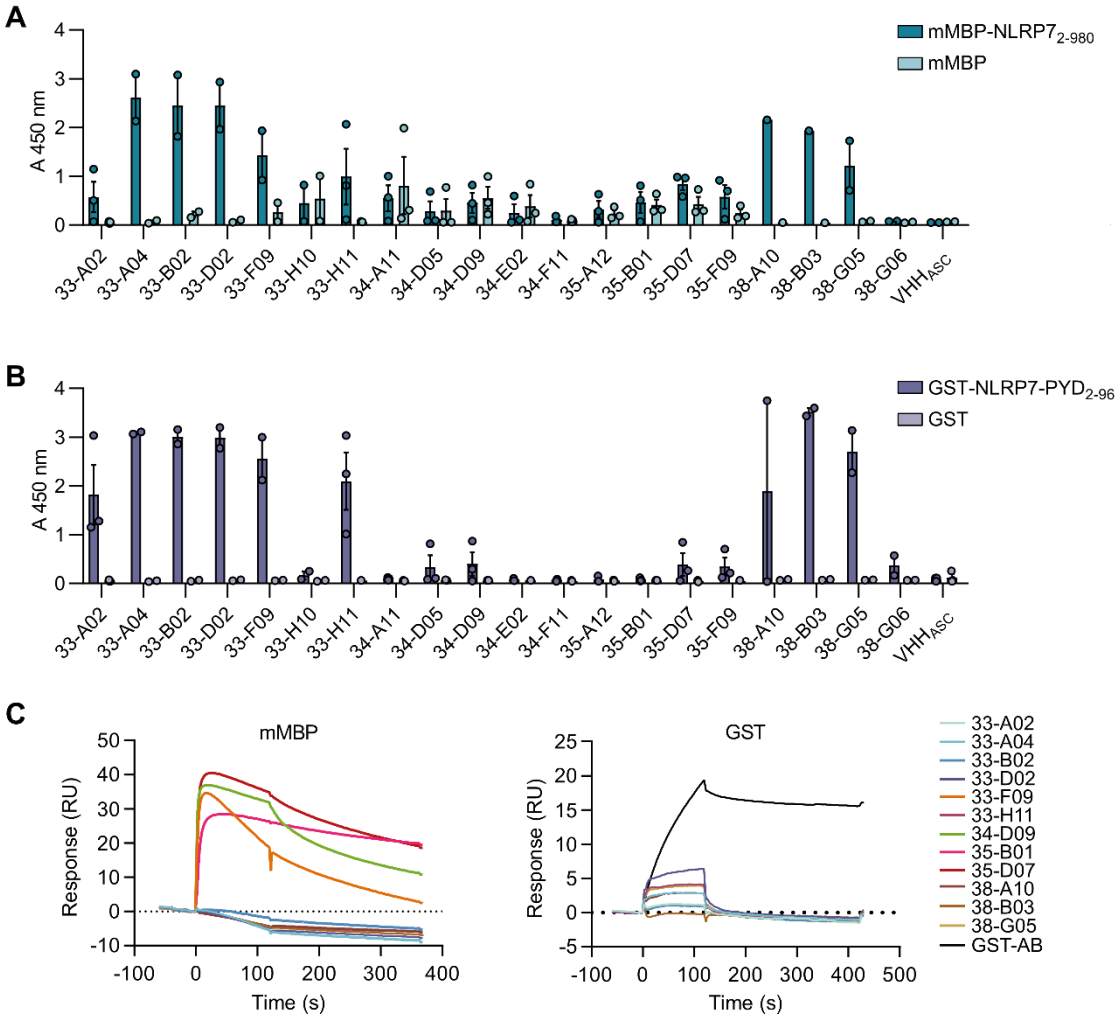

Figure 13: Identification of specific NLRP7 nanobodies by ELISA and SPR. ELISA plates were coated with mMBP-NLRP7$_{2-980}$, mMBP (**A**), GST-tev-NLRP7-PYD$_{2-96}$ or GST (**B**) and incubated with the potential NLRP7-nanobodies at 100 nM concentration. Nanobody-binding was detected using an HRP-coupled antibody directed against the HA-tag fused to the nanobodies and the addition of TMB substrate. The absorbance at 450 nm was detected using a plate reader. Data is presented as mean of two individual experiments with SEM. **C)** mMBP and GST were immoblized on a SPR sensor chip using antibodies. Binding of the nanobodies to mMBP and GST was tested at a nanobody concentration of 256 nM.

4.2.3. Phylogenetic analysis of NLRP7-PYD binding nanobodies

The relationship of the nanobodies was analysed based on their amino acid sequence. As expected, the nanobodies differ mainly in the length and composition of their CDRs, with the greatest diversity observed in CDR3 (Figure 14A). Nanobody 33-B02 and 33-H11 showed the highest similarity and differed in only two amino acids (1.91 % of their amino acid sequence), suggesting a similar binding epitope and mode of action. The three binders obtained from immunization with the NLRP7-PYD showed the greatest diversity and differed in at least 9.54 % of their amino acids (Figure 14B).

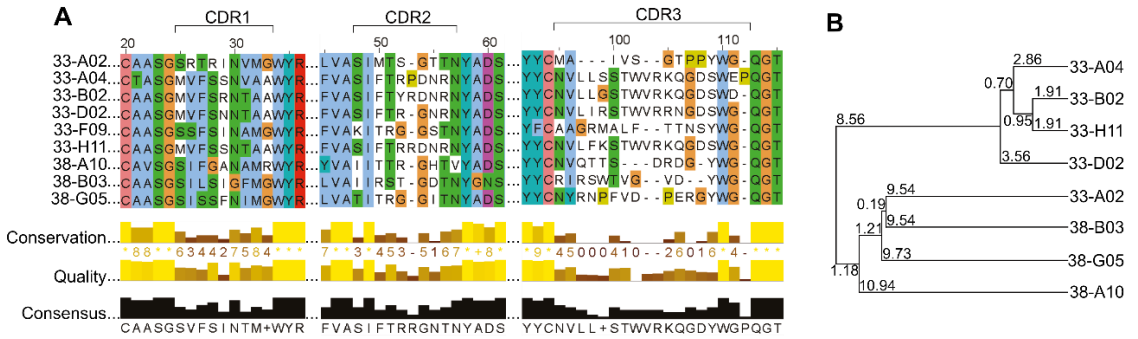

Figure 14: Phylogenetic analysis of the NLRP7-PYD binding nanobodies. A) Amino acid sequence alignment of the NLRP7 targeting nanobodies showing the three complementary determining regions (CDR1-3). **B)** Average distance tree based on the amino acid sequence of the nanobodies. The tree displays the average distance using percent identity and was calculated using the software Jalview.

4.2.4. NLRP7-targeting nanobodies bind to full length NLRP7 with affinities in the nanomolar range

The binding affinities of the NLRP7-targeting nanobodies were determined by SPR using full length mMBP-NLRP7 as immobilized ligand and single cycle kinetics with a sequential increase of the nanobody concentration. All nanobodies bound the full length protein with high affinities in the nanomolar range. The strongest binder was nanobody 38-A10 with a dissociation constant of 0.02 nM and a slow dissociation rate. Nanobody 38-B03 showed the second highest

affinity with a dissociation constant of 0.07 nM. The other nanobodies bound with affinities in the low nanomolar range varying from 1.06 to 16.50 nM (Figure 15).

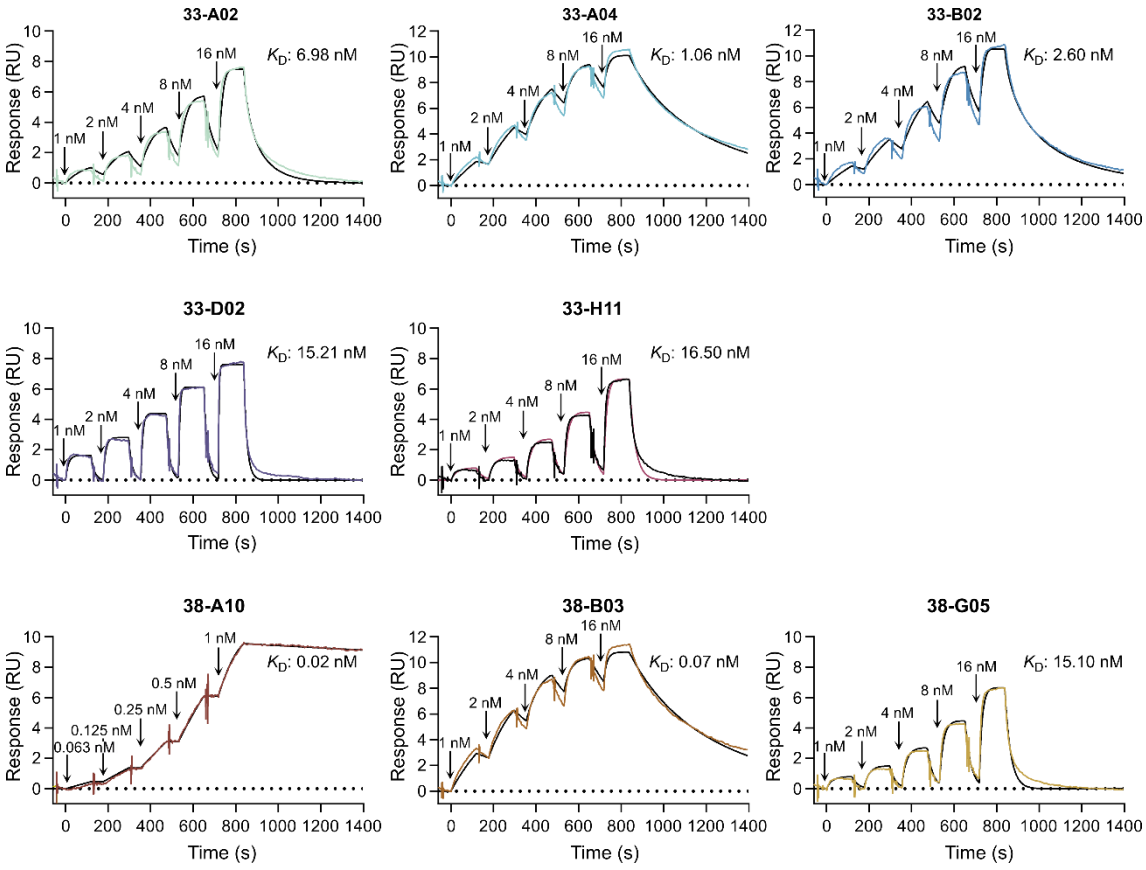

Figure 15: Binding affinities of NLRP7-binding nanobodies determined by SPR. Full length mMBP-NLRP7 was immobilized on a sensor chip using an α-mMBP antibody and nanobodies were injected as analytes at the indicated concentrations for 120 s using “single cycle kinetics”, followed by a dissociation period of 55 s. Dissociation constants (KDs) were determined applying a 1:1 binding model.

4.2.5. NLRP7 nanobodies bind to two distinct epitopes on the NLRP7-PYD

The epitope specificity of pairs of nanobodies was determined in a competitive binding assay. Two nanobodies were sequentially tested for binding to the antigen mMBP-NLRP7$_{2\text{-}980}$. If binding of the second nanobody is blocked by binding of the first nanobody, both nanobodies recognize the same or overlapping epitopes, whereas simultaneous binding of both nanobodies reveals recognition of different epitopes (Figure 16A). For nanobodies 33-A02, 33-D02, 33-A04, 33-

B02, 33-H11 and 38-A10 only one association event was observed when used in combination, indicating that these nanobodies recognize the same or overlapping epitopes. In contrast, the nanobodies 38-G05 and 38-B03 additionally bound to NLRP7 when used in combination with the aforementioned nanobodies, indicating that these two nanobodies recognize an alternative surface epitope (Figure 16B,C). Taken together, the eight nanobodies tested recognize two distinct epitopes on the NLRP7-PYD, with one group of six nanobodies sharing an overlapping epitope that is distinct from the epitope of the second group of nanobodies, which comprises two binders.

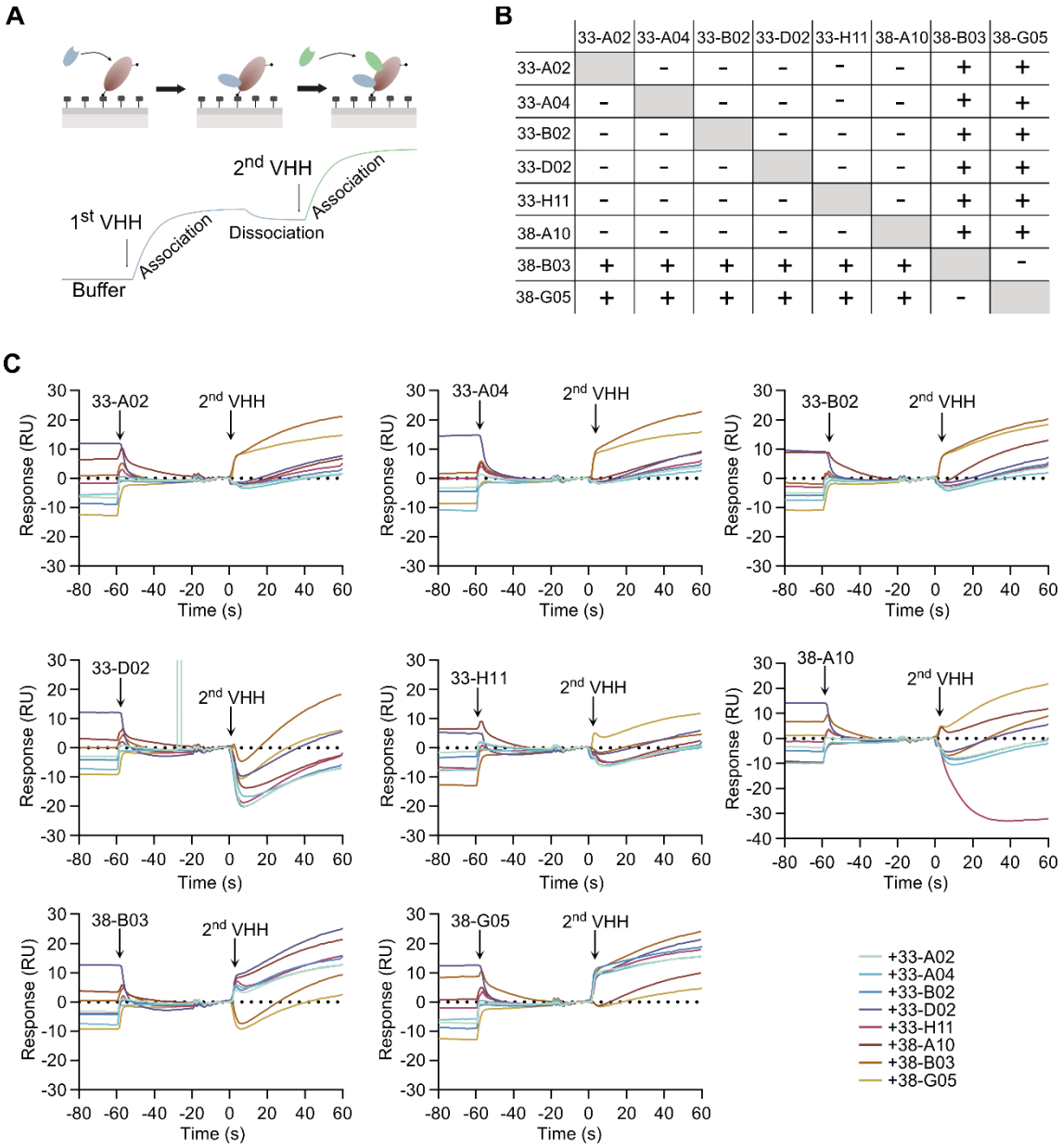

	33-A02	33-A04	33-B02	33-D02	33-H11	38-A10	38-B03	38-G05
33-A02		-	-	-	-	-	+	+
33-A04	-		-	-	-	-	+	+
33-B02	-	-		-	-	-	+	+
33-D02	-	-	-		-	-	+	+
33-H11	-	-	-	-		-	+	+
38-A10	-	-	-	-	-		+	+
38-B03	+	+	+	+	+	+		-
38-G05	+	+	+	+	+	+	-	

Figure 16: Epitope binning of the NLRP7 nanobodies. **A)** Two nanobodies were tested for binding to mMBP-NLRP7$_{2\text{-}980}$ one after the other at concentrations of 256 nM. If binding of the second nanobody is blocked by binding of the first nanobody, both nanobodies recognize the same or overlapping epitopes, whereas simultaneous binding of both nanobodies reveals recognition of different epitopes. **B)** Interaction matrix of the NLRP7 nanobodies based on the results obtained from the epitope binning experiment. **C)** SPR sensorgrams of the epitope binning experiment.

4.2.6. Applications of NLRP7-targeting nanobodies

4.2.6.1. NLRP7-targeting nanobodies are functional as intrabodies

To test whether the NLRP7 nanobodies were also functional when expressed intracellularly as intrabodies, a LUMIER assay was performed. In this assay, the HA-tagged nanobodies were co-expressed with renilla luciferase-tagged NLRP7 in HEK293T cells. The interaction between the nanobodies and NLRP7 was determined by pulling down the nanobody with an HA-specific antibody and detecting presence or absence of co-immunoprecipitated NLRP7 by examining the luciferase activity of the sample (Figure 17A). The nanobodies obtained from the NLRP7-PYD immunization (38-A10, 38-B03 and 38-G05) pulled down NLRP7 most effectively, but also in the samples containing 33-A04, 33-A02 and 33-B02 higher levels of luciferase activity than in the negative control were observed, in which an unspecific nanobody was used (Figure 17B).

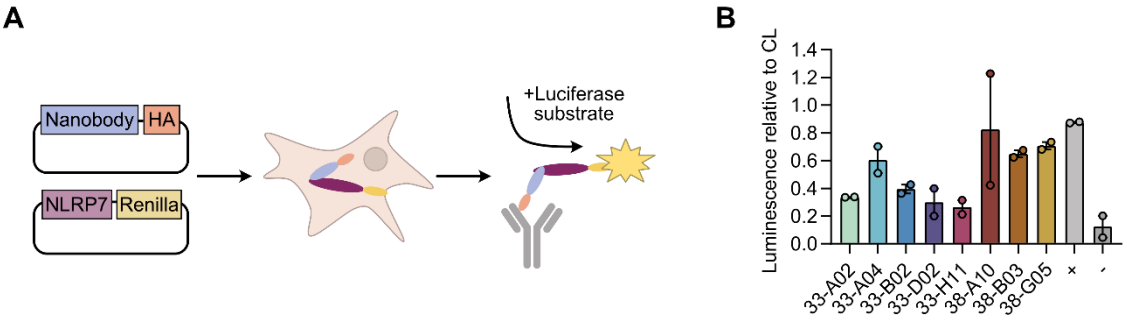

Figure 17: Identification of NLRP7 intrabodies. A) HEK293T cells were co-transfected with plasmids encoding NLRP7-renilla and an HA-tagged nanobody. Cells were lysed and a pull down was performed using an αHA-antibody. Luciferase substrate was added and luciferase activity was measured using a plate reader. **B)** The luminescence is depicted as ratio of the luminescence of the IP and the total cell lysate. Positive control: NLRP1-CARD + NLRP1-CARD nanobody. Negative control: NLRP1-CARD nanobody + renilla-luciferase tagged NLRP7 The mean of two independent experiments is shown with SEM.

4.2.6.2. NLRP7-targeting nanobodies do not function as crystallization chaperones

One application of nanobodies in structural biology is their use as crystallization chaperones. In this study, two NLRP7-targeting nanobodies were tested for their function as crystallization chaperones. Nanobodies 38-A10 and 38-B03 were selected for crystallization trials based on their high affinities for NLRP7 (0.02 and 0.07 nM, respectively), their binding to two different epitopes as determined by SPR and their stability when expressed in the cytosol. For co-crystallization, the nanobodies were mixed with recombinant NLRP7-PYD protein in 1.5x molar excess and unbound nanobody was removed by SEC (Figure 18A,B). For both complexes, initial crystals were obtained using commercially available screens (Figure 18C,D). An initial crystal obtained for the NLRP7-PYD-38-A10 complex diffracted at 2 Å during X-ray analysis at the synchrotron and a dataset was collected. However, due to difficulties in the crystal packing, it was not possible to determine the structure of the complex. For the same complex, also initial crystals diffracting at 8 Å were obtained using commercial screens. By optimizing the salt concentration and pH value, performing an additive screen and using streaking and micro seeding as seeding techniques crystals diffracting at 4-5 Å could be obtained. However, crystals diffracting at higher resolutions could not be grown (Figure 18E). To validate that the NLRP7-PYD and the nanobody are contained in the optimized crystals, one crystal was analysed by SDS-PAGE. The crystal was washed twice in reservoir solution before loading on the gel. Both proteins were detected on the gel indicating that the PYD-nanobody complex did not dissociate during crystallization (Figure 18F).

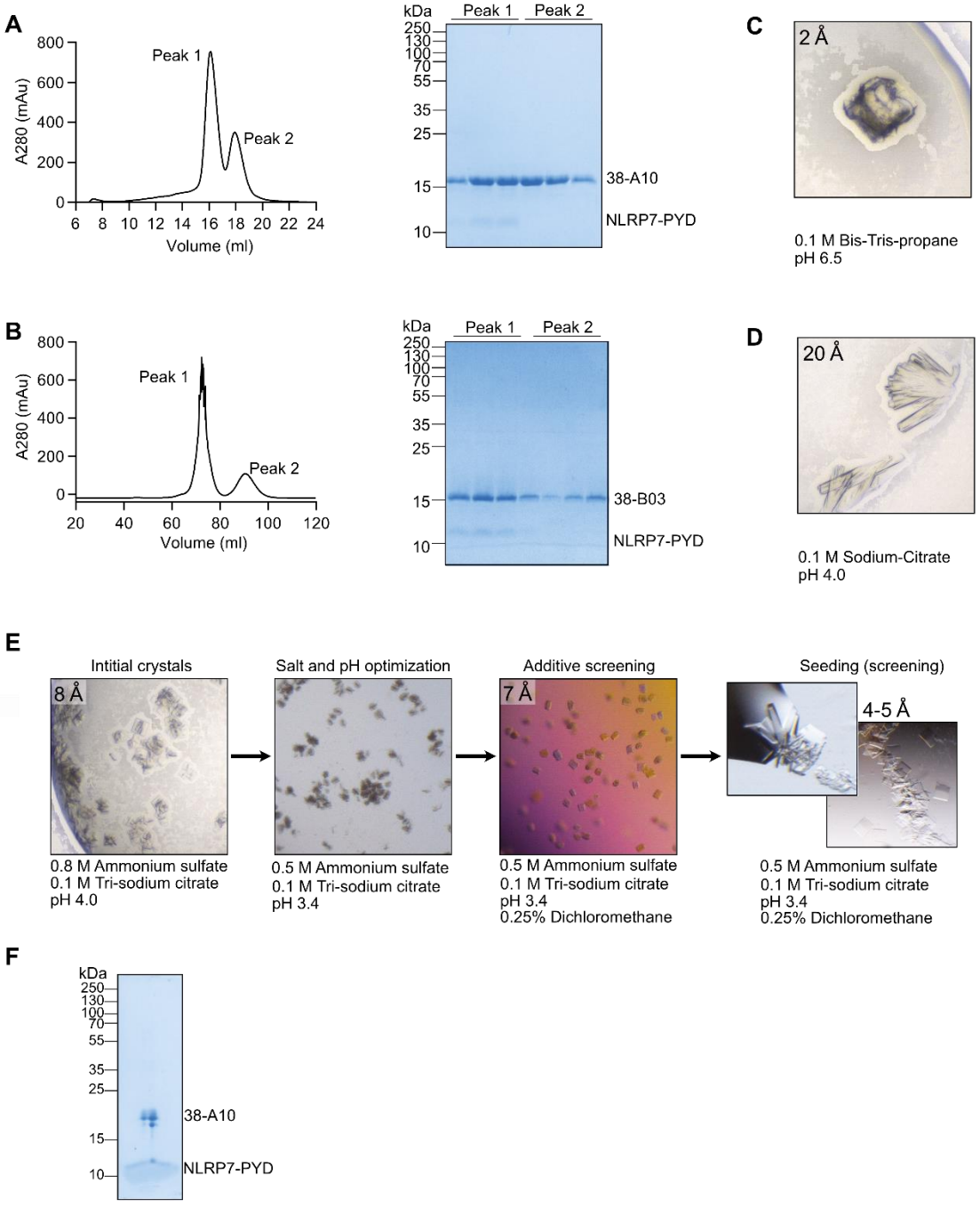

Figure 18: Co-crystallization trials of the NLRP7-PYD in complex with the nanobodies 38-A10 and 38-B03. A) SEC elution chromatogram and SDS-PAGE of elution fractions of the NLRP7-PYD-38-A10 complex. For complex formation, the nanobody was added in 1.5x molar excess. Unbound nanobody was removed during SEC. **B)** As in A, using nanobody 38-B03. **C)** Initial crystal obtained for the NLRP7-PYD-38-A10 complex at a protein concentration of 20 mg/ml, and the indicated reservoir composition. **D)** Initial crystals obtained for the NLRP7-PYD-38-B03 complex at a protein concentration of 20 mg/ml and the indicated reservoir composition. **E)** Optimization of crystallization conditions for

the NLRP7-PYD-38-A10 complex. Initial crystals were optimized by varying the salt concentration and pH value, performing an additive screen and using different seeding methods. **F)** SDS-PAGE of a crystal obtained for the NLRP7-PYD in complex with 38-A10 after the optimization of crystallization conditions. The crystal was washed twice in reservoir solution before loading on the gel.

4.2.6.3. NLRP7-targeting nanobodies specifically detect NLRP7 in Western Blot analysis

Unlike conventional antibodies, nanobodies typically recognize conformational epitopes in the native protein (De Genst *et al.*, 2006). However, in some cases, nanobodies were also able to recognize a linearized target (Beghein and Gettemans, 2017b). Here, six of the NLRP7-targeting nanobodies were tested for their ability to detect linearized and denatured NLRP7 in western blot analysis at a concentration of 5 µg/ml and incubation with the western blot membrane overnight. A commercially available HRP-coupled anti-VHH antibody was used as secondary antibody. The six nanobodies tested detected recombinant full-length MBP-NLRP7 with different efficacies. The best results were obtained with nanobodies 38-A10 and 38-B03, the nanobodies 33-A02 and 33-A04 were also able to detect NLRP7 but gave weaker signals and the nanobodies 33-D02 and 38-G05 were not functional as primary detection reagents for NLRP7 in western blot (Figure 19A). Nanobody 38-A10 was then used to detect endogenous NLRP7 expression in various cell systems. The cell systems were chosen due to their common application in immunology research (HL60, PBMC, THP-1, PM1) or their ovarian origin (Skov3, ovarian carcinoma), as NLRP7 has been reported to play a role in both, innate immune responses as well as female reproduction (Khare *et al.*, 2012, Akoury *et al.*, 2015). As control, recombinant MBP-NLRP7 was used. The nanobody was able to detect NLRP7 in all cell systems tested, but also gave a weak background signal. However, a distinct band for NLRP7 can be recognized in all samples (Figure 19B).

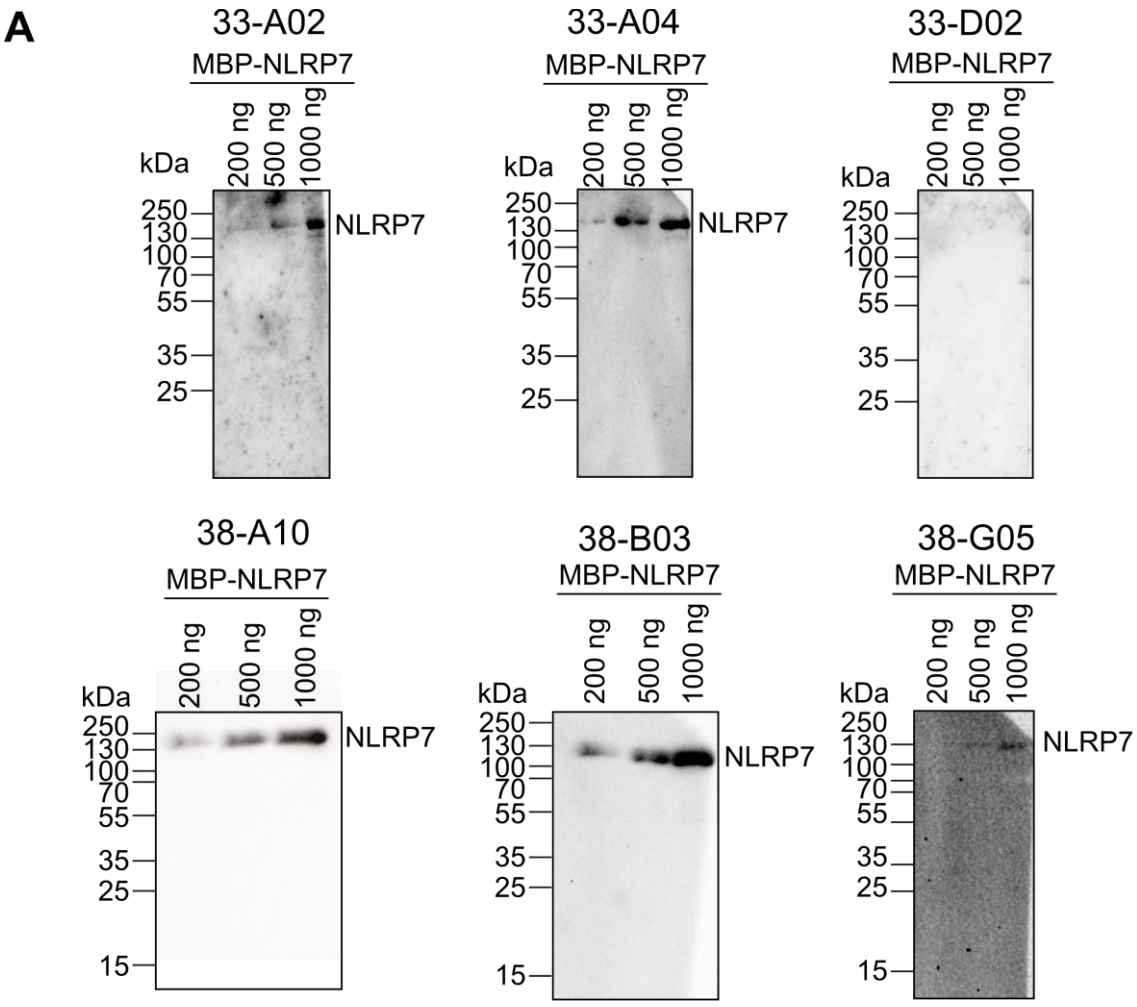
A
33-A02
MBP-NLRP7
200 ng
500 ng
1000 ng
kDa
250
130
100
70
55
35
25
NLRP7
33-A04
MBP-NLRP7
200 ng
500 ng
1000 ng
kDa
250
130
100
70
55
35
25
NLRP7
33-D02
MBP-NLRP7
200 ng
500 ng
1000 ng
kDa
250
130
100
70
55
35
25
38-A10
MBP-NLRP7
200 ng
500 ng
1000 ng
kDa
250
130
100
70
55
35
25
15
NLRP7
38-B03
MBP-NLRP7
200 ng
500 ng
1000 ng
kDa
250
130
100
70
55
35
25
15
NLRP7
38-G05
MBP-NLRP7
200 ng
500 ng
1000 ng
kDa
250
130
100
70
55
35
25
15
NLRP7

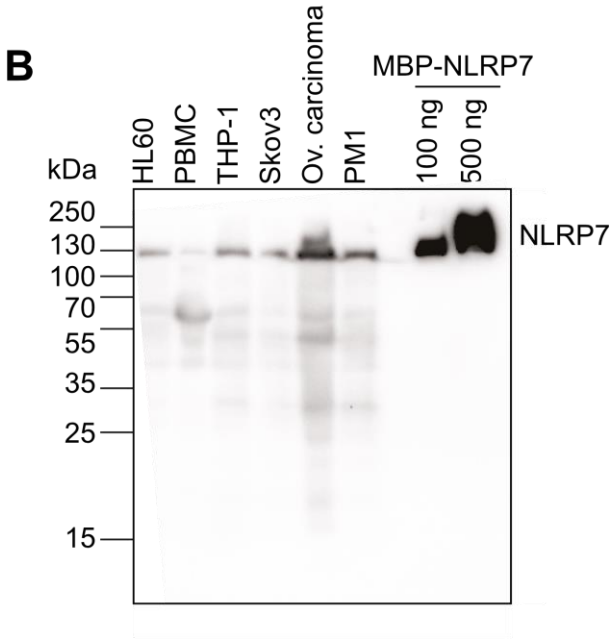
B
HL60
PBMC
THP-1
Skov3
Ov. carcinoma
PM1
MBP-NLRP7
100 ng
500 ng
kDa
250
130
100
70
55
35
25
15
NLRP7

Figure 19: NLRP7-targeting nanobodies as primary detection agents in western blot. A) Nanobodies 33-A02, 33-A04, 33-D02, 38-A10, 38-B03 and 38-G05 were tested for detection of dentaured NLRP7 on a western blot membrane. The nanobodies were used at a concentration of 5 µg/ml in PBS and incubated with the western blot membranes over night. An HRP-coupled anti-VHH antibody was used as secondary antibody. **B)** The nanobody 38-A10 was used to detect endogenously expressed NLRP7 in six different cell system using the conditions described in A).

4.3. Discussion

NLRP7 targeting nanobodies were generated to provide a tool for studying NLRP7 biochemically and in cell systems. By immunization of two llamas with either full length mMBP-NLRP7$_{980}$ or the NLRP7-PYD$_{2-96}$ eight nanobodies binding to the PYD within full length NLRP7 could be generated. These nanobodies bind to NLRP7 with high affinities in the pico- to nanomolar range.

Although one animal was immunized with full length NLRP7, only PYD binding nanobodies were identified from this immunization. This can have several reasons. In the immunization process, the protein of interest has to be mixed with adjuvants to enhance the immune response of the llama. Some proteins tend to bind to the adjuvant or degrade when mixed with the adjuvant solution (Estey *et al.*, 2009). It may be, that full length NLRP7 partially degraded during the immunization process, so that only the PYD remained as antigen. Moreover, some protein domains can be more immunogenic than others (van de Garde *et al.*, 2019). It may therefore be, that the PYD of NLRP7 elicits a stronger immune response than the NACHT or LRR domains. If possible, the NACHT and LLR domains could be expressed as single domains and used for immunization in order to obtain nanobodies targeting these domains. Another way to circumvent the problem of protein instability is the production of sybodies (Zimmermann *et al.*, 2018). Sybodies are synthetic nanobodies that are selected *in vitro* under controlled conditions circumventing immunization of animals. To find specific binders, a ribosome display using a synthetic sybody mRNA library followed by two rounds of phage display is performed, which has the advantage that all steps can be carried out the desired temperature using buffer conditions suitable for the stabilization of the protein of interest (Zimmermann *et al.*, 2020). Another strategy for the production of nanobodies against difficult to purify proteins is genetic immunization. In this approach, cDNA expression plasmids encoding for the protein of interest are delivered into skin cells of the camelid, where the protein is expressed in its native conformation (Eden *et al.*, 2018). However, this methods works best for cell surface or secreted proteins (Greenfield, 2021).

In this thesis, it was aimed to co-crystallize the NLRP7-PYD with the nanobodies 38-A10, 38-B03 and both nanobodies together, since they recognize different epitopes. However, although protein crystals could be grown, none of the crystals diffracted to resolutions that allowed determination of the structure of the protein complex. The already existing structure of the NLRP7-PYD has been determined using NMR and therefore it is not known, whether the crystallization of the NLRP7-PYD alone is feasible (Pinheiro *et al.*, 2010). The nanobodies tested here, did not facilitate the production of high diffraction NLRP7-PYD crystals. Nevertheless, they may facilitate the crystallization of the full length protein. In the course of this thesis, only small amounts of full length NLRP7 could be purified from insect cells and the MBP-tag used for expression and purification of the protein could not be removed effectively. A new approach to obtain protein suitable for crystallization could be the co-expression of tag-free NLRP7 together with the HA-His-tagged nanobody in the cytoplasm of *Sf9* insect cells or HEK cells, using the nanobody for affinity purification. Moreover, cryo-electron microscopy could be used to determine the structure of full length NLRP7 since lower quantities of protein are sufficient for this method (Bhella, 2019).

Four of the nanobodies showed robust binding to NLRP7 when expressed as intrabodies in HEK293T cells. This opens a broad spectrum of applications for the nanobodies in cell biology. For example, cell lines with endogenous NLRP7 expression, such as THP-1 cells, could be modified to inducibly express an NLRP7 nanobody fused to a fluorescent protein which would allow tracing of NLRP7 under different conditions, for example in cells treated with or without acLP. It could also be tested whether the nanobodies have an activating or inhibiting effect on NLRP7. Some of the nanobodies tested here also detected denatured NLRP7 on western blot membranes. Therefore, the nanobodies could also be tested for applications in immunofluorescence and immunohistochemistry. These techniques could also prove useful for studying NLRP7 expression in tissues of HM patients.

5. GSDMD targeting nanobodies block pore assembly

5.1. Introduction

Gasdermin D is the key mediator of pyroptosis, the final common step of all inflammasome pathways. The structure of full length human GSDMD in its autoinhibited state was first determined by X-ray crystallography in 2019 (Liu *et al.*, 2019). In the autoinhibited state, GSDMD consists of an N- and C-terminal domain (NTD and CTD, respectively) connected by a flexible linker. The CTD of GSDMD binds to the NTD to prevent pyroptosis. This is achieved by docking of the β1-β2 loop found in the NTD into a hydrophobic pocket in the CTD. The interaction between both subdomains is mainly mediated by W48, F49 and W50 found in the β1-β2 loop. Cleavage by pro-inflammatory caspases releases the GSDMD NTD from the autoinhibitory CTD, allowing the NTD to undergo large conformational changes and bind to acidic lipids found in cellular membranes, including phosphatidylinositol phosphates (PIPs), phosphatidylserine (PS) and cardiolipin (CL) (Liu *et al.*, 2016; Sborgi *et al.*, 2016). The interaction of GSDMD with acidic lipids is thought to be mediated by four positively charged residues in the NTD (R138, K146, R152, R154 in mice/R137, K145, R151, R153 in human) and mutation of these residues abolishes membrane binding (Liu *et al.*, 2016).

The structure of the GSDMD pore was determined by cryo-EM, revealing two different conformational states of the pore: a membrane-associated pre-pore and a mature membrane-spanning pore (Xia *et al.*, 2021). The mature pore consists of 31-34 NTD subunits with the 33 subunit pore having an inner diameter of 215 Å and spanning 80 Å in height. Three membrane binding basic patches could be deduced from the pore structure, of which two are found in the globular domain of the activated NTD, whereas one is found the in the β7-β8 hairpin. One of the basic patches found in the globular domain is formed by the β1-β2 loop which is also important for stabilizing the auto-inhibited state of GSDMD. Interestingly, the aromatic residues (W48, F49 and W50) that dock into the hydrophobic pocket in the CTD in the autoinhibited state, form a hydrophobic anchor in the activated state which is thought to partially insert into lipid bilayer, while the surrounding basic residues interact with acidic lipids.

The exact mechanism of pore assembly and pre-pore to pore transition is not yet completely understood. Recent molecular simulations suggest a concentration-dependent process, in which low concentrations of GSDMD NTD at the membrane lead to the formation of small oligomers and sublytic pores that have the potential to grow into larger pores, whereas high concentrations of GSDMD NTD lead to the assembly of larger pre-pores (Schaefer and Hummer, 2022). GSDMD pores open and close dynamically dependent on the phosphoinositide environment in the membrane (Santa Cruz Garcia *et al.*, 2022). Gasdermin D pores enable the release of the pro-inflammatory cytokines IL-1β and IL-18, which initiates further immune responses (Shi *et al.*, 2015; Kayagaki *et al.*, 2015; Sborgi *et al.*, 2016; Xia *et al.*, 2021; Evavold *et al.*, 2018; Heilig *et al.*, 2018).

Pyroptosis provides a valuable mechanism in the host defence against pathogens by inducing inflammation in the infected tissue. However, dysregulated or excessive pyroptosis can also contribute to disease. In several monogenic autoinflammatory diseases, autoactivation of inflammasome components contributes to GSDMD activation and sterile inflammation. Mutations in pyrin are the cause for the autoinflammatory disorders familial Mediterranean fever (FMF) and pyrin associated autoinflammation with neutrophilic dermatosis (PAAND), both characterized by episodes of fever, rashes and pain (Nigrovic *et al.*, 2020). The cryopyrin associated periodic syndrome (CAPS) summarizes diseases caused by mutations in NLRP3 including familial cold inflammatory syndrome (FCAS), Muckle-Wells syndrome MWS), and neonatal onset multisystem inflammatory disease (NOMID) also characterized by fevers, rashes and systemic inflammation (Booshehri and Hoffman, 2019). Disease causing mutations have also been found in NLRC4. These diseases are summarized as autoinflammation with infantile enterocolitis (AIFEC) and are also characterized by chronic inflammation with episodes of extreme systemic inflammation (Romberg *et al.*, 2017). Pyroptosis is also observed in other diseases associated with chronic inflammation, including Alzheimer´s disease, IBD and cardiovascular disease. GSDMD expression is increased in the cerebrospinal fluid of Alzheimer's disease patients and enhanced GSDMD cleavage as well as pyroptotic cell death

were observed in cells of patient brains (X. Zhang *et al.*, 2020; Shen *et al.*, 2021; Moonen *et al.*, 2023). Increased GSDMD expression is also observed in patients with IBD where it contributes to IL-1β release (Bulek *et al.*, 2020). However, GSDMD has also been found to have a protective effect in colitis by controlling cGAS-mediated inflammation (Ma *et al.*, 2020). Cardiovascular diseases in which pyroptosis is observed include atherosclerosis, myocardial infarction and cardiomyopathy. In cardiovascular disease, pyroptosis aggravates inflammation and contributes to the formation of atherosclerotic plaques (Zhaolin *et al.*, 2019). GSDMD-mediated pyroptosis also plays a role in diseases accompanied by excessive acute inflammation, such as sepsis. Although the cell type in which GSDMD activation contributes to sepsis is still debatable, systemic knockout or inhibition of GSDMD prevents multiple organ dysfunction in mouse sepsis models (Hu *et al.*, 2020; Silva *et al.*, 2021; Liu *et al.*, 2023).

The great importance of GSDMD in a wide range of diseases requires a detailed understanding of its function and regulatory mechanisms, as well as the discovery of a novel specific inhibitor. Here, six GSDMD targeting nanobodies were characterized biochemically, biophysically and with structural biological means in regard to their binding affinity, binding epitopes, and effect on GSDMD pore formation and stability. For this, the proteins were recombinantly expressed and analysed using surface plasmon resonance spectroscopy (SPR), nano differential scanning fluorimetry (nanoDSF), liposome leakage assays and X-ray crystallography.

5.2. Results

5.2.1. Identification of six unique GSDMD-binding nanobodies

Nanobodies targeting GSDMD were generated by Florian I. Schmidt and colleagues, Institute of Innate Immunity, Bonn. The process of nanobody generation and their cellular characterization is described in (Schiffelers *et al*, 2023). To characterize the nanobodies biochemically and biophysically, the nanobodies and human wild-type, full length GSDMD were recombinantly expressed in *E. coli* cells with C-terminal His- and N-terminal His-SUMO fusion tags, respectively. The proteins were purified by Ni-NTA affinity chromatography followed by size exclusion chromatography (SEC) (Figure 20A, B). In the case of GSDMD the His-SUMO tag was cleaved off using homemade ULP1 sumo protease prior to SEC (Figure 20C). Furthermore, a GSDMD deletion construct was generated, in which the long linker between the N-terminal and C-terminal domains, as well as a disordered region in the NTD were deleted (hGSDMD(Δ184-194/Δ247-272)). Deletion of these regions previously facilitated the crystallization of GSDMD (Liu *et al.*, 2019), and larger amounts of highly homogeneous protein could be produced that way (Figure 20D).

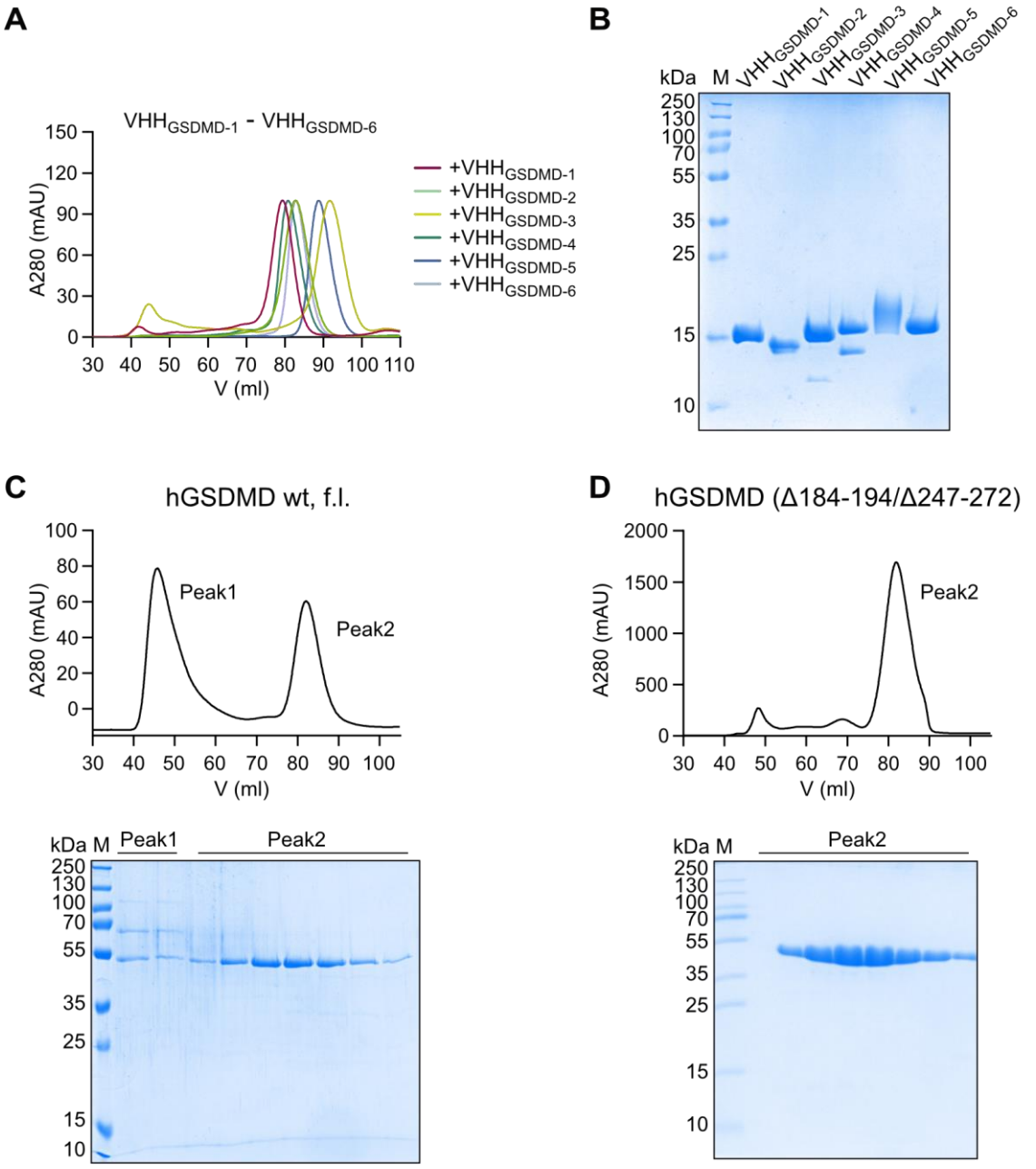

Figure 20: Nanobodies and GSDMD variants used in this study. A) SEC elution chromatogram and **B)** SDS-PAGE of the recombinantly expressed and purified nanobodies $VHH_{GSDMD-1}$ to $VHH_{GSDMD-6}$. **C)** SEC elution chromatogram and SDS-PAGE analysis of wild type, full length, human GSDMD (1-484). **D)** SEC elution chromatogram and SDS-PAGE analysis of a human GSDMD variant (1-484; residues 184-194 and 247-272 were deleted).

Phylogenetic analysis of the six GSDMD-targeting nanobodies revealed that they differed by at least 7.6 % in their amino acid sequence and showed great diversity in the length and composition of their complementarity determining region 3

(CDR3), which can be an indicator of different biochemical properties (Figure 21A,B). Sequence analysis also revealed two cysteine residues in the CDR3 of $VHH_{GSDMD-6}$ that have the potential to form an additional disulfide bond that could prevent the functional expression of this nanobody under reducing conditions. In a first experiment, the binding of the nanobodies was analyzed by surface plasmon resonance (SPR) spectroscopy and the binding affinities were determined using multi-cycle kinetics (Figure 21C). Nanobodies $VHH_{GSDMD-1, -2, -3,}$ and $_{-5}$ bound to GSDMD with high affinities in the nanomolar range and showed rapid association and slow dissociation rates. The strongest binder was $VHH_{GSDMD-1}$ with a dissociation constant of 0.55 nM. $VHH_{GSDMD-2, -3}$ and $_{-5}$ had dissociation constants of 8.2 nM, 2.2 nM, and 4.1 nM, respectively. In contrast, $VHH_{GSDMD-4}$ and $VHH_{GSDMD-6}$ exhibited significantly lower binding affinities in the low micromolar to high nanomolar range. Due to its low affinity, $VHH_{GSDMD-4}$ was excluded from further SPR experiments.

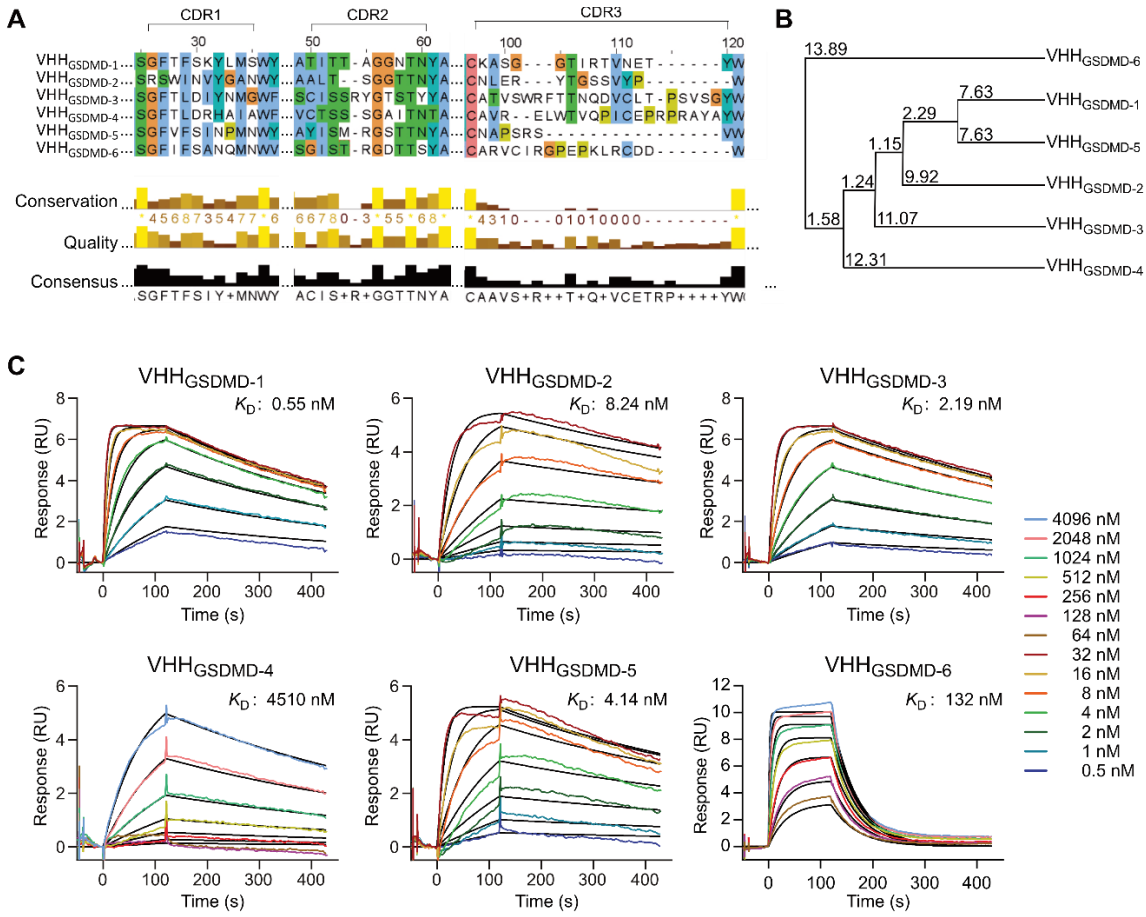

Figure 21: Identification of six unique GSDMD-binding nanobodies. A) Amino acid sequence alignment of the GSDMD targeting nanobodies showing the three complementary determining regions (CDR1-3). **B)** Average distance tree based on the amino acid sequence of the nanobodies. The tree displays the average distance using percent identity and was calculated using the software Jalview. **C)** Determination of binding affinities using surface plasmon resonance (SPR). Chemically biotinylated GSDMD was immobilized on a sensor chip and nanobodies were injected as analytes at the indicated concentrations for 120 s, followed by dissociation for 300 s. Dissociation constants (K_Ds) were determined from the association and dissociation fits by applying a 1:1 binding model.

5.2.2. Characterization of binding epitopes using SPR

Binding epitopes of the nanobodies on GSDMD were analyzed using an SPR-based epitope binning assay. Chemically biotinylated GSDMD was immobilized on an SPR sensor chip and nanobodies were injected as analytes in a pair-wise manner to test whether they compete for overlapping or distinct epitopes on GSDMD (Figure 22A). $VHH_{GSDMD-1}$ and $VHH_{GSDMD-5}$ competed for an overlapping epitope with all other nanobodies (Figure 22B,E,G). $VHH_{GSDMD-2}$ and VHH_{GSDMD-}

$_3$ competed for one epitope but for both nanobodies, additional binding of $VHH_{GSDMD-6}$ was observed (Figure 22C,D,F,G). According to these observations, $VHH_{GSDMD-1}$ and $VHH_{GSDMD-5}$, as well as $VHH_{GSDMD-2}$ and $VHH_{GSDMD-3}$, were grouped into one epitope bin, whereas $VHH_{GSDMD-6}$ stands alone (Figure 22H).

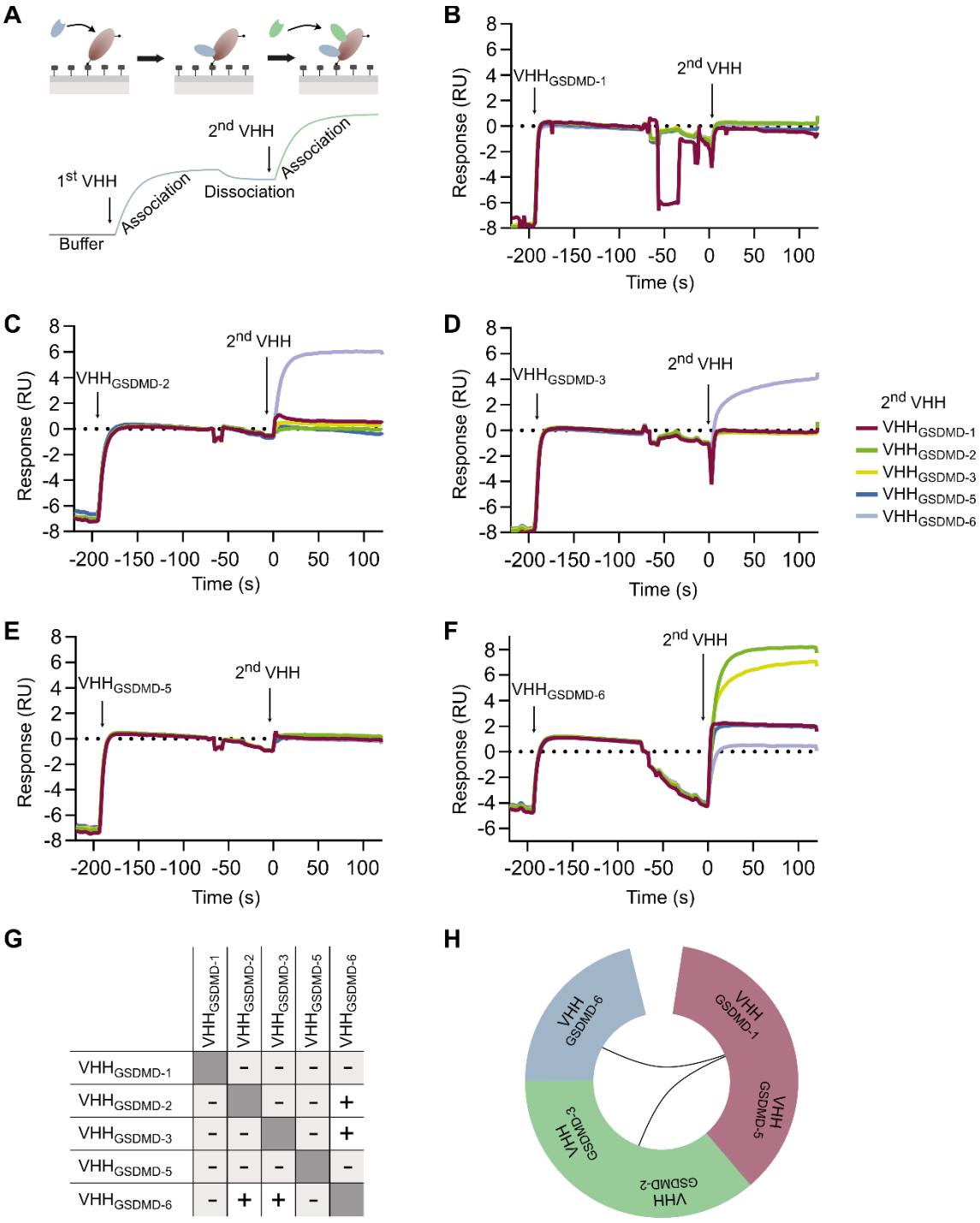

Figure 22: SPR-based epitope binning of GSDMD targeting nanobodies. A) Epitope binning assay. Chemically biotinylated GSDMD was immobilized on an SPR sensor chip and the competitive binding of nanobodies was tested in a pairwise manner. Association of the second nanobody to a distinct epitope can be observed as a second association event in the SPR sensorgram. **B)** Epitope binning assay with $VHH_{GSDMD-1}$ applied in a first binding step followed by a second binding step with one nanobody out of the pool of five ($VHH_{GSDMD-1, -2, -3, -5,}$ and -

$_6$). **C-F)** As in b, starting with VHH$_{GSDMD-2}$, $_{-3}$, $_{-5}$ and $_{-6}$, respectively. Interaction matrix of VHH$_{GSDMD-1 – 6}$. **G)** Interaction matrix of VHH$_{GSDMD-1 – 6}$. **H)** Binning of the nanobodies according to their properties in the competitive binding assay.

5.2.3. Two nanobodies inhibit assembly of functional GSDMD pores *in vitro*

A liposome leakage assay was used to test whether nanobody binding affects the formation of functional GSDMD pores. GSDMD and nanobodies were added in equimolar ratios to calcein-loaded liposomes and after the addition of caspase-4, calcein release through GSDMD pores was monitored by measuring the fluorescence at 525 nm (Figure 23A). As a control, the caspase inhibitor VX-765 was used, which completely inhibited the calcein release (Figure 23B). The addition of VHH$_{GSDMD-1}$ inhibited the calcein release to the same extent as the addition of VX-765, indicating that the assembly of functional GSDMD pores was almost completely abrogated. VHH$_{GSDMD-2}$ also had an inhibitory effect, although to a lesser extent than VHH$_{GSDMD-1}$, indicating that the pore formation was partially abrogated at a 1:1 stoichiometry of GSDMD and nanobody. Addition of VHH$_{GSDMD-6}$ also partially reduced the dye release, but less effectively than VHH$_{GSDMD-1}$ and VHH$_{GSDMD-2}$. VHH$_{GSDMD-3}$, $_{-4}$ and $_{-5}$ rather tended to increase the calcein leakage and had no inhibitory effect on GSDMD pore formation (Figure 23B).

The degree of inhibition of GSDMD pore formation measured by inhibition of dye release in the leakage assay was determined at high nanobody concentrations (10 µM, 20:1 ratio to GSDMD) in comparison to the sample without nanobody addition (Figure 23C). At this high concentration, VHH$_{GSDMD-1}$, VHH$_{GSDMD-2}$ and VHH$_{GSDMD-6}$ inhibited the GSDMD pore formation by 87 %, 75 % and 40 % at the endpoint of the experiment, respectively. In contrast, VHH$_{GSDMD-3}$, VHH$_{GSDMD-4}$ and VHH$_{GSDMD-5}$ showed almost no inhibition. The IC$_{50}$ values for the most potent inhibitors, VHH$_{GSDMD-1}$ and VHH$_{GSDMD-2}$, were obtained by adding the nanobodies at concentrations ranging from 10 nM to 10 µM to the assay. For VHH$_{GSDMD-1}$ an IC$_{50}$ value of 0.22 ± 0.01 µM was determined, while the value obtained for VHH$_{GSDMD-2}$ was 0.65 ± 0.11 µM (Figure 23D,E).

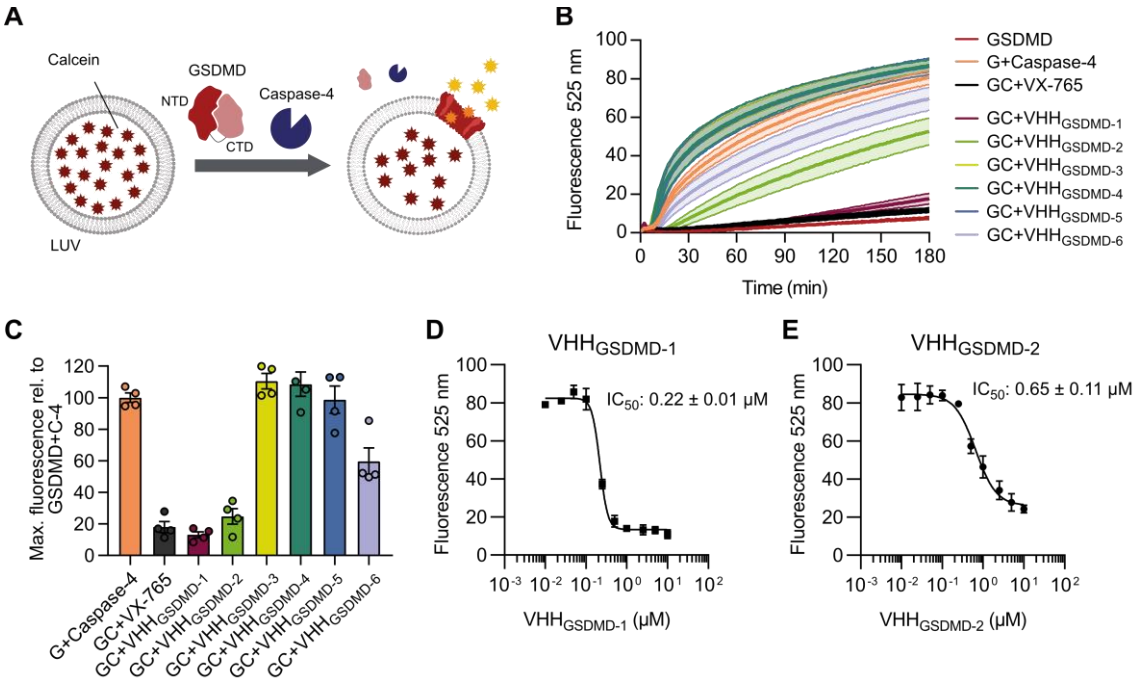

Figure 23: Two nanobodies inhibit the assembly of functional GSDMD pores in vitro. A) Liposomes composed of POPC, PE, and CL in a 32:55:13 ratio were loaded with the self-quenching dye calcein. GSDMD (or GSDMD-3C) and nanobodies were added in equimolar ratios (0.5 µM). After the addition of 0.2 µM caspase-4 (or 3C protease), calcein release was observed by detecting the fluorescence emitted at 525 nm after excitation at 485 nm. **B)** Liposomes, GSDMD (G), nanobodies, and caspase-4 (C) were incubated at 37°C for 180 min and calcein release was detected every minute. VX-765 was used at 0.125 µM concentration. n = 5 independent experiments, the mean ± SEM is shown. **C)** The nanobodies were added in a 20:1 ratio (10 µM) to GSDMD to the leakage assay. The maximal fluorescence after 180 min is shown relative to the maximal fluorescence obtained for the GSDMD+Caspase-4 sample. n = 4 independent experiments, the mean ± SEM is shown. **D, E)** Dose response curves of $VHH_{GSDMD-1}$ and $VHH_{GSDMD-2}$ in the liposome leakage assay. n = 2 independent experiments, the mean ± SEM is shown.

5.2.4. Inhibitory nanobodies increase the thermal stability of GSDMD

The thermal stability of the nanobodies and their effect on the thermostability of GSDMD was investigated using a thermal shift assay by nano-differential scanning fluorimetry (nanoDSF). Nanobodies $VHH_{GSDMD-1}$, $_{-2}$, $_{-3}$ and $_{-5}$ were thermally stable and exhibited unfolding temperatures above 50°C. $VHH_{GSDMD-1}$ was the most stable nanobody with a melting temperature of 67.6°C (
Figure **24**A). GSDMD alone showed an unfolding temperature of 50.2°C at a concentration of 5 µM. The nanobodies were titrated to GSDMD in increasing concentrations from 1 to 50 µM, revealing a shifted fluorescence peak distinct from the peaks observed for GSDMD or nanobody alone, indicating GSDMD-nanobody complex formation (
Figure **24**C-H). At equimolar concentrations, the two strongly inhibiting nanobodies ($VHH_{GSDMD-1}$, $VHH_{GSDMD-2}$) increased the thermal stability of GSDMD by 5.8 and 9.4°C, respectively (
Figure **24**B,C,D). In contrast, the non-inhibitory nanobodies $VHH_{GSDMD-4}$ and $VHH_{GSDMD-5}$ had a slightly destabilizing effect and decreased the melting temperature of GSDMD by up to 2.5°C. $VHH_{GSDMD-3}$ and $VHH_{GSDMD-6}$ increased the thermal stability of GSDMD by 4.2°C.

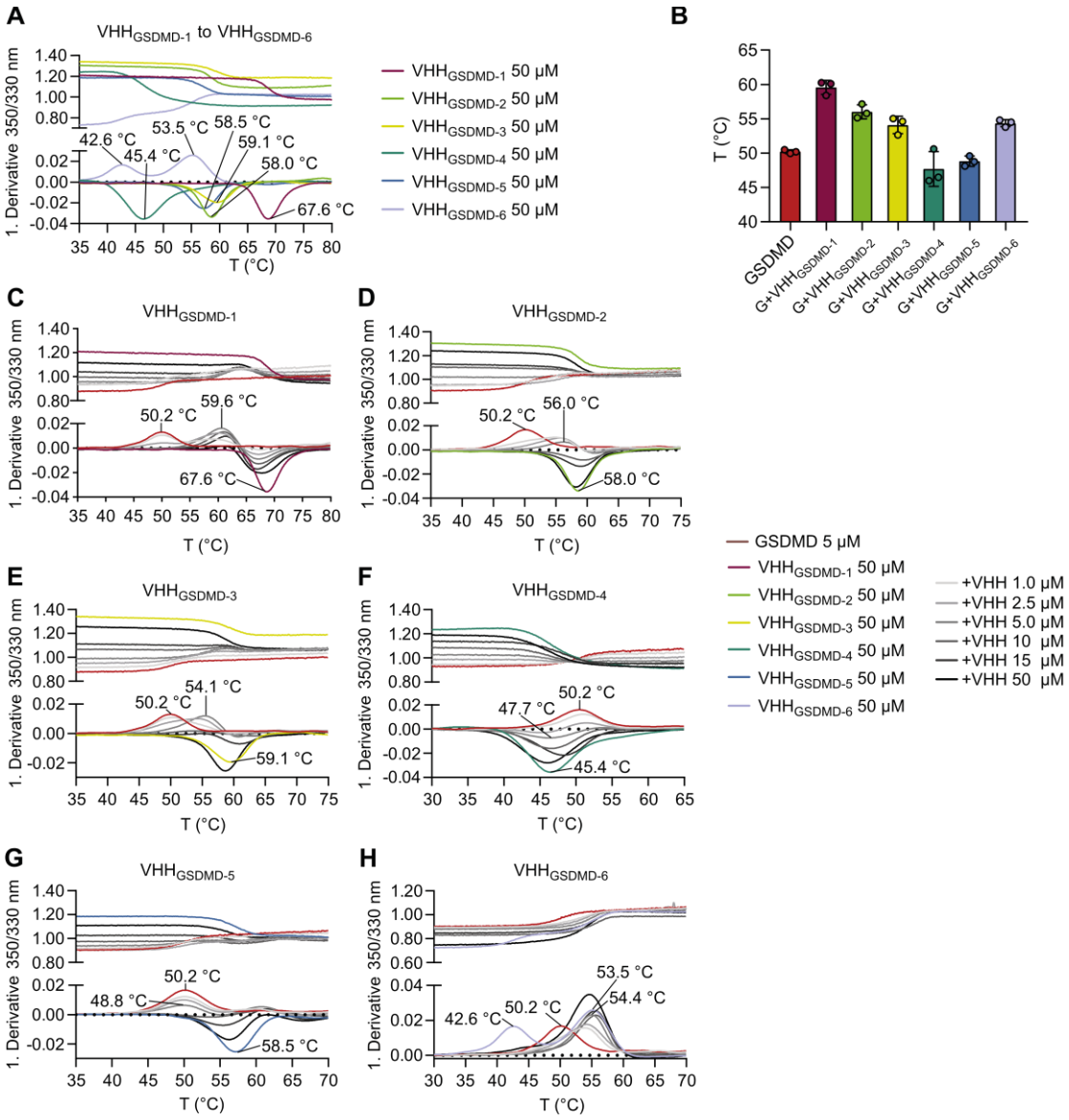

I

Sample	Molarity (µM)	Tm (°C)	SD
GSDMD	5	50.2	0.3
VHH$_{GSDMD-1}$	50	67.6	1.2
VHH$_{GSDMD-2}$	50	58.0	0.5
VHH$_{GSDMD-3}$	50	59.1	1.8
VHH$_{GSDMD-4}$	50	45.4	2.2
VHH$_{GSDMD-5}$	50	58.5	2.9
VHH$_{GSDMD-6}$	50	42.6	0.2
VHH$_{GSDMD-6}$	50	53.5	1.3
GSDMD + VHH$_{GSDMD-1}$	5 + 5	59.6	1.0
GSDMD + VHH$_{GSDMD-2}$	5 + 5	56.0	1.0
GSDMD + VHH$_{GSDMD-3}$	5 + 5	54.1	1.3
GSDMD + VHH$_{GSDMD-4}$	5 + 5	47.7	2.5
GSDMD + VHH$_{GSDMD-5}$	5 + 5	48.8	0.8
GSDMD + VHH$_{GSDMD-6}$	5 + 5	54.4	0.5

Figure 24: Thermal stability of GSDMD, VHHGSDMD-1 - -6 and GSDMD-nanobodies complexes. A) Unfolding temperatures of $GSDMD_{VHH-1 - -6}$ determined at 50 µM concentration by nanoDSF. **B)** Melting temperatures of the GSDMD-nanobody complexes at equimolar concentration (5 µM). N = 3 independent experiments, data represented with SD. **C-H)**, 5 µM GSDMD was mixed with increasing concentrations of the respective nanobody (1-50 µM). **I)** Summary of melting temperatures.

5.2.5. Crystal structure of GSDMD in complex with two nanobodies

To map the epitopes of the nanobodies in detail and to elucidate the molecular mechanism by which $VHH_{GSDMD-1,}$ and $_{-2}$, inhibit GSDMD pore formation, crystallization studies of the GSDMD-nanobody complexes were initiated. For crystallization studies, a GSDMD construct in which the linker region between the two domains (residues 247-272) and residues 184-194 in the NTD were deleted, was used. Crystallization trials were also performed using wild type full length GSDMD, but without success. Also, crystallization of the GSDMD-$VHH_{GSDMD-1}$ complex was not successful, although different commercially available screens, protein concentrations, and crystallization temperatures were tested.

In contrast, crystallization trials were successful for a tripartite complex consisting of GSDMD, $VHH_{GSDMD-2}$ and $VHH_{GSDMD-6}$. To obtain a homogenous protein complex for crystallization, GSDMD was mixed with the nanobodies in a 1:1.5:1.5 ratio, and excess of nanobody was removed by gel filtration (Figure 25A, B). Protein eluting in Peak1 from the SEC column, containing GSDMD and both of the nanobodies, was concentrated to 20 mg/ml prior to crystallization. Crystallization trials were set up using the sitting-drop vapor diffusion method and commercially available screens (Chapter 2.4.8.2). In a first attempt, an initial crystal diffracting to 3 Å could be grown in a condition containing 0.1 M tri-sodium-citrate pH 5.0 and 20% PEG 6K. However, these crystals were not reproducible. By further screening crystallization conditions, initial crystals were obtained using the Memgold crystallization screen and crystals were further optimized by varying the pH, salt and PEG concentrations. Well-diffracting crystals were reproducibly grown using a reservoir condition consisting of 0.04 M NaCl, 25.8 % (v/v) PEG 400 and 0.05 M Na_3Cit pH 4.4 at 20°C (Figure 25C). The crystals were harvested, frozen and the diffraction experiment was carried out at the “Deutsches Elektronen-Synchroton” (DESY) in Hamburg, Germany. A dataset of diffraction images was collected revealing well-defined diffraction spots to a resolution of 2 Å. The dataset was processed as described in Chapter 2.4.8.2. and phases were obtained by molecular replacement using the structures of human GSDMD (PDB 6n9o) (Liu *et al.*, 2019) and a BC2 nanobody (PDB 5ivo) (Braun *et al.*, 2016) as search models. This way, the crystal structure of the GSDMD-nanobody complex

was determined at 1.9 Å resolution. The structure was refined using the programs phenix.refine, Coot and Isolde as described in Chapter 2.4.8.2.

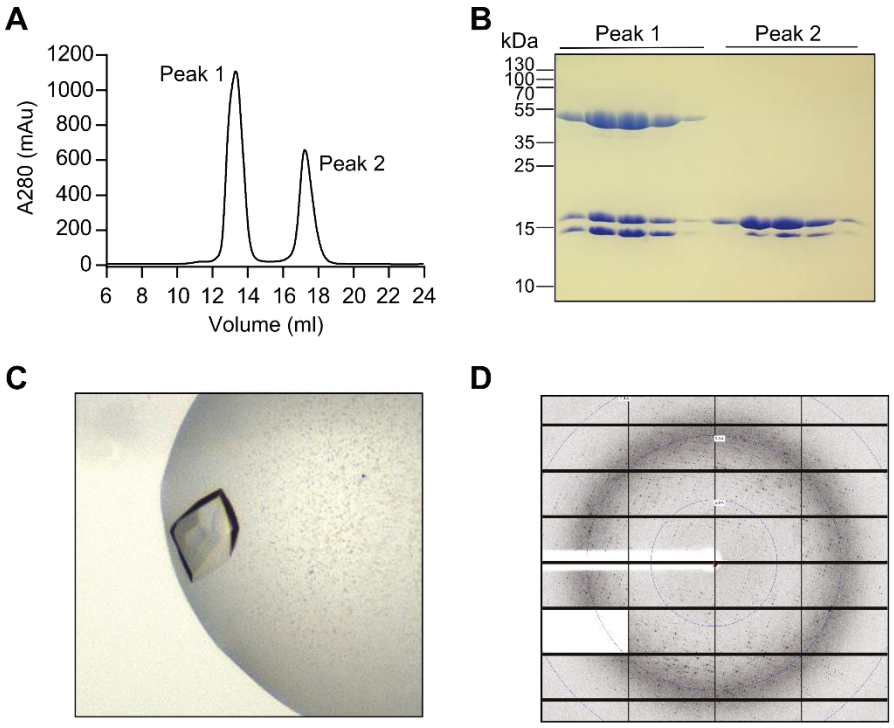

Figure 25: Crystallization of the GSDMD nanobody complexes. A) GSDMD Δ184-194/Δ247-272 was mixed with an 1.5 fold molar excess of $VHH_{GSDMD-2}$ and $VHH_{GSDMD-6}$. Excess nanobody was removed by SEC using a Superdex 200 10/300 GL column. **B)** SDS-PAGE of the Peak1 and Peak2 fractions obtained from SEC of the GSDMD nanobody solution described in a. Protein eluting in peak1 was used for crystallization experiments. **C)** Protein crystal of the GSDMD-$VHH_{GSDMD-2}$-$VHH_{GSDMD-6}$ grown at 20 mg/ml using a reservoir solution containing 0.07 M NaCl, 22 % (v/v) PEG 400 and 0.05 M Na3Cit pH 4.5 at 20°C. **D)** Exemplary X-ray diffraction image acquired at the DESY synchrotron.

GSDMD and nanobodies are found in 1:1:1 stoichiometry with the two nanobodies unambiguously identified by their characteristic CDR regions. Two heterotrimeric GSDMD–$VHH_{GSDMD-2}$–$VHH_{GSDMD-6}$ complexes form the asymmetric unit of the crystal lattice and were refined to a R_{work} of 21.2 % and R_{free} of 24.9 % with good stereochemistry (Figure 26A,Table 27). The two GSDMD molecules found in the structure form a dimeric complex in which the NTD of one GSDMD molecule tightly interacts with the CTD of the other, resulting in a buried surface area of 4,018 $Å^2$ counting both molecules. Looking at a single

heterotrimeric complex, $VHH_{GSDMD-2}$ is bound to the NTD of GSDMD, while $VHH_{GSDMD-6}$ interacts with the NTD and the CTD as well as the linker connecting both domains, stabilizing the twinned assembly of the mixed NTD–CTD' and NTD'–CTD formation (Figure 28A).

Since GSDMD has not been previously reported to form dimers, we hypothesized that the observed complex formation might be a crystallographic artifact. To clarify this, the GSDMD-nanobody complex was analyzed by size exclusion chromatography coupled to multi-angle light scattering (SEC-MALS). The complex of GSDMD, $VHH_{GSDMD-2}$, and $VHH_{GSDMD-6}$ had an apparent molecular weight of 69.2 kDa, consistent with a 1:1:1 complex with a calculated molecular weight of 79.7 kDa (Figure 26B). Therefore, we conclude that the dimerization of the two heterotrimeric complexes occurred during crystallization. The interaction of the mutually twisted N- and C-terminal domains of the two GSDMD molecules is similar to the interactions between the two domains observed in the previously determined crystal structure of human GSDMD (PDB 6n9o) (Liu *et al.*, 2019). Superimposition of our NTD–CTD' complex with the previous structure results in a root mean square deviation (RMSD) of 2.17 Å over 333 Cα atoms, while the NTD overlays with an RMSD value of 1.14 Å over 136 atoms and the CTD with 1.15 Å over 186 atoms (Figure 26C).

Table 27: Crystallographic data collection and refinement statistics

	GSDMD–$VHH_{GSDMD-2}$–$VHH_{GSDMD-6}$ complex
Data collection [a]	
Beam line	DESY PETRA III p13
Wavelength (Å)	0.976255
Space group	P 3_1
Unit cell: a, b, c (Å) α, β, γ (°)	108.35, 108.35, 124.04 90, 90, 120
Resolution range (Å)	93.84–1.86 (1.926–1.86)
Unique reflections	136,535
Multiplicity	2.0 (2.0)
Completeness (%)	99.66 (96.73)
Mean I/sigma(I)	17.43 (0.73)
R_{meas}	0.023 (1.209)
$CC_{1/2}$	1.0 (0.443)
Reflections used in refinement	136,351 (13,167)
Reflections used for R-free	1997 (193)
Refinement	
Model content	A, D: GSDMD (1-484, Δ184-194/Δ247-272) B, E: $VHH_{GSDMD-2}$ (1-118) C, F: $VHH_{GSDMD-6}$ (1-123)
# of atoms macromolecules	9700
# of ligands	0
# of solvent	559
Solvent content (%)	50
R_{work}	0.2124 (0.3297)
R_{free}	0.2493 (0.3204)
RMS deviations bonds [Å]	0.008
RMS deviations angles [°]	0.79
Ramachandran favored (%)	96.24
Ramachandran allowed (%)	3.35
Average B-factor	49.55
Macromolecules	49.621
ligands	–
solvent	48.37
PDB accession code	7z1x

[a] Values in parentheses are for the highest resolution shell.
R_{free}-value is equivalent to the R-value but is calculated for 5 % of the reflections chosen at random and omitted from the refinement process.

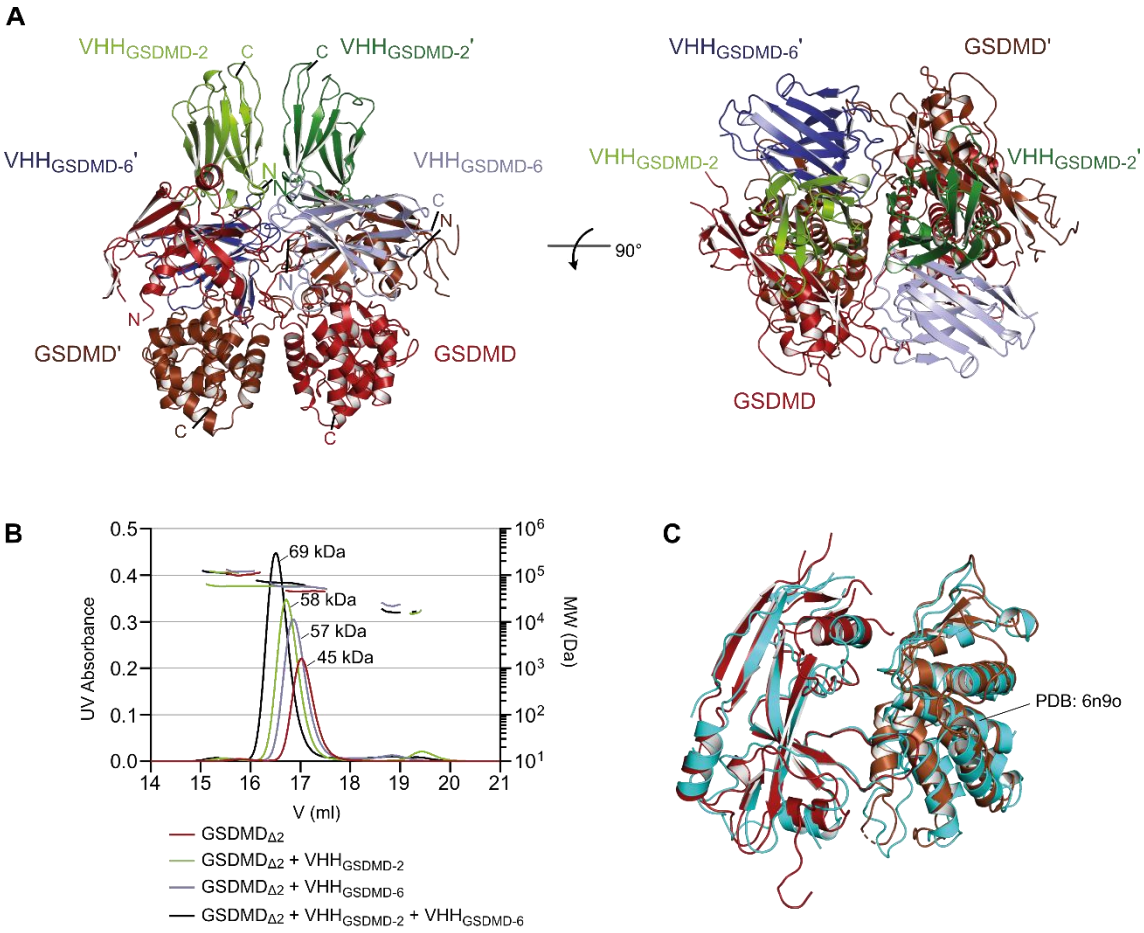

Figure 26: Crystal structure of GSDMD in complex with VHHGSDMD-2 and VHHGSDMD-6. A) Cartoon representation of the GSDMD-VHH$_{GSDMD-2}$-VHH$_{GSDMD-6}$ structure consisting of two heterotrimeric complexes: GSDMD-VHH$_{GSDMD-2}$-VHH$_{GSDMD-6}$ and GSDMD'-VHH$_{GSDMD-2'}$-VHH$_{GSDMD-6'}$ **B)** SEC-MALS analysis of the GSDMD-VHH$_{GSDMD-2}$-VHH$_{GSDMD-6}$ complex using an Superose 6 GL 10/300 column. **C)** Superimposition of the complex of GSDMD NTD and GSDMD' CTD (brown) with the previous GSDMD crystal structure (PDB 6n9o, cyan).

5.2.6. Binding interfaces of GSDMD–VHH interactions

The CDR1, -2 and -3 segments of $VHH_{GSDMD-2}$ comprise 10, 9 and 12 residues, respectively, and the nanobody backbone is stabilized by a conserved disulfide bond between C22 and C95. The interface between $VHH_{GSDMD-2}$ and GSDMD is mainly formed by CDR1 and CDR3 of $VHH_{GSDMD-2}$, while the CDR2 does not contribute significantly to the interaction. In contrast, all three CDRs $VHH_{GSDMD-6}$ are involved in binding to GSDMD (Figure 27A). Electrostatic interactions are crucial for the interaction of both nanobodies with GSDMD. The positively charged CDRs of $VHH_{GSDMD-2}$ bind to an acidic cleft on the GSDMD surface involving residues E15, D17, E21, D126, and E162. The CDRs of $VHH_{GSDMD-6}$ contact with the acidic residues D224, D226, D228, D234, and D275, and the backbone of $VHH_{GSDMD-6}$ contacts residues E448 and E459 on the GSDMD surface (Figure 27B).

Binding of $VHH_{GSDMD-2}$ to GSDMD results in a buried surface area of 1521 $Å^2$ counting both molecules. A pronounced salt bridge is formed between R99 in CDR3 of $VHH_{GSDMD-2}$ which is sandwiched between E21 and E162 in the GSDMD NTD (Figure 27C). In addition, the backbone carboxyl groups of neighboring residues Y100 and T101 in the CDR3 form intermolecular hydrogen bonds with R78 of GSDMD. Another hydrogen bond is formed between the CDR3 residue W108 and N128 on the GSDMD surface. Supporting hydrophobic contacts are formed between F232 of GSDMD with V105, Y106, R26 and W28 of $VHH_{GSDMD-2}$, and Y100 in the CDR3 of $VHH_{GSDMD-2}$, which is sandwiched between H18 and F80 of GSDMD.

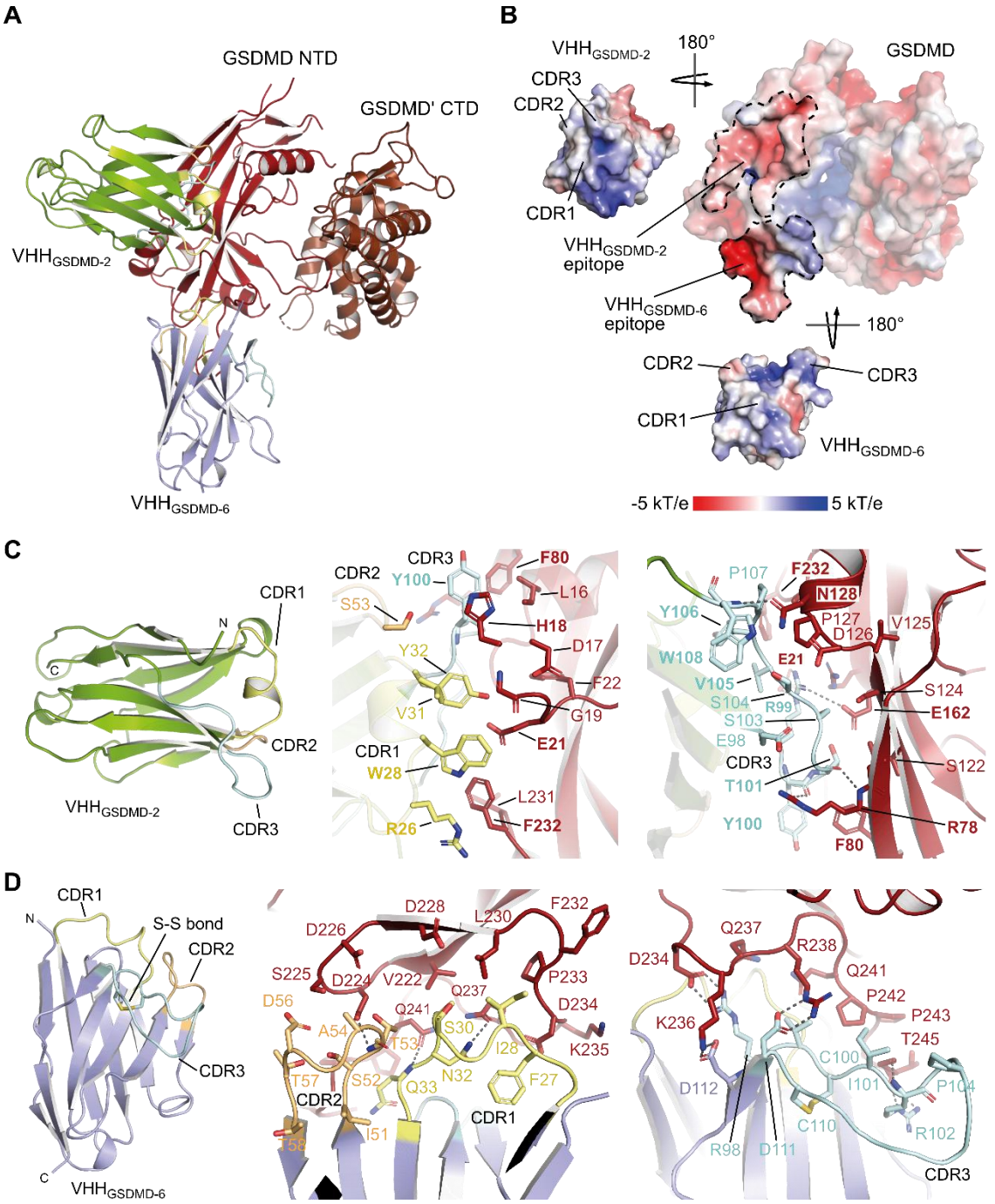

Figure 27: Interfaces between GSDMD and VHHGSDMD-2 and VHHGSDMD-6. A) Cartoon representation of the GSDMD NTD/GSDMD' CTD–VHH$_{GSDMD-2}$–VHH$_{GSDMD-6}$ structure showing GSDMD, GSDMD' NTD, VHH$_{GSDMD-2}$, and VHH$_{GSDMD-6}$. The CDR1, -2, and -3 regions are highlighted in yellow, orange, and cyan, respectively. **B)** Electrostatic surface potential of the GSDMD–nanobody complex. The VHH$_{GSDMD-2}$ and VHH$_{GSDMD-6}$ epitopes are highlighted with dotted lines. **C)** The VHH$_{GSDMD-2}$ to GSDMD interface. **D)** The VHH$_{GSDMD-6}$ to GSDMD interface.

$VHH_{GSDMD-6}$ was essential for the crystallization of high-resolution GSDMD-nanobody complexes by acting as a crystallization chaperone. The buried surface area of this interaction is exceptionally large with 2,615 $Å^2$ counting both molecules, covering the NTD of GSDMD with the CDRs and the CTD with a β-barrel side. This two-sided interaction is only possible by the twisted assembly of the N- and C-terminal domains of GSDMD to form two GSDMD–$VHH_{GSDMD-2}$–$VHH_{GSDMD-6}$ complexes in the asymmetric unit and may be the reason for the twist (Figure 27A, Figure 28A). The CDR3 of $VHH_{GSDMD-6}$ is particularly long comprising 15 residues, and is stabilized by an additional disulfide bond between C100 and C110; a feature that contributes to the indistinguishable identification of the two nanobodies in the crystallographic electron density map (Figure 28B). The charged cluster D234, K236 and R238 towards the end of the NTD in GSDMD is targeted by the CDR3 through a tight salt bridge interaction with D111 (to R238), followed by R98 (to D234) and complemented by D112 (to K236) (Figure 27D). R109 of the $VHH_{GSDMD-6}$-CDR3 instead loops to the CTD of GSDMD and interacts with E417 and the main chain carboxy group of Q411 (Figure 28C). Several additional interactions are found between CDRs 1 and 2 and the NTD of GSDMD. Residues N32 and Q33 in the CDR1 form hydrogen bonds with Q237 and Q241, whereas T53 in CDR2 contacts D224 on the GSDMD NTD (Figure 27D). I101 forms hydrophobic interactions with the linker region between the two GSDMD domains, while L45 in the loop opposing CDR1 and CDR2 of $VHH_{GSDMD-6}$ interacts with the CTD of GSDMD. Several other residues in the $VHH_{GSDMD-6}$ backbone comprising residues 39, 42-45, 47, 95, and 112-115 as well as residues 104-112 in the CDR3 contact the CTD of GSDMD, which might contribute to the role of $VHH_{GSDMD-6}$ in facilitating crystallization (Figure 28D).

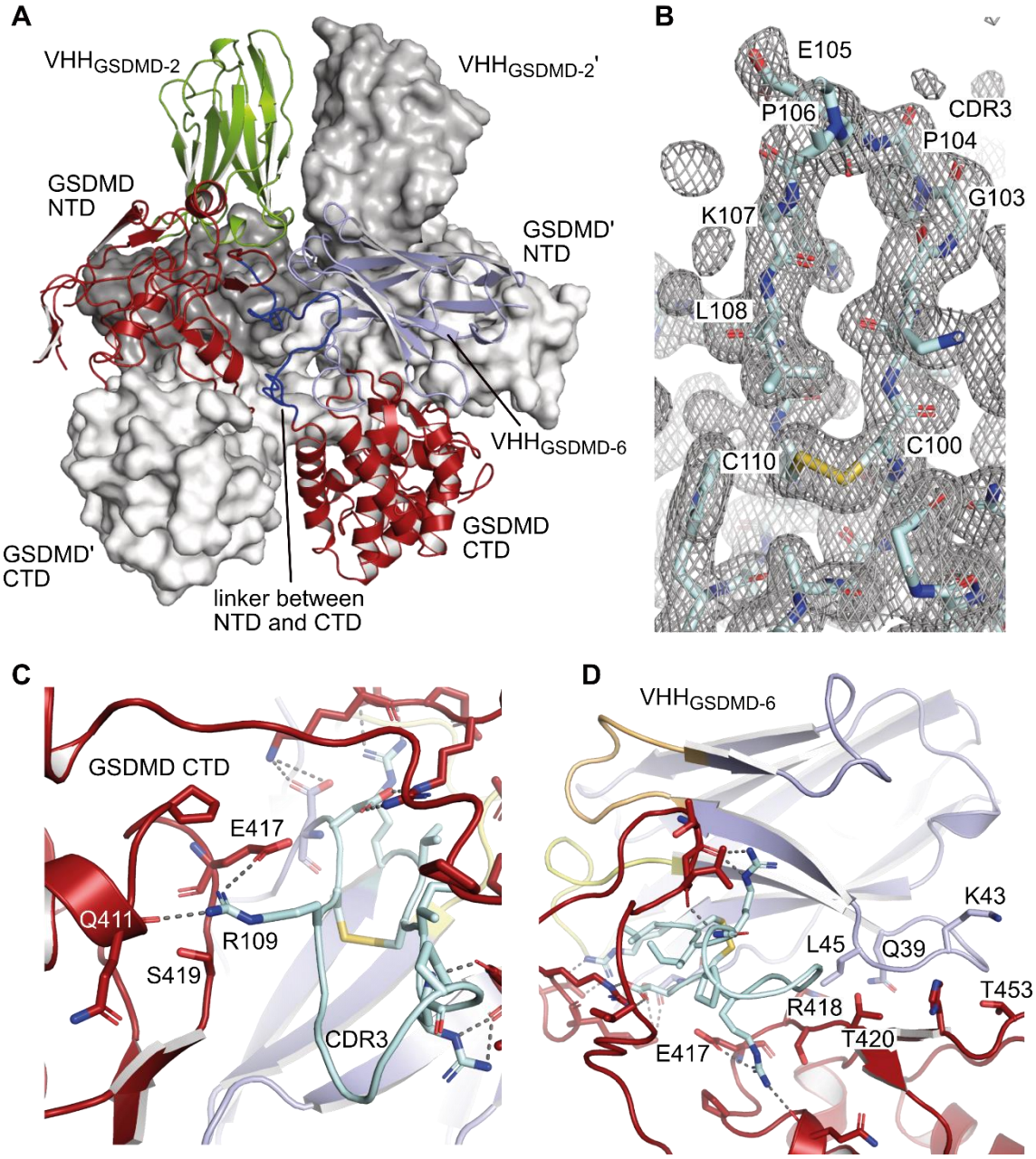

Figure 28: Details for the GSDMD–nanobody interactions. A) The N- and C-terminal domains of GSDMD are twisted in the dimer assembly of the ternary GSDMD–$VHH_{GSDMD-2}$–$VHH_{GSDMD-6}$ complexes. One trimeric complex (chains A, B, C) is shown in ribbon representation while the other one is shown as surface representation colored in grey. **B)** Electron density map of the C100–C110 disulfide bond and the entire CDR3 of $VHH_{GSDMD-6}$ at 1.0 σ. **C)** Salt bridge interactions of $VHH_{GSDMD-6}$ CRD3 to the GSDMD CTD. **D)** Hydrophobic interactions stabilize the binding of $VHH_{GSDMD-6}$ to the CTD of GSDMD.

5.2.7. GSDMD pore formation is inhibited by blocking oligomerization of the GSDMD NTD

In the liposome leakage assay, it was shown that $VHH_{GSDMD-1}$ and $VHH_{GSDMD-2}$ strongly inhibited the assembly of functional GSDMD pores *in vitro*, leading to the question, by which mechanism pore formation is abrogated. Both nanobodies were found to bind to an overlapping epitope on the GSDMD NTD in the SPR-based epitope binning experiment. An *in vitro* caspase cleavage assay was set up using recombinant full length GSDMD and human Caspase-4. A time course experiment shows the decrease of full length GSDMD over time and the corresponding appearance of cleaved N- and C-terminal domains (Figure 29a, left panel). Addition of the VHHs at a 1:1 molar ratio (VHH to GSDMD) revealed that both nanobodies did not affect GSDMD cleavage by Caspase-4 as observed by SDS-PAGE analysis (Figure 29A, right panels), suggesting that the mechanism of pyroptosis inhibition is not achieved by the inhibition of the cleavage reaction.

The cryo-EM structure of the GSDMD pore was previously determined by the Wu lab (Xia *et al.*, 2021). We superimposed our structure of the nanobody bound GSDMD NTD with this structure (PDB 6vfe) (Figure 29B). The superimposition shows that $VHH_{GSDMD-2}$ and $VHH_{GSDMD-6}$ bind to the globular part of the activated NTD. Whereas $VHH_{GSDMD-6}$ binds on top of the globular rim of the GSDMD pore and does interfere only weakly with oligomerization, $VHH_{GSDMD-2}$ binds in the oligomerization interface of the single N-termini and therefore sterically inhibits pore assembly (Figure 29C,D). Therefore, it can be concluded that $VHH_{GSDMD-2}$ directly interferes with the oligomerization of the activated GSDMD NTD. $VHH_{GSDMD-1}$ shared an overlapping epitope with both $VHH_{GSDMD-2}$ and $VHH_{GSDMD-6}$ in the SPR-based epitope binning which suggests that also this nanobody binds to the globular rim of the GSDMD pore and likely also inhibits oligomerization.

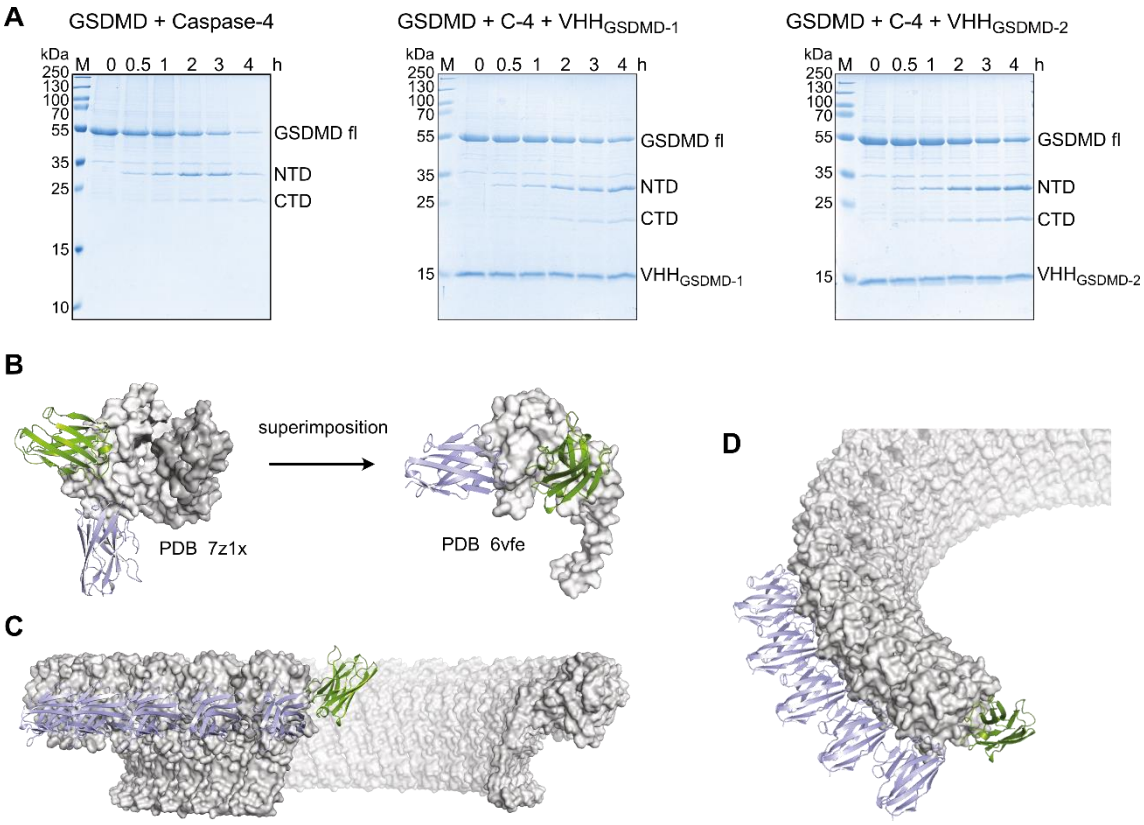

Figure 29: Mechanism of the inhibition of GSDMD pore formation. A) Recombinant GSDMD was incubated with an equimolar amount of $VHH_{GSDMD-1}$ or $VHH_{GSDMD-2}$ and caspase-4 at 37°C for 4 h. GSDMD cleavage by caspase-4 was analyzed by SDS-PAGE. **B)** Superimposition of the GSDMD NTD bound to two nanobodies with the cryo-EM structure of the activated GSDMD NTD (6vfe) showing the position of the nanobodies in the pore-forming active conformation of GSDMD. **C, D)** Superimposition of the nanobody-bound GSDMD NTD with the cryo-EM structure of the activated GSDMD NTD (6vfe) int the context of the formed GSDMD pore.

5.3. Discussion

GSDMD is the key mediator of pyroptosis, the final common step of all inflammasome pathways. Since pyroptosis is involved in many diseases, a deep understanding of the mechanisms underlying GSDMD pore formation and its regulatory processes is essential, and inhibition of GSDMD is an attractive strategy to treat excessive inflammation. To inhibit GSDMD, specific drugs with few off-target effects are desirable. However, there are currently no drugs available that exclusively target GSDMD.

Recently, three small molecules that were initially found to target other proteins were discovered to also bind to and inhibit GSDMD. The first small molecule, necrosulfonamide (NSA), was described in 2018 as GSDMD inhibitor (Rathkey *et al.*, 2018). NSA was initially found to inhibit the protein MLKL, the executioner of necroptosis (Liao *et al.*, 2014). NSA covalently binds to C191 in the GSDMD NTD, which inhibits GSDMD oligomerization and pyroptosis in cell lines and primary cells, and prolongs survival in murine sepsis models (Rathkey *et al.*, 2018). NSA has also been used in a mouse model of acute myocardial infarction, where it inhibited pyroptotic cell death, resulting a reduced infarct size (Jiang *et al.*, 2022). In 2020, dimethyl fumarate, the active ingredient of the drug Tecfidera, was found to inhibit pyroptosis by succination of cysteine residues in GSDMD, thereby blocking its processing by caspases (Humphries *et al.*, 2020). Tecfidera is an FDA-approved drug for the treatment of multiple sclerosis (MS), a disease associated with elevated levels of IL-1β, and MS patients treated with DMF showed reduced levels of IL-1β and cleaved GSDMD in their PBMCs. Due to its anti-inflammatory properties, DMF is also used to treat psoriasis, and anti-cancer properties of DMF have also been noted (Saidu *et al.*, 2019). DMF has been shown to target a wide range of proteins, including the cytoskeletal components actin and tubulin, KEAP1 - a protein involved in the antioxidant response - proteins of the NF-κB pathway, glutathione, the G protein coupled receptor HCA_2 expressed in immune cells, and GAPDH an enzyme involved in glycolysis (Saidu *et al.*, 2019). Also in 2020, another FDA-approved drug, disulfiram (DSF), was found to modify C191 in GSDMD, abrogating GSDMD pore formation, inhibiting pyroptosis, and prolonging survival in murine sepsis models (Hu *et al.*, 2020). The

efficacy of DSF in murine sepsis models has also been validated by another group (Silva *et al.*, 2021), and DSF is currently being tested in clinical trials for the treatment of COVID-19 (Vora *et al.*, 2021). DSF is FDA-approved for the treatment of alcohol dependence. DSF inhibits the enzyme alcohol dehydrogenase, and when consumed in combination with alcohol, DSF causes an aversive reaction with symptoms including diaphoresis, nausea, palpitations and facial flushing (Stokes and Abdijadid, 2022). DSF has also been shown to inhibit the proteasome and induce apoptosis in breast cancer cells, and as an inhibitor of the P-glycoprotein efflux pump has an anti-fungal effect (Chen *et al.*, 2006; Khan *et al.*, 2007).

NSA, DMF and DSF are cysteine reactive compounds, that are prone to non-specific binding and uncontrolled reactivity, which can lead to adverse effects in the human body (Yang *et al.*, 2022). All three molecules have also been shown to bind to other molecules, making them unsuitable for the use in basic research if specific pathways need to be unraveled. For example, DSF has been shown to inhibit the NLRP3 inflammasome and caspases, including caspase-1, which are also important components of the pyroptotic pathway (Nobel et al. 1997; Deng et al. 2020). Moreover, it is unclear that any of them have a physiologic effect to target GSDMD in human pathology.

In this study, six unique GSDMD-targeting nanobodies were characterized. The nanobodies bind specifically to GSDMD as shown by our colleagues (Schiffelers *et al*., 2023), and four of the nanobodies ($VHH_{GSDMD-1}$, $_{-2}$, $_{-3}$ and $_{-5}$) bind to GSDMD with affinities in the low nanomolar range as determined by SPR. Interestingly, two of these nanobodies, $VHH_{GSDMD-1}$ and $VHH_{GSDMD-2}$, inhibited GSDMD pore formation in a liposome leakage assay, whereas $VHH_{GSDMD-3}$ and $VHH_{GSDMD-5}$ had no inhibitory effect on GSDMD. This opens up many applications for the nanobodies in areas where inhibition of GSDMD is desired.

The mechanism, by which $VHH_{GSDMD-2}$, and probably also $VHH_{GSDMD-1}$, inhibit GSDMD pore formation, was revealed by a combination of *in vitro* caspase cleavage assays, X-ray crystallography and SPR-based epitope binning. While caspase cleavage was unaffected by either nanobody, the high-resolution crystal structure of GSDMD in complex with $VHH_{GSDMD-2}$ revealed, that $VHH_{GSDMD-2}$

sterically blocks GSDMD pore assembly by binding to an epitope located in the oligomerization interface of the activated GSDMD NTD. $VHH_{GSDMD-1}$ shared an overlapping epitope with $VHH_{GSDMD-2}$ and $VHH_{GSDMD-6}$ epitopes in the epitope binning assay. Since the epitopes of $VHH_{GSDMD-2}$ and $VHH_{GSDMD-6}$ are known, and $VHH_{GSDMD-1}$ did not inhibit caspase cleavage, but did inhibit pore formation, it is likely that also $VHH_{GSDMD-1}$ inhibits the oligomerization of the GSDMD NTD. By sterically inhibiting oligomerization rather than targeting reactive cysteine residues in GSDMD, these nanobodies provide a novel mechanism of pyroptosis inhibition. Purification of the GSDMD-nanobody complexes as well as SPR-based binding experiments were performed in the presence of 5 mM DTT, indicating that the nanobodies retain their binding ability even under reducing conditions, and should not be affected by the reducing milieu of the cytoplasm. Indeed, Schiffelers et al. showed, that $VHH_{GSDMD-1}$ and $VHH_{GSDMD-2}$ can be expressed in the cytoplasm, and that expression of $VHH_{GSDMD-1}$ and $VHH_{GSDMD-2}$ in THP-1 cells inhibited pyroptosis induced by activation of the NLRC4 and NLRP3 inflammasomes (Schiffelers *et al.*, 2023). In addition, extracellular application of the nanobodies reduced pyroptosis, suggesting that the nanobodies can enter the cell through initial GSDMD pores, and this way inhibit the assembly of lytic pores. To investigate the full potential of the nanobodies as GSDMD specific drugs, *in vivo* studies will be required. Next to the extracellular application of the nanobodies, also the delivery to the cytoplasm of cells using cell penetrating peptide fusions or nanobody mRNA could be tested (Herce *et al.*, 2017; Gaston *et al.*, 2019; Messer and Butler, 2020; X. Zhou *et al.*, 2020; Collado Camps *et al.*, 2021). The non-inhibitory nanobodies could be applied for varying experiments. For example, they could be used to follow the process of GSDMD pore formation in *in vitro* approaches such as fluorescence microscopy, to detect assembled GSDMD pores, or to purify GSDMD pores from cell extracts.

To grow GSDMD-containing crystals that diffract at high resolutions, the addition of $VHH_{GSDMD-6}$ was essential. $VHH_{GSDMD-6}$ contributed to the formation of the crystal lattice by interacting with the GSDMD molecules of the neighboring complex (SI Figure 1) and enabled the generation of fast growing, reproducible, well diffracting GSDMD crystals. High resolution is critical to determine the crystal

structures of proteins in complex with small molecules. Therefore, the combination of $VHH_{GSDMD-2}$ and $VHH_{GSDMD-6}$ could be used to facilitate crystallization of GSDMD with small molecule inhibitors that may be discovered in the future. In the structure described here, the stretch of amino acids 184-194 was deleted in the GSDMD construct to facilitate crystallization. However, we could successfully reconstitute this stretch of amino acids into the GSDMD crystallization construct, and by using the combination of $VHH_{GSDMD-2}$ and $VHH_{GSDMD-6}$, were able to reproducibly grow crystals that diffract up to 2.1 Å resolution, although without showing electron density for this section.

Unfortunately, it was not possible to crystallize GSDMD in complex with $VHH_{GSDMD-1}$. In order to characterize the binding epitope of $VHH_{GSDMD-1}$ in detail, the following experiments could be performed. First, the search for crystallization conditions could be continued, by testing further commercial screens or by changing the crystallization method from vapour diffusion to e.g. microbatch-under-oil crystallization (Luft *et al.*, 2003). Next, cryo-EM could be used instead of X-ray crystallography to determine the structure of the complex. Recent advances in single-particle cryo-EM allow the structure determination of small proteins down to 39 kDa, so that the size of the GSDMD-$VHH_{GSDMD-1}$ complex (67 kDa) should not hinder the experiment (Fan *et al.*, 2019). Another method for determining binding epitopes is hydrogen/deuterium exchange mass spectrometry (HDX-MS). In this approach, the nanobody-bound or unbound protein is exposed to deuterium, resulting in rapid hydrogen-deuterium exchange in accessible regions. The hydrogen-deuterium exchange is then followed by mass spectrometry, which reveals regions that were inaccessible for the hydrogen-deuterium exchange due to nanobody-binding (Konermann *et al.*, 2011; Ständer *et al.*, 2021).

Taken together, the GSDMD-targeting nanobodies are valuable tools for studying and inhibiting GSDMD. In structural biology, the use of $VHH_{GSDMD-2}$ and $VHH_{GSDMD-6}$ as crystallization chaperones enabled the production of reproducible, well-diffracting crystals, which can be of benefit if new insights require high-resolution crystal structures of GSDMD. $VHH_{GSDMD-1}$ and $VHH_{GSDMD-2}$ provide a new and promising approach for specific inhibition of GSDMD in biochemical and

cell-based assays. The therapeutic potential of these nanobodies in chronic disease or acute inflammation will need to be tested in mouse models and can serve as a starting point for the development of new, GSDMD specific drugs.

6. Overall Discussion

6.1. The role of NLRP7 in innate immunity

Innate immune responses rely on the recognition of pathogen- or damage-associated molecular patterns by pattern recognition receptors (PRRs) (Takeuchi and Akira, 2010). An important innate immune pathway is the inflammasome pathway, in which activated cytosolic PRRs initiate the assembly of inflammasomes, leading to activation of pro-inflammatory caspases and ultimately, pyroptotic cell death mediated by GSDMD (Martinon *et al.*, 2002; Shi *et al.*, 2015; He *et al.*, 2015). PRRs capable of assembling inflammasomes are found in several protein families, including the NLR, ALR and TRIM families. In the NLR protein family, well-characterized inflammasome-assembling PRRs include NLRC4, NLRP1, NLRP3 and NLRP6 (Vance, 2015; Yu *et al.*, 2018; Angosto-Bazarra, Molina-López, *et al.*, 2022; Akbal *et al.*, 2022). NLRP1, NLRP3 and NLRP6, belong to the NLRP subfamily of NLRs, which are characterized by their N-terminal PYD. In the case of NLRP3 and NLRP6, the PYD is essential for downstream signalling through interaction with the adaptor protein ASC (MacDonald *et al.*, 2013). NLRP7 is also a member of the NLRP protein family, and given its similarity to NLRP3 and NLRP6 in domain architecture and amino acid sequence (31.7 % and 30.7 % precent identity, respectively), it could be assumed, that NLRP7 also forms inflammasomes in a manner similar to that of NLRP3 or NLRP6. This would include NLRP7 self-oligomerization, the recruitment of the adaptor protein ASC via homotypic PYD-PYD interactions and the recruitment of caspase-1 by ASC through CARD-CARD interactions. However, homology and function do not necessarily correlate (Pearson, 2013), and the role of NLRP7 in innate immunity needs to be carefully studied. Although NLRP7 inflammasome formation has been described in human macrophages and macrophage like cell lines (Khare *et al.*, 2012; Bednash *et al.*, 2017), evidence for a role of NLRP7 in inflammasome activation is sparse.

In this thesis, quantification of ASC speck formation in HEK cell-based reporter systems was used as a readout for inflammasome activation. Overexpression

and/or stimulation of inflammasome forming PRRs in this system is usually sufficient to induce ASC specking, which was shown for NLRP3, NLRC4 and pyrin in this thesis. However, neither overexpression, nor stimulation of NLRP7 with reported NLRP7 activators, induced ASC specking in this system. This raised the question, of whether NLRP7 is indeed capable of interacting with ASC for inflammasome assembly, or what conditions are required for this to occur.

ASC specks are filamentous structures, that are formed when self-oligomerization of a sensor protein (e.g. NLRP3, pyrin) provides a nucleation seed for ASC filamentation, which in turn nucleates caspase-1 filamentation (Sahillioglu *et al.*, 2014; Lu *et al.*, 2015; Shen *et al.*, 2019; Hochheiser, Behrmann, *et al.*, 2022). The nucleation seed for ASC polymerization is provided by the PYDs of the oligomerized PRRs, which form short PYD-filaments (Xiao *et al.*, 2023). When the PYDs of these PRRs are expressed as single domains, they can form long filaments, which causes difficulties in their production as recombinant proteins. For example, the PYD of AIM2 immediately precipitated when the MBP solubility-tag for used for expression was cleaved off, and even uncleaved GFP-PYD fusions eluted in filamentous structures of the SEC column (Lu *et al.*, 2015). The NLRP3 PYD needs to be kept in a low pH buffer to avoid the formation of spontaneous filaments after removal of the N-terminal solubility-tag (Hochheiser, Behrmann, *et al.*, 2022) and also for NLRP6, spontaneous filament formation was observed as soon as the MBP-fusion-tag used for expression and purification was removed (Shen *et al.*, 2019). In contrast, as shown in this thesis and also by others (Pinheiro *et al.*, 2010), the NLRP7-PYD can be expressed as a soluble homogenous monomer and stays monomeric after cleavage of the affinity tag.

Given that the recombinant NLRP7-PYD did not spontaneously form filaments and that overexpression of NLRP7 in HEK cells did not induce ASC speck formation, it can be hypothesized that NLRP7 may not be able to provide a nucleation seed for ASC filamentation because its own PYD is incapable of forming filaments. A structure-based sequence alignment of the NLRP7-PYD with the four PYDs whose filament structures are available (NLRP3, NLRP6, AIM2 and ASC), revealed that some residues required for filamentation in other PYDs are conserved in the NLRP7-PYD (e.g. E15, K23, P42, W43, E47, E56, N79)

whereas others are not (SI Figure 2). To further confirm that the NLRP7-PYD is incapable of filament formation, additional experiments should be performed, including the overexpression of the NLRP7-PYD in HEK293T ASC-BFP reporter cells and the monitoring of the hydrodynamic radius of recombinant NLRP7-PYD over time by dynamic light scattering (DLS).

In this thesis, it was not only observed, that NLRP7 failed to induce ASC specking in HEK reporter cells. In addition, it was observed that co-expression of NLRP7 together with NLRP3 reduced the amount of ASC specks induced by NLRP3 overexpression, whereas the co-transfection of NLRP7 with NLRC4 or pyrin increased the frequency of ASC specks induced by these PRRs. The mechanism behind this remains unclear and requires further investigation. Nevertheless, speculations can be made that can serve as a basis for future experiments. NLRP3 and pyrin both induce ASC speck formation by interacting with ASC through PYD-PYD interactions. Since NLRP7 had an inhibiting effect on NLRP3- but not on pyrin-mediated ASC specks, it is more likely that the inhibiting effect of NLRP7 on NLRP3 arises from direct interaction with NLRP3, rather than with ASC. However it may also be that NLRP7 binds to monomeric ASC without inducing ASC filamentation, partially blocking NLRP3 association, but allowing binding of pyrin and NLRC4. Whether NLRP7 can directly interact with NLRP3, NLRC4, pyrin or monomeric ASC could be tested using co-immunoprecipitation, pulldown assays or direct binding techniques such as surface plasmon resonance (SPR).

Inhibition of inflammasome assembly has already been shown for another class of proteins: the pyrin domain-only proteins (POPs). The POP family comprises three members, POP1-3 , all of which negatively regulate inflammasome signaling by binding to PYDs of inflammasome components (Indramohan *et al.*, 2018). POP1 has been shown to directly bind to the ASC-PYD (Stehlik et al. 2003; de Almeida et al. 2015) and inhibit NLRP3 inflammasome assembly (de Almeida *et al.*, 2022). Also POP2 inhibits inflammasome assembly by interacting with the ASC-PYD (Ratsimandresey *et al.*, 2017), and moreover interaction with the PYDs of NLRP1, NLRP2, NLRP4 and NLRP12 was observed (Dorfleutner *et al.*, 2007). Interestingly, the closest

relatives of POP2 are the PYDs of NLRP2 and NLRP7, which share 68 % and 43 % of sequence identity, respectively (Park, 2012). POP3 has been shown to inhibit ALR inflammasomes by binding to AIM2 and IFI16 (Khare *et al.*, 2014). In a novel study, the target specificity and inhibition mechanism of POP1, POP2 and POP3 were reanalyzed using computational and *in vitro* approaches (Mazanek *et al.*, 2022). By co-transfection of fluorescently-tagged ASC-PYD and POP constructs in HEK293T cells, *in vitro* polymerization assays and negative stain EM, the authors found that not POP1, but POP2 and POP3 directly inhibited ASC filament formation. All three POPs inhibited filament formation of the AIM2 and IFI16 PYDs and POP1 and POP3 inhibited also NLRP3 and NLRP6 PYD filament formation. Therefore, it will be interesting to study the effect of full length NLRP7 or the NLRP7-PYD only on filament formation by the NLRP3- and ASC-PYDs.

In contrast to the inhibiting effect of NLRP7 on NLRP3-ASC speck formation, co-expression of NLRP7 with NLRC4 drastically increased the amount of NLRC4-ASC specks. Unlike NLRPs, NLRC4 contains an N-terminal CARD as effector domain. The CARD domain of NLRC4 can form filaments that directly nucleate filamentation of the caspase-1 CARD domain, leading to caspase-1 activation (L. Zhang *et al.*, 2015; Li *et al.*, 2018). In addition, the NLRC4-CARD can interact with the CARD of ASC, leading to ASC speck formation (Broz *et al.*, 2010; Proell *et al.*, 2013; Man *et al.*, 2014). It may therefore be that binding of NLRP7 to the ASC-PYD via PYD-PYD interactions would still allow or even enhance the binding of NLRC4 to ASC via CARD-CARD interactions. This may explain the opposite effects of NLRP7 on the PYD-NLR NLRP3 and the CARD-NLR NLRC4.

In endogenous settings, NLRC4 activation and self-oligomerization requires binding of an activated NAIP, the actual sensor protein. The interaction between NAIP and NLRC4 is mediated by residues in the NACHT domains of both proteins and induces conformational changes in NLRC4, which allow its self-oligomerization (Bauer and Rauch, 2020). Therefore, it can be speculated that NLRP7 can interact with NLRC4 in a way that opens the NLRC4 conformation and promotes NLRC4 self-oligomerization, leading to the increase in ASC specks observed when NLRP7 and NLRC4 were co-expressed. A similar mechanism has previously been observed for NLRC4 and the Vitamin D receptor (VDR).

Binding of VDR to NLRC4 promoted the association of NAIP and NLRC4 and positively regulated NLRC4 inflammasome formation (Chen *et al.*, 2022).

Taken together, the role of NLRP7 in innate immunity remains still largely elusive. To gain deeper insights into the functions of NLRP7, some tools will be required that are not available yet. Since NLRP7 is only expressed in primates, mouse models are not an option to study NLRP7. Instead, human cell lines with endogenous NLRP7 expression could be used. For this, control cells deficient in NLRP7 will be necessary. So far, NLRP7 studies relied on siRNA knockdown of NLRP7. Generating NLRP7 knockout cell lines using the CRISPR/Cas9 technology to ensure a complete loss of function of the *NLRP7* gene could provide new reliable controls. However, in this thesis, knocking out NLRP7 in THP-1 cells using CRISPR/Cas9 was not successful. In a new approach, the NLRP7 nanobodies generated in this thesis could be used to create nanobody-based degraders of NLRP7 and deplete NLRP7 on the protein level. Moreover, inflammasome reconstitution in HEK293 cell lines is a valuable tool to study inflammasome components in a simplified environment and analyze protein-protein interactions, the influence of mutations, PTMs and the effect of potential inflammasome activators or inhibitors. In this thesis, the NLRP7 inflammasome could not be reconstituted in HEK293T cells. Therefore, conditions that reliably lead to NLRP7 activation will need to be identified to establish a system in which NLRP7 can be comprehensively studied.

6.2. Dual roles of NLRPs in innate immunity and reproduction

The NLRP protein family consists of 14 members, some of which are well established inflammasome activators. However, not all NLRPs appear to be important for inflammasome activation and innate immunity. As described in chapter 1.7.4, mutations and NSVs in NLRP7 are associated with reproductive disorders rather than primarily auto-inflammatory phenotypes. Already in 2009, Tian et al., performed a comprehensive phylogenetic analysis of the mammalian *NLRP* genes and described an evolutionary and functional divergence of NLRPs, allowing their separation in reproductive and inflammatory NLRPs (Tian *et al.*, 2009). According to this analysis, the group of NLRPs with a role in inflammation includes NLRP1, NLRP3, NLRP6, NLRP10 and NLRP12, whereas NLRP2, NLRP4, NLRP5, NLRP7, NLRP8, NLRP9, NLRP11, NLRP13 and NLRP14 are found among the reproductive NLRPs. Consistent with this, NLRP1, NLRP3 and NLRP6 are extensively studied inflammatory NLRPs and many aspects of their activation and function in inflammation are understood (Yu *et al.*, 2018; Shen *et al.*, 2019; Akbal *et al.*, 2022). NLRP10 has only recently been identified as an inflammasome sensor and has been reported to be activated in response to mitochondrial damage (Próchnicki *et al.*, 2023; Zheng *et al.*, 2023). The role of NLRP12 in innate immunity appears to be context-dependent and can be both pro- and anti-inflammatory. For example, NLRP12 has been reported to assemble inflammasomes in response to *Yersinia pestis* infection (Vladimer *et al.*, 2012), but has also been reported to negatively regulate NF-κB signalling in the context of *Salmonella enterica serovar Typhymurium* and *Mycobacterium tuberculosis* infection (Tuladhar and Kanneganti, 2020).

Evidence also exists that justifies the classification of some of the other NLRPs as reproductive NLRPs. NLRP2, like NLRP5, is a component of the subcortical maternal complex (SCMC), an essential multiprotein complex expressed in mammalian oocytes and preimplantation embryos, that is required for zygote development (Mahadevan *et al.*, 2017; Zheng *et al.*, 2021). NLRP2 is the closest relative of NLRP7, and like NLRP7, also NLRP2 has been associated with recurrent miscarriage (Huang *et al.*, 2013). In addition, mutations in NLRP2 have been found to cause early human embryonic arrest, fertilization failure and poor

IVF/ICSI success rates (Sang *et al.*, 2021). NLRP2 deficiency negatively affected the reproductive outcomes of mice (Kuchmiy *et al.*, 2016; Mahadevan *et al.*, 2017), but had no effect on their innate and adaptive immunity (Kuchmiy *et al.*, 2016).

As a component of the SCMC, also NLRP5 plays an essential role in reproduction (Bebbere *et al.*, 2016). As for NLRP2, also mutations in NLRP5 were found to cause early embryonic arrest, infertility, and total fertilization failure in human patients (Mu *et al.*, 2019; Li *et al.*, 2021; Huang *et al.*, 2022; Tong *et al.*, 2022). In addition, mutations in NLRP5 are associated with multilocus imprinting disorders, which has also been observed for NLRP7 (Docherty *et al.*, 2015).

The role of human NLRP9 in reproduction is not yet known, but in mice, Nlrp9a, b and c are involved in preimplantation development (Amoushahi *et al.*, 2020; Kanzaki *et al.*, 2020).

NLRP14 has been found to play a dual role in innate immunity and reproduction. NLRP14 is responsible for the down-regulating nucleic acid sensing during fertilization, when the sperm DNA becomes exposed to the oocyte cytoplasm. This is achieved through the interaction of NLRP14 and TBK1, a central kinase in innate immune sensing of nucleic acids (R. Zhou *et al.*, 2020), which targets TBK1 for ubiquitination and degradation (Abe *et al.*, 2017). Furthermore, NLRP14 is the only NLRP for which a role in male fertility has been described, and mutations in NLRP14 cause defects in spermatogenesis that are associated with male sterility (Westerveld *et al.*, 2006; Yin *et al.*, 2020).

Although the phylogenetic analysis performed by Tian et al. suggests a role for NLRP8, NLRP11 and NLRP13 in reproduction, this has not been experimentally validated yet, and although NLRP4 is expressed in human and mouse preimplantation embryos, its role in reproduction is not understood yet (Zhang *et al.*, 2008; Chang *et al.*, 2013; Peng *et al.*, 2015). Moreover, for some of the NLRPs that play a role in reproduction, also functions in innate immunity have been reported. For example, NLRP2 has been described to exert both pro- and anti-inflammatory functions. These include the upregulation of NF-κB regulated cytokines and chemokines through interaction with IKKa (Rossi *et al.*, 2019), inflammasome formation in astrocytes (Minkiewicz *et al.*, 2013), and the negative

regulation of TBK1 signalling through direct interaction with TBK1 (Yang *et al.*, 2018).

Like NLRP2, NLRP4 has been reported to negatively regulate TBK1 by recruiting the E3 ligase DTX4, leading to TBK1 degradation and negative regulation of type 1 interferon signalling (Cui *et al.*, 2012; An *et al.*, 2015; Lin *et al.*, 2016). In addition, NLRP4 plays a role in antibacterial autophagy by regulating the recruitment of GTPases (Nozawa *et al.*, 2017).

While NLRP11 does not itself form an inflammasomes (Ellwanger *et al.*, 2018), NLRP11 has been described to promote the activation of the NLRP3 inflammasome in human macrophages (Gangopadhyay *et al.*, 2022). Furthermore, NLRP11 negatively regulates NF-κB and type I interferon signalling (Ellwanger *et al.*, 2018), and was found to do so by disrupting the MAVS signalosome, which is activated through RLR signalling(Qin *et al.*, 2017).

This overview demonstrates that the line between reproductive and inflammatory NLRPs cannot be drawn sharply and that some NLRPs exert dual functions that are fine-tuned by the biochemical environment they are found in.

6.3. Inflammatory processes in human pregnancy

Several NLRPs were found to exert functions in inflammation as well as reproduction. Inflammatory processes are essential for normal female reproduction and are observed during ovulation, menstruation, implantation and the onset of labour (Jabbour *et al.*, 2009). These sterile inflammatory processes are induced by tissue injury or remodelling processes associated with the different steps of reproduction and are usually rapidly resolved (Jabbour *et al.*, 2009). The maintenance of pregnancy also depends on finely tuned immunological adaptations at the fetomaternal interface. During the menstrual cycle, the endometrium undergoes morphological and functional changes, known as decidualization, which prepare the endometrium for implantation of the embryo. Decidualization involves inflammatory events such as infiltration of leukocytes, and an increase in vascular permeability and is, among other functions, important to protect the embryo from maternal immune responses

(Jabbour *et al.*, 2009; Okada *et al.*, 2018). The majority of innate immune cells in the decidua are NK cells, but also macrophages and dendritic cells are represented (Granot *et al.*, 2012). Uterine NK cells secrete cytokines and chemokines that attract placental extravillous trophoblasts, promote angiogenesis and attract macrophages to promote tissue remodelling (Male, 2021). Extravillous trophoblasts which invade into the endometrium in turn activate maternal innate immune cells, which is important for pregnancy success (Male, 2021). Cytokines and interferons that are important for successful implantation include IL-6 , IL-1, leukemia inhibitory factor (LIF), and IFN-γ (Yockey and Iwasaki, 2018). Regulatory T cells are also important for implantation by controlling inflammation and supporting modifications maternal vascularity through secretion of IL-10 and TGF-β (Robertson *et al.*, n.d.).

NLRP proteins are mostly associated with the secretion of IL-1β and IL-18 downstream of inflammasome assembly. Both cytokines are members of the IL-1 cytokine family, which has been shown to play an important role in the fetomaternal interaction during implantation and placentation (Equils *et al.*, 2020).

Cytokine levels at the fetal-maternal interface must be precisely balanced to maintain the pregnancy, and both elevated and decreased cytokine levels can lead to pregnancy loss. For example, elevated levels of IL-1β levels have been observed in the deciduas of patients with recurrent pregnancy loss (Löb *et al.*, 2021), but also low levels of IL-1β and IL-6 have been described to contribute to recurrent miscarriage (Wolff *et al.*, 2000). The role of NLRPs in inflammasome formation and cytokine secretion in the decidua has not yet been described. While mutations in NLRP7 can cause reproductive disorders and female infertility, mutations in other NLRPs such as NLRP1 or NLRP3 do not affect female fertility and in fact, the disease causing mutations are often inherited (Zhong *et al.*, 2016; Booshehri and Hoffman, 2019). Investigating the role of NLRP proteins in human pregnancy could contribute to the understanding of the regulation of cytokine secretion in early embryonic development.

6.4. Nanobodies as tools to study innate immune pathways

Nanobodies are already being used to study innate immune pathways. For example, an NLRP1-binding nanobody was used to specifically activate the NLRP1 inflammasome through nanobody-mediated ubiquitination of NLRP1 in cell biological assays (Jenster *et al.*, 2023). In addition, an ASC-CARD-targeting nanobody was used to stabilize ASC-filaments, allowing the structure determination of the ASC-PYD-filament (Schmidt *et al.*, 2016) and ASC-targeting nanobodies have also been shown to attenuate inflammation *in vivo* by disassembling post-pyroptotic ASC specks (Bertheloot *et al.*, 2022). Nanobodies have also been used to gain insight into the molecular mechanisms of the complement system, another important branch of the innate immune system, by specifically targeting and inhibiting different molecules of the complement cascade (Zarantonello *et al.*, 2021). Moreover, nanobodies can be used to label immune cells and observe their biodistribution *in vivo* (De Groeve *et al.*, 2010).

In this thesis, we analysed NLRP7- and GSDMD-targeting nanobodies. These two sets of nanobodies highlight applications for nanobodies and open new perspectives to investigate NLRP7 and GSDMD. While $VHH_{GSDMD\text{-}1}$ and $VHH_{GSDMD\text{-}2}$ inhibited GSDMD pore formation *in vitro*, $VHH_{GSDMD\text{-}2}$ and $VHH_{GSDMD\text{-}6}$ functioned as crystallization chaperones. Schiffelers et al. made use of the inhibitory function of $VHH_{GSDMD\text{-}1}$ and $VHH_{GSDMD\text{-}2}$ to gain new insights into the mechanism of GSDMD pore formation (Schiffelers *et al.*, 2023). By expressing the fluorescently-tagged nanobodies together with the fluorescently-tagged GSDMD NTD in HEK293T cells, Schiffelers et al. showed that membrane association of the GSDMD NTD does not require oligomerization or the formation of pre-pores. Since activation of the NLRP7 inflammasome was not achieved in this thesis, it is yet unclear whether the NLRP7-targeting nanobodies have an inhibiting effect on NLRP7. However, the NLRP7 nanobodies could be used to degrade NLRP7 in cells endogenously expressing NLRP7. Cells deficient of NLRP7 are a necessary control when studying NLRP7 function in systems with endogenous NLPR7 expression. We attempted to knockout NLRP7 in THP-1 cells using the CRISPR/Cas9 methodology, however this approach was not successful. The failure of a genetic knockout of NLRP7 may be attributed to the

low efficiency of sgRNAs that can be designed for the NLRP7 gene (https://chopchop.cbu.uib.no/results/1681371916268.9507/, 13.04.2023). This technical problem could possibly be circumvented by fusing an NLRP7-nanobody to an E3 ligase and targeting NLRP7 for proteasomal degradation. Taken together, nanobodies provide a valuable tool for specific inhibition and activation of innate immune components, allow the determination of flexible protein structures and function as crystallization chaperones for the determination of high-resolution structures.

6.5. Nanobodies as therapeutics to treat auto-inflammatory disease

Many diseases are associated with acute or chronic inflammation, including autoinflammatory diseases, cardiovascular disease and cancer, and inflammasome activation is a major contributor to this inflammation. As pyroptosis is the final common step of all inflammasome pathways, inhibition of pyroptosis is an attractive strategy to attenuate inflammation (Yu *et al.*, 2021). As a key mediator of pyroptosis, GSDMD is a promising drug target. However, to date, no GSDMD-specific small molecule inhibitor has been identified. In this thesis, two GSDMD-binding nanobodies were found to inhibit GSDMD pore formation *in vitro*, providing a new starting point for the development of GSDMD-targeting drugs.

Today, two nanobody-based drugs are already in clinical use. In 2019, Cablivi® (caplacizumab-yhdp) was approved by the FDA for the treatment of patients with acquired thrombotic thrombocytopenic pupura (aTTP), a rare blood-clotting disorder (https://www.fda.gov/drugs/resources-information-approved-drugs/fda-approved-caplacizumab-yhdp, 13.04.2023). This nanobody-based drug was developed by the company Ablynx which is now part of the company Sanofi. Caplacizumab is a humanized bivalent nanobody consisting of two copies of an identical nanobody connected by a tri-alanine linker, that binds to the protein von Willebrand factor (vWF), an oligomeric glycoprotein involved in blood homeostasis (European Medicines Agency, 2018). The structure of caplacizumab bound to the A1 domain of vWF suggests that caplacizumab

binding traps vWF in a conformational state that is unable to bind to platelets, thereby inhibiting blood clotting (Lee *et al.*, 2021).

In 2022, another nanobody-based drug, ozoralizumab (Nanozora ®), has been approved in Japan for the treatment of rheumatoid arthritis. Ozoralizumab is a trivalent bispecific humanized nanobody construct consisting of two anti-TNFα nanobodies and one anti-human serum albumin (HSA) nanobody and was developed by Taisho Pharmaceutical Co. Ltd under licence from Ablynx, Sanofi (Keam, 2023). The two different TNFα targeting nanobodies in ozoralizumab bind to two distinct subunits of TNFα, while binding to HSA by the third nanobody prolongs the half-life of the drug (Ishiwatari-Ogata *et al.*, 2022).

In addition, a number of nanobody-based drugs are currently tested in clinical trials. In 2021, a phase 2b study investigating the therapeutic potential of sonelokimab (M1095) in the treatment of plaque-type psoriasis was completed with positive results (Papp *et al.*, 2021). Sonelokimab is a trivalent nanobody construct consisting of one nanobody directed against IL-17A, a second nanobody directed against IL-17F and a third nanobody that binds HSA.

The available nanobody-based drugs and those in development illustrate that often further engineering of the nanobody is required to generate a construct with therapeutic potential. The generation of multivalent nanobodies has in many cases increased the binding affinity and potency of nanobody constructs. Apart from the afore mentioned nanobody-drugs, also other studies describe an enhancement of nanobody potency by multivalency. For example, multivalent nanobodies directed against the spike protein of SARS-CoV-2 neutralized the virus more than 100 times more effectively than single nanobodies (Koenig *et al.*, 2021). Another study showed, that increasing the valency of death receptor 5 (DR5) nanobody agonists correlated with their potency to induce cell death in tumour cells, with pentamers being the most effective.

While the two GSDMD-inhibiting nanobodies studied in this thesis, $VHH_{GSDMD\text{-}1}$ and $VHH_{GSDMD\text{-}2}$, bind to an overlapping epitope, precluding their cooperativity, $VHH_{GSDMD\text{-}2}$ and $VHH_{GSDMD\text{-}6}$ were found to bind cooperatively to GSDMD. This would allow the generation of a multivalent GSDMD-targeting nanobody which may increase the potency of $VHH_{GSDMD\text{-}2}$. Also for NLRP7 nanobodies binding to

two different epitopes on the NLRP7-PYD were identified in this thesis, which would also allow the generation of bivalent NLRP7 nanobodies.

Another modification necessary for the application of nanobodies as drugs, is their humanization. The camelid VHH domain framework differs from the human heavy chain variable domain in about ten amino acids, which have to be mutated to their human equivalent for therapeutic applications in order to reduce immunogenicity of the nanobody (Vincke *et al.*, 2009). Current nanobody-based drugs are directed against extracellular targets. Since nanobodies are typically unable to cross the plasma membrane, specific measures must be taken to target intracellular proteins, such as components of the inflammasome. Strategies for the intracellular delivery of nanobodies are currently under intense investigation. In a recent study, mRNA encoding nanobodies was introduced into cells and nanobody expression and binding was observed as early as 3 h after transfection (X. Zhou *et al.*, 2020). In addition, a multivalent anti-botulinum neurotoxin nanobody construct was encoded as replicating RNA, mixed with a cationic nanocarrier and delivered to mice by intramuscular injection. Nanobody expression was detected 8 h after treatment and was sufficient to protect mice from the botulinum intoxication (Mukherjee *et al.*, 2022). This suggests that mRNA delivery is a promising method for nanobody delivery into the cytoplasm. Furthermore, cell-permeable peptides (CCPs) have been successfully used to deliver nanobodies to the cytoplasm. Nanobodies with specific CPPs have also been used to translocate their target proteins to the nucleus (Herce *et al.*, 2017) and to block infection by intracellular bacteria *in vitro* and in mouse models (Zhang *et al.*, 2021).

GSDMD is an intracellular protein in its inactive state, and the binding epitopes of the inhibitory GSDMD nanobodies are also located inside the cell when the GSDMD NTD associates with the plasma membrane. Of note, Schiffelers et al. showed that $VHH_{GSDMD\text{-}1}$ and $VHH_{GSDMD\text{-}2}$ inhibited pyroptosis when added to the culture medium of cells (Schiffelers *et al.*, 2023). It is likely that the nanobodies entered the cells through initially formed GSDMD pores, and inhibited further pore formation once they reached the cytoplasm. However, the above-mentioned

delivery methods could increase the amount of nanobodies reaching the cytoplasm and would also include cells, that don't present GSDMD pores.

6.6. Conclusion and future directions

In this thesis, two different proteins involved in innate immune processes were studied. NLRP7 is a protein best known for its function in reproduction, as defects in NLRP7 are associated with recurrent miscarriage, hydatidiform mole and female infertility (Sanchez-Delgado *et al.*, 2015; Soellner *et al.*, 2017). However, NLRP7 has also been described as a pattern recognition receptor in human macrophages that can initiate inflammasome formation in response to bacterial acylated lipopeptides (Khare *et al.*, 2012; Bednash, *et al.*, 2017). NLRP7 inflammasomes could not be reconstituted in HEK293T reporter cells during the course of this thesis. Nevertheless, co-expression of NLRP7 with other well-characterized PRRs had an effect on their inflammasome assembling activity. As pregnancy is an immunological complex process involving many cytokines that need to be finely balanced to guaranty pregnancy success, NLRP7 may contribute to shaping the cytokine environment in the early stages of pregnancy. This may be either by promoting cytokine release as a PRR itself, or by regulating other PRRs. Therefore, in future projects the interaction of NLRP7 with other PRRs and the inflammasome component ASC should be studied. As the cell type may influence the function of NLRP7, different cell types involved in reproduction and innate immunity with endogenous NLRP7 expression will need to be investigated. The here identified NLRP7-targeting nanobodies may facilitate these studies by serving as tools for NLRP7 detection or degradation.

In contrast to NLRP7, the role of GSDMD in innate immunity is well understood (Kayagaki *et al.*, 2015; He *et al.*, 2015). As a key mediator of pyroptosis, GSDMD is an attractive drug target to attenuate excessive inflammation downstream of inflammasome activation. The GSDMD-targeting nanobodies characterized in this thesis may serve as starting point for the generation of GSDMD-specific drugs. To generate potent drugs out of the nanobodies, some modifications and further experiments will be necessary. *In vivo* models using mice that express human GSDMD will be needed to assess the potency of the nanobodies in the

context of disease. In addition, the nanobodies will need to be humanized, and potentially their valency will need to be increased by connecting nanobodies binding to different epitopes. Moreover, delivery strategies of the nanobodies to the cytoplasm must examined in order to also target also cells, which don’t present GSDMD pores.

To conclude, the work presented in this thesis provides new insights into NLRP7 biochemistry and describes nanobodies, both as tools to study NLRP7 and as a new strategy to inhibit GSDMD pore formation.

References

Abe, T. *et al.* (2017) 'Germ-Cell-Specific Inflammasome Component NLRP14 Negatively Regulates Cytosolic Nucleic Acid Sensing to Promote Fertilization'. *Immunity*, 46(4), pp. 621–634. DOI: 10.1016/j.immuni.2017.03.020

Abi Nahed, R. *et al.* (2019) 'NLRP7 Is Increased in Human Idiopathic Fetal Growth Restriction and Plays a Critical Role in Trophoblast Differentiation'. *Journal of Molecular Medicine*, 97(3), pp. 355–367. DOI: 10.1007/s00109-018-01737-x

Adams, P.D. *et al.* (2010) 'PHENIX: A Comprehensive Python-Based System for Macromolecular Structure Solution'. *Acta Crystallographica Section D: Biological Crystallography*, 66(Pt 2), pp. 213–221. DOI: 10.1107/S0907444909052925

Adiyaman, R. and McGuffin, L.J. (2019) 'Methods for the Refinement of Protein Structure 3D Models'. *International Journal of Molecular Sciences*, 20(9), p. 2301. DOI: 10.3390/ijms20092301

Agier, J., Pastwińska, J. and Brzezińska-Błaszczyk, E. (2018) 'An Overview of Mast Cell Pattern Recognition Receptors'. *Inflammation Research*, 67(9), pp. 737–746. DOI: 10.1007/s00011-018-1164-5

Agostini, L. *et al.* (2004) 'NALP3 Forms an IL-1beta-Processing Inflammasome with Increased Activity in Muckle-Wells Autoinflammatory Disorder'. *Immunity*, 20(3), pp. 319–325. DOI: 10.1016/s1074-7613(04)00046-9

Aguilar, G. *et al.* (2019) 'Using Nanobodies to Study Protein Function in Developing Organisms'. *Antibodies*, 8(1), p. 16. DOI: 10.3390/antib8010016

Akbal, A. *et al.* (2022) (11) 'How Location and Cellular Signaling Combine to Activate the NLRP3 Inflammasome'. *Cellular & Molecular Immunology*, 19(11), pp. 1201–1214. DOI: 10.1038/s41423-022-00922-w

Akira, S., Uematsu, S. and Takeuchi, O. (2006) 'Pathogen Recognition and Innate Immunity'. *Cell*, 124(4), pp. 783–801. DOI: 10.1016/j.cell.2006.02.015

Akita, K. *et al.* (1997) 'Involvement of Caspase-1 and Caspase-3 in the Production and Processing of Mature Human Interleukin 18 in Monocytic THP.1 Cells'. *The Journal of Biological Chemistry*, 272(42), pp. 26595–26603. DOI: 10.1074/jbc.272.42.26595

Akoury, E. *et al.* (2015) 'NLRP7 and KHDC3L, the Two Maternal-Effect Proteins Responsible for Recurrent Hydatidiform Moles, Co-Localize to the Oocyte Cytoskeleton'. *Human Reproduction*, 30(1), pp. 159–169. DOI: 10.1093/humrep/deu291

Alberts, B. *et al.* (2002) ‘Programmed Cell Death (Apoptosis)’. *Molecular Biology of the Cell. 4th Edition*. Available at: https://www.ncbi.nlm.nih.gov/books/NBK26873/ (Accessed: 24 February 2023)

de Almeida, L. *et al.* (2022) ‘POP1 Inhibits MSU-Induced Inflammasome Activation and Ameliorates Gout’. *Frontiers in Immunology*, 13. Available at: https://www.frontiersin.org/articles/10.3389/fimmu.2022.912069 (Accessed: 30 March 2023)

Amarante-Mendes, G.P. *et al.* (2018) ‘Pattern Recognition Receptors and the Host Cell Death Molecular Machinery’. *Frontiers in Immunology*, 9. Available at: https://www.frontiersin.org/articles/10.3389/fimmu.2018.02379 (Accessed: 22 February 2023)

Amoushahi, M. *et al.* (2020) ‘Maternally Contributed Nlrp9b Expressed in Human and Mouse Ovarian Follicles Contributes to Early Murine Preimplantation Development’. *Journal of Assisted Reproduction and Genetics*, 37(6), pp. 1355–1365. DOI: 10.1007/s10815-020-01767-w

Amoushahi, M., Sunde, L. and Lykke-Hartmann, K. (2019) ‘The Pivotal Roles of the NOD-like Receptors with a PYD Domain, NLRPs, in Oocytes and Early Embryo Development†’. *Biology of Reproduction*, 101(2), pp. 284–296. DOI: 10.1093/biolre/ioz098

An, T. *et al.* (2015) ‘DYRK2 Negatively Regulates Type I Interferon Induction by Promoting TBK1 Degradation via Ser527 Phosphorylation’. *PLoS Pathogens*, 11(9), p. e1005179. DOI: 10.1371/journal.ppat.1005179

Ancient Missense Mutations in a New Member of the RoRet Gene Family Are Likely to Cause Familial Mediterranean Fever. The International FMF Consortium. (1997) *Cell*, 90(4), pp. 797–807. DOI: 10.1016/s0092-8674(00)80539-5

Andreeva, L. *et al.* (2021) ‘NLRP3 Cages Revealed by Full-Length Mouse NLRP3 Structure Control Pathway Activation’. *Cell*, 184(26), pp. 6299-6312.e22. DOI: 10.1016/j.cell.2021.11.011

Angosto-Bazarra, D., Alarcón-Vila, C., *et al.* (2022) ‘Evolutionary Analyses of the Gasdermin Family Suggest Conserved Roles in Infection Response despite Loss of Pore-Forming Functionality’. *BMC Biology*, 20(1), p. 9. DOI: 10.1186/s12915-021-01220-z

Angosto-Bazarra, D., Molina-López, C. and Pelegrín, P. (2022) (1) ‘Physiological and Pathophysiological Functions of NLRP6: Pro- and Anti-Inflammatory Roles’. *Communications Biology*, 5(1), pp. 1–8. DOI: 10.1038/s42003-022-03491-w

Apoptosis: A Review of Programmed Cell Death - Susan Elmore, 2007. Available at: https://journals.sagepub.com/doi/10.1080/01926230701320337 (Accessed: 24 February 2023a)

Bauer, R. and Rauch, I. (2020) ‘The NAIP/NLRC4 Inflammasome in Infection and Pathology’. *Molecular Aspects of Medicine*, 76, p. 100863. DOI: 10.1016/j.mam.2020.100863

Bauernfeind, F.G. *et al.* (2009) ‘Cutting Edge: NF-KB Activating Pattern Recognition and Cytokine Receptors License NLRP3 Inflammasome Activation by Regulating NLRP3 Expression1’. *The Journal of Immunology*, 183(2), pp. 787–791. DOI: 10.4049/jimmunol.0901363

Beaudouin, J. *et al.* (2013) (4) ‘Caspase-8 Cleaves Its Substrates from the Plasma Membrane upon CD95-Induced Apoptosis’. *Cell Death & Differentiation*, 20(4), pp. 599–610. DOI: 10.1038/cdd.2012.156

Bebbere, D. *et al.* (2016) ‘The Subcortical Maternal Complex: Multiple Functions for One Biological Structure?’ *Journal of Assisted Reproduction and Genetics*, 33(11), pp. 1431–1438. DOI: 10.1007/s10815-016-0788-z

Bednash, J.S., Weathington, N., Londino, J., Rojas, M., Gulick, D.L., Fort, R., Han, S.H., *et al.* (2017) ‘Targeting the Deubiquitinase STAMBP Inhibits NALP7 Inflammasome Activity’. *Nature Communications*, 8. DOI: 10.1038/ncomms15203

Bednash, J.S., Weathington, N., Londino, J., Rojas, M., Gulick, D.L., Fort, R., Han, S., *et al.* (2017) (1) ‘Targeting the Deubiquitinase STAMBP Inhibits NALP7 Inflammasome Activity’. *Nature Communications*, 8(1), p. 15203. DOI: 10.1038/ncomms15203

Beghein, E. and Gettemans, J. (2017a) DOI: 10.3389/fimmu.2017.00771

Beghein, E. and Gettemans, J. (2017b) ‘Nanobody Technology: A Versatile Toolkit for Microscopic Imaging, Protein–Protein Interaction Analysis, and Protein Function Exploration’. *Frontiers in Immunology*, 8. DOI: 10.3389/fimmu.2017.00771

Bertheloot, D. *et al.* (2022) ‘Nanobodies Dismantle Post-Pyroptotic ASC Specks and Counteract Inflammation in Vivo’. *EMBO Molecular Medicine*, 14(6), p. e15415. DOI: 10.15252/emmm.202115415

Bertheloot, D., Latz, E. and Franklin, B.S. (2021) (5) ‘Necroptosis, Pyroptosis and Apoptosis: An Intricate Game of Cell Death’. *Cellular & Molecular Immunology*, 18(5), pp. 1106–1121. DOI: 10.1038/s41423-020-00630-3

Bertrand, M.J.M. and Vandenabeele, P. (2011) ‘The Ripoptosome: Death Decision in the Cytosol’. *Molecular Cell*, 43(3), pp. 323–325. DOI: 10.1016/j.molcel.2011.07.007

Bhella, D. (2019) ‘Cryo-Electron Microscopy: An Introduction to the Technique, and Considerations When Working to Establish a National Facility’. *Biophysical Reviews*, 11(4), pp. 515–519. DOI: 10.1007/s12551-019-00571-w

Bieniossek, C. *et al.* (2012) ‘MultiBac: Expanding the Research Toolbox for Multiprotein Complexes’. *Trends in Biochemical Sciences*, 37(2), pp. 49–57. DOI: 10.1016/j.tibs.2011.10.005

Bomprezzi, R. (2015) ‘Dimethyl Fumarate in the Treatment of Relapsing–Remitting Multiple Sclerosis: An Overview’. *Therapeutic Advances in Neurological Disorders*, 8(1), pp. 20–30. DOI: 10.1177/1756285614564152

Booshehri, L.M. and Hoffman, H.M. (2019) ‘CAPS and NLRP3’. *Journal of Clinical Immunology*, 39(3), pp. 277–286. DOI: 10.1007/s10875-019-00638-z

Braun, M.B. *et al.* (2016) ‘Peptides in Headlock--a Novel High-Affinity and Versatile Peptide-Binding Nanobody for Proteomics and Microscopy’. *Scientific Reports*, 6, p. 19211. DOI: 10.1038/srep19211

Brinkschulte, R. *et al.* (2022) (1) ‘ATP-Binding and Hydrolysis of Human NLRP3’. *Communications Biology*, 5(1), pp. 1–12. DOI: 10.1038/s42003-022-04120-2

Brown, G.D. (2006) (1) ‘Dectin-1: A Signalling Non-TLR Pattern-Recognition Receptor’. *Nature Reviews Immunology*, 6(1), pp. 33–43. DOI: 10.1038/nri1745

Brown, G.D., Willment, J.A. and Whitehead, L. (2018) (6) ‘C-Type Lectins in Immunity and Homeostasis’. *Nature Reviews Immunology*, 18(6), pp. 374–389. DOI: 10.1038/s41577-018-0004-8

Broz, P. *et al.* (2010) ‘Redundant Roles for Inflammasome Receptors NLRP3 and NLRC4 in Host Defense against Salmonella’. *Journal of Experimental Medicine*, 207(8), pp. 1745–1755. DOI: 10.1084/jem.20100257

Broz, P. and Dixit, V.M. (2016) (7) ‘Inflammasomes: Mechanism of Assembly, Regulation and Signalling’. *Nature Reviews Immunology*, 16(7), pp. 407–420. DOI: 10.1038/nri.2016.58

Broz, P., Pelegrín, P. and Shao, F. (2020) ‘The Gasdermins, a Protein Family Executing Cell Death and Inflammation’. *Nature Reviews Immunology*, 20(3), pp. 143–157. DOI: 10.1038/s41577-019-0228-2

Bruns, A.M. and Horvath, C.M. (2015) ‘LGP2 Synergy with MDA5 in RLR-Mediated RNA Recognition and Antiviral Signaling’. *Cytokine*, 74(2), pp. 198–206. DOI: 10.1016/j.cyto.2015.02.010

Bulek, K. *et al.* (2020) ‘Epithelial-Derived Gasdermin D Mediates Nonlytic IL-1β Release during Experimental Colitis’. *The Journal of Clinical Investigation*, 130(8), pp. 4218–4234. DOI: 10.1172/JCI138103

Chan, A.H. and Schroder, K. (2019) ‘Inflammasome Signaling and Regulation of Interleukin-1 Family Cytokines’. *Journal of Experimental Medicine*, 217(1), p. e20190314. DOI: 10.1084/jem.20190314

Chan, F.K.-M., Moriwaki, K. and De Rosa, M.J. (2013) 'Detection of Necrosis by Release of Lactate Dehydrogenase (LDH) Activity'. *Methods in Molecular Biology (Clifton, N.J.)*, 979, pp. 65–70. DOI: 10.1007/978-1-62703-290-2_7

Chang, B. *et al.* (2013) 'Developmental Expression and Possible Functional Roles of Mouse Nlrp4e in Preimplantation Embryos'. *In Vitro Cellular & Developmental Biology. Animal*, 49(7), pp. 548–553. DOI: 10.1007/s11626-013-9638-9

Chen, D. *et al.* (2006) 'Disulfiram, a Clinically Used Anti-Alcoholism Drug and Copper-Binding Agent, Induces Apoptotic Cell Death in Breast Cancer Cultures and Xenografts via Inhibition of the Proteasome Activity'. *Cancer Research*, 66(21), pp. 10425–10433. DOI: 10.1158/0008-5472.CAN-06-2126

Chen, J. and Chen, Z.J. (2018) 'PtdIns4P on Dispersed Trans-Golgi Network Mediates NLRP3 Inflammasome Activation'. *Nature*, 564(7734), pp. 71–76. DOI: 10.1038/s41586-018-0761-3

Chen, K.W. *et al.* (2019) 'Extrinsic and Intrinsic Apoptosis Activate Pannexin-1 to Drive NLRP3 Inflammasome Assembly'. *The EMBO Journal*, 38(10), p. e101638. DOI: 10.15252/embj.2019101638

Chen, L. *et al.* (2021) (11) 'NOD-like Receptors in Autoimmune Diseases'. *Acta Pharmacologica Sinica*, 42(11), pp. 1742–1756. DOI: 10.1038/s41401-020-00603-2

Chen, V.B. *et al.* (2010) 'MolProbity: All-Atom Structure Validation for Macromolecular Crystallography'. *Acta Crystallographica. Section D, Biological Crystallography*, 66(Pt 1), pp. 12–21. DOI: 10.1107/S0907444909042073

Chen, X. *et al.* (2016) (9) 'Pyroptosis Is Driven by Non-Selective Gasdermin-D Pore and Its Morphology Is Different from MLKL Channel-Mediated Necroptosis'. *Cell Research*, 26(9), pp. 1007–1020. DOI: 10.1038/cr.2016.100

Chen, X. *et al.* (2022) 'Vitamin D Receptor Enhances NLRC4 Inflammasome Activation by Promoting NAIPs–NLRC4 Association'. *EMBO Reports*, 23(9), p. e54611. DOI: 10.15252/embr.202254611

Chou, W.-C. *et al.* (2023) 'The NLR Gene Family: From Discovery to Present Day'. *Nature Reviews Immunology*, pp. 1–20. DOI: 10.1038/s41577-023-00849-x

Christgen, S. *et al.* (2020) 'Identification of the PANoptosome: A Molecular Platform Triggering Pyroptosis, Apoptosis, and Necroptosis (PANoptosis)'. *Frontiers in Cellular and Infection Microbiology*, 10. Available at: https://www.frontiersin.org/articles/10.3389/fcimb.2020.00237 (Accessed: 28 February 2023)

Chu, L.H. *et al.* (2015) ‘An Updated View on the Structure and Function of PYRIN Domains’. *Apoptosis : An International Journal on Programmed Cell Death*, 20(2), pp. 157–173. DOI: 10.1007/s10495-014-1065-1

Clark, R. and Kupper, T. (2005) ‘Old Meets New: The Interaction Between Innate and Adaptive Immunity’. *Journal of Investigative Dermatology*, 125(4), pp. 629–637. DOI: 10.1111/j.0022-202X.2005.23856.x

Cogswell, J.P. *et al.* (1994) ‘NF-Kappa B Regulates IL-1 Beta Transcription through a Consensus NF-Kappa B Binding Site and a Nonconsensus CRE-like Site’. *Journal of Immunology (Baltimore, Md.: 1950)*, 153(2), pp. 712–723.

Collado Camps, E. *et al.* (2021) (7) ‘CPPs to the Test: Effects on Binding, Uptake and Biodistribution of a Tumor Targeting Nanobody’. *Pharmaceuticals*, 14(7), p. 602. DOI: 10.3390/ph14070602

Collin, M. and Bigley, V. (2018) ‘Human Dendritic Cell Subsets: An Update’. *Immunology*, 154(1), pp. 3–20. DOI: 10.1111/imm.12888

Collin, R.W.J. *et al.* (2007) ‘Involvement of DFNB59 Mutations in Autosomal Recessive Nonsyndromic Hearing Impairment’. *Human Mutation*, 28(7), pp. 718–723. DOI: 10.1002/humu.20510

Compan, V. and López-Castejón, G. (2016) ‘Functional Reconstruction of NLRs in HEK293 Cells’. In *Methods in Molecular Biology*. Humana Press Inc., pp. 217–221. DOI: 10.1007/978-1-4939-3566-6_15

Cui, J. *et al.* (2012) ‘NLRP4 Negatively Regulates Type I Interferon Signaling by Targeting the Kinase TBK1 for Degradation via the Ubiquitin Ligase DTX4’. *Nature Immunology*, 13(4), pp. 387–395. DOI: 10.1038/ni.2239

D, Z., L, K. and E, E. (2021) ‘The NLRP6 Inflammasome’. *Immunology*, 162(3). DOI: 10.1111/imm.13293

Damiano, J.S. *et al.* (2004) ‘Heterotypic Interactions among NACHT Domains: Implications for Regulation of Innate Immune Responses’. *The Biochemical Journal*, 381(Pt 1), pp. 213–219. DOI: 10.1042/BJ20031506

David, K.K. *et al.* (2009) ‘Parthanatos, a Messenger of Death’. *Frontiers in Bioscience (Landmark Edition)*, 14, pp. 1116–1128.

De Genst, E. *et al.* (2006) ‘Molecular Basis for the Preferential Cleft Recognition by Dromedary Heavy-Chain Antibodies’. *Proceedings of the National Academy of Sciences*, 103(12), pp. 4586–4591. DOI: 10.1073/pnas.0505379103

De Groeve, K. *et al.* (2010) ‘Nanobodies as Tools for In Vivo Imaging of Specific Immune Cell Types’. *Journal of Nuclear Medicine*, 51(5), pp. 782–789. DOI: 10.2967/jnumed.109.070078

de Almeida, L. *et al.* (2015) ‘The PYRIN Domain-Only Protein POP1 Inhibits Inflammasome Assembly and Ameliorates Inflammatory Disease’. *Immunity*, 43(2), pp. 264–276. DOI: 10.1016/j.immuni.2015.07.018

Degterev, A. *et al.* (2005) (2) ‘Chemical Inhibitor of Nonapoptotic Cell Death with Therapeutic Potential for Ischemic Brain Injury’. *Nature Chemical Biology*, 1(2), pp. 112–119. DOI: 10.1038/nchembio711

Deng, W. *et al.* (2020) ‘Disulfiram Suppresses NLRP3 Inflammasome Activation to Treat Peritoneal and Gouty Inflammation’. *Free Radical Biology and Medicine*, 152, pp. 8–17. DOI: 10.1016/j.freeradbiomed.2020.03.007

Deng, W. *et al.* (2022) (7897) ‘Streptococcal Pyrogenic Exotoxin B Cleaves GSDMA and Triggers Pyroptosis’. *Nature*, 602(7897), pp. 496–502. DOI: 10.1038/s41586-021-04384-4

Dessau, M.A. and Modis, Y. (2011) ‘Protein Crystallization for X-Ray Crystallography’. *Journal of Visualized Experiments: JoVE*, (47), p. 2285. DOI: 10.3791/2285

Devant, P. *et al.* (2023) ‘Gasdermin D Pore-Forming Activity Is Redox-Sensitive’. *Cell Reports*, 42(1), p. 112008. DOI: 10.1016/j.celrep.2023.112008

Dinarello, C. *et al.* (2013) ‘Interleukin-18 and IL-18 Binding Protein’. *Frontiers in Immunology*, 4. Available at: https://www.frontiersin.org/articles/10.3389/fimmu.2013.00289 (Accessed: 1 March 2023)

Dinarello, C.A. (2009) ‘Immunological and Inflammatory Functions of the Interleukin-1 Family’. *Annual Review of Immunology*, 27(1), pp. 519–550. DOI: 10.1146/annurev.immunol.021908.132612

Dinarello, C.A. *et al.* (1998) ‘Overview of Interleukin-18: More than an Interferon-Gamma Inducing Factor’. *Journal of Leukocyte Biology*, 63(6), pp. 658–664.

Ding, J. *et al.* (2016) ‘Pore-Forming Activity and Structural Autoinhibition of the Gasdermin Family’. *Nature*, 535(7610), pp. 111–116. DOI: 10.1038/nature18590

Docherty, L.E. *et al.* (2015) ‘Mutations in NLRP5 Are Associated with Reproductive Wastage and Multilocus Imprinting Disorders in Humans’. *Nature Communications*, 6, p. 8086. DOI: 10.1038/ncomms9086

Domínguez-Ruiz, M. *et al.* (2022) ‘Novel Pathogenic Variants in PJVK, the Gene Encoding Pejvakin, in Subjects with Autosomal Recessive Non-Syndromic Hearing Impairment and Auditory Neuropathy Spectrum Disorder’. *Genes*, 13(1), p. 149. DOI: 10.3390/genes13010149

Dorfleutner, A. *et al.* (2007) ‘Cellular Pyrin Domain-Only Protein 2 Is a Candidate Regulator of Inflammasome Activation’. *Infection and Immunity*, 75(3), pp. 1484–1492. DOI: 10.1128/IAI.01315-06

Drouin, M., Saenz, J. and Chiffoleau, E. (2020) ‘C-Type Lectin-Like Receptors: Head or Tail in Cell Death Immunity’. *Frontiers in Immunology*, 11. Available at: https://www.frontiersin.org/articles/10.3389/fimmu.2020.00251 (Accessed: 22 February 2023)

Du, C. *et al.* (2000) ‘Smac, a Mitochondrial Protein That Promotes Cytochrome c-Dependent Caspase Activation by Eliminating IAP Inhibition’. *Cell*, 102(1), pp. 33–42. DOI: 10.1016/s0092-8674(00)00008-8

Duéñez-Guzmán, E.A. and Haig, D. (2014) DOI: 10.1007/s00239-014-9614-3

Duhoo, Y. *et al.* (2017) ‘Camelid Nanobodies Used as Crystallization Chaperones for Different Constructs of PorM, a Component of the Type IX Secretion System from *Porphyromonas Gingivalis*’. *Acta Crystallographica Section F Structural Biology Communications*, 73(5), pp. 286–293. DOI: 10.1107/S2053230X17005969

Ebner, S. *et al.* (2004) ‘Expression of C-Type Lectin Receptors by Subsets of Dendritic Cells in Human Skin’. *International Immunology*, 16(6), pp. 877–887. DOI: 10.1093/intimm/dxh088

Eden, T. *et al.* (2018) ‘A CDNA Immunization Strategy to Generate Nanobodies against Membrane Proteins in Native Conformation’. *Frontiers in Immunology*, 8. Available at: https://www.frontiersin.org/articles/10.3389/fimmu.2017.01989 (Accessed: 10 March 2023)

Eggermann, T. *et al.* (2022) ‘Trans-Acting Genetic Variants Causing Multilocus Imprinting Disturbance (MLID): Common Mechanisms and Consequences’. *Clinical Epigenetics*, 14(1), p. 41. DOI: 10.1186/s13148-022-01259-x

Ellwanger, K. *et al.* (2018) ‘The NLR Family Pyrin Domain-Containing 11 Protein Contributes to the Regulation of Inflammatory Signaling’. *The Journal of Biological Chemistry*, 293(8), pp. 2701–2710. DOI: 10.1074/jbc.RA117.000152

Emsley, P. and Cowtan, K. (2004) ‘Coot: Model-Building Tools for Molecular Graphics’. *Acta Crystallographica. Section D, Biological Crystallography*, 60(Pt 12 Pt 1), pp. 2126–2132. DOI: 10.1107/S0907444904019158

Endrizzi, M.G. *et al.* (2000) ‘Genomic Sequence Analysis of the Mouse Naip Gene Array’. *Genome Research*, 10(8), pp. 1095–1102. DOI: 10.1101/gr.10.8.1095

Enkhbayar, P. *et al.* (2004) ‘Structural principles of leucine-rich repeat (LRR) proteins’. *Proteins: Structure, Function, and Bioinformatics*, 54(3), pp. 394–403. DOI: 10.1002/prot.10605

Equils, O. *et al.* (2020) ‘The Role of the IL-1 System in Pregnancy and the Use of IL-1 System Markers to Identify Women at Risk for Pregnancy Complications†’. *Biology of Reproduction*, 103(4), pp. 684–694. DOI: 10.1093/biolre/ioaa102

Estey, T. *et al.* (2009) ‘Evaluation of Chemical Degradation of a Trivalent Recombinant Protein Vaccine Against Botulinum Neurotoxin by LysC Peptide Mapping and MALDI-TOF Mass Spectrometry’. *Journal of Pharmaceutical Sciences*, 98(9), pp. 2994–3012. DOI: 10.1002/jps.21543

European Medicines Agency. (2018) ‘Assessment Report Cablivi - EMEA/H/C/004426/0000’. Available at: https://www.ema.europa.eu/en/documents/assessment-report/cablivi-epar-public-assessment-report_en.pdf (Accessed: 5 April 2023)

Evavold, C.L. *et al.* (2021) ‘Control of Gasdermin D Oligomerization and Pyroptosis by the Ragulator-Rag-MTORC1 Pathway’. *Cell*, 184(17), pp. 4495-4511.e19. DOI: 10.1016/j.cell.2021.06.028

Evavold, C.L. *et al.* (2018) ‘The Pore-Forming Protein Gasdermin D Regulates Interleukin-1 Secretion from Living Macrophages’. *Immunity*, 48(1), pp. 35-44.e6. DOI: 10.1016/j.immuni.2017.11.013

Fan, X. *et al.* (2019) (1) ‘Single Particle Cryo-EM Reconstruction of 52 KDa Streptavidin at 3.2 Angstrom Resolution’. *Nature Communications*, 10(1), p. 2386. DOI: 10.1038/s41467-019-10368-w

Feng, S., Fox, D. and Man, S.M. (2018) ‘Mechanisms of Gasdermin Family Members in Inflammasome Signaling and Cell Death’. *Journal of Molecular Biology*, 430(18, Part B), pp. 3068–3080. DOI: 10.1016/j.jmb.2018.07.002

Fields, J.K., Günther, S. and Sundberg, E.J. (2019) ‘Structural Basis of IL-1 Family Cytokine Signaling’. *Frontiers in Immunology*, 10. Available at: https://www.frontiersin.org/articles/10.3389/fimmu.2019.01412 (Accessed: 1 March 2023)

Fink, S.L. and Cookson, B.T. (2006) ‘Caspase-1-Dependent Pore Formation during Pyroptosis Leads to Osmotic Lysis of Infected Host Macrophages’. *Cellular Microbiology*, 8(11), pp. 1812–1825. DOI: 10.1111/j.1462-5822.2006.00751.x

Flp-In System: For Generating Constitutive Expression Cell Lines - DE. Available at: https://www.thermofisher.com/de/de/home/references/protocols/proteins-expression-isolation-and-analysis/protein-expression-protocol/flp-in-system-for-generating-constitutive-expression-cell-lines.html (Accessed: 24 January 2023b)

Fogarty, C.E. and Bergmann, A. (2015) ‘The Sound of Silence: Signaling by Apoptotic Cells’. *Current Topics in Developmental Biology*, 114, pp. 241–265. DOI: 10.1016/bs.ctdb.2015.07.013

Fore, F. *et al.* (2020) ‘TLR10 and Its Unique Anti-Inflammatory Properties and Potential Use as a Target in Therapeutics’. *Immune Network*, 20(3), p. e21. DOI: 10.4110/in.2020.20.e21

Franchi, L. *et al.* (2006) ‘Cytosolic Flagellin Requires Ipaf for Activation of Caspase-1 and Interleukin 1beta in Salmonella-Infected Macrophages’. *Nature Immunology*, 7(6), pp. 576–582. DOI: 10.1038/ni1346

Frank, D. and Vince, J.E. (2019) (1) ‘Pyroptosis versus Necroptosis: Similarities, Differences, and Crosstalk’. *Cell Death & Differentiation*, 26(1), pp. 99–114. DOI: 10.1038/s41418-018-0212-6

Friker, L.L. *et al.* (2020) ‘β-Amyloid Clustering around ASC Fibrils Boosts Its Toxicity in Microglia’. *Cell Reports*, 30(11), pp. 3743-3754.e6. DOI: 10.1016/j.celrep.2020.02.025

Gadjeva, M. (2014) ‘Overview’. In Gadjeva, M. (ed.) *The Complement System: Methods and Protocols*. Methods in Molecular Biology. Totowa, NJ: Humana Press, pp. 1–9. DOI: 10.1007/978-1-62703-724-2_1

Gangopadhyay, A. *et al.* (2022) ‘NLRP3 Licenses NLRP11 for Inflammasome Activation in Human Macrophages’. *Nature Immunology*, 23(6), pp. 892–903. DOI: 10.1038/s41590-022-01220-3

Gao, H. *et al.* (2021) ‘Dysregulated Microbiota-Driven Gasdermin D Activation Promotes Colitis Development by Mediating IL-18 Release’. *Frontiers in Immunology*, 12, p. 4318. DOI: 10.3389/fimmu.2021.750841

Gao, W. *et al.* (2016) ‘Site-Specific Phosphorylation and Microtubule Dynamics Control Pyrin Inflammasome Activation’. *Proceedings of the National Academy of Sciences*, 113(33), pp. E4857–E4866. DOI: 10.1073/pnas.1601700113

van de Garde, M.D.B. *et al.* (2019) ‘Prediction and Validation of Immunogenic Domains of Pneumococcal Proteins Recognized by Human CD4+ T Cells’. *Infection and Immunity*, 87(6), pp. e00098-19. DOI: 10.1128/IAI.00098-19

Gaston, J. *et al.* (2019) (1) ‘Intracellular Delivery of Therapeutic Antibodies into Specific Cells Using Antibody-Peptide Fusions’. *Scientific Reports*, 9(1), p. 18688. DOI: 10.1038/s41598-019-55091-0

Gawas, U.B., Mandrekar, V.K. and Majik, M.S. (2019) ‘Chapter 5 - Structural Analysis of Proteins Using X-Ray Diffraction Technique’. In Meena, S.N. and Naik, M.M. (eds.) *Advances in Biological Science Research*. Academic Press, pp. 69–84. DOI: 10.1016/B978-0-12-817497-5.00005-7

Girardin, S.E. *et al.* (2003) ‘Nod2 Is a General Sensor of Peptidoglycan through Muramyl Dipeptide (MDP) Detection*’. *Journal of Biological Chemistry*, 278(11), pp. 8869–8872. DOI: 10.1074/jbc.C200651200

Grandemange, S. *et al.* (2017) ‘A New Autoinflammatory and Autoimmune Syndrome Associated with NLRP1 Mutations: NAIAD (NLRP1-Associated Autoinflammation with Arthritis and Dyskeratosis)’. *Annals of the Rheumatic Diseases*, 76(7), pp. 1191–1198. DOI: 10.1136/annrheumdis-2016-210021

Granot, I., Gnainsky, Y. and Dekel, N. (2012) ‘Endometrial Inflammation and Effect on Implantation Improvement and Pregnancy Outcome’. *Reproduction*, 144(6), pp. 661–668. DOI: 10.1530/REP-12-0217

Greenfield, E.A. (2021) ‘CDNA Immunization of Mice, Rats, and Hamsters’. *Cold Spring Harbor Protocols*, 2021(5). DOI: 10.1101/pdb.prot100354

Grenier, J.M. *et al.* (2002) ‘Functional Screening of Five PYPAF Family Members Identifies PYPAF5 as a Novel Regulator of NF-KB and Caspase-1’. *FEBS Letters*, 530(1–3), pp. 73–78. DOI: 10.1016/S0014-5793(02)03416-6

Gu, Y. *et al.* (1997) ‘Activation of Interferon-γ Inducing Factor Mediated by Interleukin-1β Converting Enzyme’. *Science*, 275(5297), pp. 206–209. DOI: 10.1126/science.275.5297.206

Guasconi, L. *et al.* (2011) ‘C-Type Lectins on Macrophages Participate in the Immunomodulatory Response to Fasciola Hepatica Products’. *Immunology*, 133(3), pp. 386–396. DOI: 10.1111/j.1365-2567.2011.03449.x

Guimarães-Costa, A.B. *et al.* (2012) ‘ETosis: A Microbicidal Mechanism beyond Cell Death’. *Journal of Parasitology Research*, 2012, p. 929743. DOI: 10.1155/2012/929743

Gullett, J.M., Tweedell, R.E. and Kanneganti, T.-D. (2022) (9) ‘It’s All in the PAN: Crosstalk, Plasticity, Redundancies, Switches, and Interconnectedness Encompassed by PANoptosis Underlying the Totality of Cell Death-Associated Biological Effects’. *Cells*, 11(9), p. 1495. DOI: 10.3390/cells11091495

Gunning, P.W. and Hardeman, E.C. (2018) ‘Fundamental Differences’. *ELife*, 7, p. e34477. DOI: 10.7554/eLife.34477

Hamers-Casterman, C. *et al.* (1993) ‘Naturally Occurring Antibodies Devoid of Light Chains’. *Nature*, 363(6428), pp. 446–448. DOI: 10.1038/363446a0

Hansen, J.M. *et al.* (2021) ‘Pathogenic Ubiquitination of GSDMB Inhibits NK Cell Bactericidal Functions’. *Cell*, 184(12), pp. 3178-3191.e18. DOI: 10.1016/j.cell.2021.04.036

Hart, S.P., Dransfield, I. and Rossi, A.G. (2008) ‘Phagocytosis of Apoptotic Cells’. *Methods (San Diego, Calif.)*, 44(3), pp. 280–285. DOI: 10.1016/j.ymeth.2007.11.009

Haubrich, J. *et al.* (2021) ‘A Nanobody Activating Metabotropic Glutamate Receptor 4 Discriminates between Homo- and Heterodimers’. *Proceedings of the*

National Academy of Sciences of the United States of America, 118(33), p. e2105848118. DOI: 10.1073/pnas.2105848118

He, S. *et al.* (2009) 'Receptor Interacting Protein Kinase-3 Determines Cellular Necrotic Response to TNF-α'. *Cell*, 137(6), pp. 1100–1111. DOI: 10.1016/j.cell.2009.05.021

He, W. *et al.* (2015) 'Gasdermin D Is an Executor of Pyroptosis and Required for Interleukin-1β Secretion'. *Cell Research*, 25(12), pp. 1285–1298. DOI: 10.1038/cr.2015.139

He, Y. *et al.* (2016) (7590) 'NEK7 Is an Essential Mediator of NLRP3 Activation Downstream of Potassium Efflux'. *Nature*, 530(7590), pp. 354–357. DOI: 10.1038/nature16959

Heilig, R. *et al.* (2018) 'The Gasdermin-D Pore Acts as a Conduit for IL-1β Secretion in Mice'. *European Journal of Immunology*, 48(4), pp. 584–592. DOI: 10.1002/eji.201747404

Herce, H.D. *et al.* (2017) (8) 'Cell-Permeable Nanobodies for Targeted Immunolabelling and Antigen Manipulation in Living Cells'. *Nature Chemistry*, 9(8), pp. 762–771. DOI: 10.1038/nchem.2811

Herce, H.D. *et al.* (2013) 'Visualization and Targeted Disruption of Protein Interactions in Living Cells'. *Nature Communications*, 4(1), pp. 1–8. DOI: 10.1038/ncomms3660

Hochheiser, I.V., Behrmann, H., *et al.* (2022) 'Directionality of PYD Filament Growth Determined by the Transition of NLRP3 Nucleation Seeds to ASC Elongation'. *Science Advances*, 8(19), p. eabn7583. DOI: 10.1126/sciadv.abn7583

Hochheiser, I.V., Pilsl, M., *et al.* (2022) (7904) 'Structure of the NLRP3 Decamer Bound to the Cytokine Release Inhibitor CRID3'. *Nature*, 604(7904), pp. 184–189. DOI: 10.1038/s41586-022-04467-w

Hou, Y.N. *et al.* (2022) (1) 'A Conformation-Specific Nanobody Targeting the Nicotinamide Mononucleotide-Activated State of SARM1'. *Nature Communications*, 13(1), p. 7898. DOI: 10.1038/s41467-022-35581-y

Hsu, H., Xiong, J. and Goeddel, D.V. (1995) 'The TNF Receptor 1-Associated Protein TRADD Signals Cell Death and NF-KB Activation'. *Cell*, 81(4), pp. 495–504. DOI: 10.1016/0092-8674(95)90070-5

Hu, J.J. *et al.* (2020) (7) 'FDA-Approved Disulfiram Inhibits Pyroptosis by Blocking Gasdermin D Pore Formation'. *Nature Immunology*, 21(7), pp. 736–745. DOI: 10.1038/s41590-020-0669-6

Hu, Z. *et al.* (2013) ‘Crystal Structure of NLRC4 Reveals Its Autoinhibition Mechanism’. *Science*, 341(6142), pp. 172–175. DOI: 10.1126/science.1236381

Huang, D.C.S. *et al.* (1999) ‘Activation of Fas by FasL Induces Apoptosis by a Mechanism That Cannot Be Blocked by Bcl-2 or Bcl-XL’. *Proceedings of the National Academy of Sciences*, 96(26), pp. 14871–14876. DOI: 10.1073/pnas.96.26.14871

Huang, J.-Y. *et al.* (2013) ‘A Genetic Association Study of NLRP2 and NLRP7 Genes in Idiopathic Recurrent Miscarriage’. *Human Reproduction*, 28(4), pp. 1127–1134. DOI: 10.1093/humrep/det001

Huang, J.-Y. *et al.* (2017) ‘NLRP7 Contributes to in Vitro Decidualization of Endometrial Stromal Cells’. *Reproductive Biology and Endocrinology*, 15(1), p. 66. DOI: 10.1186/s12958-017-0286-x

Huang, L. *et al.* (2022) ‘Novel Mutations in NLRP5 and PATL2 Cause Female Infertility Characterized by Primarily Oocyte Maturation Abnormality and Consequent Early Embryonic Arrest’. *Journal of Assisted Reproduction and Genetics*, 39(3), pp. 711–718. DOI: 10.1007/s10815-022-02412-4

Huang, L.S. *et al.* (2020) ‘MtDNA Activates CGAS Signaling and Suppresses the YAP-Mediated Endothelial Cell Proliferation Program to Promote Inflammatory Injury’. *Immunity*, 52(3), pp. 475-486.e5. DOI: 10.1016/j.immuni.2020.02.002

Humphries, F. *et al.* (2020) ‘Succination Inactivates Gasdermin D and Blocks Pyroptosis’. *Science (New York, N.Y.)*, 369(6511), pp. 1633–1637. DOI: 10.1126/science.abb9818

Ibrahim, A.F.M. *et al.* (2020) ‘Antibody RING-Mediated Destruction of Endogenous Proteins’. *Molecular Cell*, 79(1), pp. 155-166.e9. DOI: 10.1016/j.molcel.2020.04.032

Indramohan, M., Stehlik, C. and Dorfleutner, A. (2018) ‘COPs and POPs Patrol Inflammasome Activation’. *Journal of Molecular Biology*, 430(2), pp. 153–173. DOI: 10.1016/j.jmb.2017.10.004

Infevers - Tabular List. Available at: https://infevers.umai-montpellier.fr/web/search.php (Accessed: 27 February 2023c)

Ingram, J.R., Schmidt, F.I. and Ploegh, H.L. (2018a) ‘Exploiting Nanobodies’ Singular Traits’. *Annual Review of Immunology*, 36(1), pp. 695–715. DOI: 10.1146/annurev-immunol-042617-053327

Ingram, J.R., Schmidt, F.I. and Ploegh, H.L. (2018b) ‘Exploiting Nanobodies’ Singular Traits’. *Annual Review of Immunology*, 36(1). DOI: 10.1146/annurev-immunol-042617-053327

Inohara, N. *et al.* (2001) ‘Human Nod1 Confers Responsiveness to Bacterial Lipopolysaccharides’. *The Journal of Biological Chemistry*, 276(4), pp. 2551–2554. DOI: 10.1074/jbc.M009728200

Invitrogen. ‘Gateway Technology - User Guide’.

Ishiwatari-Ogata, C. *et al.* (2022) ‘Ozoralizumab, a Humanized Anti-TNFα NANOBODY® Compound, Exhibits Efficacy Not Only at the Onset of Arthritis in a Human TNF Transgenic Mouse but Also During Secondary Failure of Administration of an Anti-TNFα IgG’. *Frontiers in Immunology*, 13. Available at: https://www.frontiersin.org/articles/10.3389/fimmu.2022.853008 (Accessed: 14 March 2023)

Jabbour, H.N. *et al.* (2009) ‘Inflammatory Pathways in Female Reproductive Health and Disease’. *Reproduction*, 138(6), pp. 903–919. DOI: 10.1530/REP-09-0247

Jenster, L.-M. *et al.* (2023) ‘P38 Kinases Mediate NLRP1 Inflammasome Activation after Ribotoxic Stress Response and Virus Infection’. *The Journal of Experimental Medicine*, 220(1), p. e20220837. DOI: 10.1084/jem.20220837

Jiang, K. *et al.* (2022) ‘Gasdermin D Inhibition Confers Antineutrophil-Mediated Cardioprotection in Acute Myocardial Infarction’. *The Journal of Clinical Investigation*, 132(1). DOI: 10.1172/JCI151268

Jimenez, A.J. *et al.* (2014) ‘ESCRT Machinery Is Required for Plasma Membrane Repair’. *Science*, 343(6174), p. 1247136. DOI: 10.1126/science.1247136

Jin, M.S. *et al.* (2007) ‘Crystal Structure of the TLR1-TLR2 Heterodimer Induced by Binding of a Tri-Acylated Lipopeptide’. *Cell*, 130(6), pp. 1071–1082. DOI: 10.1016/j.cell.2007.09.008

Kabsch, W. (2010) ‘XDS’. *Acta Crystallographica Section D: Biological Crystallography*, 66(2), pp. 125–132. DOI: 10.1107/S0907444909047337

Kalogiannidis, I. *et al.* (2018) DOI: 10.1007/s10815-018-1202-9

Kaneko, N. *et al.* (2019) ‘The Role of Interleukin-1 in General Pathology’. *Inflammation and Regeneration*, 39(1), p. 12. DOI: 10.1186/s41232-019-0101-5

Kang, J.Y. *et al.* (2009) ‘Recognition of Lipopeptide Patterns by Toll-like Receptor 2-Toll-like Receptor 6 Heterodimer’. *Immunity*, 31(6), pp. 873–884. DOI: 10.1016/j.immuni.2009.09.018

Kanzaki, S. *et al.* (2020) ‘Involvement of Nlrp9a/b/c in Mouse Preimplantation Development’. *Reproduction (Cambridge, England)*, 160(2), pp. 181–191. DOI: 10.1530/REP-19-0516

Karki, R. *et al.* (2016) 'NLRC3 Is an Inhibitory Sensor of PI3K-MTOR Pathways in Cancer'. *Nature*, 540(7634), pp. 583–587. DOI: 10.1038/nature20597

Kato, H. *et al.* (2006) 'Differential Roles of MDA5 and RIG-I Helicases in the Recognition of RNA Viruses'. *Nature*, 441(7089), pp. 101–105. DOI: 10.1038/nature04734

Kaur, D. *et al.* (2019) 'PRRDB 2.0: A Comprehensive Database of Pattern-Recognition Receptors and Their Ligands'. *Database*, 2019, p. baz076. DOI: 10.1093/database/baz076

Kawai, T. *et al.* (2005) (10) 'IPS-1, an Adaptor Triggering RIG-I- and Mda5-Mediated Type I Interferon Induction'. *Nature Immunology*, 6(10), pp. 981–988. DOI: 10.1038/ni1243

Kawai, T. and Akira, S. (2007) 'Signaling to NF-KB by Toll-like Receptors'. *Trends in Molecular Medicine*, 13(11), pp. 460–469. DOI: 10.1016/j.molmed.2007.09.002

Kawasaki, T. and Kawai, T. (2014) 'Toll-Like Receptor Signaling Pathways'. *Frontiers in Immunology*, 5. Available at: https://www.frontiersin.org/articles/10.3389/fimmu.2014.00461 (Accessed: 17 February 2023)

Kayagaki, N. *et al.* (2015) 'Caspase-11 Cleaves Gasdermin D for Non-Canonical Inflammasome Signalling'. *Nature*, 526(7575), pp. 666–671. DOI: 10.1038/nature15541

Kayagaki, N. *et al.* (2021) (7848) 'NINJ1 Mediates Plasma Membrane Rupture during Lytic Cell Death'. *Nature*, 591(7848), pp. 131–136. DOI: 10.1038/s41586-021-03218-7

Kayagaki, N. *et al.* (2011) (7371) 'Non-Canonical Inflammasome Activation Targets Caspase-11'. *Nature*, 479(7371), pp. 117–121. DOI: 10.1038/nature10558

Keam, S.J. (2023) 'Ozoralizumab: First Approval'. *Drugs*, 83(1), pp. 87–92. DOI: 10.1007/s40265-022-01821-0

Kell, A.M. and Gale, M. (2015) 'RIG-I in RNA Virus Recognition'. *Virology*, 479–480, pp. 110–121. DOI: 10.1016/j.virol.2015.02.017

Kelly, B. and O'Neill, L.A. (2015) (7) 'Metabolic Reprogramming in Macrophages and Dendritic Cells in Innate Immunity'. *Cell Research*, 25(7), pp. 771–784. DOI: 10.1038/cr.2015.68

Kerr, J.F.R., Wyllie, A.H. and Currie, A.R. (1972) (4) 'Apoptosis: A Basic Biological Phenomenon with Wideranging Implications in Tissue Kinetics'. *British Journal of Cancer*, 26(4), pp. 239–257. DOI: 10.1038/bjc.1972.33

Khalid, N. and Azimpouran, M. (2022) *Necrosis*. StatPearls Publishing Available at: https://www.ncbi.nlm.nih.gov/books/NBK557627/ (Accessed: 24 February 2023)

Khan, S. *et al.* (2007) 'Antifungal Potential of Disulfiram'. *Nihon Ishinkin Gakkai Zasshi = Japanese Journal of Medical Mycology*, 48(3), pp. 109–113. DOI: 10.3314/jjmm.48.109

Khare, S. *et al.* (2012) 'An NLRP7-Containing Inflammasome Mediates Recognition of Microbial Lipopeptides in Human Macrophages'. *Immunity*, 36(3), pp. 464–476. DOI: 10.1016/j.immuni.2012.02.001

Khare, S. *et al.* (2014) (4) 'The PYRIN Domain–Only Protein POP3 Inhibits ALR Inflammasomes and Regulates Responses to Infection with DNA Viruses'. *Nature Immunology*, 15(4), pp. 343–353. DOI: 10.1038/ni.2829

Kile, R.L. and Rusk, H.A. (1940) 'A CASE OF COLD URTICARIA WITH AN UNUSUAL FAMILY HISTORY'. *Journal of the American Medical Association*, 114(12), pp. 1067–1068. DOI: 10.1001/jama.1940.62810120003010b

Kingeter, L.M. and Lin, X. (2012) (2) 'C-Type Lectin Receptor-Induced NF-KB Activation in Innate Immune and Inflammatory Responses'. *Cellular & Molecular Immunology*, 9(2), pp. 105–112. DOI: 10.1038/cmi.2011.58

Kinoshita, T. *et al.* (2005) 'PYPAF3, a PYRIN-Containing APAF-1-like Protein, Is a Feedback Regulator of Caspase-1-Dependent Interleukin-1β Secretion'. *Journal of Biological Chemistry*, 280(23), pp. 21720–21725. DOI: 10.1074/jbc.M410057200

Kobayashi, K.S. and van den Elsen, P.J. (2012) (12) 'NLRC5: A Key Regulator of MHC Class I-Dependent Immune Responses'. *Nature Reviews Immunology*, 12(12), pp. 813–820. DOI: 10.1038/nri3339

Koenig, P.-A. *et al.* (2021) 'Structure-Guided Multivalent Nanobodies Block SARS-CoV-2 Infection and Suppress Mutational Escape'. *Science*, 371(6530), p. eabe6230. DOI: 10.1126/science.abe6230

Kofoed, E.M. and Vance, R.E. (2011) (7366) 'Innate Immune Recognition of Bacterial Ligands by NAIPs Determines Inflammasome Specificity'. *Nature*, 477(7366), pp. 592–595. DOI: 10.1038/nature10394

Konermann, L., Pan, J. and Liu, Y.-H. (2011) 'Hydrogen Exchange Mass Spectrometry for Studying Protein Structure and Dynamics'. *Chemical Society Reviews*, 40(3), pp. 1224–1234. DOI: 10.1039/c0cs00113a

Kostura, M.J. *et al.* (1989) 'Identification of a Monocyte Specific Pre-Interleukin 1 Beta Convertase Activity.' *Proceedings of the National Academy of Sciences*, 86(14), pp. 5227–5231. DOI: 10.1073/pnas.86.14.5227

Kothakota, S. *et al.* (1997) ‘Caspase-3-Generated Fragment of Gelsolin: Effector of Morphological Change in Apoptosis’. *Science*, 278(5336), pp. 294–298. DOI: 10.1126/science.278.5336.294

Kou, Y.C. *et al.* (2008) ‘A Recurrent Intragenic Genomic Duplication, Other Novel Mutations in NLRP7 and Imprinting Defects in Recurrent Biparental Hydatidiform Moles’. *Molecular Human Reproduction*, 14(1), pp. 33–40. DOI: 10.1093/molehr/gam079

Kuchmiy, A.A. *et al.* (2016) ‘NLRP2 Controls Age-Associated Maternal Fertility’. *Journal of Experimental Medicine*, 213(13), pp. 2851–2860. DOI: 10.1084/jem.20160900

Lavergne, M. *et al.* (2020) ‘Human Amnion Epithelial Cells (AECs) Respond to the FSL-1 Lipopeptide by Engaging the NLRP7 Inflammasome’. *Frontiers in Immunology*, 11. Available at: https://www.frontiersin.org/articles/10.3389/fimmu.2020.01645 (Accessed: 15 March 2023)

Lee, H.T. *et al.* (2021) ‘High-Resolution Structure of the VWF A1 Domain in Complex with Caplacizumab, the First Nanobody-Based Medicine for Treating Acquired TTP’. *Biochemical and Biophysical Research Communications*, 567, pp. 49–55. DOI: 10.1016/j.bbrc.2021.06.030

León Machado, J.A. and Steimle, V. (2021) (3) ‘The MHC Class II Transactivator CIITA: Not (Quite) the Odd-One-Out Anymore among NLR Proteins’. *International Journal of Molecular Sciences*, 22(3), p. 1074. DOI: 10.3390/ijms22031074

Li, D. and Wu, M. (2021) (1) ‘Pattern Recognition Receptors in Health and Diseases’. *Signal Transduction and Targeted Therapy*, 6(1), pp. 1–24. DOI: 10.1038/s41392-021-00687-0

Li, J. *et al.* (2020) (2) ‘Ferroptosis: Past, Present and Future’. *Cell Death & Disease*, 11(2), pp. 1–13. DOI: 10.1038/s41419-020-2298-2

Li, M. *et al.* (2021) ‘A New NLRP5 Mutation Causes Female Infertility and Total Fertilization Failure’. *Gynecological Endocrinology: The Official Journal of the International Society of Gynecological Endocrinology*, 37(3), pp. 283–284. DOI: 10.1080/09513590.2020.1832069

Li, Y. *et al.* (2018) ‘Cryo-EM Structures of ASC and NLRC4 CARD Filaments Reveal a Unified Mechanism of Nucleation and Activation of Caspase-1’. *Proceedings of the National Academy of Sciences*, 115(43), pp. 10845–10852. DOI: 10.1073/pnas.1810524115

Liao, D. *et al.* (2014) ‘Necrosulfonamide Inhibits Necroptosis by Selectively Targeting the Mixed Lineage Kinase Domain-like Protein’. *MedChemComm*, 5(3), pp. 333–337. DOI: 10.1039/C3MD00278K

Lightfield, K.L. *et al.* (2008) ‘Critical Function for Naip5 in Inflammasome Activation by a Conserved Carboxy-Terminal Domain of Flagellin’. *Nature Immunology*, 9(10), pp. 1171–1178. DOI: 10.1038/ni.1646

Lin, A. and Loré, K. (2017) ‘Granulocytes: New Members of the Antigen-Presenting Cell Family’. *Frontiers in Immunology*, 8. Available at: https://www.frontiersin.org/articles/10.3389/fimmu.2017.01781 (Accessed: 22 February 2023)

Lin, M. *et al.* (2016) ‘USP38 Inhibits Type I Interferon Signaling by Editing TBK1 Ubiquitination through NLRP4 Signalosome’. *Molecular Cell*, 64(2), pp. 267–281. DOI: 10.1016/j.molcel.2016.08.029

van der Linden, R. *et al.* (2000) ‘Induction of Immune Responses and Molecular Cloning of the Heavy Chain Antibody Repertoire of Lama Glama’. *Journal of Immunological Methods*, 240(1–2), pp. 185–195. DOI: 10.1016/s0022-1759(00)00188-5

Liston, A. and Masters, S.L. (2017) (3) ‘Homeostasis-Altering Molecular Processes as Mechanisms of Inflammasome Activation’. *Nature Reviews Immunology*, 17(3), pp. 208–214. DOI: 10.1038/nri.2016.151

Liu, F. *et al.* (2023) ‘Neutrophil-Specific Depletion of Gasdermin D Does Not Protect against Murine Sepsis’. *Blood*, 141(5), pp. 550–554. DOI: 10.1182/blood.2022016931

Liu, M. *et al.* (2022) ‘The Regulatory Role of NLRX1 in Innate Immunity and Human Disease’. *Cytokine*, 160, p. 156055. DOI: 10.1016/j.cyto.2022.156055

Liu, T. *et al.* (2017) (1) ‘NF-KB Signaling in Inflammation’. *Signal Transduction and Targeted Therapy*, 2(1), pp. 1–9. DOI: 10.1038/sigtrans.2017.23

Liu, X. *et al.* (2021) ‘Channelling Inflammation: Gasdermins in Physiology and Disease’. *Nature Reviews Drug Discovery*, 20(5), pp. 384–405. DOI: 10.1038/s41573-021-00154-z

Liu, X. *et al.* (2016) (7610) ‘Inflammasome-Activated Gasdermin D Causes Pyroptosis by Forming Membrane Pores’. *Nature*, 535(7610), pp. 153–158. DOI: 10.1038/nature18629

Liu, Z. *et al.* (2020) ‘Caspase-1 Engages Full-Length Gasdermin D through Two Distinct Interfaces That Mediate Caspase Recruitment and Substrate Cleavage’. *Immunity*, 53(1), pp. 106-114.e5. DOI: 10.1016/j.immuni.2020.06.007

Liu, Z. *et al.* (2019) ‘Crystal Structures of the Full-Length Murine and Human Gasdermin D Reveal Mechanisms of Autoinhibition, Lipid Binding, and Oligomerization’. *Immunity*, 51(1), pp. 43-49.e4. DOI: 10.1016/j.immuni.2019.04.017

Löb, S. *et al.* (2021) 'Interleukin-1 Beta Is Significantly Upregulated in the Decidua of Spontaneous and Recurrent Miscarriage Placentas'. *Journal of Reproductive Immunology*, 144, p. 103283. DOI: 10.1016/j.jri.2021.103283

Loiarro, M., Ruggiero, V. and Sette, C. (2010) 'Targeting TLR/IL-1R Signalling in Human Diseases'. *Mediators of Inflammation*, 2010, pp. 1–12. DOI: 10.1155/2010/674363

van Loo, G. *et al.* (2002) 'The Serine Protease Omi/HtrA2 Is Released from Mitochondria during Apoptosis. Omi Interacts with Caspase-Inhibitor XIAP and Induces Enhanced Caspase Activity'. *Cell Death and Differentiation*, 9(1), pp. 20–26. DOI: 10.1038/sj.cdd.4400970

Loo, Y.-M. *et al.* (2008) 'Distinct RIG-I and MDA5 Signaling by RNA Viruses in Innate Immunity'. *Journal of Virology*, 82(1), pp. 335–345. DOI: 10.1128/JVI.01080-07

LOREY, S.L., HUANG, Y.C. and SHARMA, V. (2004) 'Constitutive Expression of Interleukin-18 and Interleukin-18 Receptor MRNA in Tumour Derived Human B-Cell Lines'. *Clinical and Experimental Immunology*, 136(3), pp. 456–462. DOI: 10.1111/j.1365-2249.2004.02465.x

Löw, C. *et al.* (2013) 'Nanobody Mediated Crystallization of an Archeal Mechanosensitive Channel'. *PLoS ONE*, 8(10), p. e77984. DOI: 10.1371/journal.pone.0077984

Lu, A. *et al.* (2015) (1) 'Plasticity in PYD Assembly Revealed by Cryo-EM Structure of the PYD Filament of AIM2'. *Cell Discovery*, 1(1), pp. 1–14. DOI: 10.1038/celldisc.2015.13

Luft, J.R. *et al.* (2003) 'A Deliberate Approach to Screening for Initial Crystallization Conditions of Biological Macromolecules'. *Journal of Structural Biology*, 142(1), pp. 170–179. DOI: 10.1016/S1047-8477(03)00048-0

Ma, C. *et al.* (2020) 'Gasdermin D in Macrophages Restrains Colitis by Controlling CGAS-Mediated Inflammation'. *Science Advances*, 6(21), p. eaaz6717. DOI: 10.1126/sciadv.aaz6717

MacDonald, J.A. *et al.* (2013) 'Biochemical and Structural Aspects of the ATP-Binding Domain in Inflammasome-Forming Human NLRP Proteins'. *IUBMB Life*, 65(10), pp. 851–862. DOI: 10.1002/iub.1210

Machtens, D.A. *et al.* (2022) 'The Inflammasome Activity of NLRP3 Is Independent of NEK7 in HEK293 Cells Co-Expressing ASC'. *International Journal of Molecular Sciences*, 23(18), p. 10269. DOI: 10.3390/ijms231810269

Magnotti, F. *et al.* (2019) 'Pyrin Dephosphorylation Is Sufficient to Trigger Inflammasome Activation in Familial Mediterranean Fever Patients'. *EMBO Molecular Medicine*, 11(11), p. e10547. DOI: 10.15252/emmm.201910547

Magupalli, V.G. *et al.* (2020) 'HDAC6 Mediates an Aggresome-like Mechanism for NLRP3 and Pyrin Inflammasome Activation'. *Science (New York, N.Y.)*, 369(6510), p. eaas8995. DOI: 10.1126/science.aas8995

Mahadevan, S. *et al.* (2017) 'Maternally Expressed NLRP2 Links the Subcortical Maternal Complex (SCMC) to Fertility, Embryogenesis and Epigenetic Reprogramming'. *Scientific Reports*, 7, p. 44667. DOI: 10.1038/srep44667

Male, V. (2021) 'Medawar and the Immunological Paradox of Pregnancy: In Context'. *Oxford Open Immunology*, 2(1), p. iqaa006. DOI: 10.1093/oxfimm/iqaa006

Man, S.M. *et al.* (2014) 'Inflammasome Activation Causes Dual Recruitment of NLRC4 and NLRP3 to the Same Macromolecular Complex'. *Proceedings of the National Academy of Sciences*, 111(20), pp. 7403–7408. DOI: 10.1073/pnas.1402911111

Manji, G.A. *et al.* (2002) 'PYPAF1, a PYRIN-Containing Apaf1-like Protein That Assembles with ASC and Regulates Activation of NF-KB *'. *Journal of Biological Chemistry*, 277(13), pp. 11570–11575. DOI: 10.1074/jbc.M112208200

Marshall, J.S. *et al.* (2018) 'An Introduction to Immunology and Immunopathology'. *Allergy, Asthma & Clinical Immunology*, 14(2), p. 49. DOI: 10.1186/s13223-018-0278-1

Martinon, F., Burns, K. and Tschopp, J. (2002) 'The Inflammasome: A Molecular Platform Triggering Activation of Inflammatory Caspases and Processing of ProIL-Beta'. *Molecular Cell*, 10(2), pp. 417–426. DOI: 10.1016/s1097-2765(02)00599-3

Matz, H. and Dooley, H. (2019) DOI: 10.1016/j.dci.2018.09.007

Mazanek, Z. *et al.* (2022) DOI: 10.1101/2022.08.02.502519

McCoy, A.J. *et al.* (2007) 'Phaser Crystallographic Software'. *Journal of Applied Crystallography*, 40(Pt 4), pp. 658–674. DOI: 10.1107/S0021889807021206

McGeough, M.D. *et al.* (2017) 'TNF Regulates Transcription of NLRP3 Inflammasome Components and Inflammatory Molecules in Cryopyrinopathies'. *Journal of Clinical Investigation*, 127(12), pp. 4488–4497. DOI: 10.1172/JCI90699

McKee, C.M. and Coll, R.C. (2020) 'NLRP3 Inflammasome Priming: A Riddle Wrapped in a Mystery inside an Enigma'. *Journal of Leukocyte Biology*, 108(3), pp. 937–952. DOI: 10.1002/JLB.3MR0720-513R

McNab, F. *et al.* (2015) (2) 'Type I Interferons in Infectious Disease'. *Nature Reviews Immunology*, 15(2), pp. 87–103. DOI: 10.1038/nri3787

McPherson, A. and Gavira, J.A. (2014) ‘Introduction to Protein Crystallization’. *Acta Crystallographica Section F Structural Biology Communications*, 70(1), pp. 2–20. DOI: 10.1107/S2053230X13033141

Messaed, C. *et al.* (2011) ‘NLRP7, a Nucleotide Oligomerization Domain-like Receptor Protein, Is Required for Normal Cytokine Secretion and Co-Localizes with Golgi and the Microtubule-Organizing Center’. *Journal of Biological Chemistry*, 286(50), pp. 43313–43323. DOI: 10.1074/jbc.M111.306191

Messer, A. and Butler, D.C. (2020) ‘Optimizing Intracellular Antibodies (Intrabodies/Nanobodies) to Treat Neurodegenerative Disorders’. *Neurobiology of Disease*, 134, p. 104619. DOI: 10.1016/j.nbd.2019.104619

Meunier, E. and Broz, P. (2017) ‘Evolutionary Convergence and Divergence in NLR Function and Structure’. *Trends in Immunology*, 38(10), pp. 744–757. DOI: 10.1016/j.it.2017.04.005

Miao, E.A. *et al.* (2006) ‘Cytoplasmic Flagellin Activates Caspase-1 and Secretion of Interleukin 1beta via Ipaf’. *Nature Immunology*, 7(6), pp. 569–575. DOI: 10.1038/ni1344

Miao, N. *et al.* (2023) (1) ‘Oxidized Mitochondrial DNA Induces Gasdermin D Oligomerization in Systemic Lupus Erythematosus’. *Nature Communications*, 14(1), p. 872. DOI: 10.1038/s41467-023-36522-z

Miller, J.M. and Enemark, E.J. (2016) ‘Fundamental Characteristics of AAA+ Protein Family Structure and Function’. *Archaea*, 2016, p. 9294307. DOI: 10.1155/2016/9294307

Minkiewicz, J., de Rivero Vaccari, J.P. and Keane, R.W. (2013) ‘Human Astrocytes Express a Novel NLRP2 Inflammasome’. *Glia*, 61(7), pp. 1113–1121. DOI: 10.1002/glia.22499

Mitchell, L.E. (2021) ‘Maternal Effect Genes: Update and Review of Evidence for a Link with Birth Defects’. *Human Genetics and Genomics Advances*, 3(1), p. 100067. DOI: 10.1016/j.xhgg.2021.100067

Mitchell, L.S. and Colwell, L.J. (2018) ‘Comparative Analysis of Nanobody Sequence and Structure Data’. *Proteins*, 86(7), pp. 697–706. DOI: 10.1002/prot.25497

Moghaddas, F. *et al.* (2018) ‘Autoinflammatory Mutation in NLRC4 Reveals a Leucine-Rich Repeat (LRR)–LRR Oligomerization Interface’. *Journal of Allergy and Clinical Immunology*, 142(6), pp. 1956-1967.e6. DOI: 10.1016/j.jaci.2018.04.033

Monteiro, J.T. and Lepenies, B. (2017) (3) ‘Myeloid C-Type Lectin Receptors in Viral Recognition and Antiviral Immunity’. *Viruses*, 9(3), p. 59. DOI: 10.3390/v9030059

Moonen, S. *et al.* (2023) ‘Pyroptosis in Alzheimer’s Disease: Cell Type-Specific Activation in Microglia, Astrocytes and Neurons’. *Acta Neuropathologica*, 145(2), pp. 175–195. DOI: 10.1007/s00401-022-02528-y

Moynagh, P.N. (2005) ‘TLR Signalling and Activation of IRFs: Revisiting Old Friends from the NF-KappaB Pathway’. *Trends in Immunology*, 26(9), pp. 469–476. DOI: 10.1016/j.it.2005.06.009

Mu, J. *et al.* (2019) ‘Mutations in NLRP2 and NLRP5 Cause Female Infertility Characterised by Early Embryonic Arrest’. *Journal of Medical Genetics*, 56(7), pp. 471–480. DOI: 10.1136/jmedgenet-2018-105936

Muckle, T.J. (1979) ‘The “Muckle–Wells” Syndrome’. *British Journal of Dermatology*, 100(1), pp. 87–92. DOI: 10.1111/j.1365-2133.1979.tb03572.x

Mukherjee, J. *et al.* (2022) (1) ‘Intramuscular Delivery of Formulated RNA Encoding Six Linked Nanobodies Is Highly Protective for Exposures to Three Botulinum Neurotoxin Serotypes’. *Scientific Reports*, 12(1), p. 11664. DOI: 10.1038/s41598-022-15876-2

Mullins, B. and Chen, J. (2021) ‘NLRP9 in Innate Immunity and Inflammation’. *Immunology*, 162(3), pp. 262–267. DOI: 10.1111/imm.13290

Murdoch, S. *et al.* (2006) (3) ‘Mutations in NALP7 Cause Recurrent Hydatidiform Moles and Reproductive Wastage in Humans’. *Nature Genetics*, 38(3), pp. 300–302. DOI: 10.1038/ng1740

Murphy, Kenneth. (2017) *Janeway’s Immunobiology*. 9th Edition. New York, USA and Abingdon, UK: Garland Science, Taylor & Francis Group, LLC

Muyldermans, S. (2013) ‘Nanobodies: Natural Single-Domain Antibodies’. *Annual Review of Biochemistry*, 82(1), pp. 775–797. DOI: 10.1146/annurev-biochem-063011-092449

Naderer, T. and Fulcher, M.C. (2018) ‘Targeting Apoptosis Pathways in Infections’. *Journal of Leukocyte Biology*, 103(2), pp. 275–285. DOI: 10.1189/JLB.4MR0717-286R

Najjar, M. *et al.* (2016) ‘RIPK1 and RIPK3 Kinases Promote Cell Death-Independent Inflammation by Toll-like Receptor 4’. *Immunity*, 45(1), pp. 46–59. DOI: 10.1016/j.immuni.2016.06.007

Ng, A. and Xavier, R.J. (2011) ‘Leucine-Rich Repeat (LRR) Proteins: Integrators of Pattern Recognition and Signaling in Immunity’. *Autophagy*, 7(9), pp. 1082–1084. DOI: 10.4161/auto.7.9.16464

Nguyen, L.K., Kholodenko, B.N. and von Kriegsheim, A. (2018) ‘Rac1 and RhoA: Networks, Loops and Bistability’. *Small GTPases*, 9(4), pp. 316–321. DOI: 10.1080/21541248.2016.1224399

Nigrovic, P.A., Lee, P.Y. and Hoffman, H.M. (2020) 'Monogenic Autoinflammatory Disorders: Conceptual Overview, Phenotype, and Clinical Approach'. *Journal of Allergy and Clinical Immunology*, 146(5), pp. 925–937. DOI: 10.1016/j.jaci.2020.08.017

NLRP7 - NACHT, LRR and PYD Domains-Containing Protein 7 - Homo Sapiens (Human) | UniProtKB | UniProt. Available at: https://www.uniprot.org/uniprotkb/Q8WX94/entry#sequences (Accessed: 26 January 2023d)

Nobel, C.S. *et al.* (1997) 'Disulfiram Is a Potent Inhibitor of Proteases of the Caspase Family'. *Chemical Research in Toxicology*, 10(12), pp. 1319–1324. DOI: 10.1021/tx970131m

Novick, D. *et al.* (1999) 'Interleukin-18 Binding Protein: A Novel Modulator of the Th1 Cytokine Response'. *Immunity*, 10(1), pp. 127–136. DOI: 10.1016/s1074-7613(00)80013-8

Nozawa, T. *et al.* (2017) 'The Intracellular Microbial Sensor NLRP4 Directs Rho-Actin Signaling to Facilitate Group A Streptococcus-Containing Autophagosome-like Vacuole Formation'. *Autophagy*, 13(11), pp. 1841–1854. DOI: 10.1080/15548627.2017.1358343

Okada, H., Tsuzuki, T. and Murata, H. (2018) 'Decidualization of the Human Endometrium'. *Reproductive Medicine and Biology*, 17(3), pp. 220–227. DOI: 10.1002/rmb2.12088

Onoufriadis, A. *et al.* (2018) 'Exome Sequencing and Genotyping Identify a Rare Variant in NLRP7 Gene Associated With Ulcerative Colitis'. *Journal of Crohn's and Colitis*, 12(3), pp. 321–326. DOI: 10.1093/ecco-jcc/jjx157

Opoku, E. *et al.* (2021) 'Gasdermin D Mediates Inflammation-Induced Defects in Reverse Cholesterol Transport and Promotes Atherosclerosis'. *Frontiers in Cell and Developmental Biology*, 9, p. 715211. DOI: 10.3389/fcell.2021.715211

Orning, P. *et al.* (2018) 'Pathogen Blockade of TAK1 Triggers Caspase-8–Dependent Cleavage of Gasdermin D and Cell Death'. *Science*, 362(6418), pp. 1064–1069. DOI: 10.1126/science.aau2818

Paidimuddala, B. *et al.* (2023) (2) 'Mechanism of NAIP—NLRC4 Inflammasome Activation Revealed by Cryo-EM Structure of Unliganded NAIP5'. *Nature Structural & Molecular Biology*, 30(2), pp. 159–166. DOI: 10.1038/s41594-022-00889-2

Papp, K.A. *et al.* (2021) 'IL17A/F Nanobody Sonelokimab in Patients with Plaque Psoriasis: A Multicentre, Randomised, Placebo-Controlled, Phase 2b Study'. *Lancet (London, England)*, 397(10284), pp. 1564–1575. DOI: 10.1016/S0140-6736(21)00440-2

Pardon, E. *et al.* (2014) (3) ‘A General Protocol for the Generation of Nanobodies for Structural Biology’. *Nature Protocols*, 9(3), pp. 674–693. DOI: 10.1038/nprot.2014.039

Park, H.H. (2012) ‘PYRIN Domains and Their Interactions in the Apoptosis and Inflammation Signaling Pathway’. *Apoptosis*, 17(12), pp. 1247–1257. DOI: 10.1007/s10495-012-0775-5

Pasparakis, M. and Vandenabeele, P. (2015) (7534) ‘Necroptosis and Its Role in Inflammation’. *Nature*, 517(7534), pp. 311–320. DOI: 10.1038/nature14191

Patel, M.N. *et al.* (2017) ‘Inflammasome Priming in Sterile Inflammatory Disease’. *Trends in Molecular Medicine*, 23(2), pp. 165–180. DOI: 10.1016/j.molmed.2016.12.007

Paz, S. *et al.* (2011) (6) ‘A Functional C-Terminal TRAF3-Binding Site in MAVS Participates in Positive and Negative Regulation of the IFN Antiviral Response’. *Cell Research*, 21(6), pp. 895–910. DOI: 10.1038/cr.2011.2

Pearson, W.R. (2013) ‘An Introduction to Sequence Similarity (“Homology”) Searching’. *Current Protocols in Bioinformatics*, 42(1). DOI: 10.1002/0471250953.bi0301s42

Peng, H. *et al.* (2015) ‘Expression and Localization of Nlrp4g in Mouse Preimplantation Embryo’. *Zygote (Cambridge, England)*, 23(6), pp. 846–851. DOI: 10.1017/S0967199414000525

Piliarik, M., Vaisocherová, H. and Homola, J. (2009) ‘Surface Plasmon Resonance Biosensing’. In Rasooly, A. and Herold, K.E. (eds.) *Biosensors and Biodetection*. Methods in Molecular Biology™. Totowa, NJ: Humana Press, pp. 65–88. DOI: 10.1007/978-1-60327-567-5_5

Pinheiro, A.S. *et al.* (2010) ‘Three-Dimensional Structure of the NLRP7 Pyrin Domain Insight into Pyrin-Pyrin-Mediated Effector Domain Signaling in Innate Immunity’. *Journal of Biological Chemistry*, 285(35), pp. 27402–27410. DOI: 10.1074/jbc.M110.113191

Platnich, J.M. *et al.* (2018) ‘Shiga Toxin/Lipopolysaccharide Activates Caspase-4 and Gasdermin D to Trigger Mitochondrial Reactive Oxygen Species Upstream of the NLRP3 Inflammasome’. *Cell Reports*, 25(6), pp. 1525-1536.e7. DOI: 10.1016/j.celrep.2018.09.071

Popoff, M.R. (2014) ‘Bacterial Factors Exploit Eukaryotic Rho GTPase Signaling Cascades to Promote Invasion and Proliferation within Their Host’. *Small GTPases*, 5, p. e28209. DOI: 10.4161/sgtp.28209

Popovic, M., Azpiroz, F. and Chuva de Sousa Lopes, S.M. (2021) (8) ‘Engineered Models of the Human Embryo’. *Nature Biotechnology*, 39(8), pp. 918–920. DOI: 10.1038/s41587-021-01004-4

Próchnicki, T. *et al.* (2023) ‘Mitochondrial Damage Activates the NLRP10 Inflammasome’. *Nature Immunology*, pp. 1–9. DOI: 10.1038/s41590-023-01451-y

Proell, M. *et al.* (2013) ‘The CARD Plays a Critical Role in ASC Foci Formation and Inflammasome Signalling’. *Biochemical Journal*, 449(3), pp. 613–621. DOI: 10.1042/BJ20121198

Proell, M. *et al.* (2008) ‘The Nod-Like Receptor (NLR) Family: A Tale of Similarities and Differences’ Gay, N. (ed.). *PLoS ONE*, 3(4), p. e2119. DOI: 10.1371/journal.pone.0002119

Qian, J. *et al.* (2007) ‘Women Heterozygous for NALP7/NLRP7 Mutations Are at Risk for Reproductive Wastage: Report of Two Novel Mutations’. *Human Mutation*, 28(7), pp. 741–741. DOI: 10.1002/humu.9498

Qin, Y. *et al.* (2017) ‘NLRP11 Disrupts MAVS Signalosome to Inhibit Type I Interferon Signaling and Virus-Induced Apoptosis’. *EMBO Reports*, 18(12), pp. 2160–2171. DOI: 10.15252/embr.201744480

Radian, A.D. *et al.* (2015) ‘ATP Binding by NLRP7 Is Required for Inflammasome Activation in Response to Bacterial Lipopeptides’. *Molecular Immunology*, 67(2 Pt B), pp. 294–302. DOI: 10.1016/j.molimm.2015.06.013

Rashidi, M. *et al.* (2019) ‘The Pyroptotic Cell Death Effector Gasdermin D Is Activated by Gout-Associated Uric Acid Crystals but Is Dispensable for Cell Death and IL-1β Release’. *Journal of Immunology (Baltimore, Md.: 1950)*, 203(3), pp. 736–748. DOI: 10.4049/jimmunol.1900228

Rathinam, V.A.K. *et al.* (2010) (5) ‘The AIM2 Inflammasome Is Essential for Host Defense against Cytosolic Bacteria and DNA Viruses’. *Nature Immunology*, 11(5), pp. 395–402. DOI: 10.1038/ni.1864

Rathkey, J.K. *et al.* (2018) ‘Chemical Disruption of the Pyroptotic Pore-Forming Protein Gasdermin D Inhibits Inflammatory Cell Death and Sepsis’. *Science Immunology*, 3(26). DOI: 10.1126/sciimmunol.aat2738

Ratsimandresey, R.A. *et al.* (2017) (1) ‘The PYRIN Domain-Only Protein POP2 Inhibits Inflammasome Priming and Activation’. *Nature Communications*, 8(1), p. 15556. DOI: 10.1038/ncomms15556

Ravin, K.A. and Loy, M. (2016) ‘The Eosinophil in Infection’. *Clinical Reviews in Allergy & Immunology*, 50(2), pp. 214–227. DOI: 10.1007/s12016-015-8525-4

Rehwinkel, J. and Gack, M.U. (2020) (9) ‘RIG-I-like Receptors: Their Regulation and Roles in RNA Sensing’. *Nature Reviews Immunology*, 20(9), pp. 537–551. DOI: 10.1038/s41577-020-0288-3

Rex, D.A.B. *et al.* (2020) ‘A Comprehensive Pathway Map of IL-18-Mediated Signalling’. *Journal of Cell Communication and Signaling*, 14(2), pp. 257–266. DOI: 10.1007/s12079-019-00544-4

Reynaud, D. *et al.* (2021) (12) ‘NLRP7 Promotes Choriocarcinoma Growth and Progression through the Establishment of an Immunosuppressive Microenvironment’. *Cancers*, 13(12), p. 2999. DOI: 10.3390/cancers13122999

Robertson, S.A., Care, A.S. and Moldenhauer, L.M. ‘Regulatory T Cells in Embryo Implantation and the Immune Response to Pregnancy’. *The Journal of Clinical Investigation*, 128(10), pp. 4224–4235. DOI: 10.1172/JCI122182

Rogers, C. *et al.* (2019) (1) ‘Gasdermin Pores Permeabilize Mitochondria to Augment Caspase-3 Activation during Apoptosis and Inflammasome Activation’. *Nature Communications*, 10(1), p. 1689. DOI: 10.1038/s41467-019-09397-2

Rogers, N.C. *et al.* (2005) ‘Syk-Dependent Cytokine Induction by Dectin-1 Reveals a Novel Pattern Recognition Pathway for C Type Lectins’. *Immunity*, 22(4), pp. 507–517. DOI: 10.1016/j.immuni.2005.03.004

Romberg, N., Vogel, T.P. and Canna, S.W. (2017) ‘NLRC4 Inflammasomopathies’. *Current Opinion in Allergy and Clinical Immunology*, 17(6), pp. 398–404. DOI: 10.1097/ACI.0000000000000396

Rossant, J. and Tam, P.P.L. (2022) ‘Early Human Embryonic Development: Blastocyst Formation to Gastrulation’. *Developmental Cell*, 57(2), pp. 152–165. DOI: 10.1016/j.devcel.2021.12.022

Rossi, M.N. *et al.* (2019) ‘NLRP2 Regulates Proinflammatory and Antiapoptotic Responses in Proximal Tubular Epithelial Cells’. *Frontiers in Cell and Developmental Biology*, 7, p. 252. DOI: 10.3389/fcell.2019.00252

Rothbauer, U. *et al.* (2006) (11) ‘Targeting and Tracing Antigens in Live Cells with Fluorescent Nanobodies’. *Nature Methods*, 3(11), pp. 887–889. DOI: 10.1038/nmeth953

Rühl, S. *et al.* (2018) ‘ESCRT-Dependent Membrane Repair Negatively Regulates Pyroptosis Downstream of GSDMD Activation’. *Science*, 362(6417), pp. 956–960. DOI: 10.1126/science.aar7607

S, K. *et al.* (2012) ‘An NLRP7-Containing Inflammasome Mediates Recognition of Microbial Lipopeptides in Human Macrophages’. *Immunity*, 36(3). DOI: 10.1016/j.immuni.2012.02.001

de Sa Pinheiro, A. *et al.* (2009) ‘Backbone and Sidechain 1H, 15N and 13C Assignments of the NLRP7 Pyrin Domain’. *Biomolecular NMR Assignments*, 3(2), pp. 207–209. DOI: 10.1007/s12104-009-9176-2

Sahillioglu, A.C. *et al.* (2014) 'Structural and Dynamics Aspects of ASC Speck Assembly'. *Structure*, 22(12), pp. 1722–1734. DOI: 10.1016/j.str.2014.09.011

Saidu, N.E.B. *et al.* (2019) 'Dimethyl Fumarate, a Two-Edged Drug: Current Status and Future Directions'. *Medicinal Research Reviews*, 39(5), pp. 1923–1952. DOI: 10.1002/med.21567

Sakahira, H., Enari, M. and Nagata, S. (1998) 'Cleavage of CAD Inhibitor in CAD Activation and DNA Degradation during Apoptosis'. *Nature*, 391(6662), pp. 96–99. DOI: 10.1038/34214

Samson, A.L. *et al.* (2020) (1) 'MLKL Trafficking and Accumulation at the Plasma Membrane Control the Kinetics and Threshold for Necroptosis'. *Nature Communications*, 11(1), p. 3151. DOI: 10.1038/s41467-020-16887-1

Sanchez David, R.Y. *et al.* (2019) 'LGP2 Binds to PACT to Regulate RIG-I- and MDA5-Mediated Antiviral Responses'. *Science Signaling*, 12(601), p. eaar3993. DOI: 10.1126/scisignal.aar3993

Sanchez-Delgado, M. *et al.* (2015) 'Absence of Maternal Methylation in Biparental Hydatidiform Moles from Women with NLRP7 Maternal-Effect Mutations Reveals Widespread Placenta-Specific Imprinting'. *PLOS Genetics*, 11(11), p. e1005644. DOI: 10.1371/journal.pgen.1005644

Sandall, C.F., Ziehr, B.K. and MacDonald, J.A. (2020) 'ATP-Binding and Hydrolysis in Inflammasome Activation'. *Molecules*, 25(19), p. 4572. DOI: 10.3390/molecules25194572

Sang, Q. *et al.* (2021) 'Genetic Factors as Potential Molecular Markers of Human Oocyte and Embryo Quality'. *Journal of Assisted Reproduction and Genetics*, 38(5), pp. 993–1002. DOI: 10.1007/s10815-021-02196-z

Santa Cruz Garcia, A.B. *et al.* (2022) (1) 'Gasdermin D Pores Are Dynamically Regulated by Local Phosphoinositide Circuitry'. *Nature Communications*, 13(1), p. 52. DOI: 10.1038/s41467-021-27692-9

Sarhan, J. *et al.* (2018) 'Caspase-8 Induces Cleavage of Gasdermin D to Elicit Pyroptosis during Yersinia Infection'. *Proceedings of the National Academy of Sciences*, 115(46), pp. E10888–E10897. DOI: 10.1073/pnas.1809548115

Sborgi, L. *et al.* (2016) 'GSDMD Membrane Pore Formation Constitutes the Mechanism of Pyroptotic Cell Death'. *The EMBO Journal*, 35(16), pp. 1766–1778. DOI: 10.15252/embj.201694696

Schaefer, S.L. and Hummer, G. (2022) 'Sublytic Gasdermin-D Pores Captured in Atomistic Molecular Simulations' Faraldo-Gómez, J.D. (ed.). *ELife*, 11, p. e81432. DOI: 10.7554/eLife.81432

Schmid-Burgk, J.L. *et al.* (2016) ‘A Genome-Wide CRISPR (Clustered Regularly Interspaced Short Palindromic Repeats) Screen Identifies NEK7 as an Essential Component of NLRP3 Inflammasome Activation *’. *Journal of Biological Chemistry*, 291(1), pp. 103–109. DOI: 10.1074/jbc.C115.700492

Schmid-Burgk, J.L. *et al.* (2015) ‘Caspase-4 Mediates Non-Canonical Activation of the NLRP3 Inflammasome in Human Myeloid Cells’. *European Journal of Immunology*, 45(10), pp. 2911–2917. DOI: 10.1002/eji.201545523

Schmidt, F.I. *et al.* (2016) ‘A Single Domain Antibody Fragment That Recognizes the Adaptor ASC Defines the Role of ASC Domains in Inflammasome Assembly’. *The Journal of Experimental Medicine*, 213(5), pp. 771–790. DOI: 10.1084/jem.20151790

Schnappauf, O. *et al.* (2019) ‘The Pyrin Inflammasome in Health and Disease’. *Frontiers in Immunology*, 10. Available at: https://www.frontiersin.org/articles/10.3389/fimmu.2019.01745 (Accessed: 28 February 2023)

Schneider, C.A., Rasband, W.S. and Eliceiri, K.W. (2012) (7) ‘NIH Image to ImageJ: 25 Years of Image Analysis’. *Nature Methods*, 9(7), pp. 671–675. DOI: 10.1038/nmeth.2089

Seok, J.K. *et al.* (2021) ‘Regulation of the NLRP3 Inflammasome by Post-Translational Modifications and Small Molecules’. *Frontiers in Immunology*, 11. Available at: https://www.frontiersin.org/articles/10.3389/fimmu.2020.618231 (Accessed: 23 February 2023)

Sester, D.P. *et al.* (2015) ‘A Novel Flow Cytometric Method To Assess Inflammasome Formation’. *The Journal of Immunology*, 194(1), pp. 455–462. DOI: 10.4049/jimmunol.1401110

Seth, R.B. *et al.* (2005) ‘Identification and Characterization of MAVS, a Mitochondrial Antiviral Signaling Protein That Activates NF-KappaB and IRF 3’. *Cell*, 122(5), pp. 669–682. DOI: 10.1016/j.cell.2005.08.012

Shen, C. *et al.* (2019) ‘Molecular Mechanism for NLRP6 Inflammasome Assembly and Activation’. *Proceedings of the National Academy of Sciences*, 116(6), pp. 2052–2057. DOI: 10.1073/pnas.1817221116

Shen, H. *et al.* (2021) ‘Pyroptosis Executive Protein GSDMD as a Biomarker for Diagnosis and Identification of Alzheimer’s Disease’. *Brain and Behavior*, 11(4), p. e02063. DOI: 10.1002/brb3.2063

Shi, J. *et al.* (2015) ‘Cleavage of GSDMD by Inflammatory Caspases Determines Pyroptotic Cell Death’. *Nature*, 526(7575), pp. 660–665. DOI: 10.1038/nature15514

Shi, J. *et al.* (2014) (7521) ‘Inflammatory Caspases Are Innate Immune Receptors for Intracellular LPS’. *Nature*, 514(7521), pp. 187–192. DOI: 10.1038/nature13683

Shibata, K. *et al.* (2000) ‘The N-Terminal Lipopeptide of a 44-KDa Membrane-Bound Lipoprotein of Mycoplasma Salivarium Is Responsible for the Expression of Intercellular Adhesion Molecule-1 on the Cell Surface of Normal Human Gingival Fibroblasts1’. *The Journal of Immunology*, 165(11), pp. 6538–6544. DOI: 10.4049/jimmunol.165.11.6538

Silva, C.M.S. *et al.* (2021) ‘Gasdermin D Inhibition Prevents Multiple Organ Dysfunction during Sepsis by Blocking NET Formation’. *Blood*, 138(25), pp. 2702–2713. DOI: 10.1182/blood.2021011525

Silvestre-Roig, C. *et al.* (2019) ‘Neutrophil Diversity in Health and Disease’. *Trends in Immunology*, 40(7), pp. 565–583. DOI: 10.1016/j.it.2019.04.012

Sims, J.E. and Smith, D.E. (2010) (2) ‘The IL-1 Family: Regulators of Immunity’. *Nature Reviews Immunology*, 10(2), pp. 89–102. DOI: 10.1038/nri2691

Singh, R., Letai, A. and Sarosiek, K. (2019) (3) ‘Regulation of Apoptosis in Health and Disease: The Balancing Act of BCL-2 Family Proteins’. *Nature Reviews Molecular Cell Biology*, 20(3), pp. 175–193. DOI: 10.1038/s41580-018-0089-8

Slim, R. and Wallace, E.P. (2013) ‘NLRP7 and the Genetics of Hydatidiform Moles: Recent Advances and New Challenges’. *Frontiers in Immunology*, 4. DOI: 10.3389/fimmu.2013.00242

Smyth, M.S. and Martin, J.H.J. (2000) ‘X Ray Crystallography’. *Molecular Pathology*, 53(1), pp. 8–14. DOI: 10.1136/mp.53.1.8

Soellner, L. *et al.* (2017) ‘Maternal Heterozygous NLRP7 Variant Results in Recurrent Reproductive Failure and Imprinting Disturbances in the Offspring’. *European Journal of Human Genetics*, 25(8), pp. 924–929. DOI: 10.1038/ejhg.2017.94

Song, A. *et al.* (2018) ‘Salient Type 1 Interleukin 1 Receptor Expression in Peripheral Non-Immune Cells’. *Scientific Reports*, 8, p. 723. DOI: 10.1038/s41598-018-19248-7

Soper, J.T. (2021) ‘Gestational Trophoblastic Disease: Current Evaluation and Management’. *Obstetrics & Gynecology*, 137(2), p. 355. DOI: 10.1097/AOG.0000000000004240

Sosa Cuevas, E. *et al.* (2022) ‘Unique CLR Expression Patterns on Circulating and Tumor-Infiltrating DC Subsets Correlated with Clinical Outcome in Melanoma Patients’. *Frontiers in Immunology*, 13. Available at: https://www.frontiersin.org/articles/10.3389/fimmu.2022.1040600 (Accessed: 21 February 2023)

Spel, L. *et al.* (2022) ‘CDC42 Regulates PYRIN Inflammasome Assembly’. *Cell Reports*, 41(7). DOI: 10.1016/j.celrep.2022.111636

Ständer, S. *et al.* (2021) ‘Epitope Mapping of Polyclonal Antibodies by Hydrogen–Deuterium Exchange Mass Spectrometry (HDX-MS)’. *Analytical Chemistry*, 93(34), pp. 11669–11678. DOI: 10.1021/acs.analchem.1c00696

Stehlik, C. *et al.* (2003) ‘The PAAD/PYRIN-Only Protein POP1/ASC2 Is a Modulator of ASC-Mediated Nuclear-Factor-Kappa B and pro-Caspase-1 Regulation.’ *Biochemical Journal*, 373(Pt 1), pp. 101–113. DOI: 10.1042/BJ20030304

Steiner, A. *et al.* (2022) ‘Recessive NLRC4-Autoinflammatory Disease Reveals an Ulcerative Colitis Locus’. *Journal of Clinical Immunology*, 42(2), pp. 325–335. DOI: 10.1007/s10875-021-01175-4

Stokes, M. and Abdijadid, S. (2022) *Disulfiram*. StatPearls Publishing Available at: https://www.ncbi.nlm.nih.gov/books/NBK459340/ (Accessed: 24 March 2023)

Stutz, A. *et al.* (2013) ‘ASC Speck Formation as a Readout for Inflammasome Activation’. In *Methods in Molecular Biology (Clifton, N.J.)*. Methods Mol Biol, pp. 91–101. DOI: 10.1007/978-1-62703-523-1_8

Su, S.-B. *et al.* (2021) ‘TLR10: Insights, Controversies and Potential Utility as a Therapeutic Target’. *Scandinavian Journal of Immunology*, 93(4), p. e12988. DOI: 10.1111/sji.12988

Sun, L. *et al.* (2012) ‘Mixed Lineage Kinase Domain-like Protein Mediates Necrosis Signaling Downstream of RIP3 Kinase’. *Cell*, 148(1–2), pp. 213–227. DOI: 10.1016/j.cell.2011.11.031

Taabazuing, C.Y., Okondo, M.C. and Bachovchin, D.A. (2017) (4) ‘Pyroptosis and Apoptosis Pathways Engage in Bidirectional Crosstalk in Monocytes and Macrophages’. *Cell Chemical Biology*, 24(4), p. undefined-undefined. DOI: 10.1016/j.chembiol.2017.03.009

Takeuchi, O. and Akira, S. (2010) ‘Pattern Recognition Receptors and Inflammation’. *Cell*, 140(6), pp. 805–820. DOI: 10.1016/j.cell.2010.01.022

Taylor, G.L. (2010) ‘Introduction to Phasing’. *Acta Crystallographica Section D: Biological Crystallography*, 66(Pt 4), pp. 325–338. DOI: 10.1107/S0907444910006694

Thapa, R.J. *et al.* (2013) ‘Interferon-Induced RIP1/RIP3-Mediated Necrosis Requires PKR and Is Licensed by FADD and Caspases’. *Proceedings of the National Academy of Sciences*, 110(33), pp. E3109–E3118. DOI: 10.1073/pnas.1301218110

The French FMF Consortium *et al.* (1997) (1) ‘A Candidate Gene for Familial Mediterranean Fever’. *Nature Genetics*, 17(1), pp. 25–31. DOI: 10.1038/ng0997-25

Tian, X., Pascal, G. and Monget, P. (2009) ‘Evolution and Functional Divergence of NLRPgenes in Mammalian Reproductive Systems’. *BMC Evolutionary Biology*, 9(1), p. 202. DOI: 10.1186/1471-2148-9-202

Tissue Expression of GSDMD - Summary - The Human Protein Atlas. Available at: https://www.proteinatlas.org/ENSG00000104518-GSDMD/tissue (Accessed: 17 March 2023e)

Tong, X. *et al.* (2022) ‘Mutations in OOEP and NLRP5 Identified in Infertile Patients with Early Embryonic Arrest’. *Human Mutation*, 43(12), pp. 1909–1920. DOI: 10.1002/humu.24448

Tower, J. (2015) ‘Programmed Cell Death in Aging’. *Ageing Research Reviews*, 23(Pt A), pp. 90–100. DOI: 10.1016/j.arr.2015.04.002

Traenkle, B., Kaiser, P.D. and Rothbauer, U. (2016) ‘Nanobody Platform for Determination of Protein Structure, Application Of’. In *Encyclopedia of Analytical Chemistry*. Chichester, UK: John Wiley & Sons, Ltd, pp. 1–14. DOI: 10.1002/9780470027318.a9548

Trindade, B.C. and Chen, G.Y. (2020) ‘NOD1 and NOD2 in Inflammatory and Infectious Diseases’. *Immunological Reviews*, 297(1), pp. 139–161. DOI: 10.1111/imr.12902

Tsai, P.-Y. *et al.* (2019) ‘NLRP7 Is Involved in the Differentiation of the Decidual Macrophages’. *International Journal of Molecular Sciences*, 20(23), p. 5994. DOI: 10.3390/ijms20235994

Tuladhar, S. and Kanneganti, T.-D. (2020) ‘NLRP12 in Innate Immunity and Inflammation’. *Molecular Aspects of Medicine*, 76, p. 100887. DOI: 10.1016/j.mam.2020.100887

Tummers, B. and Green, D.R. (2017) ‘Caspase-8: Regulating Life and Death’. *Immunological Reviews*, 277(1), pp. 76–89. DOI: 10.1111/imr.12541

Uchański, T. *et al.* (2019) ‘Megabodies Expand the Nanobody Toolkit for Protein Structure Determination by Single-Particle Cryo-EM’. *BioRxiv*, p. 812230. DOI: 10.1101/812230

Uchański, T., Pardon, E. and Steyaert, J. (2020) DOI: 10.1016/j.sbi.2020.01.003

Van Den Eeckhout, B., Tavernier, J. and Gerlo, S. (2021) ‘Interleukin-1 as Innate Mediator of T Cell Immunity’. *Frontiers in Immunology*, 11. Available at: https://www.frontiersin.org/articles/10.3389/fimmu.2020.621931 (Accessed: 1 March 2023)

Vance, R.E. (2015) ‘The NAIP/NLRC4 Inflammasomes’. *Current Opinion in Immunology*, 32, pp. 84–89. DOI: 10.1016/j.coi.2015.01.010

Velloso, F.J. *et al.* (2019) ‘NOD-like Receptors: Major Players (and Targets) in the Interface between Innate Immunity and Cancer’. *Bioscience Reports*, 39(4), p. BSR20181709. DOI: 10.1042/BSR20181709

Viganò, E. *et al.* (2015) (1) ‘Human Caspase-4 and Caspase-5 Regulate the One-Step Non-Canonical Inflammasome Activation in Monocytes’. *Nature Communications*, 6(1), p. 8761. DOI: 10.1038/ncomms9761

Vincke, C. *et al.* (2009) ‘General Strategy to Humanize a Camelid Single-Domain Antibody and Identification of a Universal Humanized Nanobody Scaffold*’. *Journal of Biological Chemistry*, 284(5), pp. 3273–3284. DOI: 10.1074/jbc.M806889200

Vladimer, G.I. *et al.* (2012) ‘The NLRP12 Inflammasome Recognizes Yersinia Pestis’. *Immunity*, 37(1), pp. 96–107. DOI: 10.1016/j.immuni.2012.07.006

Voehringer, D. (2012) ‘Basophil Modulation by Cytokine Instruction’. *European Journal of Immunology*, 42(10), pp. 2544–2550. DOI: 10.1002/eji.201142318

Volchuk, A. *et al.* (2020) ‘Indirect Regulation of HMGB1 Release by Gasdermin D’. *Nature Communications*, 11(1), p. 4561. DOI: 10.1038/s41467-020-18443-3

Vora, S.M., Lieberman, J. and Wu, H. (2021) (11) ‘Inflammasome Activation at the Crux of Severe COVID-19’. *Nature Reviews Immunology*, 21(11), pp. 694–703. DOI: 10.1038/s41577-021-00588-x

Wang, C.M. *et al.* (2009) ‘Identification of 13 Novel NLRP7 Mutations in 20 Families with Recurrent Hydatidiform Mole; Missense Mutations Cluster in the Leucine-Rich Region’. *Journal of Medical Genetics*, 46(8), pp. 569–575. DOI: 10.1136/jmg.2008.064196

Wang, H. *et al.* (2014) ‘Mixed Lineage Kinase Domain-like Protein MLKL Causes Necrotic Membrane Disruption upon Phosphorylation by RIP3’. *Molecular Cell*, 54(1), pp. 133–146. DOI: 10.1016/j.molcel.2014.03.003

Wang, K. *et al.* (2020) ‘Structural Mechanism for GSDMD Targeting by Autoprocessed Caspases in Pyroptosis’. *Cell*, 180(5), pp. 941-955.e20. DOI: 10.1016/j.cell.2020.02.002

Wang, L. *et al.* (2002) ‘PYPAF7, a Novel PYRIN-Containing Apaf1-like Protein That Regulates Activation of NF-KB and Caspase-1-Dependent Cytokine Processing *’. *Journal of Biological Chemistry*, 277(33), pp. 29874–29880. DOI: 10.1074/jbc.M203915200

Wang, L., Li, S. and Dorf, M.E. (2012) 'NEMO Binds Ubiquitinated TANK-Binding Kinase 1 (TBK1) to Regulate Innate Immune Responses to RNA Viruses'. *PLoS ONE*, 7(9), p. e43756. DOI: 10.1371/journal.pone.0043756

Wang, Y. *et al.* (2017) (7661) 'Chemotherapy Drugs Induce Pyroptosis through Caspase-3 Cleavage of a Gasdermin'. *Nature*, 547(7661), pp. 99–103. DOI: 10.1038/nature22393

Wang, Y. *et al.* (2016) DOI: 10.2147/IJN.S107194

Waterhouse, A.M. *et al.* (2009) 'Jalview Version 2—a Multiple Sequence Alignment Editor and Analysis Workbench'. *Bioinformatics*, 25(9), pp. 1189–1191. DOI: 10.1093/bioinformatics/btp033

Weindel, C.G. *et al.* (2022) 'Mitochondrial ROS Promotes Susceptibility to Infection via Gasdermin D-Mediated Necroptosis'. *Cell*, 185(17), pp. 3214-3231.e23. DOI: 10.1016/j.cell.2022.06.038

Welzel, T. and Kuemmerle-Deschner, J.B. (2021) 'Diagnosis and Management of the Cryopyrin-Associated Periodic Syndromes (CAPS): What Do We Know Today?' *Journal of Clinical Medicine*, 10(1), p. 128. DOI: 10.3390/jcm10010128

Wen, J. *et al.* (2021) 'Updating the NLRC4 Inflammasome: From Bacterial Infections to Autoimmunity and Cancer'. *Frontiers in Immunology*, 12. Available at: https://www.frontiersin.org/articles/10.3389/fimmu.2021.702527 (Accessed: 22 February 2023)

Westerveld, G.H. *et al.* (2006) 'Mutations in the Testis-Specific NALP14 Gene in Men Suffering from Spermatogenic Failure'. *Human Reproduction (Oxford, England)*, 21(12), pp. 3178–3184. DOI: 10.1093/humrep/del293

Wolff, M. von. *et al.* (2000) 'Regulated Expression of Cytokines in Human Endometrium throughout the Menstrual Cycle: Dysregulation in Habitual Abortion'. *Molecular Human Reproduction*, 6(7), pp. 627–634. DOI: 10.1093/molehr/6.7.627

Wu, Y. *et al.* (2022) (1) 'Cell Pyroptosis in Health and Inflammatory Diseases'. *Cell Death Discovery*, 8(1), pp. 1–8. DOI: 10.1038/s41420-022-00998-3

Xi, R. *et al.* (2021) 'Up-Regulation of Gasdermin C in Mouse Small Intestine Is Associated with Lytic Cell Death in Enterocytes in Worm-Induced Type 2 Immunity'. *Proceedings of the National Academy of Sciences*, 118(30), p. e2026307118. DOI: 10.1073/pnas.2026307118

Xia, S. *et al.* (2021) 'Gasdermin D Pore Structure Reveals Preferential Release of Mature Interleukin-1'. *Nature*, 593(7860), pp. 607–611. DOI: 10.1038/s41586-021-03478-3

Xia, S., Ruan, J. and Wu, H. (2019) ‘Monitoring Gasdermin Pore Formation in Vitro’. *Methods in Enzymology*, 625, pp. 95–107. DOI: 10.1016/bs.mie.2019.04.024

Xiao, L., Magupalli, V.G. and Wu, H. (2023) (7944) ‘Cryo-EM Structures of the Active NLRP3 Inflammasome Disc’. *Nature*, 613(7944), pp. 595–600. DOI: 10.1038/s41586-022-05570-8

Xu, H. *et al.* (2014) (7517) ‘Innate Immune Sensing of Bacterial Modifications of Rho GTPases by the Pyrin Inflammasome’. *Nature*, 513(7517), pp. 237–241. DOI: 10.1038/nature13449

Yang, F. *et al.* (2022) ‘Comparative Reactivity Profiling of Cysteine-Specific Probes by Chemoproteomics’. *Current Research in Chemical Biology*, 2, p. 100024. DOI: 10.1016/j.crchbi.2022.100024

Yang, J. *et al.* (2013) ‘Human NAIP and Mouse NAIP1 Recognize Bacterial Type III Secretion Needle Protein for Inflammasome Activation’. *Proceedings of the National Academy of Sciences of the United States of America*, 110(35), pp. 14408–14413. DOI: 10.1073/pnas.1306376110

Yang, Y. *et al.* (2018) ‘NLRP2 Negatively Regulates Antiviral Immunity by Interacting with TBK1’. *European Journal of Immunology*, 48(11), pp. 1817–1825. DOI: 10.1002/eji.201847589

Yao, G. *et al.* (2022) ‘Nanobodies as Solubilization Chaperones for the Expression and Purification of Inclusion-Body Prone Proteins’. *Chemical Communications*, 58(17), pp. 2898–2901. DOI: 10.1039/D1CC07105J

Yin, H. *et al.* (2023) (1) ‘Insights into the GSDMB-Mediated Cellular Lysis and Its Targeting by IpaH7.8’. *Nature Communications*, 14(1), p. 61. DOI: 10.1038/s41467-022-35725-0

Yin, Y. *et al.* (2020) ‘A Noncanonical Role of NOD-like Receptor NLRP14 in PGCLC Differentiation and Spermatogenesis’. *Proceedings of the National Academy of Sciences of the United States of America*, 117(36), pp. 22237–22248. DOI: 10.1073/pnas.2005533117

Yockey, L.J. and Iwasaki, A. (2018) ‘Role of Interferons and Cytokines in Pregnancy and Fetal Development’. *Immunity*, 49(3), pp. 397–412. DOI: 10.1016/j.immuni.2018.07.017

Yu, C.-H. *et al.* (2018) ‘Mechanisms of NLRP1-Mediated Autoinflammatory Disease in Humans and Mice’. *Journal of Molecular Biology*, 430(2), pp. 142–152. DOI: 10.1016/j.jmb.2017.07.012

Yu, J.-W. *et al.* (2006) (2) ‘Cryopyrin and Pyrin Activate Caspase-1, but Not NF-KB, via ASC Oligomerization’. *Cell Death & Differentiation*, 13(2), pp. 236–249. DOI: 10.1038/sj.cdd.4401734

Yu, P. *et al.* (2021) (1) ‘Pyroptosis: Mechanisms and Diseases’. *Signal Transduction and Targeted Therapy*, 6(1), pp. 1–21. DOI: 10.1038/s41392-021-00507-5

Zamboni, D.S. *et al.* (2006) ‘The Birc1e Cytosolic Pattern-Recognition Receptor Contributes to the Detection and Control of Legionella Pneumophila Infection’. *Nature Immunology*, 7(3), pp. 318–325. DOI: 10.1038/ni1305

Zanoni, I. *et al.* (2016) ‘An Endogenous Caspase-11 Ligand Elicits Interleukin-1 Release from Living Dendritic Cells’. *Science*, 352(6290), pp. 1232–1236. DOI: 10.1126/science.aaf3036

Zarantonello, A. *et al.* (2021) ‘Nanobodies Provide Insight into the Molecular Mechanisms of the Complement Cascade and Offer New Therapeutic Strategies’. *Biomolecules*, 11(2), p. 298. DOI: 10.3390/biom11020298

Zhang, C. *et al.* (2022) ‘Identification and Characterization of Inhibitory Nanobody against P38δ’. *Biochemical and Biophysical Research Communications*, 600, pp. 60–66. DOI: 10.1016/j.bbrc.2022.01.080

Zhang, L. *et al.* (2015) ‘Cryo-EM Structure of the Activated NAIP2-NLRC4 Inflammasome Reveals Nucleated Polymerization’. *Science*, 350(6259), pp. 404–409. DOI: 10.1126/science.aac5789

Zhang, P. *et al.* (2020) ‘Abnormal Processing of IL-1β in NLRP7-Mutated Monocytes in Hydatidiform Mole Patients’. *Clinical and Experimental Immunology*, 202(1), pp. 72–79. DOI: 10.1111/cei.13472

Zhang, P. *et al.* (2008) ‘Expression Analysis of the NLRP Gene Family Suggests a Role in Human Preimplantation Development’. *PloS One*, 3(7), p. e2755. DOI: 10.1371/journal.pone.0002755

Zhang, P., Liu, X. and Cao, X. (2015) (3) ‘Extracellular Pattern Recognition Molecules in Health and Diseases’. *Cellular & Molecular Immunology*, 12(3), pp. 255–257. DOI: 10.1038/cmi.2014.81

Zhang, W. *et al.* (2021) ‘An Intracellular Nanobody Targeting T4SS Effector Inhibits Ehrlichia Infection’. *Proceedings of the National Academy of Sciences*, 118(18), p. e2024102118. DOI: 10.1073/pnas.2024102118

Zhang, X. *et al.* (2020) ‘Oligodendroglial Glycolytic Stress Triggers Inflammasome Activation and Neuropathology in Alzheimer’s Disease’. *Science Advances*, 6(49), p. eabb8680. DOI: 10.1126/sciadv.abb8680

Zhaolin, Z. *et al.* (2019) ‘Role of Pyroptosis in Cardiovascular Disease’. *Cell Proliferation*, 52(2), p. e12563. DOI: 10.1111/cpr.12563

Zheng, D. *et al.* (2023) ‘Epithelial Nlrp10 Inflammasome Mediates Protection against Intestinal Autoinflammation’. *Nature Immunology*. DOI: 10.1038/s41590-023-01450-z

Zheng, W. *et al.* (2021) ‘Expanding the Genetic and Phenotypic Spectrum of the Subcortical Maternal Complex Genes in Recurrent Preimplantation Embryonic Arrest’. *Clinical Genetics*, 99(2), pp. 286–291. DOI: 10.1111/cge.13858

Zhong, F.L. *et al.* (2016) ‘Germline NLRP1 Mutations Cause Skin Inflammatory and Cancer Susceptibility Syndromes via Inflammasome Activation’. *Cell*, 167(1), pp. 187-202.e17. DOI: 10.1016/j.cell.2016.09.001

Zhou, B. and Abbott, D.W. (2021) ‘Gasdermin E Permits Interleukin-1 Beta Release in Distinct Sublytic and Pyroptotic Phases’. *Cell Reports*, 35(2). DOI: 10.1016/j.celrep.2021.108998

Zhou, R., Zhang, Q. and Xu, P. (2020) ‘TBK1, a Central Kinase in Innate Immune Sensing of Nucleic Acids and Beyond’. *Acta Biochimica Et Biophysica Sinica*, 52(7), pp. 757–767. DOI: 10.1093/abbs/gmaa051

Zhou, X. *et al.* (2020) ‘Rapid Delivery of Nanobodies/VHHs into Living Cells via Expressing In Vitro-Transcribed MRNA’. *Molecular Therapy - Methods & Clinical Development*, 17, pp. 401–408. DOI: 10.1016/j.omtm.2020.01.008

Zhou, Y. *et al.* (2016) ‘Virulent Mycobacterium Bovis Beijing Strain Activates the NLRP7 Inflammasome in THP-1 Macrophages’. pp. 1–13. DOI: 10.1371/journal.pone.0152853

Zhou, Z. *et al.* (2020) ‘Granzyme A from Cytotoxic Lymphocytes Cleaves GSDMB to Trigger Pyroptosis in Target Cells’. *Science*, 368(6494), p. eaaz7548. DOI: 10.1126/science.aaz7548

Zhu, S. *et al.* (2017) ‘Nlrp9b Inflammasome Restricts Rotavirus Infection in Intestinal Epithelial Cells’. *Nature*, 546(7660), p. 667. DOI: 10.1038/nature22967

Zimmermann, I. *et al.* (2020) (5) ‘Generation of Synthetic Nanobodies against Delicate Proteins’. *Nature Protocols*, 15(5), pp. 1707–1741. DOI: 10.1038/s41596-020-0304-x

Zimmermann, I. *et al.* (2018) ‘Synthetic Single Domain Antibodies for the Conformational Trapping of Membrane Proteins’ Forrest, L. (ed.). *ELife*, 7, p. e34317. DOI: 10.7554/eLife.34317

Zou, H. *et al.* (1999) ‘An APAF-1·Cytochrome c Multimeric Complex Is a Functional Apoptosome That Activates Procaspase-9 *’. *Journal of Biological Chemistry*, 274(17), pp. 11549–11556. DOI: 10.1074/jbc.274.17.11549

Zou, J. *et al.* (2021) ‘The Versatile Gasdermin Family: Their Function and Roles in Diseases’. *Frontiers in Immunology*, 12, p. 751533. DOI: 10.3389/fimmu.2021.751533

Zou, Z. *et al.* (2020) ‘MTOR Signaling Pathway and MTOR Inhibitors in Cancer: Progress and Challenges’. *Cell & Bioscience*, 10(1), p. 31. DOI: 10.1186/s13578-020-00396-1

Appendix

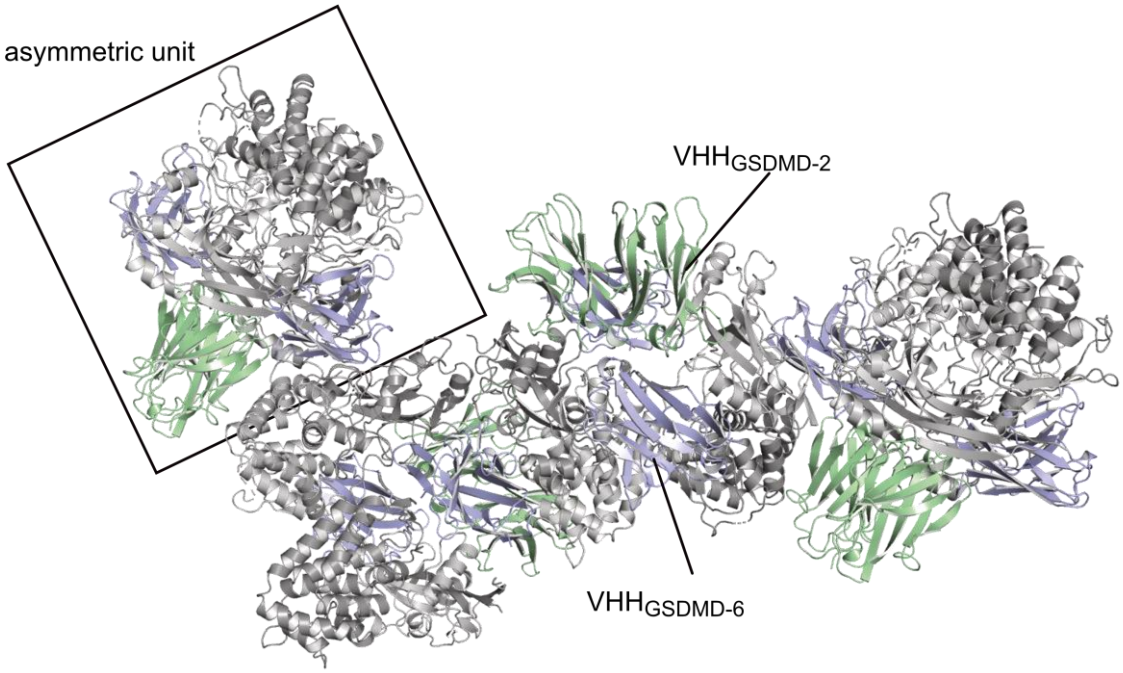

SI Figure 1: Crystal packing of the GSDMD-VHH$_{GSDMD-2}$-VHH$_{GSDMD-6}$ complex.

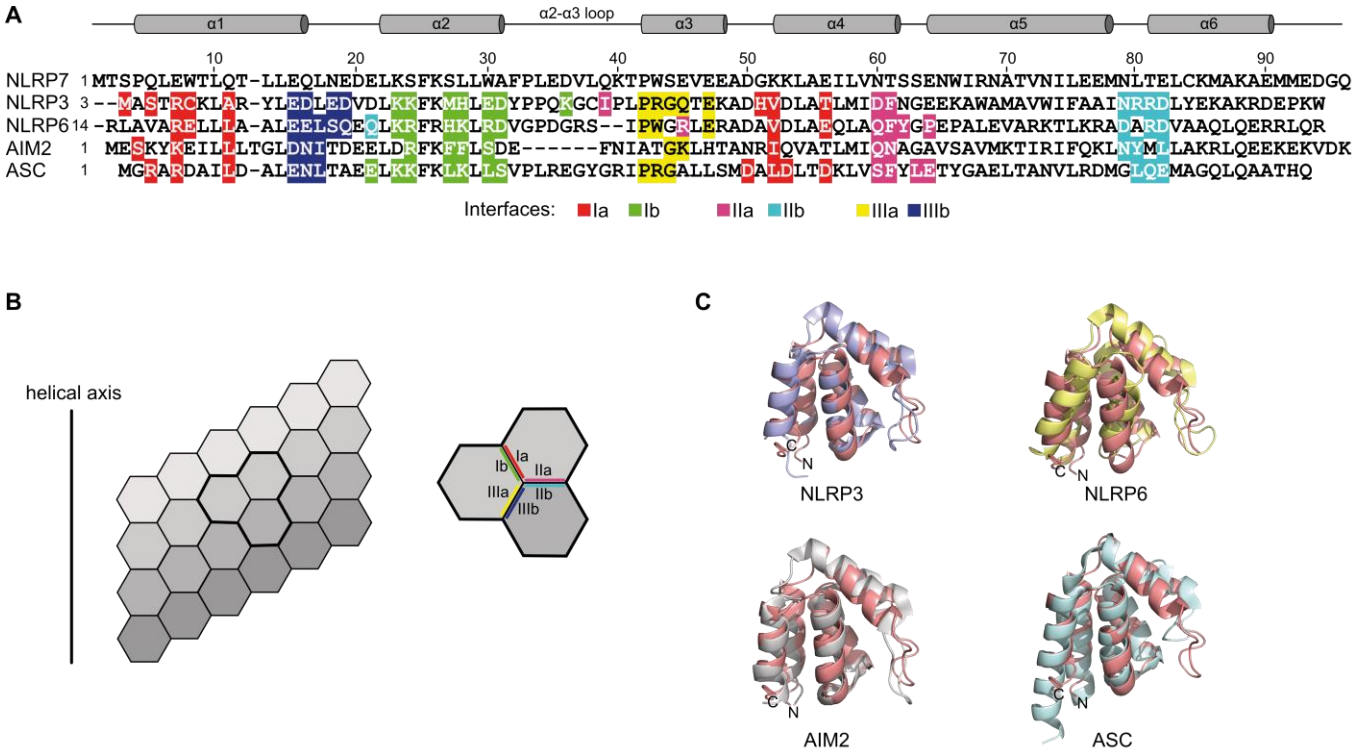

SI Figure 2: Alignment of the NLRP7-PYD with filament forming PYDs. A) Structure-based sequence alignment of the NLRP7-PYD with the PYDs of NLRP3, NLRP6, AIM2 and ASC. **B)** The PYDs of NLRP3, NLRP6, AIM2 and ASC are known to assemble helical filaments. The interactions between the individual PYD molecules are mediated at three interfaces (Ia-Ib, IIa-IIb, IIIa-IIIb). **C)** Superimposition of the structure of the NLRP7-PYD (PDB: 2KM6) with the structures of the NLRP3-PYD (7PZD), NLRP6-PYD (PDB: 6NCV), AIM2-PYD (PDB: 7K3R) and the ASC-PYD (PDB: 6Z2G).

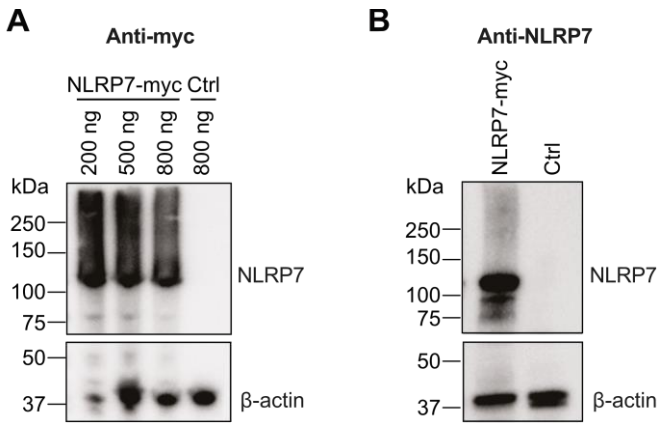

SI Figure 3: Validation of the anti-NLRP7 antibody (NBP2-94507, Novusbio). **A)** Western blot showing NLRP7$_{980}$-expression levels in HEK293T cells 24 h after transfection with indicated amounts of pCDNA-3.1-N-NLRP7$_{980}$-myc or empty vector (pCDNA-3.1-EGFP). Primary antibody: anti-myc-tag (Clone 9B11, #2276, Cell Signaling Technology). **B)** Western blot showing NLRP7$_{980}$-expression levels in HEK293T cells 24 h after transfection with 500 ng of pCDNA-3.1-N-NLRP7$_{980}$-myc or empty vector (pCDNA-3.1-EGFP). Primary antibody: (NBP2-94507, Novusbio).

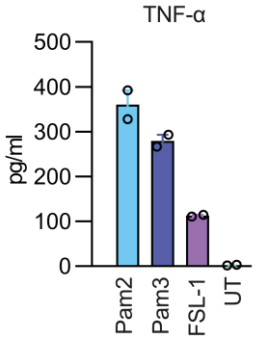

SI Figure 4: Validation of acLP activity. ELISA showing TNF-α levels in the supernatant of THP-1 cells treated with either 2 µg/ml Pam2CSK4 (Pam2), Pam3CSK4 (Pam3) or FSL-1 over night. UT: untreated. n = 1, 2 biological replicates.